A Wiener Chaos Based Approach to Stability Analysis of Stochastic Shear Flows

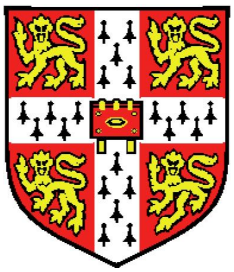

Simon James Cattell

Emmanuel College

University of Cambridge

This Dissertation is Submitted for the degree of

Doctor of Philosophy

April 2018

Declaration

This thesis describes work carried out in the Department of Applied Mathematics and Theoretical Physics of the University of Cambridge. The dissertation is the result of my own work, including nothing which is the outcome of work done in collaboration, except where specifically indicated in the text. All numerical calculations were computed using my own Python code, with the exception of sparse grid construction. Sparse grids were constructed using the Toolkit for Adaptive Stochastic Modelling and Non-Intrusive Approximation, which was developed at the Oak Ridge National Laboratory. Experimental shear flow data was kindly provided by Prof. Michael Gaster and Barry Crowley at City University. No part of the work contained herein has been submitted to any other university or place of learning for any degree, diploma or other qualification.

Acknowledgements

Firstly, I would like to thank my supervisor, Prof. Nigel Peake, for his guidance and support, knowing exactly when to steer me in the right direction, and when to give the freedom to pursue more independent ideas. Without his patience, knowledge and encouragement, this thesis would not have been possible. In addition to my supervisor, I would also like to thank my thesis committee, Dr. Stephen Cowley and Prof. Peter Schmid, not only for their insightful comments and encouragement, but also for the questions which incentivised me to widen my research. Further, I extend my thanks to Prof. Michael Gaster, for our stimulating discussions on the Blasius boundary layer, and Barry Crowley, who kindly provided the experimental data to motivate this thesis. I must also thank my office mates, Doran Khamis and Ridhwaan Suliman, who were always happy to help out, share ideas and provide a little distraction. Of course, no acknowledgement would be complete without giving thanks to my family. I am endlessly grateful for the support of my parents. This work was funded by EPSRC, whom I would also like to thank. Finally, my thanks go to Emmanuel College, who kindly provided a home.

Abstract

A Wiener Chaos Based Approach to Stability Analysis of Stochastic Shear Flows
Simon James Cattell

As the aviation industry expands, consuming oil reserves, generating carbon dioxide gas and adding to environmental concerns, there is an increasing need for drag reduction technology. The ability to maintain a laminar flow promises significant reductions in drag, with economic and environmental benefits. Whilst development of flow control technology has gained interest, few studies investigate the impacts that uncertainty, in flow properties, can have on flow stability. Inclusion of uncertainty, inherent in all physical systems, facilitates a more realistic analysis, and is therefore central to this research. To this end, we study the stability of stochastic shear flows, and adopt a framework based upon the Wiener Chaos expansion for efficient numerical computations. We explore the stability of stochastic Poiseuille, Couette and Blasius boundary layer type base flows, presenting stochastic results for both the modal and non modal problem, contrasting with the deterministic case and identifying the responsible flow characteristics.

From a numerical perspective we show that the Wiener Chaos expansion offers a highly efficient framework for the study of relatively low dimensional stochastic flow problems, whilst Monte Carlo methods remain superior in higher dimensions. Further, we demonstrate that a Gaussian auto-covariance provides a suitable model for the stochasticity present in typical wind tunnel tests, at least in the case of a Blasius boundary layer.

From a physical perspective we demonstrate that it is neither the number of inflection points in a defect, nor the input variance attributed to a defect, that influences the variance in stability characteristics for Poiseuille flow, but the shape/symmetry of the defect. Conversely, we show the symmetry of defects to be less important in the case of the Blasius boundary layer, where we find that defects which increase curvature in the vicinity of the critical point generally reduce stability. In addition, we show that

defects which enhance gradients in the outer regions of a boundary layer can excite centre modes with the potential to significantly impact neutral curves. Such effects can lead to the development of an additional lobe at lower wave-numbers, can be related to jet flows, and can significantly reduce the critical Reynolds number.

Contents

List of Figures

Chapter 1

Introduction

1.1 Overview

Stochastic partial differential equations (SPDEs) are an effective means of modelling complex physical phenomena, such as wave propagation [58], diffusion through random media [59], randomly forced Navier-Stokes equations [5], [90], [91], [89], and many other applications in materials science, chemistry and biology. In many instances, the dominant dynamics are modelled with deterministic physical laws, whilst stochastic processes represent the unresolved small scales and inherent uncertainties. The resulting equations are usually PDEs with uncertain coefficients, initial conditions, or random forcing. Unlike deterministic PDEs, the resulting solutions are random fields, and it is therefore important to quantify their statistical characteristics, the mean, variance and higher statistical moments.

The most popular numerical method for solving SPDEs is currently Monte Carlo (MC) simulation. However, this has a rather slow rate of convergence. Although a number of acceleration techniques have been developed, the method remains inefficient, especially for nonlinear SPDEs. Besides the MC method, the polynomial chaos expansion (PCE) has been gaining popularity as an alternative means of performing numerical stochastic computations. Here, we are primarily concerned with the Karhunen-Loève expansion (KLE), and the Itô-Wiener chaos expansion (WCE), and we study their applicability to problems concerning the stability of stochastic shear flows. More specifically, we consider stochastic Poiseuille, Couette and Blasius type flows.

1.2 Uncertainty Quantification

Scientific research and engineering design are increasingly reliant on computer simulations. Such simulations are often idealised forms of reality, and do not account for uncertainty, which is present in all physical systems. Such uncertainty has numerous sources, it may not be possible to precisely determine boundary conditions, forcing terms or a system's physical properties. Deterministic analysis can thus be rather limited, and we would ideally like a means to quantify the uncertainty in the resulting calculations, in turn allowing risk based decision making. For example, weather forecasts produce a prediction of the forthcoming weather, yet the actual weather is notoriously likely to differ. Another example is aircraft design, where computational fluid dynamics (CFD) software can easily produce a profile for a proposed design, but gives no estimate of how far the performance can deviate from the design, when small variations in flow conditions or manufacturing imperfections are present. Prototyping and physical testing are the only means to be certain, but this is not only time consuming but costly. Hence, if we were able to quantify the uncertainty in computer simulations, we would have a cheap and efficient means of risk analysis, which could be used to make more informed (risk based) decisions.

The principal objectives of uncertainty quantification are variance analysis, risk analysis and uncertainty management. That is, we would like to quantify the variation of a system about its mean, determine probabilities of the system exceeding certain critical operational thresholds, compare the relative importance of different uncertain sources and reduce the dominant ones. Clearly, with the ability to accurately quantify errors and uncertainties, computer simulations will become much more powerful tools in science and engineering.

1.3 Numerical Methods for Stochastic Partial Differential Equations

Monte Carlo (MC) methods are currently the most popular numerical technique for simulating solutions of SPDEs [41]. The idea is to simply sample the random parameters in the SPDEs and solve the governing equations realisation by realisation. For a given realisation of the random inputs, the SPDEs become deterministic and are thus solved via regular numerical methods. One solves the SPDEs many times, with different realisations, and approximates statistical moments with ensemble averages. MC simulations are not only simple to implement, but robust and have the ability to simultaneously deal with many sources of randomness.

Based on the central limit theorem, Monte Carlo ensemble averages converge at a rate of $\frac{1}{\sqrt{N}}$, where N is the total number of realisations. That is, if $x_i, i = 1, 2, ...N$, are independent identically distributed random variables with mean μ and standard deviation σ, then the long run average converges to the mean with standard error $\frac{\sigma}{\sqrt{N}}$, i.e $\frac{\frac{\sum_{i=1}^{N} x_i}{N} - \mu}{\frac{\sigma}{\sqrt{N}}} \sim \mathcal{N}(0, 1)$. This is a somewhat slow rate of convergence, and various acceleration techniques have thus been developed, such as quasi-Monte Carlo, antithetic variables, control variates, stratified sampling, importance and rejection sampling. These techniques are often effective for numerical integration type problems. However, their applicability to simulating nonlinear SPDEs is rather limited. Probability distributions are explicitly known for integration problems, and we can therefore tune an acceleration technique to the particular distribution. Due to the nonlinear dynamics of SPDEs, the distribution of the random solution will not generally be known in explicit form, the dynamics of the SPDEs evolve and transform the initial randomness, and the random solution may thus have very different distributions from the source. As a consequence, acceleration techniques based on source uncertainty may not work well for the random solutions themselves.

Other acceleration techniques, such as measure transformations and martingale representations, aim to reduce variance by exploiting the inherent stochastic structures of the problem. These methods rely on the availability of analytic information about the random solutions, and are therefore limited to simple stochastic ordinary differential equations. As a result, MC simulations combined with various acceleration techniques can still be computationally expensive, and alternative numerical methods are much desired, especially for SPDEs with complicated stochastic inputs.

In recently years, polynomial chaos expansions have gained popularity as a promising alternative to MC simulations, for the numerical solution of SPDEs. Originally developed by Norbert Wiener [92] in 1938, using Hermite polynomials, the Wiener chaos expansion constructs an orthonormal random basis for expanding homogeneous chaos depending on white noise. Wiener used this expansion to study problems in statistical mechanics. Based on Wiener's original idea, Cameron and Martin [11] developed a more explicit and intuitive formulation for the Wiener-Hermite expansion. Their development is based on an explicit discretization of the white noise process through its Fourier expansion. The approach is not only simpler to understand but more convenient to use, and has hence replaced Wiener's original formulation. This Fourier-Hermite expansion is commonly called a Wiener chaos expansion, and has become a useful tool in stochastic analysis involving white noise [30]. Xiu and Karniadakis [94] later generalised the Wiener chaos expansion to include other orthogonal polynomials, before using it to study flow-structure

interactions [15].

1.4 Stability of Shear Flows

Being constantly immersed in fluids, the study of fluid motion is a natural interest to us all. A flow is termed unstable when small excitations transform regular, ordered motion into unsteady, erratic motion. We commonly encounter both stable and unstable flows. We experience many natural flow fields, such as breathing air, swimming in water, feeling the gust of winds, typhoons, tornadoes and the ocean currents. Further, there are many unnatural flows which we are familiar with, the flow around an aerofoil, boat sails, hulls, turbines, steam engines and pumps. We are concerned with categorising, modelling, predicting and ultimately controlling the stability of such flows, and adopt the Navier Stokes equations as a reliable model for our stability analyses.

Hydrodynamic stability theory studies the transition from a stable to unstable fluid flow. This is traditionally achieved by modal, or eigenvalue analysis, perturbing a flow, linearizing about a steady state and searching for unstable eigenvalues (those in the complex upper half-plane which grow exponentially in time). Whilst eigenvalue analysis is known to correctly predict the stability of flows governed by normal operators (operators with orthogonal eigenvectors), analysis and experiments disagree when operators are not normal. For instance, plane Poiseuille flow, governed by a non-normal linear operator, is predicted eigenvalue stable for Reynolds numbers not exceeding 5772 [55], yet some experiments have proven unstable at Reynolds numbers as low as 1000 [61]. More recent studies have focused on the non-normality of the underlying operator. Henningson [34], Butler and Farrell [37], and Trefethen [86] showed that small perturbations to such flows can be significantly amplified whilst all eigenvalues remain in the lower complex half-plane.

These works indicated that some eigenvalues can be extremely sensitive to operator perturbations, and that transient effects should not be ignored. All such studies consider generic operator perturbations. Such generic perturbations may introduce artificial coupling and a more structured perturbation may be more realistic. That is, it may be more physically meaningful to perturb only those parts of the operator corresponding to the base flow. In this way one has the capacity to investigate velocity profiles more commonly found in experiments by making a modification, or adding noise, to the traditional deterministic base flows studied. Bottaro et al [9] performed such a study, investigating the sensitivity of the Orr-Sommerfeld operator's eigenvalues for variations in a plane Couette base flow. They showed

that sufficiently large modifications to the base flow induce linear instability, with the critical Reynolds number varying as r^{-1} (where r is an energy based measure of the size of the modification $\delta U(y)$, $r^2 = \int_y \delta U^2(y) dy$).

We extend such studies by taking a statistical view. In reality, there is inherent variation in physical systems, or simply a lack of information to specify the governing parameters. Random fluctuations in parameter values may have a fundamental effect on solutions, such as transient growth. To alleviate the limitations of deterministic analysis, we propose a stochastic framework, based upon generalised polynomial chaos. Adopting this framework, we here relax the assumption that the base flow is deterministic and known. One may argue that such modified flows do not satisfy the Navier-Stokes equations. However, there is no steady, incompressible, inviscid, unidirectional base flow that does not satisfying the Euler equations. An arbitrary profile is therefore in convective equilibrium, slowly diffusing at a rate which is inversely proportional to the Reynolds number. If the growth rate of the instability is faster than such diffusion, then the velocity profile can effectively be frozen for stability analysis. Bottaro et al [9] demonstrates that this is indeed the case for plane Couette flow.

1.5 Summary of Work

We study the linear temporal stability of simple parallel stochastic shear flows, namely Poiseuille, Couette and Blasius type profiles. We adopt a framework based upon the Wiener Chaos expansion, and supplement these analyses with Monte Carlo simulations. We focus centrally on the Poiseuille and Blasius type flows, present stochastic versions of the spectra, the neutral curve and the perturbation energy growth function.

This current chapter provides an introduction to the topic, chapter two sets out the mathematical theory of numerical methods for stochastic computations, and chapter three summarises stability theory. This is all well established theory upon which we rely in later chapters. The originality in this work is found in chapters four to six, where we amalgamate stability theory with spectral methods for stochastic computations, and study the stability of shear flows subject to stochastic defects. Chapter four motivates the choice of stochasticity and details the numerical implementation. In chapter five, we extensively study the stability of a Poiseuille base flow with stochastic defects, making a brief comparison with the Couette type flow, and in chapter six we study the stochastic Blasius boundary layer.

From a numerical perspective, we show that the Wiener Chaos expansion offers a

highly efficient framework for the study of relatively low dimensional stochastic flow problems, whilst Monte Carlo methods remain superior in higher dimensions.

From a physical perspective, we demonstrate that a Gaussian auto-covariance provides a suitable model for the stochasticity present in typical wind tunnel tests, at least in the case of a Blasius boundary layer. We also show that stochasticity becomes increasingly important as the correlation length of the base flow is reduced. Spectral analysis reveals that modes in the vicinity of the Y-branch are much more sensitive to stochastic defects than those further away. Furthermore, we show such stochastic spectral analysis to be bounded by the log resolvent norm contours of the ϵ-pseudospectra, which are associated with a more general unstructured perturbation. We also show that neutral curves can be highly sensitive to stochastic defects, which can significantly reduce the critical Reynolds number and may partially explain the deviations between theory and experiment, which are commonly observed. Our transient analyses reveal that stochastic defects have no initial impact on perturbation energy growth and, in general, the effects of stochasticity accumulate with time. We show that variability (standard deviation) in the perturbation energy growth increases almost linearly, relative to the mean, with time, in the case of Poiseuille flow, whilst variability in the Couette flow remains of a negligible magnitude at all times. We also show that it is neither the number of inflection points in a defect, nor the input variance attributed to a defect, that influences the variance in perturbation energy growth attributed to that defect, for Poiseuille flow. We conclude that instability, arising from stochastic imperfections, must therefore be of a non-inflectional nature, and viscous instead. More precisely, we show that defects which increase velocity gradients can enhance energy transfer from the base flow to the perturbations. Furthermore, when these defects are anti-symmetric about the channel centre-line, an increase in energy transfer in one region of the channel is typically cancelled by a decrease in another, and it is therefore the symmetric defects which contribute most. Conversely, the symmetry of defects is less important in the case of the Blasius boundary layer, where we find that defects which increase curvature in the vicinity of the critical point generally reduce stability. In addition, we show that defects which enhance gradients in the outer regions of a boundary layer can be related to jet flows, and can significantly impact neutral curves, with the development of an additional lobe at lower wave-numbers, which can significantly reduce the critical Reynolds number.

Chapter 2

Numerical Methods for Stochastic Computations

In this chapter, the fundamentals of stochastic spectral expansions are presented. We focus on random processes in L^2 and seek the Fourier-like expansions which converge with respect to the associated norm. Before presenting the theory of stochastic spectral expansions, we briefly review the conventional approach to stochastic simulation, Monte Carlo and its variants.

To clarify the discussion, a brief introduction of notation is first provided.

Let $(\Omega, \mathscr{F}, P)$ be a probability space, and $\omega \in \Omega$ be a random event, where Ω is a sample space, $\mathscr{F}$ is a σ-algebra on Ω, and $P : \mathscr{F} \to [0, 1]$ is a probability measure on $\mathscr{F}$. Let $L^2(\Omega, P)$ denote the Hilbert space of second-order random variables on $(\Omega, \mathscr{F}, P)$, with inner product $\langle ., . \rangle$ and norm $\|.\|$

$$\langle u, v \rangle_\Omega = \int_\Omega u(\omega)v(\omega)dP(\omega) = \mathrm{E}[uv] \ \forall \ u, v \in L^2(\Omega, P), \tag{2.1}$$

$$\|u\|_\Omega = \langle u, u \rangle_\Omega^{\frac{1}{2}} < \infty. \tag{2.2}$$

We will consider second-order stochastic processes of dimension d, indexed by $\mathbf{x} \in \Theta$, $u(\mathbf{x},\omega) : \Theta x \Omega \to \mathbb{R}$, and assume that all realisations are almost surely in the Hilbert space.

2.1 Monte Carlo Methods

In applied mathematics and statistics, we commonly encounter problems involving numerical integration, where the integrands are discontinuous or high dimensional.

The Monte Carlo (MC) method [79], applicable to all square integrable functions and independent of the problem dimension, is a practical and very popular approach to numerical integration. The method, commonly used to approximate statistical moments with empirical averages, is justified by the law of large numbers and is based upon the point sampling paradigm. Efficiency is highly dependent upon sample placement and generally improved with increased uniformity of samples. Quasi-Monte Carlo (QMC) employs deterministic inputs to more evenly cover the input space, and generally converges faster than the traditional (random sampling) MC approach.

We briefly review traditional MC sampling and discuss stratification methods, such as jittering, and multi-stratification methods, such as Latin Hypercube sampling (LHS). These techniques aim to improve efficiency by evenly distributing the sampling points between a large number of hyper-rectangular sub-domains of the unit hypercube $[0,1)^d$, which represents the input domain. In this context, one can view QMC as the logical limit of stratification.

2.1.1 Crude Monte Carlo

Suppose we are tasked with computing the probabilistic average of the scalar random variable $u(\omega)$, which we may write in integral form

$$\bar{u} = \int_\Omega u(\omega) dP(\omega) = \int_\Omega u(\omega) p(\omega) d\omega, \tag{2.3}$$

where $p(\omega)$ is the probability density function on Ω, $p(\omega) \geq 0$ and $\int_\Omega p(\omega) d\omega = 1$.

In crude MC sampling, we generate n independent samples, $\omega_1, ..., \omega_n$, from the density $p(\omega)$, empirically estimate the average

$$\bar{u} \approx \tilde{u}_n = \frac{1}{n} \sum_{i=1}^{n} u(\omega_i), \tag{2.4}$$

and appeal to the strong law of large numbers, which states that crude MC always converges to the right answer as n increases without bound. More formally, $\tilde{u}_n$ almost surely equals $\bar{u}$ as $n \to \infty$, that is $P(\lim_{n\to\infty} \tilde{u}_n = \bar{u}) = 1$.

Suppose that $u(\omega)$ has finite variance, $\sigma^2 = \mathrm{Var}[u(\omega)] := \int_\Omega (u(\omega) - \bar{u})^2 p(\omega) d\omega$, then we have that $\mathrm{E}[(\tilde{u}_n - \bar{u})^2] = \frac{\sigma^2}{n}$, and the root mean square error (RMSE) of sampling decays as the square root of the number of samples. Compared to classical quadrature rules [16], for smooth low dimensional functions, this is a rather slow rate

of convergence. However, crude MC often remains superior in higher dimensions, or when integrating discontinuous functions.

2.1.2 Stratification

Recalling that MC methods converge with the root mean square error, $\frac{\sigma}{\sqrt{n}}$, it is clear that we may reduce the error by either increasing the number of samples or reducing the process variance. Stratification takes the second approach, aiming to reduce the sample variance. If the domain of ω is written as the union of strata, $\Omega = \cup_{i=1}^{h} \Omega_i$, where $\Omega_i \cap \Omega_j = \emptyset \ , \forall i \neq j$. Integration is then performed within each stratum and finally combined for the final result. One typically maps from the domain of interest Ω, to a more convenient space, namely the d dimensional unit hypercube $\Omega^* = [0,1)^d$. This space is then easily sampled, by drawing samples from the standard uniform distribution, $U[0,1)$.

The method proceeds by taking a set of samples from each strata, say $\omega_i^1, ..., \omega_i^{n_i}$ are the n_i samples from the ith strata, then the results are combined

$$\bar{u} \approx \tilde{u}_{strat}^h = \sum_{i=1}^{h} \frac{|\Omega_i|}{n_i} \sum_{j=1}^{n_i} u(\omega_i^j), \tag{2.5}$$

where $|\Omega_i|$ denotes the volume of the ith stratum, and we have h strata in total.

Taking the expectation of this expression, we get

$$\begin{aligned} \mathrm{E}[\tilde{u}_{strat}^h] &= \sum_{i=1}^{h} \frac{|\Omega_i|}{n_i} \sum_{j=1}^{n_i} \mathrm{E}[u(\omega_i^j)] = \sum_{i=1}^{h} \frac{|\Omega_i|}{n_i} \left\{ \frac{n_i}{|\Omega_i|} \int_{\Omega_i} u(\omega) d\omega \right\} \\ &= \sum_{i=1}^{h} \int_{\Omega_i} u(\omega) d\omega = \int_{\cup_{i=1}^{h} \Omega_i = \Omega} u(\omega) d\omega = \bar{u}, \end{aligned}$$

where the last equality holds because the strata are pairwise disjoint. From this expression, we can clearly see that $\tilde{u}_{strat}^h$ is an unbiased estimate of $\bar{u}$.

The stratified variance depends on the sample size, n_i, which is commonly allocated on a proportional basis such that $n_i = n\frac{|\Omega_i|}{|\Omega|}$. Noting that $\omega \sim U[0,1)^d$, $i(\omega)$ is a random variable taking the value l with probability $|\Omega_l|$, the variance formula reads

$$\sigma^2 = \mathrm{Var}[u(\omega)] = \mathrm{E}[\mathrm{Var}[u(\omega)|i(\omega)]] + \mathrm{Var}[\mathrm{E}[u(\omega)|i(\omega)]]$$
$$= \sum_{i=1}^{h} |\Omega_i|\sigma_i^2 + \sum_{i=1}^{h} |\Omega_i| \left\{\mu_i - \bar{u}\right\}^2,$$

where $\mu_i = \frac{1}{|\Omega_i|}\int_{\Omega_i} u(\omega)d\omega$. The variance thus has contributions from both within and between strata. Now consider the variance of the stratified estimate

$$\mathrm{Var}[\tilde{u}^h_{strat}] = \sum_{i=1}^{h} \frac{|\Omega_i|^2}{n_i}\sigma_i^2 = \frac{1}{n}\sum_{i=1}^{h} |\Omega_i|^2\sigma_i^2 \leq \frac{\sigma^2}{n}, \tag{2.6}$$

which implies that stratified sampling with proportional allocation does not increase the variance. In fact, the variance of crude MC provides an upper bound tot the variance of stratified MC. Proportional allocation is not always optimal, if estimates of σ_i are indeed available, they should be used to optimise allocation. However, poor estimates can result in sampling with variance exceeding the crude MC approach and it is therefore advisable to stick to proportional allocation, unless one is very certain of their σ_i estimates. A common form of stratification, suited to the unit hypercube is Jitter [31]. The idea is to partition the unit cube, $[0,1)^d$, into $h = m^d$ congruent cubical regions and take a single point from each.

It is worth noting that any function which is constant within strata will be integrated without error. Let $u^i_{dev}(\omega) = u(\omega) - \mu_i$ define the deviation of $u(\omega)$ from the mean within the ith strata, then stratified sampling reduces the MC variance from $\frac{\sigma^2[u(\omega)]}{n}$ to $\frac{\sigma^2[u^i_{dev}(\omega)]}{n}$.

2.1.3 Multiple Stratification and Latin Hypercube Sampling

Suppose we wish to sample n points in $[0,1)^2$. Sampling one point from each of n equally spaced vertical strata may be a good strategy, but only if the function of interest depended primarily on the horizontal coordinate. Conversely, if the vertical coordinate was more important, we should slice the hypercube into horizontal strata. However, it is possible to stratify both ways with the same sample size, and this is termed Latin hypercube sampling (LHS) [48], or n-rooks sampling [77]. As an example, we plot LHS samples for $n = 10$ in figure 2.1:

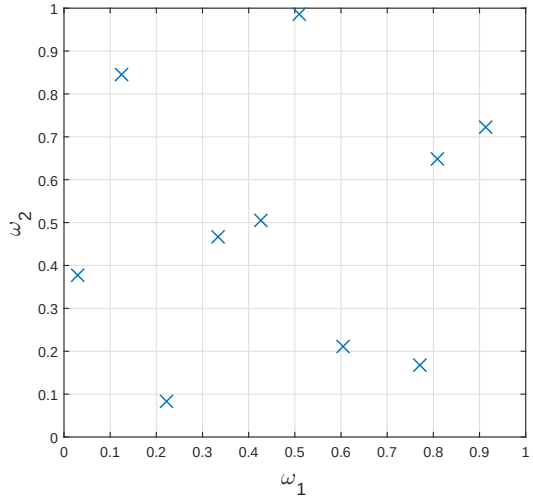

Figure 2.1: Example of Latin-Hypercube samples on the unit cube $[0,1)^2$, with $n = 10$.

We know that stratification with proportional allocation is at least as good as crude MC, and the same is almost true for LHS. It can be shown [57], for $n \geq 2$, $d \geq 1$ and any square integrable function, $u(\omega)$, that the LHS variance is no greater than $\frac{\sigma^2}{n-1}$, and in the worst case LHS is like crude MC with one sample less.

2.2 Spectral Methods

We next present the theory of stochastic spectral expansions, namely the Karhunen-Loève and polynomial chaos (or more specifically, the Wiener chaos) expansions. Unless otherwise stated, we take from the comprehensive review of Maitre and Knio [47].

2.2.1 Karhunen-Loève Expansion

The Karhunen-Loève expansion (KLE) [45],[38], also known as proper orthogonal decomposition (POD), or principal component analysis (PCA) in the finite dimensional case, is a spectral decomposition of a stochastic processes in terms of the eigenfunctions of its auto-covariance function. Let $K_u(\mathbf{x}, \mathbf{x}')$ be the auto-covariance function of the stochastic process $u(\mathbf{x}, \omega)$. Being an auto-covariance function, this kernel is bounded, symmetric and positive definite, and in accordance with Mercer's theorem [50], there exists a complete set of eigenvalues and orthogonal eigenfunc-

tions, $\{\gamma_i, e_i(\mathbf{x})\}$, such that

$$K_u(\mathbf{x}, \mathbf{x}') = \sum_{i=1}^{\infty} \gamma_i e_i(\mathbf{x}) e_i(\mathbf{x}'). \tag{2.7}$$

Exploiting orthogonality of the basis, the eigenvalues and eigenfunctions are recovered as solutions of the homogeneous Fredholm integral equation of the second kind

$$\int_{\Theta} K_u(\mathbf{x}, \mathbf{x}') e_j(\mathbf{x}') d\mathbf{x}' = \sum_{i=1}^{\infty} \gamma_i e_i(\mathbf{x}) \int_{\Theta} e_i(\mathbf{x}') e_j(\mathbf{x}') d\mathbf{x}' = \sum_{i=1}^{\infty} \gamma_i e_i(\mathbf{x}) \delta_{ij} = \gamma_j e_j(\mathbf{x}). \tag{2.8}$$

The stochastic process $u(\mathbf{x}, \omega)$ can then be decomposed

$$u(\mathbf{x}, \omega) = \overline{u}(\mathbf{x}) + \sum_{i=1}^{\infty} \sqrt{\gamma_i} e_i(\mathbf{x}) \zeta_i(\omega), \tag{2.9}$$

where $\zeta_i(\omega) = \frac{1}{\sqrt{\gamma_i}} \langle u(\mathbf{x}, \omega), e_i(\mathbf{x}) \rangle_{\Theta}$ are zero mean, unit variance, mutually orthogonal random variables, and $\overline{u}(\mathbf{x})$ is the mean of the process.

The auto-covariance can be recovered from the underlying process, and the expansions are clearly consistent

$$\begin{aligned} K_u(\mathbf{x}, \mathbf{x}') &= \mathrm{E}[(u(\mathbf{x}) - \overline{u}(\mathbf{x}))(u(\mathbf{x}') - \overline{u}(\mathbf{x}'))] \\ &= \mathrm{E}[\sum_{i=1}^{\infty} \sum_{j=1}^{\infty} \sqrt{\gamma_i} \sqrt{\gamma_j} e_i(\mathbf{x}) e_j(\mathbf{x}') \zeta_i(\omega) \zeta_j(\omega)] \\ &= \sum_{i=1}^{\infty} \sum_{j=1}^{\infty} \sqrt{\gamma_i} \sqrt{\gamma_j} e_i(\mathbf{x}) e_j(\mathbf{x}') \delta_{ij} \\ &= \sum_{i=1}^{\infty} \gamma_i e_i(\mathbf{x}) e_i(\mathbf{x}'). \end{aligned}$$

In practice, the expansion must be truncated to a finite number of terms, d, which is effectively the number of stochastic dimensions. The truncation error decreases monotonically with the number of retained terms, and the expansion is known to be optimal in minimising the mean squared error. If we assume that the eigenvalues are arranged in descending order, $\gamma_1 \geq \gamma_2 \geq ... \geq \gamma_d$, and limit the expansion to

only d terms, we get an error

$$\epsilon_d(u(\mathbf{x},\omega)) = \sum_{i>d} \sqrt{\gamma_i} e_i(\mathbf{x})\zeta_i(\omega). \tag{2.10}$$

And a mean squared error

$$\begin{aligned}
\epsilon_d^2(u(\mathbf{x},\omega)) &= \mathrm{E}[\sum_{i>d}\sum_{j>d} \sqrt{\gamma_i} e_i(\mathbf{x})\zeta_i(\omega)\sqrt{\gamma_j} e_j(\mathbf{x})\zeta_j(\omega)] \\
&= \sum_{i>d}\sum_{j>d} \sqrt{\gamma_i} e_i(\mathbf{x})\sqrt{\gamma_j} e_j(\mathbf{x})\delta_{ij} \\
&= \sum_{i>d} \gamma_i.
\end{aligned}$$

In other words, no other approximation in a series of d terms results in a smaller mean squared error. The expansion will converge for any distribution, and the rate of spectral decay is proportional to the process's degree of correlation. If a process is poorly correlated, a higher number of terms is needed, and in the limit when the process is white noise, i.e.$K_u(\mathbf{x},\mathbf{x}') \sim \delta(||\mathbf{x}-\mathbf{x}'||)$, an infinite number of terms would be required.

2.2.1.1 Numerical Solution

The numerical solution of the Fredholm integral equation is based upon the fundamental idea of seeking an approximate solution in some finite space,

$$V = span\left\{h_1(\mathbf{x}), h_2(\mathbf{x}), ...h_N(\mathbf{x})\right\}, \tag{2.11}$$

and expressing the solution as a linear combination in the basis functions. Letting $\{h_n(\mathbf{x}); n = 1, ..., N\}$ form a complete basis in the Hilbert space $L^2(\Theta)$, we approximate each eigenfunction as a truncated expansion in this basis,

$$e_i(\mathbf{x}) = \sum_{k=1}^{N} d_k^i h_k(\mathbf{x}), i = 1, ..., N, \tag{2.12}$$

where d_k^i are constant coefficients for the ith eigenfunction. Introducing the expan-

sion gives a residual error,

$$\varepsilon_d = \sum_{k=1}^{N} d_k^i \left(\int_{-1}^{1} K_u(\mathbf{x}, \mathbf{x}') h_k(\mathbf{x}') d\mathbf{x}' - \gamma_i h_k(\mathbf{x}) \right). \tag{2.13}$$

In order to determine the approximate solution we must solve for the N coefficients in the expansion, and we must therefore generate a set of N simultaneous equations in these coefficients. Various methods for determining the coefficients exist, and generally involve minimising the residual in some sense. The residual is not only a function of the chosen coefficients but also depends upon the spatial position, and it is therefore common to attempt to minimise the residual in an average sense across the whole domain. One means of achieving this is via a collocation method [24], by simply demanding the residual be zero at a set of N distinct points. Another means of determining the coefficients is via the Galerkin method [25], which is a special case of the weighted residual method [21]. The method of weighted residuals requires that the residual be orthogonal to a set of N weight functions. The Galerkin method assumes the approximating basis as the weight functions, and the idea here is to seek the coefficients such that the residual is orthogonal to the space spanned by the approximating basis, which is analogous to least squares where the residual is orthogonal to the fitted solution. Demanding the residual to be orthogonal to each of the N basis functions gives N simultaneous equations which can be solved for the coefficients. For completeness, it should be noted that the collocation method also belongs to the general class of weighted residuals, where the weight functions are delta functions centred on the collocation points.

The least-squares principle is equivalent to demanding the true error $(e_i(\mathbf{x}) - \sum_{k=1}^{N} d_k^i h_k(\mathbf{x}))$ to be orthogonal to the space V. With an integral equation we do not know the error, as we do not know the true $e_i(\mathbf{x})$, so we must instead require the residual ε_d to be orthogonal to V. This is exactly what the Galerkin method does, it is based on the projection of the residual onto the space of approximating polynomials, its accuracy is thus optimal in an L^2 sense and we therefore select this method.

We therefore seek the coefficients d_k^i such that the residual is orthogonal to the space spanned by the approximating basis, $< \varepsilon_d, h_j(\mathbf{x}) >= 0, \forall j = 1, ..., N$. Enforcement of the constraint yields a system of equations,

$$\sum_{k=1}^{d} d_k^i \left(\int_{-1}^{1} \int_{-1}^{1} K_u(\mathbf{x}, \mathbf{x}') h_k(\mathbf{x}') h_j(\mathbf{x})) d\mathbf{x} d\mathbf{x}' - \gamma_i \int_{-1}^{1} h_k(\mathbf{x}) h_j(\mathbf{x}) d\mathbf{x} \right) = 0, \tag{2.14}$$

which, omitting the index of the eigenfunction, can be written in matrix form as a generalised eigenvalue problem,

$$[\mathbf{K} - \gamma\mathbf{M}]\mathbf{d} = 0, \tag{2.15}$$

where $K_{ij} = \int_{-1}^{1}\int_{-1}^{1} K_u(\mathbf{x},\mathbf{x}')h_i(\mathbf{x})h_j(\mathbf{x}')d\mathbf{x}d\mathbf{x}'$, and $M_{ij} = \int_{-1}^{1} h_i(\mathbf{x})h_j(\mathbf{x})d\mathbf{x}$. This eigenvalue problem can be solved numerically for the N eigen-pairs, which are in turn used to reconstruct the original expansion basis, $e_i(\mathbf{x}) = \sum_{k=1}^{N} d_k^i h_k(\mathbf{x})$.

One of the considerations in this numerical solution is the cost of the computations. When the correlation kernel decays rapidly with $\mid \mathbf{x}-\mathbf{x}' \mid$ the eigenfunctions tend to be highly oscillatory, and a large number of basis functions, $h_i(\mathbf{x})$, are consequently required for adequate approximation. In turn, the dimension of the matrices become large and the computational cost increases. Conversely, when the process is strongly correlated the correlation decay is much slower and a much smaller basis is sufficient.

2.2.1.2 Gaussian Processes

As discussed, the KLE expands a stochastic process with the eigenfunctions of its correlation kernel. There are actually infinitely many second-order processes with the same correlation kernel and thus the same set of expanding eigenfunctions. Such processes, sharing the same auto-covariance, are distinguished by the joint probability of the random variables. By construction, these random variables are zero mean, unit variance and mutually orthogonal. In many instances, the random process is (assumed to be) Gaussian, leading to significant simplifications. The KLE of a Gaussian process involves random variables which are not only uncorrelated but independent. Further, the joint probability density factors as

$$\mu^d(\boldsymbol{\zeta}(\omega)) = \prod_{j=1}^{d} \frac{1}{\sqrt{2\pi}} \exp\left(\frac{-\zeta_j^2(\omega)}{2}\right) d\zeta_j(\omega), \tag{2.16}$$

which greatly simplifies the sampling of the process.

Essentially, the KLE is an expansion in deterministic functions (eigenfunctions) and random variables. The deterministic functions are fixed by the form of the auto-correlation, but the joint probability law of the random variables remains unknown. Specifically, one can only ascertain that the random variables have zero mean, unit variance, and are mutually orthogonal. One could modify the structure of the KLE by relaxing its bi-orthogonal condition, so offering more flexibility. In particular, one could prescribe a priori the functional form of the random coefficients in the

expansion, for instance as polynomials of independent random variables with given distribution, and then seek the (not necessarily) deterministic functions that minimise a given error norm. Such an approach corresponds precisely to polynomial chaos decomposition which we outline next.

2.2.2 Polynomial Chaos Expansion

Let $\{\zeta_i(\omega)\}_{i=1}^{\infty}$ be a sequence of centred, normalised, mutually orthogonal Gaussian variables. Let $\hat{\Gamma}_O$ denote the space of polynomials in $\{\zeta_i(\omega)\}_{i=1}^{\infty}$ having degree no greater than O. Let Γ_O be the set of polynomials in $\hat{\Gamma}_O$ but orthogonal to $\hat{\Gamma}_{O-1}$, and let $\tilde{\Gamma}_O$ be the space spanned by Γ_O. That is

$$\hat{\Gamma}_O = \hat{\Gamma}_{O-1} \oplus \tilde{\Gamma}_O, \tag{2.17}$$

$$L^2(\Theta, P) = \oplus_{i=0}^{i=\infty} \tilde{\Gamma}_i. \tag{2.18}$$

Subspace $\tilde{\Gamma}_O$ is called the Oth homogeneous chaos. Γ_O is called the polynomial chaos of order O, and consists of all polynomials of order O, involving all possible combinations of the random variables $\{\zeta_i(\omega)\}_{i=1}^{\infty}$.

Every second-order (finite variance) random variable $u(\omega) \in L^2(\Omega, P)$ admits a polynomial chaos (PC) representation of the form [11]

$$\begin{aligned} u(\omega) =& u_0\Gamma_0 + \sum_{i_1=1}^{\infty} u_{i_1}\Gamma_1(\zeta_{i_1}(\omega)) \\ &+ \sum_{i_1=1}^{\infty}\sum_{i_2=1}^{i_1} u_{i_1 i_2}\Gamma_2(\zeta_{i_1}(\omega), \zeta_{i_2}(\omega)) \\ &+ \sum_{i_1=1}^{\infty}\sum_{i_2=1}^{i_1}\sum_{i_3=1}^{i_2} u_{i_1 i_2 i_3}\Gamma_3(\zeta_{i_1}(\omega), \zeta_{i_2}(\omega), \zeta_{i_3}(\omega)) \\ &+ \dots . \end{aligned}$$

This expansion is convergent in the mean square sense, and, by construction, all polynomials are mutually orthogonal with respect to the Gaussian measure associated with $\{\zeta_i(\omega)\}_{i=1}^{\infty}$, i.e. $\prod_{j=1}^{\infty} \frac{1}{\sqrt{2\pi}} \exp\left(\frac{-\zeta_j^2(\omega)}{2}\right) d\zeta_j(\omega)$.

Whilst the outlined construction involves an infinite collection of normalised, uncorrelated, Gaussian random variables, the representation is restricted to a finite

number in practice. The expansion restricted to a dimension d and order O is the subspace of $\tilde{\Gamma}_O$ generated by the elements that involve only d random variables. The infinite sums are subsequently replaced by finite sums over d dimensions. For instance, for an expansion with two dimensions ($d = 2$) we have

$$\begin{aligned} u(\omega) =& u_0\Gamma_0 + \sum_{i_1=1}^{2} u_{i_1}\Gamma_1(\zeta_{i_1}(\omega)) \\ &+ \sum_{i_1=1}^{2}\sum_{i_2=1}^{i_1} u_{i_1 i_2}\Gamma_2(\zeta_{i_1}(\omega), \zeta_{i_2}(\omega)) \\ &+ \sum_{i_1=1}^{2}\sum_{i_2=1}^{i_1}\sum_{i_3=1}^{i_2} u_{i_1 i_2 i_3}\Gamma_3(\zeta_{i_1}(\omega), \zeta_{i_2}(\omega), \zeta_{i_3}(\omega)) \\ &+ \dots , \end{aligned}$$

which can be written as

$$\begin{aligned} u(\omega) =& u_0\Gamma_0 + u_1\Gamma_1(\zeta_1(\omega)) + u_2\Gamma_1(\zeta_2(\omega)) \\ &+ u_{11}\Gamma_2(\zeta_1(\omega), \zeta_1(\omega)) + u_{21}\Gamma_2(\zeta_2(\omega), \zeta_1(\omega)) + u_{22}\Gamma_2(\zeta_2(\omega), \zeta_2(\omega)) \\ &+ u_{111}\Gamma_3(\zeta_1(\omega), \zeta_1(\omega), \zeta_1(\omega)) + u_{211}\Gamma_3(\zeta_2(\omega), \zeta_1(\omega), \zeta_1(\omega)) + u_{221}\Gamma_3(\zeta_2(\omega), \zeta_2(\omega), \zeta_1(\omega)) \\ &+ u_{222}\Gamma_3(\zeta_2(\omega), \zeta_2(\omega), \zeta_2(\omega)) + \dots . \end{aligned}$$

In order to more simply manipulate polynomial chaos expansions, we rely on a univocal relation between the functionals, $\Gamma(\boldsymbol{\zeta})$, and new functionals, $\Phi(\boldsymbol{\zeta})$. The multi-dimensional functionals, $\Phi(\boldsymbol{\zeta})$, will be constructed as suitable products of one dimensional functions, $\phi_i(\zeta_j)$, depending on the total order O. Here $\phi_i(\zeta_j)$ is the ith one dimensional polynomial in the basis, in the jth variable ζ_j. The compact expression is then

$$u(\omega) = \sum_{i=0}^{\infty} u_i \Phi_i(\zeta_1(\omega), \zeta_2(\omega), \dots). \tag{2.19}$$

The deterministic expansion coefficients, u_i, are simply termed PC coefficients, it is conveniently assumed that $\Phi_0 = \Gamma_0$, and the univocal relation is set such that the functionals, Φ_i, are ordered in ascending polynomial order.

In order to form such a basis, let $\boldsymbol{\alpha}^i = (\alpha_1^i, ..., \alpha_d^i)$ define a multi-index with non-negative integer components, where α_j^i indicates the order of the jth one-

dimensional polynomial in the *ith* multi-dimensional polynomial. The multi index can be created recursively, and the interested reader may refer to appendix B.2 Multi-Index Construction for more information. Letting $\lambda(O)$ define a set of these multi-indices,

$$\lambda(O) = \left\{ \boldsymbol{\alpha_i} : \sum_{j=1}^{d} \alpha_j^i = O \right\}, \tag{2.20}$$

the *Oth* order polynomial chaos basis is then constructed as

$$\Gamma_O = \left\{ \cup_{\boldsymbol{\alpha} \in \lambda(O)} \prod_{\alpha_1}^{\alpha_d} \phi_{\alpha_i}(\zeta_i(\omega)) \right\}. \tag{2.21}$$

And for two dimensions we can express the expansion as

$$\begin{aligned} u(\omega) =& u_0\Phi_0 + u_1\phi_1(\zeta_1(\omega)) + u_2\phi_1(\zeta_2(\omega)) \\ &+ u_{11}\phi_2(\zeta_1(\omega)) + u_{21}\phi_1(\zeta_2(\omega))\phi_1(\zeta_1(\omega)) + u_{22}\phi_2(\zeta_2(\omega)) \\ &+ u_{111}\phi_3(\zeta_1(\omega)) + u_{211}\phi_1(\zeta_2(\omega))\phi_2(\zeta_1(\omega)) + u_{221}\phi_2(\zeta_2(\omega))\phi_1(\zeta_1(\omega)) \\ &+ u_{222}\phi_3(\zeta_2(\omega)) + \dots . \end{aligned}$$

2.2.2.1 Hermite Polynomials

The Hermite polynomials form a convenient choice for the one dimensional basis functions $\phi_i()$. Let z be a unit normal random variable and dz be the Lebesgue measure, then $\mu(dz) = \rho(z)dz = \frac{1}{\sqrt{2\pi}} \exp\left(\frac{-z^2}{2}\right)dz$ is the Gaussian measure. The normalised Hermite polynomials $\{H_n(z); n = 0, 1, ...\}$, defined as

$$H_n(z) = (n!)^{-\frac{1}{2}}(-1)^n \exp\left(\frac{z^2}{2}\right)\frac{\partial^n}{\partial z^n}\exp\left(\frac{-z^2}{2}\right), \tag{2.22}$$

form a complete orthonormal basis in the Hilbert space $L^2(\mathbb{R}, \mu)$ [13]. Noting $H_0(z) = 1$, the expectation and variance can be expressed as

$$\mathrm{E}[H_i(z)] = \langle H_i(z), 1\rangle_\Omega = \langle H_i(z), H_0(z)\rangle_\Omega = \delta_{io}, \tag{2.23}$$

and

$$\mathrm{Var}[H_i(z)] = \mathrm{E}[(H_i(z) - \delta_{io})^2] = \begin{cases} 0, & \text{if i} = 0 \\ \langle H_i(z), H_i(z)\rangle_\Omega = 1, & \text{otherwise} \end{cases}. \tag{2.24}$$

2.2.2.2 Wiener Chaos Expansion

When adopting the Hermite polynomials as the basis, the Polynomial chaos expansion is commonly termed the Wiener chaos expansion. Formally, every function in the Hilbert space, $f(z) \in L^2(\mathbb{R}, \mu)$, has a Fourier-Hermite expansion

$$f(z) = \sum_{i=0}^{\infty} f_i H_i(z). \tag{2.25}$$

The Fourier-Hermite series is usually called the Wiener chaos expansion (WCE), a spectral expansion of the stochastic solution in probability space, representing the randomness of the solution analytically by a set of random bases with deterministic coefficients. If we have a way to compute the deterministic WCE coefficients dynamically, we can recover all probabilistic information. Once the chaos coefficients are known, the statistics of the system response can be estimated directly and inexpensively from the expansion. For example, the mean and the variance can be obtained analytically as

$$\mathrm{E}[f(z)] = \sum_{i=0}^{\infty} f_i \mathrm{E}[H_i(z)] = f_0, \tag{2.26}$$

$$\mathrm{Var}[f(z)] = \sum_{i=0}^{\infty} f_i^2 \mathrm{Var}[H_i(z)] = \sum_{i=1}^{\infty} f_i^2. \tag{2.27}$$

Furthermore, other statistics and probabilities can be estimated by sampling the polynomial expansion.

The Fourier-Hermite expansion can be extended to multi-dimensions. If we truncate the series to d terms, and let $\boldsymbol{\alpha}^i = (\alpha_1^i, ..., \alpha_d^i)$ define a finite dimension multi-index with non-negative integer components, the multivariate Hermite polynomials, often called Wick products, are then given by the tensor product

$$H_{\alpha^i}(\boldsymbol{\zeta}(\omega)) = H_{\alpha^i}(\zeta_1(\omega), ..., \zeta_d(\omega)) = \prod_{j=1}^{d} H_{\boldsymbol{\alpha}_j^i}(\zeta_j(\omega)), \tag{2.28}$$

$\{H_{\alpha^i}(\boldsymbol{\zeta}(\omega))\}$ forms an orthonormal basis in the Hilbert space $L^2(\mathbb{R}^d, \mu^d)$, where $\boldsymbol{\zeta}(\omega) = (\zeta_1(\omega), ..., \zeta_d(\omega))$, and μ^d is a d-dimensional measure on $\mathbb{R}^d$. The first five $1D$ Hermite polynomials are plotted in figure 2.2, and the first six $2D$ Hermite polynomials are plotted in figures 2.3, 2.4 and 2.5.

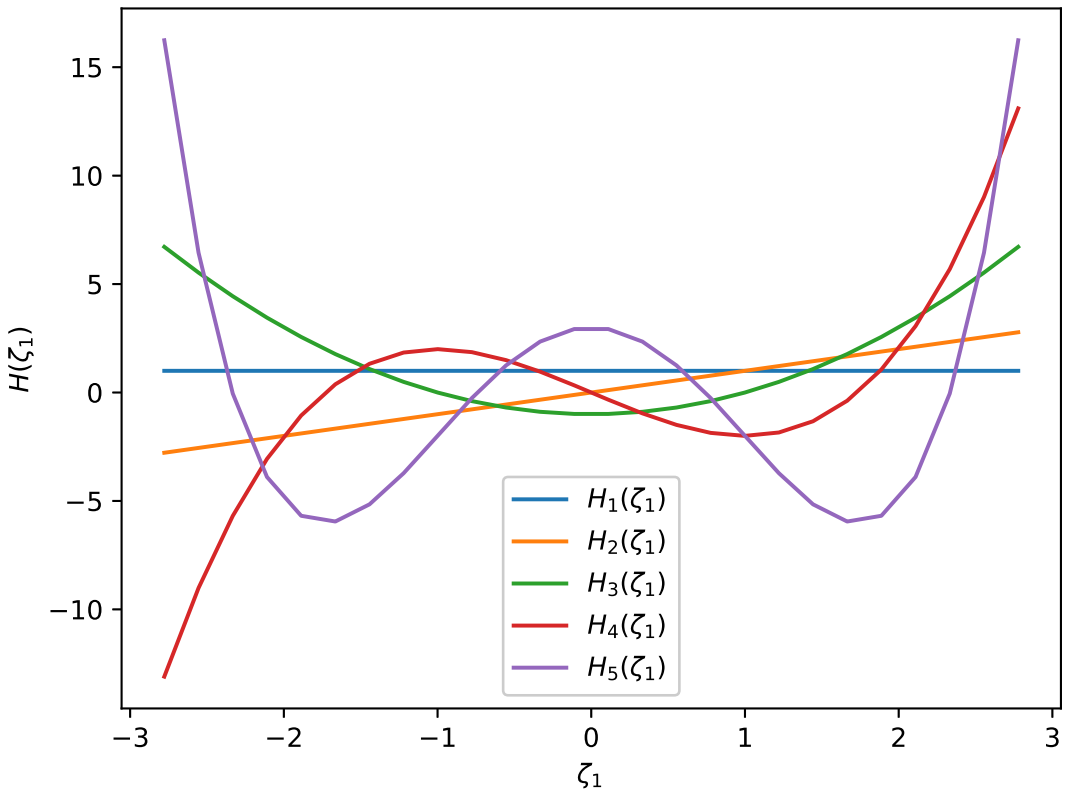

Figure 2.2: 1D Hermite polynomials.

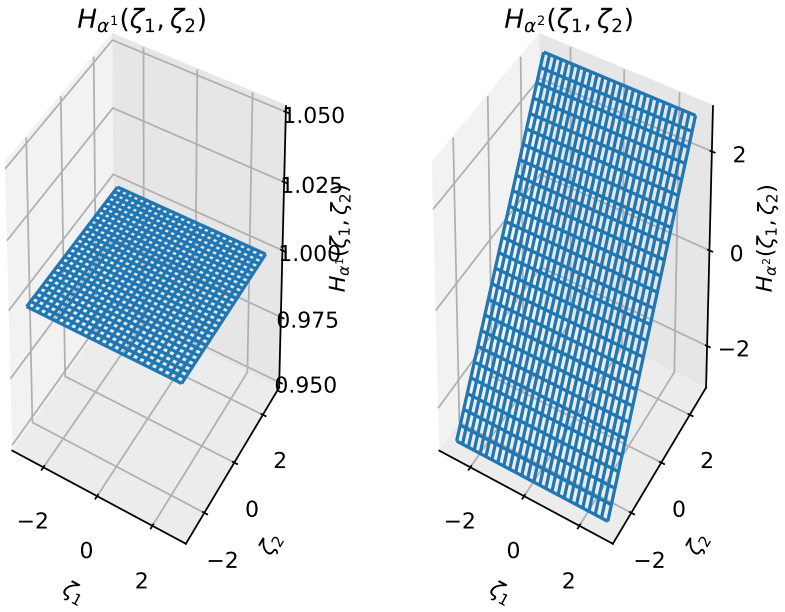

Figure 2.3: 2D Hermite polynomials. $H_{\alpha^1}(\boldsymbol{\zeta}(\omega))$ (left) and $H_{\alpha^2}(\boldsymbol{\zeta}(\omega))$ (right).

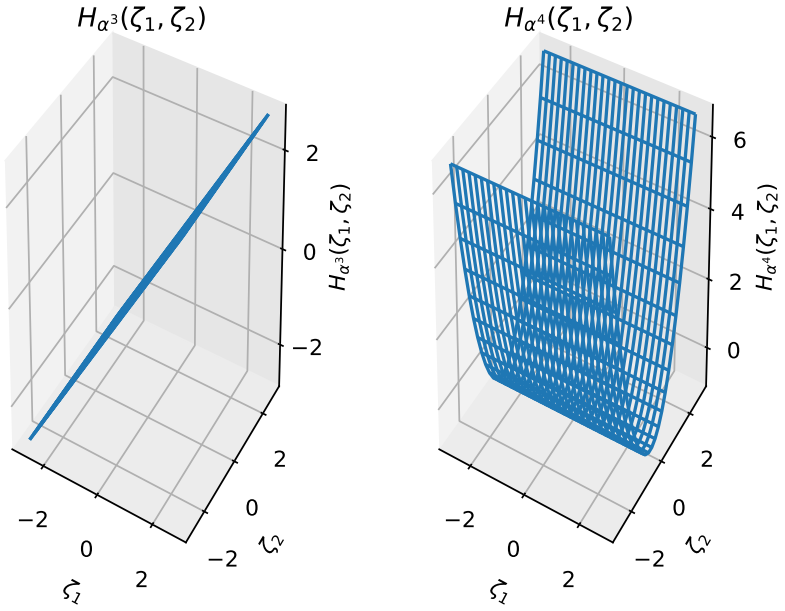

Figure 2.4: 2D Hermite polynomials. $H_{\alpha^3}(\boldsymbol{\zeta}(\omega))$ (left) and $H_{\alpha^4}(\boldsymbol{\zeta}(\omega))$ (right).

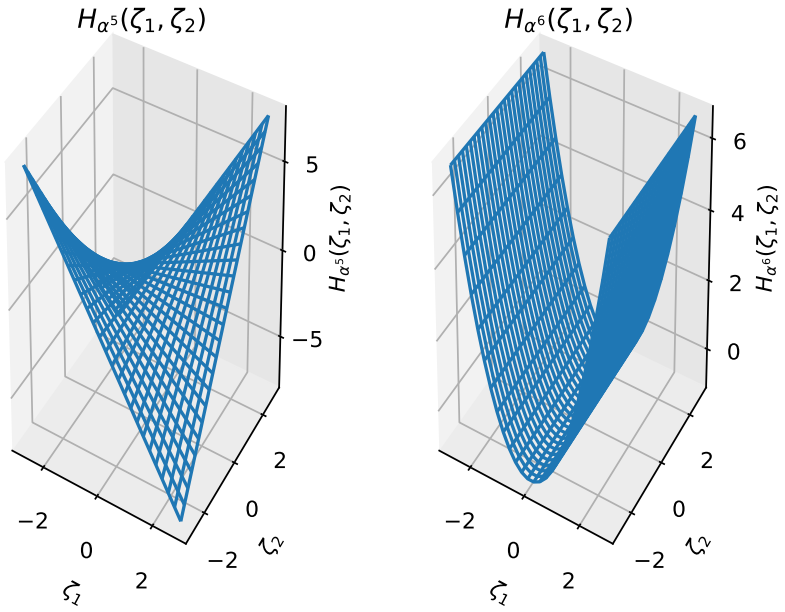

Figure 2.5: 2D Hermite polynomials. $H_{\alpha^5}(\boldsymbol{\zeta}(\omega))$ (left) and $H_{\alpha^6}(\boldsymbol{\zeta}(\omega))$ (right).

Suppose $f(\boldsymbol{\zeta}(\omega))$ is a random function such that $\mathrm{E}[f^2(\boldsymbol{\zeta}(\omega))] < \infty$, then $f(.) \in L^2(\mathbb{R}^d, \mu^d)$, and the Fourier-Hermite expansion exists. This expansion must be truncated in two ways, in the number of random variables and the total order of the Wick products. Limiting the number of random variables to d and the total order of the Wick products to O leads to an expansion with $N = \frac{(O+d)!}{O!d!}$ terms. One limits the total polynomial order of the Wick products by defining the index set

$$I_O = \{\boldsymbol{\alpha} :\mid \boldsymbol{\alpha} \mid \leq O\}, \tag{2.29}$$

where $\mid \boldsymbol{\alpha} \mid = \alpha_1 + ... + \alpha_d$.

The expansion, mean and variance are then

$$f(\boldsymbol{\zeta}(\omega)) = \sum_{\boldsymbol{\alpha_i} \in I_O} f_{\alpha^i} H_{\alpha^i}(\boldsymbol{\zeta}(\omega)) = \sum_{i=0}^{N} f_{\alpha^i} H_{\alpha^i}(\boldsymbol{\zeta}(\omega)), \tag{2.30}$$

$$\mathrm{E}[f(\boldsymbol{\zeta}(\omega))] = \sum_{\boldsymbol{\alpha_i} \in I_O} f_{\alpha^i} \mathrm{E}[H_{\alpha^i}(\boldsymbol{\zeta}(\omega))] = \sum_{\boldsymbol{\alpha_i} \in I_O} f_{\alpha^i} \mathrm{E}[H_{\alpha^i}(\boldsymbol{\zeta}(\omega))] = f_{\alpha^0}, \tag{2.31}$$

$$\mathrm{Var}[f(\boldsymbol{\zeta}(\omega))] = \sum_{\boldsymbol{\alpha_i} \in I'_O} f^2_{\alpha^i} \mathrm{Var}[H_{\alpha^i}(\boldsymbol{\zeta}(\omega))] = \sum_{\boldsymbol{\alpha_i} \in I'_O} f^2_{\alpha^i} = \sum_{i=1}^{N} f^2_{\alpha^i}. \tag{2.32}$$

The truncation error is itself a random variable and the expansion converges in the mean squared sense as both d and O go to infinity [11].

2.2.2.3 Non Intrusive Spectral Projection

In polynomial chaos, one must estimate the chaos coefficients for a set of basis functions. To reduce non-linearity and improve convergence, the bases are chosen such that they are orthogonal with respect to the associated probability weighting function, as is the case with the Hermite polynomials and the Gaussian measure, used to formulate the WCE. If the Hermite polynomials are orthogonal with respect to the Gaussian measure, then the Wick products are orthogonal with respect to the measure $\mu^d(d\boldsymbol{\zeta}(\omega)) = \prod_{j=1}^{d} \frac{1}{\sqrt{2\pi}} \exp\left(\frac{-\zeta_j^2(\omega)}{2}\right) d\zeta_j(\omega)$, which is the joint probability density over the d dimensional stochastic space. That is

$$\begin{aligned}
\langle H_{\alpha^i}(\boldsymbol{\zeta}(\omega)), H_{\alpha^j}(\boldsymbol{\zeta}(\omega))\rangle_\Omega = &\int_{\zeta_1(\omega)} \dots \int_{\zeta_d(\omega)} \prod_{n=1}^{d} H_{\boldsymbol{\alpha}_n^i}(\zeta_n(\omega)) \prod_{m=1}^{d} H_{\boldsymbol{\alpha}_m^j}(\zeta_m(\omega)) \\
&\prod_{p=1}^{d} \frac{1}{\sqrt{2\pi}} \exp\left(\frac{-\zeta_p^2(\omega)}{2}\right) d\zeta_p(\omega) \\
&= \int_{\zeta_1(\omega)} H_{\boldsymbol{\alpha}_1^i}(\zeta_1(\omega)) H_{\boldsymbol{\alpha}_1^j}(\zeta_1(\omega)) \frac{1}{\sqrt{2\pi}} \exp\left(\frac{-\zeta_1^2(\omega)}{2}\right) d\zeta_1(\omega) \dots \\
&\int_{\zeta_d(\omega)} H_{\boldsymbol{\alpha}_d^i}(\zeta_d(\omega)) H_{\boldsymbol{\alpha}_d^j}(\zeta_d(\omega)) \frac{1}{\sqrt{2\pi}} \exp\left(\frac{-\zeta_d^2(\omega)}{2}\right) d\zeta_d(\omega) \\
&= \langle H_{\alpha_1^i}(\zeta_1(\omega)), H_{\alpha_1^j}(\zeta_1(\omega))\rangle_\Omega \dots \langle H_{\alpha_d^i}(\zeta_d(\omega)), H_{\alpha_d^j}(\zeta_d(\omega))\rangle_\Omega \\
&= \prod_{n=1}^{d} \langle H_{\alpha_n^i}(\zeta_n(\omega)), H_{\alpha_n^j}(\zeta_n(\omega))\rangle_\Omega = \delta_{ij}.
\end{aligned}$$

One may therefore compute the chaos coefficients by exploiting orthogonality of the basis

$$f_{\alpha^i} = \langle f(\boldsymbol{\zeta}(\omega)), H_{\alpha^i}(\boldsymbol{\zeta}(\omega))\rangle_\Omega = \int_{\zeta_1(\omega)} \dots \int_{\zeta_d(\omega)} f(\boldsymbol{\zeta}(\omega)) H_{\alpha^i}(\boldsymbol{\zeta}(\omega)) \mu^d(d\boldsymbol{\zeta}(\omega)). \quad (2.33)$$

This multi-dimensional integral can be computationally expensive, especially for high dimensional stochastic spaces, and can be computed with tensor product or sparse grid quadrature. Gaussian quadrature rules can be chosen to match the orthogonal polynomial bases so that the weight function of the quadrature matches

the probability density in the integral. Furthermore, if one opts for sparse grid quadrature in estimating the coefficients, then the PCE should be constructed from a sum of tensor expansions in order to avoid numerical noise in the higher order coefficients.

In stochastic collocation, a response surface is formed by evaluating the system at a discrete set of collocation points. In the single dimension case, a degree n expansion takes the form

$$R(\zeta(\omega)) \approx U_i(R) \coloneqq \sum_{j=0}^{n} R(\zeta^j(\omega)) l^j(\zeta(\omega)), \tag{2.34}$$

where $R(\zeta^j(\omega))$ is the system response at collocation point $\zeta^j(\omega)$, $j = 0, 1, ...$, and $l^j(\zeta(\omega))$ is the Lagrange polynomial

$$l^j(\zeta(\omega)) = \prod_{i=0, i\neq j}^{n} \frac{\zeta(\omega) - \zeta^i(\omega)}{\zeta^j(\omega) - \zeta^i(\omega)}. \tag{2.35}$$

The collocation points are chosen to be the nodes of the Gaussian quadrature rules associated with the same orthogonal polynomials as the polynomial chaos expansion. In the multivariate case, a tensor product formulation with the multi-index $i = (i_1, ..., i_d)$, $i_j = 0, 1, 2, ...$ is applied

$$R(\boldsymbol{\zeta}(\omega)) \approx \mathbf{U_i}(R) \coloneqq U_{i_1} \oplus ... \oplus U_{i_d}(R) = \sum_{i_1=0}^{n_1} ... \sum_{i_d=0}^{n_d} R(\zeta_1^{i_1}(\omega), ..., \zeta_d^{i_d}(\omega)) l_1^{i_1}(\zeta_1(\omega)) ... l_d^{i_d}(\zeta_d(\omega)). \tag{2.36}$$

We can thus estimate the chaos coefficients as

$$f_{\alpha^i} = \langle f(\boldsymbol{\zeta}(\omega)), H_{\alpha^i}(\boldsymbol{\zeta}(\omega)) \rangle_\Omega \approx \sum_{i_1=0}^{n_1} ... \sum_{i_d=0}^{n_d} f(\zeta_{i_1}(\omega), ..., \zeta_{i_d}(\omega)) H_{\alpha^i}(\zeta_{i_1}(\omega), ..., \zeta_{i_d}(\omega)) w_{i_d} ... w_{i_1}, \tag{2.37}$$

where the quadrature weight, $w_{i_d} ... w_{i_1}$, is simply the product of the one-dimensional Gaussian quadrature weights w_{i_j}. The total number of tensor product quadrature points, $\prod_{i=1}^{d} n_i$, increases exponentially with the stochastic dimension, d, and thus gives rise to the curse of dimensionality.

2.3 Numerical Integration, Curse of Dimensionality and Sparse Grids

2.3.1 Introduction

Conventional algorithms for the numerical computation of multivariate integrals are often limited by the curse of dimensionality, meaning that the computational cost increases exponentially with the dimension of the problem. In multiple dimensions, a straightforward way to combine the nodes and weights of a one dimensional quadrature rule is by using a product rule. The nodes of the multidimensional approximation are the Kronecker product of the separate dimensions,

$$\boldsymbol{\zeta} = \zeta_1 \otimes ... \otimes \zeta_d, \tag{2.38}$$

which, with n points in each dimension, results in a grid with a total of n^d points. However, for special function classes, such as spaces of functions which have bounded mixed derivatives, Smolyak's construction [78] can overcome the curse to a certain extent. If the problem dimension, d, is large then a sparse grid can alleviate the exponential increase in the number of collocation points. We briefly review sparse grid constructions here.

Smolyak's construction forms multivariate quadrature formulas via a linear combination of tensor products of suited one dimensional formula at different multi-indices, in such a way that the exponential increase in the number of collocation points is alleviated. In this way, both the number of function evaluations and the numerical accuracy can become independent of the problem dimension up to logarithmic factors.

In the following, we consider numerical integration of functions, $f(\boldsymbol{\zeta}(\omega)) \in W_d^r$, with bounded mixed derivatives of order r, over the d-dimensional unit hypercube, $\Omega \coloneqq [-1,1]^d$, with

$$W_d^r \coloneqq \left\{ f : \Omega \to \mathbb{R}, \| \frac{\partial^{\|\mathbf{S}\|_1} f}{\partial \zeta^{s_1} ... \partial \zeta_d^{s_d}} \|_\infty < \infty, s_i \leq r \right\}, \tag{2.39}$$

$$I^d f \coloneqq \int_\Omega f(\boldsymbol{\zeta}(\omega)) d\boldsymbol{\zeta}, \tag{2.40}$$

where $\|\mathbf{S}\|_1 \coloneqq s_1 + ... + s_d$. Letting $l \in \mathbb{N}$ denote the level of the quadrature formula and d the dimension of the problem, the integral, $I^d f$, is approximated with a

sequence of n_l^d-point quadrature formulas ($n_l^d < n_{l+1}^d$),

$$Q_l^d f \coloneqq \sum_{i=1}^{n_l^d} f(\boldsymbol{\zeta}_{l_i}(\omega)) w_{l_i}, \tag{2.41}$$

with weights w_{l_i} and abscissas ζ_{l_i}. The underlying grid of abscissas is defined as

$$\Gamma_l^d \coloneqq \left\{ \boldsymbol{\zeta}_{l_i}(\omega) : 1 \leq i \leq n_l^d \right\} \subset [-1, 1]^d, \tag{2.42}$$

and the quadrature formulas are nested, $\Gamma_l^d \subset \Gamma_{l+1}^d$.

2.3.2 Nested Univariate Quadrature Formulas

Smolyak's construction has been applied with the midpoint [3], rectangle [60], trapezoidal [8], Clenshaw-Curtis [52] and Gauss [53] rules as the one-dimensional integration bases. In the following, we give a short review of nested univariate quadrature formulae, which are to be used in conjunction with Smolyak's construction. We always have $n_1^1 = 1$, $n_l^1 = \mathcal{O}(2^l)$, and $Q_1^1 = 2f(0)$.

The one-dimensional quadrature formula for a univariate function read

$$Q_l^1 f \coloneqq \sum_{i=1}^{n_l^1} f(\zeta_{l_i}(\omega)) w_{l_i} \tag{2.43}$$

$$Q_0^1 f \coloneqq 0 \tag{2.44}$$

$$\Delta_k^1 f \coloneqq (Q_k^1 - Q_{k-1}^1) f. \tag{2.45}$$

Newton-Cotes formulae [17] are a group of formulae for numerical integration based on evaluating the integrand at equidistant points. The quadrature weights are determined by integration of Lagrange polynomials through these points. In general, Newton-Cotes formulae based upon n quadrature points can exactly integrate functions of polynomial degree up to $n-1$ when n is odd, and n when even. The formula become numerically unstable (some of the weights become negative) at large n, and other methods such as Gauss quadrature are more suitable.

An n-point Gauss quadrature rule, named after Carl Friedrich Gauss, is a quadrature rule constructed to offer the highest degree of polynomial exactness, yielding an exact result for polynomials of degree $2n-1$ or less by a suitable choice of non-equidistant points and corresponding weights. That is, by clever selection of the

integration points and weights, you can accomplish about twice as much. To see this let $\{p_i(x)\}$ be a set of orthogonal polynomials over (a, b) with $p_j(x)$ representing a jth degree polynomial, and let $w(x) > 0$ be a weight such that

$$\int_a^b p_m(x)p_n(x)w(x)dx = 0 \,\forall\, m \neq n. \tag{2.46}$$

Suppose $f(x)$ is a polynomial of degree no greater than $2n-1$. Then we may write $f(x) = p_n(x)q(x) + r(x)$, where $q(x)$ and $r(x)$ are polynomials of degree no greater than $n-1$. Then

$$\int_a^b f(x)w(x)dx = \int_a^b p_n(x)q(x)w(x)dx + \int_a^b r(x)w(x)dx = \int_a^b r(x)w(x)dx, \tag{2.47}$$

since $p_n(x)$ is orthogonal to polynomials of degree no greater than $n-1$. Now let $x_0, x_1, ..., x_n - 1$ be the roots of $p_n(x)$, and let $l_i(x)$ be the ith Lagrange interpolating polynomial for these roots such that $l_i(x_j) = \delta_{ij}$, then we may write $r(x) = \sum_{i=0}^{n-1} r(x_i)l_i(x) = \sum_{i=0}^{n-1} f(x_i)l_i(x)$ since $f(x_i) = r(x_i)$. Finally

$$\int_a^b f(x)w(x)dx = \sum_{i=0}^{n-1} f(x_i) \int_a^b l_i(x)w(x)dx = \sum_{i=0}^{n-1} f(x_i)w_i, \tag{2.48}$$

where $w_i = \int_a^b l_i(x)w(x)dx$. That is, we can exactly integrate a polynomial of degree up to $2n-1$ using an n point quadrature rule.

For the case of the unit weight function, the abscissas are the zeros of the Legendre polynomials and the weights are determined to exactly integrate the associated Lagrange polynomials. When integrating with respect to the Gaussian measure (weight function), the abscissas become the roots of the Hermite polynomials and this is the case we will be most interested in. For these reasons, we adopt the Gauss-Hermite quadrature rules as the 1D formula to be used in Smolyak's construction.

2.3.3 Smolyak's Construction

The one-dimensional quadrature formula for a univariate function are used to define Smolyak's construction for d-dimensional functions, as a summation over the

simplex $\|\mathbf{k}\|_1 \leq l + d - 1$,

$$Q_l^d f \coloneqq \sum_{\|\mathbf{k}\|_1 \leq l+d-1}^{n_l^1} (\Delta_{k_1}^1 \otimes ... \otimes \Delta_{k_d}^1) f, \tag{2.49}$$

which can alternatively be written in terms of $Q_{k_j}^1$ [18]

$$Q_l^d f = \sum_{l \leq \|\mathbf{k}\|_1 \leq l+d-1}^{n_l^1} (-1)^{l+d-\|\mathbf{k}\|_1 - 1} \begin{pmatrix} d-1 \\ \|\mathbf{k}\|_1 - l \end{pmatrix} (Q_{k_1}^1 \otimes ... \otimes Q_{k_d}^1) f. \tag{2.50}$$

From this we can see that the multivariate Smolyak construction is simply a linear combination of tensor products of suited one dimensional formula at different multi-indices. When the one-dimensional quadrature formulas are nested, we consider one-dimensional difference grids

$$\Theta_l^1 \coloneqq \Gamma_l^1 \backslash \Gamma_{l-1}^1, \tag{2.51}$$

with $\Gamma_0 \coloneqq \emptyset$, and the points of the multivariate Smolyak formulation then form the sparse grid [95], which is the union of pairwise disjoint grids $\Theta_{k_1}^1 x ... x \Theta_{k_d}^1$

$$\Gamma_l^d = \cup_{\|\mathbf{k}\|_1 \leq l+d-1} \Theta_{k_1}^1 x ... x \Theta_{k_d}^1. \tag{2.52}$$

We plot examples of such sparse grids, based upon the one dimensional Gauss-Hermite rules, below in figure 2.6.

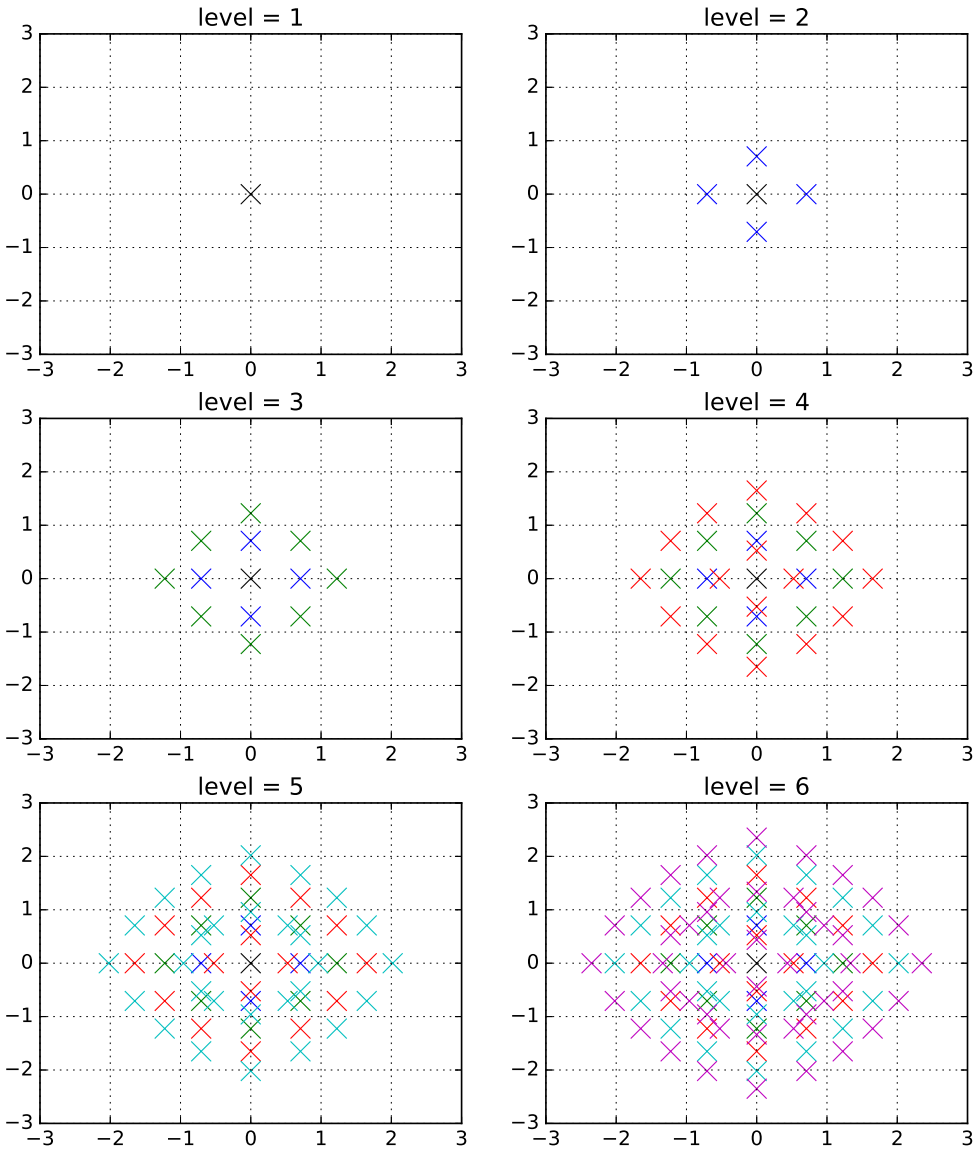

Figure 2.6: Examples of sparse grids based upon Gauss-Hermite rules in 2 dimensions at varying levels.

The pairwise disjoint grids are depicted in different colours, and the full sparse grid at a given level can be seen to be their union. Sparse grids are inefficient in low dimensions and a tensor grid is often more appropriate, the benefit of sparse grids become evident in higher dimensions. As an example, table 2.1 compares the number of nodes required in both a sparse and a tensor grid at level five for an increasing problem dimension.

d	tensor grid (n^d)	sparse grid
1	5	5
2	25	53
3	125	165
4	625	385
5	3125	781
6	15625	1433
7	78125	2437
8	390625	3905
9	1593125	5965

Table 2.1: Comparison of points used in a sparse and tensor grid at level 5.

The sparse grid is evidently far more efficient in higher dimensions, and in this particular example it becomes appropriate to switch from a tensor grid once the problem dimension reaches 4. In fact, if n_l^1 is of the order $\mathcal{O}(2^l)$, then for large d the number of points in a sparse grid, $n_l^d = \mathcal{O}(2^l l^{d-1})$, can be much less than in a tensor grid, of the order $\mathcal{O}(2^{ld})$.

Smolyak's algorithm may be written as

$$Q_l^d f = \sum_{\|\mathbf{k}\|_1 \leq l+d-1} \sum_{j_1}^{n_{k_1}} ... \sum_{j_d}^{n_{k_d}} w_{\mathbf{k_j}} f(\boldsymbol{\zeta}_{k_j}(\omega)), \tag{2.53}$$

with $\boldsymbol{\zeta_{k_j}}(\omega) \coloneqq (\zeta_{k_1 j_1}(\omega), ..., \zeta_{k_d j_d}(\omega))$, and the weights given by

$$w_{\mathbf{k_j}} = w_{k_1 j_1} ... w_{k_d j_d}. \tag{2.54}$$

Let P_l^1 denote the space of one dimensional polynomials of degree no greater than l. Then the d dimensional multivariate polynomial spaces are

$$P_l^d := \left\{ P_{k_1}^1 \otimes ... \otimes P_{k_d}^1, \|\mathbf{k}\|_1 \leq l + d - 1 \right\}. \tag{2.55}$$

If Q_l^1 is exact for P_l^1, then Q_l^d is exact for P_l^d [52].

2.4 Variance Based Sensitivity Analysis

Variance based sensitivity analysis is a probabilistic form of global sensitivity analysis [73], where output variance is divided and attributed to a set of random input

sources. For example, given a model with two inputs and one output, one may discover that 60% of the output variance is attributed to the first input, 30% to the second, and the remaining 10% a consequence of input interaction. These percentages are directly interpreted as measures of sensitivity, and are attractive as they measure sensitivity across the whole input space, they are global.

In this section we briefly outline the theory of variance based sensitivity analysis. The basic mathematical idea relies heavily on the concept of conditional expectation, so we first recall some fundamentals regarding the conditional expectation and variance. We proceed with the spectral approximation of the conditional expectation of square integrable random variables, define the Sobol decomposition and finally relate it to polynomial chaos expansions.

2.4.1 Conditional Expectation and Conditional Variance

Consider an integrable random variable $f(\omega)$ on $(\Omega, \mathscr{F}, P)$, and a sub σ-algebra $\mathscr{G} \subset \mathscr{F}$. The conditional expectation [93] of $f(\omega)$ with respect to $\mathscr{G}$, denoted $\mathrm{E}[f(\omega)|\mathscr{G}]$, is a $\mathscr{G}$ measurable function which for every $\mathscr{H} \in \mathscr{G}$ satisfies

$$\int_{\mathscr{H}} f(\omega) dP(\omega) = \int_{\mathscr{H}} \mathrm{E}[f(\omega)|\mathscr{G}] dP(\omega). \tag{2.56}$$

This is not a constructive definition, but merely a property that a conditional expectation must satisfy. Intuitively, the conditional expectation is the best estimate of $f(\omega)$ based on the information present in σ-algebra $\mathscr{G}$. The Hilbert space formulation allows us to view the conditional expectation as an orthogonal projection onto the space $L^2(\Omega, \mathscr{G}, P)$. That is, given $f(\omega) \in L^2(\Omega, \mathscr{F}, P)$, the conditional expectation, $\mathrm{E}[f(\omega)|\mathscr{G}]$, is the least squares approximation of $f(\omega)$ in the space $L^2(\Omega, \mathscr{G}, P)$.

It is also common to consider the conditional expectation with respect to a random variable. If $f(\omega)$ and $g(\omega)$ are random variables on $(\Omega, \mathscr{F}, P)$, then $\mathrm{E}[f(\omega)|g(\omega)]$ means $\mathrm{E}[f(\omega)|\sigma(g(\omega))]$, where $\sigma(g(\omega))$ denotes the σ-algebra generated by $g(\omega)$.

The concept of conditional expectation allows one to define the conditional variance [1]

$$\mathrm{Var}[f(\omega)|\mathscr{G}] = \mathrm{E}[f^2(\omega)|\mathscr{G}] - (\mathrm{E}[f(\omega)|\mathscr{G}])^2 . \tag{2.57}$$

And the total variance can be recovered

$$\mathrm{Var}[f(\omega)] = \mathrm{Var}[\mathrm{E}[f(\omega)|\mathscr{G}]] + \mathrm{E}[\mathrm{Var}[f(\omega)|\mathscr{G}]]. \tag{2.58}$$

2.4.2 Sensitivity Indices

We here provide a definition of first, second and total variance based sensitivity indices [80] [81], and derive the formulations in terms of the polynomial chaos expansion.

Definition 1: First Order Variance Sensitivity Index
Let $f(\boldsymbol{\zeta}(\omega)) \in L^2(\Omega, \sigma(\boldsymbol{\zeta}(\omega)), \mu^d)$. *For* $i \in \{1, ..., d\}$, *the first order (main effect) sensitivity indices measure the sole contribution of the ith stochastic variable,* $\zeta_i(\omega)$, *to the variance of the stochastic process* $f(\boldsymbol{\zeta}(\omega))$

$$S_i = \frac{\mathrm{Var}[\mathrm{E}[f(\boldsymbol{\zeta}(\omega))]|\zeta_i(\omega)]}{\mathrm{Var}[f(\boldsymbol{\zeta}(\omega))]}. \tag{2.59}$$

The second order sensitivity indices measure joint, or interaction effects. More specifically

Definition 2: Second Order Variance Sensitivity Index
Let $f(\boldsymbol{\zeta}(\omega)) \in L^2(\Omega, \sigma(\boldsymbol{\zeta}(\omega)), \mu^d)$. *For* $i, j \in \{1, ..., d\}$, *the second order sensitivity indices,* S_{ij}, *measure the contribution of the interaction between stochastic variables* $\zeta_i(\omega)$ *and* $\zeta_j(\omega)$ *to the variance of the stochastic process* $f(\boldsymbol{\zeta}(\omega))$

$$S_{ij} = \frac{\mathrm{Var}[\mathrm{E}[f(\boldsymbol{\zeta}(\omega))]|\zeta_i(\omega), \zeta_j(\omega)] - \mathrm{Var}[\mathrm{E}[f(\boldsymbol{\zeta}(\omega))]|\zeta_i(\omega)] - \mathrm{Var}[\mathrm{E}[f(\boldsymbol{\zeta}(\omega))]|\zeta_j(\omega)]}{\mathrm{Var}[f(\boldsymbol{\zeta}(\omega))]}. \tag{2.60}$$

Finally, following [72] we define the total sensitivity index.

Definition 3: Total Variance Sensitivity Index
Let $f(\boldsymbol{\zeta}(\omega)) \in L^2(\Omega, \sigma(\boldsymbol{\zeta}(\omega)), \mu^d)$. *For* $i, j \in \{1, ..., d\}$, *the total sensitivity index due to the ith stochastic variable,* $\zeta_i(\omega)$, *is*

$$S_i^{tot} = \frac{\mathrm{E}[\mathrm{Var}[f(\boldsymbol{\zeta}(\omega))]|\boldsymbol{\zeta}^{(-i)}(\omega)]}{\mathrm{Var}[f(\boldsymbol{\zeta}(\omega))]} = 1 - \frac{\mathrm{Var}[\mathrm{E}[f(\boldsymbol{\zeta}(\omega))]|\boldsymbol{\zeta}^{(-i)}(\omega)]}{\mathrm{Var}[f(\boldsymbol{\zeta}(\omega))]} \tag{2.61}$$

where $\boldsymbol{\zeta}^{(-i)}(\omega)$ *is the set of stochastic variables excluding the ith,* $\boldsymbol{\zeta}(\omega)\backslash\zeta_i(\omega)$.

In addition, one may like to define total sensitivity indices for a subset of random variables, and this follows logically from the above definition.

2.4.3 Polynomial Chaos Form of the Sensitivity Indices

We use the above definitions, together with the WCE, to make spectral approximations of the variance based sensitivity indices.

In practice, given a random variable in $L^2(\Omega, \sigma(\boldsymbol{\zeta}(\omega)), \mu^d)$, we use its truncated WCE, we therefore state results for functions $f(\boldsymbol{\zeta}(\omega)) \in \mathscr{V}^N \subset L^2(\Omega, \sigma(\boldsymbol{\zeta}(\omega)), \mu^d)$, where $\mathscr{V}^N = \text{Span}\left\{H_0(\boldsymbol{\zeta}(\omega)), ..., H_N(\boldsymbol{\zeta}(\omega))\right\}$.

Assuming this is a sufficiently rich approximation space, the following proposition summarises the rules for computing the variance based sensitivity indices for functions in $\mathscr{V}^N$.

Proposition: *Let* $f(\boldsymbol{\zeta}(\omega)) \in \mathscr{V}^N$*, recall that* α_i^k *indicates the order of the ith one-dimensional Hermite polynomial in the kth multi-dimensional Wick product and define the sets*

$$p_i = \left\{k \in \{1, ..., N\}\,; \alpha_i^k > 0, \alpha_j^k = 0\ \forall j \neq i\right\}, \tag{2.62}$$

$$q_{ij} = \left\{k \in \{1, ..., N\}\,; \alpha_i^k > 0, \alpha_j^k > 0, \alpha_j^m = 0\ \forall m \neq i, j\right\}, \tag{2.63}$$

$$r_i = \left\{k \in \{1, ..., N\}\,; \alpha_i^k > 0\right\}. \tag{2.64}$$

Then

$$S_i = \frac{\sum_{k\in p_i} f_{\alpha^k}^2 ||H_{\alpha^k}(\boldsymbol{\zeta}(\omega))||_{L^2(\Omega)}^2}{\sum_{k=1}^N f_{\alpha^k}^2 ||H_{\alpha^k}(\boldsymbol{\zeta}(\omega))||_{L^2(\Omega)}^2} = \frac{\sum_{k\in p_i} f_{\alpha^k}^2}{\sum_{k=1}^N f_{\alpha^k}^2}, \tag{2.65}$$

$$S_{ij} = \frac{\sum_{k\in q_{ij}} f_{\alpha^k}^2 ||H_{\alpha^k}(\boldsymbol{\zeta}(\omega))||_{L^2(\Omega)}^2}{\sum_{k=1}^N f_{\alpha^k}^2 ||H_{\alpha^k}(\boldsymbol{\zeta}(\omega))||_{L^2(\Omega)}^2} = \frac{\sum_{k\in q_{ij}} f_{\alpha^k}^2}{\sum_{k=1}^N f_{\alpha^k}^2}, \tag{2.66}$$

$$S_i^{tot} = \frac{\sum_{k\in r_i} f_{\alpha^k}^2 ||H_{\alpha^k}(\boldsymbol{\zeta}(\omega))||_{L^2(\Omega)}^2}{\sum_{k=1}^N f_{\alpha^k}^2 ||H_{\alpha^k}(\boldsymbol{\zeta}(\omega))||_{L^2(\Omega)}^2} = \frac{\sum_{k\in r_i} f_{\alpha^k}^2}{\sum_{k=1}^N f_{\alpha^k}^2}. \tag{2.67}$$

The WCE coefficients are thus sufficient to compute all variance based sensitivity measures of interest.

proof
For $f(\boldsymbol{\zeta}(\omega)) \in \mathscr{V}^N$, we have $f(\boldsymbol{\zeta}(\omega)) = \sum_{i=0}^{N} f_{\alpha^i} H_{\alpha^i}(\boldsymbol{\zeta}(\omega))$, and orthogonality of the basis thus implies that

$$\mathrm{Var}[f(\boldsymbol{\zeta}(\omega))] = \sum_{i=1}^{N} f_{\alpha^i}^2 \mathrm{Var}[H_{\alpha^i}(\boldsymbol{\zeta}(\omega))] = \sum_{i=1}^{N} f_{\alpha^i}^2. \tag{2.68}$$

From which the WCE formulations of S_i and S_{ij} immediately follow. For S_i^{tot}, note that

$$\mathrm{E}[f(\boldsymbol{\zeta}(\omega))|\boldsymbol{\zeta}^{(-i)}(\omega)] = \sum_{k \in \{0,1,\ldots,N\} \setminus r_i} f_{\alpha^k} H_{\alpha^k}(\boldsymbol{\zeta}(\omega)). \tag{2.69}$$

Hence

$$\begin{aligned}
S_i^{tot} &= \frac{\mathrm{E}[\mathrm{Var}[f(\boldsymbol{\zeta}(\omega))]|\boldsymbol{\zeta}^{(-i)}(\omega)]}{\mathrm{Var}[f(\boldsymbol{\zeta}(\omega))]} \\
&= \frac{\mathrm{Var}[f(\boldsymbol{\zeta}(\omega)] - \mathrm{Var}[\mathrm{E}[f(\boldsymbol{\zeta}(\omega)|\boldsymbol{\zeta}^{(-i)}(\omega)]]}{\mathrm{Var}[f(\boldsymbol{\zeta}(\omega)]} \\
&= \frac{\sum_{k=1}^{N} f_{\alpha^k}^2 \mathrm{Var}[H_{\alpha^k}(\boldsymbol{\zeta}(\omega))] - \sum_{k \in \{0,1,\ldots,N\} \setminus r_i} f_{\alpha^k}^2 \mathrm{Var}[H_{\alpha^k}(\boldsymbol{\zeta}(\omega))]}{\sum_{k=1}^{N} f_{\alpha^k}^2 \mathrm{Var}[H_{\alpha^k}(\boldsymbol{\zeta}(\omega))]} \\
&= \frac{\sum_{k \in r_i} f_{\alpha^k}^2 \mathrm{Var}[H_{\alpha^k}(\boldsymbol{\zeta}(\omega))]}{\sum_{k=1}^{N} f_{\alpha^k}^2 \mathrm{Var}[H_{\alpha^k}(\boldsymbol{\zeta}(\omega))]} = \frac{\sum_{k \in r_i} f_{\alpha^k}^2}{\sum_{k=1}^{N} f_{\alpha^k}^2}.
\end{aligned}$$

2.5 Summary

In this chapter we set out the mathematics of numerical methods for stochastic differential equations, covering both simulation based techniques and spectral methods. The relative advantages of each method have been discussed, along with the complications associated with the curse of dimensionality. Finally, we lay out the tools for variance based sensitivity analysis, casting the sensitivities into polynomial chaos form. We will use all of the above in the following chapters.

Chapter 3

Stability of Shear Flows

3.1 Stability and Critical Reynolds Number

3.1.1 Introduction

Fluid motion is usually classified as laminar or turbulent. A laminar flow is ordered, predictable and layered, whilst a turbulent flow is unpredictable and chaotic. Laminar flows are characterised by much smaller velocity gradients and shear stresses, and therefore produce far smaller drag forces when flowing over a surface. This is one of the major objectives in aircraft design, with the ability to maintain a laminar flow offering many economic and environmental benefits. Conversely, the chaotic motion of turbulent flows makes them an excellent choice for mixing applications, such as chemical reactors or combustion engines. In reality, as the velocity of a fluid, or the physical dimension limiting the flow, increase, laminar motion cannot be sustained and small perturbations amplify until the flow evolves into a turbulent state. This phenomenon is called transition.

The process may be divided into three stages, receptivity, disturbance growth and breakdown. The receptivity stage describes the initiation of the disturbance, usually within a boundary layer, which requires full knowledge of the ambient disturbance environment and is therefore generally the most difficult phase to predict. Once a small disturbance is established, the stability characteristic of the flow determine if it grows or decays. It may be shown, with reference to the Reynolds-Orr equation (equation describing the evolution of perturbation energy), that non-linear terms redistribute energy among different frequencies/scales whilst having no net effect on the instantaneous growth rate. Linear growth mechanisms are therefore responsible for the energy of a disturbance of any amplitude to increase. After the perturbation has reached a finite amplitude, it saturates and forms a new basic flow state which is

often unstable. Such an instability is termed secondary, to differentiate it from the primary mechanism responsible for the formation of the new unstable flow pattern. At this stage, the final non-linear breakdown begins. Breakdown is generally quite rapid and characterised by large growth rates. Since the nineteenth century, many studies of this process have been made, yet the transition process still remains largely misunderstood.

Hydrodynamic stability theory has a long history, dating back to Reynolds and Rayleigh in the 19th century. Rayleigh [64] first developed a general linear stability theory for inviscid parallel shear flows. He showed that a necessary condition for inviscid instability was that the velocity profile have an inflection point, now termed the Rayleigh criteria. Fjørtoft [22] improved the Rayleigh criterion. Given a monotonic mean velocity profile, $U(x_2)$, Fjørtoft's criteria states that $U''(x_2)(U(x_2) - U(x_2^*)) < 0$ for $x_2 \in [-1, 1]$ with $U''(x_2^*) = 0$ and x_2^* being the inflection point, implying that the inflection point has to be a maximum (rather than a minimum) of the span-wise mean vorticity. Reynolds [68] conducted a series of experiments on the instability of flow in a pipe, and showed that laminar flow breaks down when $\frac{Ud}{\upsilon}$ exceeds a critical value, where U is the maximum flow velocity, υ the kinematic viscosity of the fluid and d a length scale. This dimensionless number is now aptly termed the Reynolds number and classifies dynamically similar flows. As the flow velocity increased Reynolds discovered that the flow became turbulent, with the dye in his experiments diffusing into a chaotic motion. Later experiments investigated the effects of finite amplitude disturbances and roughened walls, both of which decreased the critical Reynolds number in pipe flow. These early experiments clearly illustrate the aims of hydrodynamic stability theory, to determine the response of a laminar flow to a disturbance of small amplitude. If the flow returns to its original laminar state, one defines the flow as stable, whereas a growing disturbance that causes a laminar flow to change into a different state is deemed unstable. Whilst instabilities often result in turbulent fluid motion, they may also take a flow into a different laminar, often more complex, state. Stability theory thus deals with the mathematical analysis of evolving disturbances, superposed on a laminar base flow.

Methods for analysing the stability of flows soon followed. To analyse the stability of a laminar flow, one must first define the velocity, pressure and temperature fields at each point in space and time, and together these fields define the basic flow. These fields must satisfy the equations of motion and appropriate boundary conditions. Once the basic flow is defined, it is perturbed slightly. The perturbations may die away, persist at the same magnitude or grow sufficiently to deform the flow and thus create a new basic state. Geometrical irregularities and vibrations are likely to

create all such possible disturbances, to some degree, and the flow is therefore only stable if it is stable to all possible disturbances. In particular, a linear equation governing the evolution of disturbances is desirable. The basic flow is assumed steady, it is perturbed and the equations are linearized by neglecting products of perturbations, which are assumed sufficiently small to justify linearisation. A linear system of partial differential equations and boundary conditions is thus obtained, whose coefficients vary in space but not time. As the disturbance velocities grow above a few percent of the base flow, non-linear effects become important and the linear equations no longer accurately predict the disturbance evolution. Although the linear equations have a limited region of validity they are important in detecting physical growth mechanisms and identifying dominant disturbance types.

This method, of normal modes, was well known for describing the stability of a dynamic system of particles, and was consequently adopted by the fluid dynamics community. To be more specific, the method proceeds by perturbing a known solution to a dynamic system, the basic state, and linearizing by neglecting products of perturbations. It is further assumed that a perturbation can be decomposed into independent modes, each varying with time t according to $\exp(-i\lambda t)$, for some complex λ. This reduces the dynamical system to an eigenvalue problem from which λ values are determined as eigenvalues, and the independent modes the eigenfunctions. Since each mode is a solution of the dynamical system, a general solution may be formed by a superposition, and this is hence the basis for the method of normal modes. A mode with $\Im(\lambda) > 0$ grows exponentially in time and is termed asymptotically unstable. Further, since a general perturbation is a superposition of modes, if $\Im(\lambda) > 0$ is found to be true for any mode then the system is deemed unstable. A mode with $\Im(\lambda) < 0$ is termed stable, and a mode with $\Im(\lambda) = 0$ is neutrally stable.

It is important to remember that a small disturbance is a superposition of normal modes, not a single one. If a basic flow is unstable, a localised initial disturbance will therefore not only grow but move. Each normal component will grow and move at its own rate, determined by its phase velocity. For instance, consider a wave-like normal component $u(x,t) = \exp\{i(\alpha x - \lambda t)\}$, where wave-number α is real and frequency λ is complex. This may be written as $u(x,t) = \exp\{\Im(\lambda)t\}\exp\{i(\alpha x - \Re(\lambda)t)\}$, which is a wave growing in time according to $\exp\{\Im(\lambda)t\}$ with a phase $\phi = \alpha x - \Re(\lambda)t$. The phase velocity is then $\frac{\Re(\lambda)}{\alpha}$, which is the speed at which the phase of the wave propagates in space. That is, the velocity at which the phase of this one frequency component of the wave travels. For such a component, any given phase of the wave (for example, the crest) will appear to travel at the phase velocity. This should be distinguished from the complex group velocity [44], $\frac{d\lambda}{d\alpha}$, which describes

the velocity at which the modulated amplitude, and hence the associated energy, of a group of normal waves move. When a group of waves of different wavelength have different propagation velocities, the wave packet of mixed wavelengths tends to spread out in space, giving rise to dispersion. If all unstable normal modes have non zero group velocity, then non are stationary and the instability is consequently called a convective instability. Conversely, if at least one unstable mode has zero group velocity then it will grow at a fixed point in space and this is therefore known as absolute instability. Technically, this relates to a pinch point in the α plane. Mathematically, the fluid problem is more complex than the particle, resulting in partial as opposed to ordinary differential equations. This, in turn, leads to many complications allowing solutions for only a few idealised flows with simple geometries. Few laminar flows have known solutions to the non-linear dynamical equations, and even fewer are simple enough to allow detailed stability analysis. Research has thus been narrow but deep. Studies focus on simple flows, with planar, axial or spherical symmetry.

Whilst these prototypes are obviously a simplification of reality, they are very helpful in understanding the physical mechanisms of instability, which, in general terms, arises from an imbalance of the forces acting upon a fluid, including inertial, viscous and external forcing. In absence of external forcing or viscosity, fluid motion is determined by the balance of internal stresses (pressure) and inertial effects. A small disturbance can disrupt this balance, grow to an appreciable magnitude and effectively result in a new basic flow state. The tendency for a perturbation to grow depends on many factors. Fluids generally traverse down pressure gradients, and this can often lead to perturbation growth. Viscosity often plays a dual role, both as a stabiliser and a destabiliser. Viscosity has a dissipative effect, and can thus act to stabilise a flow. Indeed, any bounded flow will be stable if viscosity is high enough. However, viscosity not only dissipates energy but diffuses momentum and can consequently also have a destabilising effect on some flow configurations, such as parallel shear flows. In general, for small viscosity, viscosity is primarily destabilising. However, for large viscosity (low Reynolds number), viscosity plays a stabilising role, by dissipation of energy. In addition to this, fluid boundaries have a significant impact upon stability properties. Boundaries act to constrain a flow and, in general, the closer the boundaries the more stable the flow. Boundaries can, however, also create strong shearing effects which act to destabilise a fluid. Typically, these mechanisms act contemporaneously and it is indeed the balance that determines the overall stability characteristics. For instance, viscosity, inertia and boundaries must all be considered in the analysis of a plane Poiseuille flow. In the inviscid setting, a plane Poiseuille flow is stable, but at sufficiently high

Reynolds numbers momentum diffuses from shear layers near the walls and leads to transition. In fact, a kinematic mechanism for the initial amplification of a disturbance travelling with the flow was discovered in 1907 by Orr [54].

Stability theory is now a vast and mature field, including modal theory, non modal analysis, spatial growth, adjoint techniques, parabolized stability equations, secondary instability theory and direct numerical simulations. In this chapter, we review the mathematics underlying this theory. More specifically, we set forth the equations governing small amplitude disturbances to a flow, define stability and present the well known Orr-Sommerfeld formulation. We discuss numerical discretization before presenting both modal and non-modal approaches to the problem. What we here present is now well established theory, which, unless otherwise stated, we take from the comprehensive review of Schmid and Henningson [75].

3.1.2 Non-linear Disturbance Equations

The general evolution of a fluid flow is governed by the equations of momentum and mass conservation. These are known as the Navier-Stokes equations, which for an incompressible fluid and adopting a Cartesian tensor notation, read

$$\frac{\partial u_i}{\partial t} = -u_j \frac{\partial u_i}{\partial x_j} - \frac{\partial p}{\partial x_i} + \frac{1}{Re}\nabla^2 u_i, \tag{3.1}$$

$$\frac{\partial u_i}{\partial x_i} = 0, \tag{3.2}$$

with initial and boundary conditions

$$u_i(x_i, 0) = u_i^0(x_i), \tag{3.3}$$

$$u_i(x_i, t) = 0, \forall\ x_i \in \partial_s, \tag{3.4}$$

where u_i are the velocity components, p is the pressure, x_i are spatial coordinates and ∂_s denotes a solid boundary. We will assume that the stream-wise direction corresponds to x_1, the cross-stream or normal direction to x_2, and the span-wise direction to x_3.

The equations are non-dimensionalised by a velocity scale, where we adopt the centre-line velocity, U_{cl}, for channel flows or the free-stream velocity, U_∞, for boundary layers, and the corresponding length scales are the channel half height, h, and

boundary layer thickness, δ_*. The Reynolds numbers are then $Re = \frac{U_{cl}h}{\nu}$ and $Re = \frac{U_\infty \delta_*}{\nu}$ respectively, where ν is the kinematic viscosity.

The evolution equations for the disturbance are then derived by appealing to a time independent basic state (U_i, P) and a time dependent perturbed state $(U_i + u_i', P + p')$, which both satisfy the Navier-Stokes equations. Subtracting the Navier-Stokes equations for the basic and perturbed states and omitting the prime for disturbances leads to the non-linear evolution equations

$$\frac{\partial u_i}{\partial t} = -U_j \frac{\partial u_i}{\partial x_j} - u_j \frac{\partial U_i}{\partial x_j} - \frac{\partial p}{\partial x_i} + \frac{1}{Re}\nabla^2 u_i - u_j \frac{\partial u_i}{\partial x_j}, \tag{3.5}$$

$$\frac{\partial u_i}{\partial x_i} = 0, \tag{3.6}$$

constituting an initial/boundary value problem for the evolution of the disturbance $u_i^0 = u_i(t = 0)$.

3.1.3 Definition of Stability and Critical Reynolds Number

In order to quantify the growth or decay of an initial perturbation, we need some measure of its size. One could choose geometrical size, such as the disturbed volume or absolute value of the associated vorticity. These are indeed measures of size, but the most natural choice in most cases is the disturbance kinetic energy, as we can more obviously link such a measure to stability. For instance, it is clear that a linear perturbation whose kinetic energy increases monotonically will be unstable. In a volume V, the disturbance kinetic energy per unit volume is

$$E_V = \frac{1}{2}\int_V u_i u_i dV. \tag{3.7}$$

This is not the difference in kinetic energy between the perturbed and base state but simply the kinetic energy associated with the perturbation velocity u_i. In accordance with Joseph [36], and appealing to the kinetic energy of disturbances, E_V, we define stability.

Definition 1: Stability
A solution U_i to the Navier-Stokes equations is stable to perturbations if the perturbation energy satisfies

$$\lim_{t\to\infty} \frac{E_V(t)}{E_V(0)} \to 0. \tag{3.8}$$

Alternatively, one can consider conditional stability, whereby the instability is dependent upon the initial energy of the perturbation.

Definition 2: Conditional Stability
If there exists a threshold energy $\delta > 0$, such that U_i is stable when $E_V(0) < \delta$, then the solution U_i is conditionally stable.

Global stability is a special case of conditional stability.

Definition 3: Global Stability
If the threshold energy is infinite, $\delta > \infty$, the solution is said to be globally stable.

Monotonic stability requires that the perturbation energy be a decreasing function of time, not only in the asymptotic limit of large time.

Definition 4: Monotonic Stability
A solution U_i to the Navier-Stokes equations is monotonically stable to perturbations if the perturbation energy satisfies

$$\frac{dE_V(t)}{dt} < 0, \forall t > 0. \tag{3.9}$$

Using the definitions of stability, one defines the critical Reynolds number, below which the flow is linearly, or conditionally, stable.

Definition 5: Critical Reynolds Number
For $Re > Re_L$ a flow is not stable.

When the Reynolds number exceeds the critical limit, there exists at least one infinitesimal disturbance which is unstable.

Table 3.1, below, lists critical Reynolds numbers for common shear flows, which we will later study in greater detail.

Flow	Re_L	Critical stream-wise wave number α_L
Plane Poiseuille	5772.2	1.020
Plane Couette	∞	–
Blasius Boundary Layer	519.4	0.303

Table 3.1: Critical Reynolds number of common shear flows.

These definitions of stability, listed thus far, relate to the growth of disturbances in time, we call this temporal analysis. This implies a localised disturbance, where the volume V is sufficiently large to include the complete disturbance development during the time period of interest. If the flow happens to be spatially periodic, then it suffices that the volume be large enough to contain a single complete period.

3.1.4 The Reynolds-Orr Equation

As an alternative approach to stability analysis, one may appeal to the energy method, originating from the early works of Reynolds [69] and Orr [54], and later developed further by Serrin [76]. By taking the equations which govern the dynamics of perturbations, forming a dot product with the perturbation velocity, integrating over the volume of interest and applying the condition that perturbations are zero at the domain boundaries, one arrives at the Reynolds-Orr equation,

$$\frac{dE_V}{dt} = -\int_V \frac{\partial U_i}{\partial x_j} u_i u_j dV - \frac{1}{Re}\int_V \frac{\partial u_i}{\partial x_j}\frac{\partial u_i}{\partial x_j} dV. \tag{3.10}$$

The interested reader can refer to section 5.3.2.3 for more details. Here many of the terms in the non-linear disturbance equations have dropped out in the integration process, owing to the fact they may be written as gradients after multiplication by the perturbation velocity. A non-linear term in the disturbance equations would correspond to a cubic term in the Reynolds-Orr equation, and it is thus clear that all non-linearities have dropped out. The first of the two remaining terms on the right hand side represents a transfer of energy between the base flow and the perturbations, and is due to steady shear. The second term is representative of viscous dissipation. Whilst the dissipative term is always negative, the transfer term can be positive, indicating a transfer of energy from the basic state to the disturbance. At sufficiently high Reynolds number the dissipation term can become rather small. In such a case, a positive transfer term can result in a positive right hand side and the perturbation will be gaining energy. In addition to this, the Reynolds-Orr equation implies that $\frac{1}{E_V}\frac{dE_V}{dt}$ is independent of the disturbance amplitude [36]. That is, at

a given time, the growth rate of a finite amplitude disturbance can be found from an infinitesimal disturbance with identical shape. Disturbances of the same shape but different size have the same growth rate. As noted by Henningson [33], the instantaneous growth rate of a finite amplitude disturbance is given by linear mechanisms. Further, the total growth rate is the sum of the growth rates associated with these linear mechanisms, which is a consequence of the conservative nature of the nonlinear terms in the Navier-Stokes equations.

3.2 Modal Analysis of the Viscous Problem

3.2.1 Viscous Linear Stability Equations

3.2.1.1 The Velocity-Vorticity Formulation

We consider the governing equation for infinitesimal disturbances in parallel flows. We define the base flow as $U_i = U(x_2)\delta_{1i}$, which is a flow in the stream-wise direction, x_1, varying in the cross flow direction, x_2. Introducing this mean flow profile into the disturbance equations and linearizing, we arrive at the system

$$\frac{\partial u_1}{\partial t} + U\frac{\partial u_1}{\partial x_1} + u_2 U' = -\frac{\partial p}{\partial x_1} + \frac{1}{Re}\nabla^2 u_1, \tag{3.11}$$

$$\frac{\partial u_2}{\partial t} + U\frac{\partial u_2}{\partial x_1} = -\frac{\partial p}{\partial x_2} + \frac{1}{Re}\nabla^2 u_2, \tag{3.12}$$

$$\frac{\partial u_3}{\partial t} + U\frac{\partial u_3}{\partial x_1} = -\frac{\partial p}{\partial x_3} + \frac{1}{Re}\nabla^2 u_3, \tag{3.13}$$

$$\frac{\partial u_i}{\partial x_i} = \frac{\partial u_1}{\partial x_1} + \frac{\partial u_2}{\partial x_2} + \frac{\partial u_3}{\partial x_3} = 0, \tag{3.14}$$

where primes denote derivatives with respect to the cross stream coordinate, x_2. The first three equations are the linearized momentum equation, and the fourth the continuity equation. Taking the divergence of the linearized momentum equations and making appropriate substitutions into the continuity equation we get a Poisson equation for the perturbation pressure,

$$\nabla^2 p = -2U'\frac{\partial u_2}{\partial x_1}. \tag{3.15}$$

This equation may be used with the equation describing the linearized momentum for the cross stream coordinate to eliminate p, thus giving an equation for the normal velocity perturbation, u_2. To do this, one takes the ∇^2 of the linearized momentum for the cross stream coordinate, with special care when applying the Laplacian operator to the convective term, $U\frac{\partial u_2}{\partial x_1}$, we arrive at an equation describing the evolution of the wall normal velocity, u_2,

$$\left\{(\frac{\partial}{\partial t}+U\frac{\partial}{\partial x_1})\nabla^2 - U''\frac{\partial}{\partial x_1} - \frac{1}{Re}\nabla^4\right\}u_2 = 0. \tag{3.16}$$

A second equation is needed to fully describe the evolution of the three dimensional flow field, and this conveniently involves the wall normal vorticity,

$$\eta = \frac{\partial u_1}{\partial x_3} - \frac{\partial u_3}{\partial x_1}, \tag{3.17}$$

which satisfies

$$\left\{\frac{\partial}{\partial t}+U\frac{\partial}{\partial x_1} - \frac{1}{Re}\nabla^2\right\}\eta = -U'\frac{\partial u_2}{\partial x_3}. \tag{3.18}$$

Together, the pair of equations, 3.16 and 3.18, are known as the wall normal velocity-vorticity formulation, and with appropriate boundary conditions in the far field, and solid walls,

$$u_2 = u_2' = \eta = 0, \tag{3.19}$$

and initial conditions,

$$u_2(x_1, x_2, x_3, t=0) = u_2^0(x_1, x_2, x_3), \tag{3.20}$$

$$\eta(x_1, x_2, x_3, t=0) = \eta^0(x_1, x_2, x_3), \tag{3.21}$$

form a complete description of flow evolution, in both space and time, for an arbitrary disturbance.

3.2.1.2 Orr-Sommerfeld and Squire Equations

We introduce wavelike solutions of the form

$$u_2(x_1, x_2, x_3, t) = \hat{u_2}(x_2)\exp\left\{i(\alpha x_1 + \beta x_3 - \lambda t)\right\}, \tag{3.22}$$

$$\eta(x_1, x_2, x_3, t) = \hat{\eta}(x_2) \exp\left\{i(\alpha x_1 + \beta x_3 - \lambda t)\right\}, \tag{3.23}$$

where α and β are the stream-wise and span-wise wave numbers, and λ the frequency.

At this point, we may choose to study the spatial or temporal growth of the disturbances. In a spatial analysis the frequency is real and given whilst the wave numbers are assumed complex and solved for, the perturbations can thus grow in space. Conversely, in temporal analysis the wave numbers are real and given whilst the frequency λ is assumed complex and solved for, the wavelike solutions can therefore grow in time rather than space. The definitions of stability defined thus far assume a temporal growth analysis. For disturbances generated at a fixed spatial point, temporal growth analysis is inappropriate and the definitions of stability must be adjusted accordingly. In such a case one is interested in the spatial growth of a disturbance, downstream of the generator. Such a disturbance is defined unstable when growing without bound, such that its amplitude tends to infinity in the downstream direction. Formally, it is more difficult to define spatial stability and our focus will thus be temporal. That is, we assume real wave numbers, α and β, and complex frequency λ.

Introducing the above representations into the velocity-vorticity formulation results in coupled evolution equations for $\hat{u_2}(x_2)$ and $\hat{\eta}(x_2)$,

$$\left\{(-i\lambda + i\alpha U)(D^2 - k^2) - i\alpha U'' - \frac{1}{Re}(D^2 - k^2)^2\right\}\hat{u_2} = 0, \tag{3.24}$$

$$\left\{(-i\lambda + i\alpha U) - \frac{1}{Re}(D^2 - k^2)\right\}\hat{\eta} = -i\beta U'\hat{u_2}, \tag{3.25}$$

where D^m denotes an mth order derivative operator, with derivatives taken in the cross-stream direction, and $k^2 = \alpha^2 + \beta^2$. Boundary conditions, $\hat{u_2} = D\hat{u_2} = \hat{\eta} = 0$ in the free stream and at solid walls complete the system. The first of these equations, for the wall normal velocity, is the well known Orr-Sommerfeld equation [54], [82] and the second, for the wall normal vorticity, is the Squire equation [83]. We consider the temporal problem where the spatial wave numbers, α and β, are assumed real and are known, and the frequency λ is generally complex valued. In the modal problem, λ will appear as an eigenvalue in the Orr-Sommerfeld equation, with associated complex eigenfunction $(\hat{u_2}, \hat{\eta_2})$. Inspecting the system more closely, the Orr-Sommerfeld equation is evidently homogeneous whilst the vorticity solutions of the Squire equation are forced by the Orr-Sommerfeld solutions.

The solutions to the Orr-Sommerfeld and Squire equations can be divided into two distinct classes of eigen-solutions. The first set comprises the Orr-Sommerfeld (OS) modes, which we denote as

$$\{\hat{u_{2}}_n, \hat{\eta}_n^p, \lambda_n\}_{n=1}^{N}\,, \tag{3.26}$$

where $(\hat{u_{2}}_n, \lambda_n)$ are the eigen-solutions of the homogeneous Orr-Sommerfeld equation, and $\hat{\eta}_n^p$ are the forced eigen-solutions of the Squire equation, when one inserts $\hat{u_{2}}_n$ on the right-hand side. The symbol $\hat{\eta}_n^p$, for the vorticity component of the OS mode, emphasises that it is equivalent to a particular, or forced, solution of the Squire equation. The second set of eigen-modes is the Squire (SQ) set,

$$\{\hat{u_{2}}_m = 0, \hat{\eta}_m, \lambda_m\}_{m=1}^{M}\,. \tag{3.27}$$

That is the set where the solution of the Orr-Sommerfeld equation is exactly zero and the Squire equation becomes homogeneous. It should be noted that the eigenvalues of the OS set, λ_n, are generally different to those of the SQ set, λ_m.

3.2.1.3 Squire's Theorem

Rather than consider the complex frequencies, λ, one may consider the complex phase speed, $c = \frac{\lambda}{\alpha}$, which results in a slightly modified OS equation,

$$(U-c)(D^2-k^2)\hat{u_2} - U''\hat{u_2} - \frac{1}{i\alpha Re}(D^2-k^2)^2\hat{u_2} = 0, \tag{3.28}$$

Squire's transformation is found by considering the two dimensional case, where $\beta = 0$, that is

$$(U-c)(D^2-\alpha_{2D}^2)\hat{u_2} - U''\hat{u_2} - \frac{1}{i\alpha_{2D}Re_{2D}}(D^2-\alpha_{2D}^2)^2\hat{u_2} = 0, \tag{3.29}$$

Comparing the two and three dimensional equations, it is clear that identical solutions are obtained if

$$\alpha_{2D} = k = \sqrt{\alpha^2+\beta^2}, \tag{3.30}$$

$$\alpha_{2D}Re_{2D} = \alpha Re. \tag{3.31}$$

From which it is evident that

$$Re_{2D} = \frac{\alpha}{\sqrt{\alpha^2 + \beta^2}} Re < Re, \tag{3.32}$$

which states that each three dimensional OS mode corresponds to a two dimensional OS mode at lower Reynolds number, naturally leading to Squire's theorem.

Theorem: Squire's Theorem
If Re_L is the critical Reynolds number for the onset of linear instability, for a given α and β, then the Reynolds number, Re_c, below which no exponential instability exists, for any combination of wave numbers, satisfies

$$Re_c := \min_{\alpha,\beta} Re_L(\alpha, \beta) = \min_{\alpha} Re_L(\alpha, 0). \tag{3.33}$$

The theorem implies that parallel shear flows first become unstable to two-dimensional wavelike perturbations, at a Reynolds number less than that for which an unstable three dimensional perturbation appears. The proof follows logically from Squire's theorem, which states that if a three dimensional mode is unstable, there exists a two dimensional mode which is unstable at a lower Reynolds number. It must be stressed that Squire's theorem applies only to the modal problem, and thus asymptotic instability. When we later review transient effects, we will show that three dimensional disturbances can exhibit greater transient growth than their two dimensional counterparts.

3.2.1.4 Vector Modes

Rather than consider the OS and SQ modes separately, it is more convenient, for algebraic manipulation, to consider a single system. Let $\hat{\boldsymbol{q}} = (\hat{u_2}, \hat{\eta})^T$ be the vector of wall normal velocity and vorticity modes. Then the OS and SQ equations can be written in a compact matrix form,

$$-i\lambda \begin{pmatrix} (K^2 - D^2) & 0 \\ 0 & I \end{pmatrix} \begin{pmatrix} \hat{u_2} \\ \hat{\eta} \end{pmatrix} + \begin{pmatrix} L_{OS} & 0 \\ i\beta U' & L_{SQ} \end{pmatrix} \begin{pmatrix} \hat{u_2} \\ \hat{\eta} \end{pmatrix} = 0, \tag{3.34}$$

where $L_{OS} = i\alpha U(K^2 - D^2) + i\alpha U'' + \frac{1}{Re}(K^2 - D^2)^2$ is the fourth order Orr-Sommerfeld operator, $L_{SQ} = i\alpha U - \frac{1}{Re}(D^2 - K^2)$ is the second order Squire operator, and $i\beta U'$ the coupling operator, where α and β denote the stream-wise and span-wise wave numbers. Further, $D = \partial_{x_2}$ is a differential operator, $K^2 = (\alpha^2 + \beta^2)I$,

and primes denote derivatives with respect to x_2. Clearly, the OS modes drive the Squire equation, unless β or $\hat{u_2}$ are exactly zero.

As before, the complete system of eigenfunctions can be divided into OS modes, $(\hat{u_2}, \hat{\eta}^p)^T$ and SQ modes, $(0, \hat{\eta})^T$. It should be noted that both sets of modes are formally eigen-solutions of the complete system, and it is only due to the zero off diagonal term, that is when $\hat{u_2} = 0$, that they can be divided into two distinct families. In more compact form, the equations read

$$(\mathbf{L}^{-1}\mathbf{R} - i\lambda\mathbf{I})\hat{\boldsymbol{q}} = (\mathbf{L_1} - i\lambda\mathbf{I})\hat{\boldsymbol{q}} = 0, \tag{3.35}$$

where $\mathbf{L}$ and $\mathbf{R}$ are the left and right matrices of the above formulation.

It is clear that this formulation is an eigenvalue problem for the complex frequencies, λ, corresponding to eigenvalues of the discretised operator $\mathbf{L_1} = \mathbf{L}^{-1}\mathbf{R}$. These eigenvalues describe the asymptotic stability of the flow, where an eigenvalue with positive imaginary part describes a mode growing exponentially in time. Such a mode is deemed asymptotically unstable.

3.2.2 Spectra

Here we briefly present the idea of a spectrum in a more abstract setting, before returning to the subject at hand. Eigenvalues are among the most common tools of applied mathematics, finding application not only in fluid mechanics but a diverse range of fields, such as acoustics, control theory, economics, functional analysis, Markov chains, matrix iterations, partial differential equations, quantum mechanics and vibrational analysis. In the context of matrices, let $\mathbf{A}$ be an $N \times N$ matrix with complex coefficients, $\mathbf{A} \in \mathbb{C}^{N\times N}$, let $\mathbf{v} \in \mathbb{C}^N$ and let $\lambda \in \mathbb{C}$. Then $\mathbf{v}$ is an eigenvector and λ an eigenvalue of $\mathbf{A}$ if $\mathbf{Av} = \lambda\mathbf{v}$. Even if $\mathbf{A}$ is real, its eigenvalues are generally complex, unless $\mathbf{A}$ is self-adjoint. The full set of eigenvalues is called the spectrum of $\mathbf{A}$, and is a non empty subset of the complex plane, $\mathbb{C}$, which can equivalently be defined as the set of points, z, for which the resolvent $(z - \mathbf{A})^{-1}$ does not exist. Where we use $(z - \mathbf{A})^{-1}$ to mean $(z\mathbf{I} - \mathbf{A})^{-1}$, and $\mathbf{I}$ denotes the identity matrix. The definition below summarises these ideas.

Definition 1: spectra
The spectra of $\mathbf{A} \in \mathbb{C}^{N\times N}$ *is the set* $\Lambda(\mathbf{A}) = \{z \in \mathbb{C}, ||(z - \mathbf{A})^{-1}|| = \infty\}$.

The matrix $(z - \mathbf{A})^{-1}$ is known as the resolvent of $\mathbf{A}$ at z, and the spectra is the set of points in the complex plane for which the resolvent is singular.

Most matrices possess a complete set of eigenvectors, that is a set of N linearly independent eigenvectors, each satisfying $\mathbf{A}\mathbf{v}_i = \lambda_i \mathbf{v}_i$. If matrix $\mathbf{A}$ has distinct eigenvalues, then it is certain to have a complete set of unique eigenvectors. A matrix with a complete set of eigenvectors is said to be non-defective, or diagonalizable. If $\mathbf{V}$ is the matrix whose ith column vectors is the ith eigenvector of $\mathbf{A}$, $\mathbf{v}_i$, then $\mathbf{AV} = \mathbf{V\Lambda}$, where $\mathbf{\Lambda}$ is the diagonal matrix of eigenvalues. Since the eigenvectors are linearly independent, matrix $\mathbf{V}$ is invertible and it follows that $\mathbf{A}$ is indeed diagonalizable, $\mathbf{A} = \mathbf{V\Lambda V}^{-1}$.

Whilst we have taken $\mathbf{A}$ to be a matrix, we could alternatively consider a more general linear operator, such as an infinite matrix or differential operator. In fact, matrix eigenvalue problems often arise from discretization of linear operators. The spectrum of a closed operator, defined on a Banach or Hilbert space, is defined as the set of complex numbers for which the resolvent does not exist as a bounded operator defined on the whole space. In this case one considers eigenfunctions, rather than eigenvectors, but the definitions do not change. Whilst nuances exist, the distinctions between discrete and continuous spectra is of little concern in the problems we consider in this thesis.

The use of eigenvalues is vast, allowing for diagonalization, separation of variables and asymptotic stability analysis. Furthermore, eigenvalues give character to a matrix, allowing one to take the abstraction of a matrix and portray it pictorially. We, in hydrodynamic stability analysis, are often faced with problems for which eigenvalue methods fail. These problems are characterised by matrices for which the matrix $\mathbf{V}^{-1}$, if it exists, contains very large entries, $||\mathbf{V}||||\mathbf{V}^{-1}|| >> 1$. To be more precise, the preceding condition should hold for any eigenvector matrix, not only one whose columns are poorly scaled. The condition depends on the choice of norm, $||.||$, and we will predominantly be concerned with the 2-norm, which corresponds mathematically to formulations in a Hilbert space, and physically to some measure of energy. If the condition $||\mathbf{V}||||\mathbf{V}^{-1}|| >> 1$ does indeed exist, then we say that matrix $\mathbf{A}$ is far from normal, and equivalently its eigenvectors are far from normal. At the other extreme exist normal matrices with a complete set of orthogonal eigenvectors, such as real symmetric and Hermitian matrices. In this case, if one normalises each of the eigenvectors, such that $||\mathbf{v}_j||_2 = 1$, then $||\mathbf{V}||_2 = ||\mathbf{V}^{-1}||_2 = 1$ and $||\mathbf{V}||_2||\mathbf{V}^{-1}||_2 = 1$. In this norm, it is the non-normal matrices for which eigenvalue analysis may fail. The scalar $||\mathbf{V}||_2||\mathbf{V}^{-1}||_2$ is termed the condition number of $\mathbf{V}$, and is effectively the ratio of the largest and smallest singular values of the eigenvector matrix. The condition number can theoretically

take any value from one to infinity, with one implying a normal matrix and greater values indicating a greater degree of non-normality.

3.2.2.1 Spectra of the Orr-Sommerfeld and Squire Operator

Below, in figure 3.1, we plot the spectrum for plane Poiseuille flow, at stream-wise and span-wise wave-numbers of 1.02 and 0.0 respectively, and Reynolds numbers of both 1000 (left) and 6000 (right).

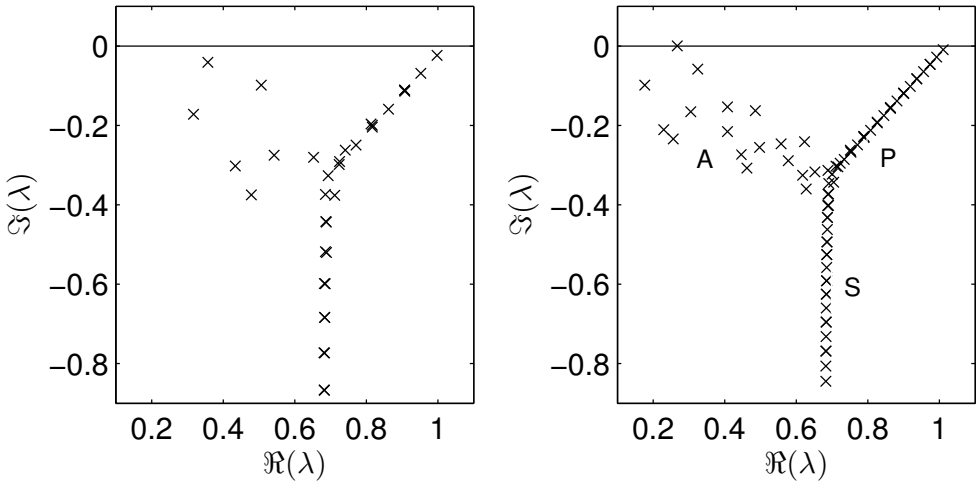

Figure 3.1: Spectrum of plane Poiseuille flow, $\alpha = 1.02$, $\beta = 0.0$, $Re = 1000$ (left), $Re = 6000$ (right).

In the leftmost sub-plot, it is observed that all eigenvalues sit in the lower half of the complex plane, and the flow is thus stable at this Reynolds number. In contrast, at a Reynolds number of 6000 there is one unstable eigenvalue which protrudes into the upper half of the complex plane. This unstable mode is termed a Tollmien-Schlichting wave [85] [74], in honour of the researchers who discovered that the Orr-Sommerfeld equation has unstable inflexionless disturbances.

In the right sub-plot the eigenvalues have been split into three distinct groups, namely the A, P and S branches, in accordance with Mack [46], with $\Re(\lambda) \to 0$ along the A branch, $\Re(\lambda) \to 1$ along the P branch, and $\Re(\lambda) \approx \frac{2}{3}$ along the S branch. Below, in figure 3.2, we plot Orr-Sommerfeld wall normal modes which are representative of each distinct branch, the left, centre and right sub-plots corresponding to A, P and S branch modes respectively.

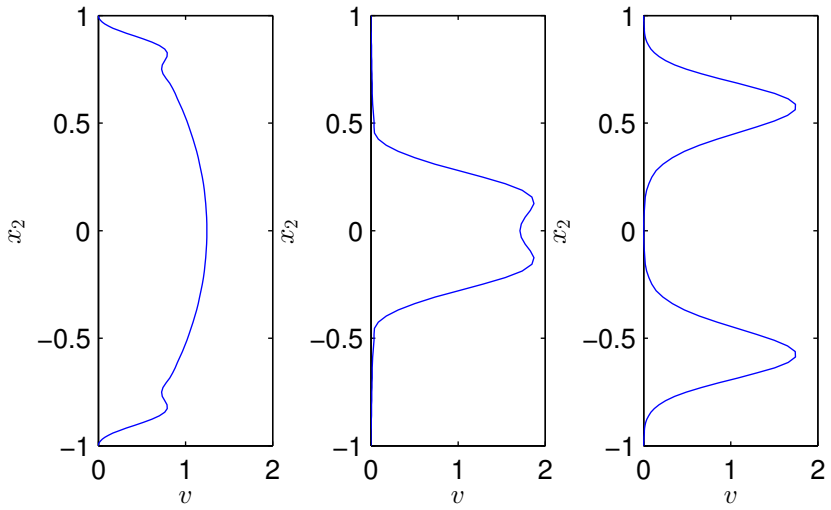

Figure 3.2: Wall normal velocity modes from A (left), P (centre) and S (right) branch of plane Poiseuille spectrum, $\alpha = 1.02$, $\beta = 0.0$, $Re = 6000$.

As depicted, eigenfunctions from the A branch are characterised by large variations in the vicinity of the wall whilst those from the P branch have much greater variations in the central channel region, and these modes are thus commonly termed wall and centre modes respectively.

3.2.3 Chebyshev Spectral Methods and Discretization of the Orr-Sommerfeld Equation

Spectral methods [27] [10], developed in a series of papers by Orszag starting in 1969 [56], are a class of numerical techniques used in applied mathematics and scientific computing to solve differential equations. The idea is to write the general solution to the differential equation as an expansion with global basis functions, such as a Fourier series which is simply a sum of sinusoids. The objective is to then determine the expansion coefficients which satisfy the differential equation in some optimal sense. The coefficients may be determined by collocation, Galerkin or Tau methods.

Spectral methods are similar to finite element methods, but, unlike finite element methods, spectral methods adopt global basis functions which are non-zero over the whole domain, whilst finite element methods use basis functions that are non-zero only on small sub-domains. For this reason, spectral methods have excellent error properties, with exponential convergence when the solution is smooth. In general, spectral techniques are computationally cheaper but become less accurate for problems with complex geometries, which is a consequence of the Gibbs phenomenon.

Spectral methods can solve ordinary differential equations (ODEs), partial differential equations (PDEs) and eigenvalue problems. When applied to time-dependent PDEs, the expansion coefficients are assumed time-dependent, and when substituted into the PDE yields a system of ODEs, in time, for the coefficients which can be solved using any numerical method for ODEs, such as collocation techniques. Eigenvalue problems for ODEs are similarly converted to matrix eigenvalue problems.

Chebyshev polynomials can be defined in many ways, such as with trigonometric functions,

$$T_n(x_2) = \cos(n \cos^{-1}(x_2)), \tag{3.36}$$

or as solutions of the singular Sturm-Liouville problem,

$$\frac{d}{dx_2}\left(\sqrt{1-x_2^2}\frac{d}{dx_2}T_n(x_2)\right) + \frac{n^2}{\sqrt{1-x_2^2}}T_n(x_2) = 0, \tag{3.37}$$

or recursively,

$$T_{n+1}(x_2) = 2T_n(x_2) - T_{n-1}(x_2), \tag{3.38}$$

with $T_0(x_2) = 1$ and $T_1(x_2) = x_2$.

For numerical reasons, we will adopt the trigonometric representation.

The Chebyshev polynomials are orthogonal with respect to the weight $\frac{1}{\sqrt{1-x_2^2}}$,

$$\int_{-1}^{1} \frac{T_n(x_2)T_m(x_2)}{\sqrt{1-x_2^2}} dx_2 = C_n \delta_{mn}, \tag{3.39}$$

where $C_0 = \pi$, $C_n = \frac{\pi}{2}, \forall n > 0$.

We use the Chebyshev polynomials to expand a dependent variable with a spectral expansion of the form

$$f(x_2) = \sum_{n=0}^{N_c} a_n T_n(x_2), \tag{3.40}$$

and evaluate at the Gauss-Lobatto points,

$$x_2^j = \cos(\frac{j\pi}{N_c}), \tag{3.41}$$

where N_c denotes the number of collocation points. Discretization of differential equations requires discretization of derivatives, which can also be expressed in terms of the Chebyshev polynomials, and computed via a recurrence relation,

$$T_0^{(k)}(x_2^j) = 0, \tag{3.42}$$

$$T_1^{(k)}(x_2^j) = T_0^{(k-1)}(x_2^j), \tag{3.43}$$

$$T_2^{(k)}(x_2^j) = 4T_1^{(k-1)}(x_2^j), \tag{3.44}$$

$$T_n^{(k)}(x_2^j) = 2nT_{n-1}^{(k-1)}(x_2^j) + \frac{n}{n-1}T_{n-1}^{(k)}(x_2^j),\ \forall n > 2, \tag{3.45}$$

where superscript $k > 0$ denotes the order of the derivative, with respect to the inhomogeneous coordinate, x_2.

Scalar products require integration of functions, which are evaluated with quadrature,

$$\int_{-1}^{1} f(x_2)dx_2 = \sum_{j=0}^{N_c} f(x_2^j)W(x_2^j), \tag{3.46}$$

where $W(x_2^j)$ is the Chebyshev integration weight function, which is found as follows

$$f(x_2) = \sum_{n=0}^{N_c} a_n T_n(x_2) = \sum_{n=0}^{N_c} c_n T_n(x_2) \sum_{j=0}^{N_c} \frac{b_j}{N_c} f(x_2^j) T_n(x_2^j). \tag{3.47}$$

Integrating,

$$\int_{-1}^{1} f(x_2)dx_2 = \sum_{j=0}^{N_c} \frac{b_j}{N_c} f(x_2^j) \sum_{n=0}^{N_c} c_n T_n(x_2^j) \int_{-1}^{1} T_n(x_2)dx_2. \tag{3.48}$$

Noting that

$$\int_{-1}^{1} T_n(x_2)dx_2 = \frac{2}{1-n^2},\ \forall\ n \text{ even}, \tag{3.49}$$

we have

$$W(x_2^j) = \frac{b_j}{N_c}\left\{2 + \sum_{n=2}^{N_c} c_n \frac{1+(-1)^n}{1-n^2} cos\left(\frac{njp\pi}{N_c}\right)\right\}. \tag{3.50}$$

3.2.4 Discretization of the Orr-Sommerfeld Equation

Here, we discretize the OS equation, using a spectral collocation method based upon the Chebyshev polynomials. The method is highly accurate and simple to implement.

The OS equation reads

$$\left(-Uk^2 - U'' - \frac{k^4}{i\alpha Re}\right)\hat{u_2} + \left(U + \frac{2k^2}{i\alpha Re}\right)D^2\hat{u_2} - \frac{1}{i\alpha Re}D^4\hat{u_2} = c(D^2 - k^2)\hat{u_2}. \tag{3.51}$$

Expanding the eigenfunctions

$$\hat{u_2}(x_2) = \sum_{n=0}^{N_c} a_n T_n(x_2), \tag{3.52}$$

and obtaining derivatives by differentiating the expansion, for instance

$$D^2\hat{u_2}(x_2) = \sum_{n=0}^{N_c} a_n T_n''(x_2), \tag{3.53}$$

we get

$$\left(-U(x_2)k^2 - U''(x_2) - \frac{k^4}{i\alpha Re}\right)\sum_{n=0}^{N_c} a_n T_n(x_2) + \left(U(x_2) + \frac{2k^2}{i\alpha Re}\right)\sum_{n=0}^{N_c} a_n T_n''(x_2) -$$
$$\frac{1}{i\alpha Re}\sum_{n=0}^{N_c} a_n T_n''''(x_2) = c\left(\sum_{n=0}^{N_c} a_n T_n''(x_2) - k^2\sum_{n=0}^{N_c} a_n T_n(x_2)\right),$$

with discretised boundary conditions,

$$\sum_{n=0}^{N_c} a_n T_n(1) = 0, \tag{3.54}$$

$$\sum_{n=0}^{N_c} a_n T_n(-1) = 0, \tag{3.55}$$

$$\sum_{n=0}^{N_c} a_n T_n'(1) = 0, \tag{3.56}$$

$$\sum_{n=0}^{N_c} a_n T_n'(-1) = 0. \tag{3.57}$$

We require that the system of equations be satisfied at the Gauss-Lobatto collocation points, allowing us to use the recursive relation for the evaluation of derivatives, and leading to a generalised eigenvalue problem,

$$\boldsymbol{A}\boldsymbol{a} = c\boldsymbol{B}\boldsymbol{a}. \tag{3.58}$$

Using the first, second, penultimate and last rows to implement the four boundary conditions, the matrix $\boldsymbol{B}$ reads

$$\boldsymbol{B} = \begin{pmatrix} T_0(1) & T_1(1) & \dots \\ T_0'(1) & T_1'(1) & \dots \\ T_0''(x_2^2) - k^2 T_0(x_2^2) & T_1''(x_2^2) - k^2 T_1(x_2^2) & \dots \\ \vdots & \vdots & \vdots \\ T_0''(x_2^{N_c-2}) - k^2 T_0(x_2^{N_c-2}) & T_1''(x_2^{N_c-2}) - k^2 T_1(x_2^{N_c-2}) & \dots \\ T_0'(1) & T_1'(1) & \dots \\ T_0(1) & T_1(1) & \dots \end{pmatrix}. \tag{3.59}$$

Matrix $\boldsymbol{A}$ follows from the left hand side of the discretised OS equation, but the rows in $\boldsymbol{A}$ corresponding to the boundary conditions are chosen to be a complex multiple of the corresponding rows in $\boldsymbol{B}$. Careful selection of this multiple ensures that spurious modes, associated with the implementation of the boundary conditions, can be mapped to an arbitrary location in the complex plane [75].

3.2.4.1 The Energy Norm Weight Matrix

Here, we formulate the energy weight matrix, which allows us to compute the energy norm as a weighted 2-norm of the Chebyshev coefficients. First, we define the

perturbation energy,

$$||\mathbf{q}(x_2)||_E^2 = \int_{-1}^{1} (|u_2'(x_2)|^2 + k^2|u_2(x_2)|^2 + |\eta(x_2)|^2)dx_2, \tag{3.60}$$

using Chebyshev polynomials, we have

$$\begin{aligned} ||\mathbf{q}(x_2)||_E^2 &= \sum_{i=0}^{N_c}\sum_{j=0}^{N_c} \int_{-1}^{1} T_i(x_2)T_j(x_2)dx_2 \left\{ k^2 u_{2_i}^* u_{2j} + \eta_i^*\eta_j + \sum_{n=0}^{N_c}\sum_{m=0}^{N_c} D_{ni}D_{mj}u_{2_n}^* u_{2m} \right\} \\ &= \mathbf{u_2}^*(k^2\mathbf{C} + \mathbf{D}^*\mathbf{C}\mathbf{D})\mathbf{u_2} + \boldsymbol{\eta}^*\mathbf{C}\boldsymbol{\eta} = (\mathbf{u_2}^*, \boldsymbol{\eta}^*)\mathbf{M}(\mathbf{u_2}^*, \boldsymbol{\eta}^*)^T, \end{aligned}$$

where

$$\mathbf{M} = \begin{pmatrix} k^2\mathbf{C} + \mathbf{D}^*\mathbf{C}\mathbf{D} & 0 \\ 0 & \mathbf{C} \end{pmatrix}, \tag{3.61}$$

is the energy weight matrix, $\mathbf{D}$ is the Chebyshev derivative matrix, $\mathbf{u_2}$ and $\boldsymbol{\eta}$ are vectors of Chebyshev coefficients for the wall normal velocity and vorticity, and the matrix $\mathbf{C}$ has components $C_{ij} = \int_{-1}^{1} T_i(x_2)T_j(x_2)dx_2$, where $T_i(x_2)$ are the Chebyshev polynomials,

$$C_{ij} = \int_{-1}^{1} T_i(x_2)T_j(x_2)dx_2 = \begin{cases} 0, & \text{if } i+j \text{ odd} \\ \frac{1}{1-(i+j)^2} + \frac{1}{1-(1-j)^2}, & \text{if } i+j \text{ even} \end{cases}. \tag{3.62}$$

The matrices are Hermitian and can therefore be factored, $k^2\mathbf{C} + \mathbf{D}^*\mathbf{C}\mathbf{D} = \mathbf{E}_\mathbf{v}^*\mathbf{E}_\mathbf{v}$, $\mathbf{C} = \mathbf{E}_\eta^*\mathbf{E}_\eta$, and we therefore have

$$||\mathbf{q}(x_2)||_E^2 = \mathbf{u_2}^*\mathbf{E}_\mathbf{v}^*\mathbf{E}_\mathbf{v}\mathbf{u_2} + \boldsymbol{\eta}^*\mathbf{E}_\eta^*\mathbf{E}_\eta\boldsymbol{\eta} = (\mathbf{F}\mathbf{a})^*(\mathbf{F}\mathbf{a}) = ||\mathbf{F}\mathbf{a}||_\mathbf{2}^\mathbf{2}, \tag{3.63}$$

where $\mathbf{a} = (\mathbf{u_2}, \boldsymbol{\eta})^t$ is the vector of Chebyshev coefficients, and $\mathbf{F}$ is the matrix we set out to formulate

$$\mathbf{F} = \begin{pmatrix} \mathbf{E}_\mathbf{v} & 0 \\ 0 & \mathbf{E}_\eta \end{pmatrix}. \tag{3.64}$$

The sub-matrices, $\mathbf{E}_\mathbf{v}$ and $\mathbf{E}_\mathbf{n}$, can be computed from a singular value decomposition (SVD) of $\mathbf{D}^*\mathbf{C}\mathbf{D} + k^2\mathbf{C}$ and $\mathbf{C}$ respectively. For instance, noting $\mathbf{C}$ is positive definite we can compute the SVD, $\mathbf{C} = \mathbf{U}\mathbf{S}\mathbf{V}^*$, where $\mathbf{U}$ and $\mathbf{V}$ contain the right and left singular vectors, and $\mathbf{S}$ is the diagonal matrix of singular values. Further,

since $\mathbf{C}$ is symmetric we must have $\mathbf{U} = \mathbf{V}$, hence $\mathbf{C} = \mathbf{USU}^* = \mathbf{U}\sqrt{\mathbf{S}^*}\sqrt{\mathbf{S}}\mathbf{U}^* = (\sqrt{\mathbf{S}}\mathbf{U}^*)^*(\sqrt{\mathbf{S}}\mathbf{U}^*) = {\mathbf{E}_\eta}^*\mathbf{E}_\eta$.

3.2.5 Sensitivity of Eigenvalues

Traditionally, hydrodynamic stability is investigated from a modal perspective, which amounts to eigenvalue analysis. That is, the system is perturbed about the mean state, then linearized before searching for unstable modes which grow exponentially in time. Naturally, one expects that a flow will behave unstably if and only if there exists such a growing mode, and much has been learned from such analyses, stable and unstable flows have been identified and distinctions made upon geometry, Reynolds and wave numbers.

For some flows, those whose instabilities are driven by thermal and centrifugal forces, such as Rayleigh-Bernard convection and Taylor-Couette flows, modal predictions match experimental results very well. However, eigenvalue analysis often fails to match experiments when flows are driven by shear forces, such as plane Poiseuille flow, which is a flow with a parabolic profile between flat stationary plates, and the Blasius boundary layer, which is the flow over a single infinite flat plate.

For the Poiseuille flow, modal analysis suggests a critical Reynolds number of 5772, yet transition has been observed in experiments at Reynolds numbers as low as 1000. Another interesting discrepancy arises in the case of Couette flow, which is a linear flow profile between flat plates, one moving relative to the other. The plane Couette flow is predicted eigenvalue stable at all Reynolds numbers, yet instability has been observed at Reynolds numbers of only 350 [87]. Such abnormalities have long been known, and traditionally were attributed to a failure in the linearisation step, arguments thus following to inspect the non-linear terms more stringently [4].

A more modern explanation of the phenomenon finds its roots in linear algebra. If all roots of a linear system are both distinct and located in the lower complex half-plane, inputs to that system may still be amplified by arbitrarily large factors when eigenfunctions are not orthogonal. Such a matrix operator, with non orthogonal eigenfunctions, is termed non-normal whilst those with an orthogonal set of eigenfunctions are called normal [39]. We will here review two common techniques for measuring eigenvalue sensitivity, adjoints and pseudospectra.

3.2.5.1 Adjoint Problem

In order to define eigenvalue sensitivity, it will be convenient to possess a set of eigenvectors which are orthogonal to the OSSQ eigenvectors, such that each eigen-

vector is orthogonal to all but one eigenvector of the discretised OSSQ operator. The eigenvalue problem with such a solution is termed the adjoint problem. If

$$(\mathbf{L_1} - i\lambda_j \mathbf{I})\hat{\boldsymbol{q}}_{\boldsymbol{j}} = 0 \tag{3.65}$$

represents the direct problem with eigenvalue λ_j and eigenvector $\hat{\boldsymbol{q}}_{\boldsymbol{j}}$, then

$$(\mathbf{L}_1^+ - i\lambda_j^+ \mathbf{I})\hat{\boldsymbol{q}}_{\boldsymbol{j}}{}^+ = 0 \tag{3.66}$$

represents the adjoint eigenvalue problem with eigenvalue λ_j^+ and eigenvector $\hat{\boldsymbol{q}}_{\boldsymbol{j}}{}^+$. The adjoint matrix $\mathbf{L}_1^+$ can be derived from an inner product and our choice of energy norm. That is

$$< \mathbf{L}_1^+ \hat{\boldsymbol{q}}_{\boldsymbol{j}}{}^+, \hat{\boldsymbol{q}}_{\boldsymbol{j}} >_E = < \hat{\boldsymbol{q}}_{\boldsymbol{j}}{}^+, \mathbf{L_1} \hat{\boldsymbol{q}}_{\boldsymbol{j}} >_E . \tag{3.67}$$

Using the energy norm weight matrix, $\mathbf{M} = \mathbf{F}^H \mathbf{F}$, we have

$$(\mathbf{L}_1^+ \hat{\boldsymbol{q}}_{\boldsymbol{j}}{}^+)^H \mathbf{M} \hat{\boldsymbol{q}}_{\boldsymbol{j}} = \hat{\boldsymbol{q}}_{\boldsymbol{j}}{}^{+H} \mathbf{M} \mathbf{L_1} \hat{\boldsymbol{q}}_{\boldsymbol{j}}, \tag{3.68}$$

from which it follows that the adjoint matrix may be written as

$$\mathbf{L}_1^+ = \mathbf{M^{-1}} \mathbf{L_1^H} \mathbf{M}. \tag{3.69}$$

Given our eigenvalue problem

$$(\mathbf{L_1} - i\lambda_j \mathbf{I})\hat{\boldsymbol{q}}_{\boldsymbol{j}} = 0, \tag{3.70}$$

we wish to quantify the change $\delta\lambda_j$ induced by a modification operator $\delta\mathbf{L_1}$ of norm much less than one. That is, we wish to solve $\delta\lambda_j$ when

$$(\mathbf{L_1} + \delta\mathbf{L_1} - i(\lambda_j + \delta\lambda_j)\mathbf{I})(\hat{\boldsymbol{q}}_{\boldsymbol{j}} + \delta\hat{\boldsymbol{q}}_{\boldsymbol{j}}) = 0. \tag{3.71}$$

Dropping terms of quadratic order or higher and simplifying, we have

$$(\mathbf{L_1} - \lambda_j \mathbf{I})\delta\hat{\boldsymbol{q}}_{\boldsymbol{j}} + (\delta\mathbf{L_1} - \delta\lambda_j \mathbf{I})\hat{\boldsymbol{q}}_{\boldsymbol{j}} = 0. \tag{3.72}$$

Taking an inner product with the adjoint eigenvector $\hat{\boldsymbol{q}}_{\boldsymbol{j}}{}^+$ in the energy-norm leads

to an expression for $\delta\lambda_j$, we have

$$< \hat{\boldsymbol{q}}_{\boldsymbol{j}}{}^{+}, (\mathbf{L_1} - \lambda_j \mathbf{I})\delta\hat{\boldsymbol{q}}_{\boldsymbol{j}} >_E = - < \hat{\boldsymbol{q}}_{\boldsymbol{j}}{}^{+}, (\delta\mathbf{L_1} - \delta\lambda_j \mathbf{I})\hat{\boldsymbol{q}}_{\boldsymbol{j}} >_E . \tag{3.73}$$

Noting $< \hat{\boldsymbol{q}}_{\boldsymbol{j}}{}^{+}, (\mathbf{L_1} - \lambda_j \mathbf{I})\delta\hat{\boldsymbol{q}}_{\boldsymbol{j}} >_E = < (\mathbf{L_1}{}^{+} - \lambda_j^{+}\mathbf{I})\hat{\boldsymbol{q}}_{\boldsymbol{j}}{}^{+}, \delta\hat{\boldsymbol{q}}_{\boldsymbol{j}} >_E$, and by definition $(\mathbf{L_1}{}^{+} - \lambda_j^{+}\mathbf{I})\hat{\boldsymbol{q}}_{\boldsymbol{j}}{}^{+} = 0$, we see that the first term on the left is zero and we are therefore left with

$$\delta\lambda_j = \frac{< \hat{\boldsymbol{q}}_{\boldsymbol{j}}{}^{+}, \delta\mathbf{L_1}\hat{\boldsymbol{q}}_{\boldsymbol{j}} >_E}{< \hat{\boldsymbol{q}}_{\boldsymbol{j}}{}^{+}, \hat{\boldsymbol{q}}_{\boldsymbol{j}} >_E} = < \hat{\boldsymbol{q}}_{\boldsymbol{j}}{}^{+}, \delta\mathbf{L_1}\hat{\boldsymbol{q}}_{\boldsymbol{j}} >_E, \tag{3.74}$$

where it is assumed that the eigenvectors are appropriately normalised. The expression can be bounded,

$$|\delta\lambda_j| \leq ||\hat{\boldsymbol{q}}_{\boldsymbol{j}}{}^{+}||_E ||\delta\mathbf{L_1}||_E ||\hat{\boldsymbol{q}}_{\boldsymbol{j}}||_E = ||\mathbf{F}\hat{\boldsymbol{q}}_{\boldsymbol{j}}{}^{+}||_2 ||\mathbf{F}\delta\mathbf{L_1}\mathbf{F}^{-1}||_2 ||\mathbf{F}\hat{\boldsymbol{q}}_{\boldsymbol{j}}||_2, \tag{3.75}$$

where subscript E and 2 denote the energy and two norm respectively. The quantity $||\hat{\boldsymbol{q}}_{\boldsymbol{j}}{}^{+}||_E ||\hat{\boldsymbol{q}}_{\boldsymbol{j}}||_E$ appears as a proportionality constant between the norm of the perturbation and the size of the deviation in the eigenvalue, and is therefore interpreted as the sensitivity, which is a property of the stability operator.

3.2.5.2 Pseudospectra

In this section we briefly outline the theory of pseudospectra [86], which are very useful for analysing the sensitivity of dynamical systems which are governed by non-normal operators, such as the OS-SQ system in which we are primarily interested. We list a number of theorems and definitions, which will be invaluable in our later analyses. Unless stated otherwise, the definitions are taken from the extensive review of Trefethen [86].

3.2.5.3 Pseudospectra of Matrices

Definition 2: ϵ-pseudospectra
The ϵ-pseudospectra of $\mathbf{A} \in \mathbb{C}^{N\times N}$ is the set $\Lambda_\epsilon(\mathbf{A})$, with the equivalent definitions:
(i) $\Lambda_\epsilon(\mathbf{A}) = \{z \in \mathbb{C}, ||(z - \mathbf{A})^{-1}|| > \epsilon^{-1}\}$.
(ii) $\Lambda_\epsilon(\mathbf{A}) = \Lambda(\mathbf{A} + \mathbf{E}),\ \forall\ \mathbf{E} \in \mathbb{C}^{N\times N}$ *with* $||\mathbf{E}|| < \epsilon$.
Assuming the norm of interest is the 2-norm, $||.|| = ||.||_2$, then the norm of a matrix is simply its largest singular value, and we have a third definition:
(iii) $\Lambda_\epsilon(\mathbf{A}) = \{z \in \mathbb{C}, s_{min}(z - \mathbf{A}) < \epsilon\}$, *where $s_{min}(z - \mathbf{A})$ denotes the smallest*

singular value of $(z - \mathbf{A})$.

Definition 2 presents a number of different ways of thinking about pseudospectra. From definition 2.i, the ϵ-pseudospectra can be understood as the open subset of the complex plane bounded by the ϵ^{-1} level curve of the resolvent norm, which is the set of complex numbers z for which the resolvent norm at z is large, larger then ϵ^{-1}. The second definition, 2.ii, of the ϵ-pseudospectra has a much clearer connection with eigenvalue perturbation theory, showing the ϵ-pseudospectra to be the set of eigenvalues of some perturbed matrix $\mathbf{A} + \mathbf{E}$, with $||\mathbf{E}|| < \epsilon$. From these definitions, it is evident that the pseudospectra associated with various ϵ form nested sets such that $\Lambda_{\epsilon_1}(\mathbf{A}) \subseteq \Lambda_{\epsilon_2}(\mathbf{A})$, $\forall\ \epsilon_1 < \epsilon_2$, and $\Lambda(\mathbf{A}) = \cap_{\epsilon>0}\Lambda_\epsilon(\mathbf{A})$. The third definition provides a convenient method for numerical computation of the pseudospectra, one can create a mesh in the complex plane, compute the smallest singular value of the resolvent norm at each point, and construct a contour plot.

Definition 3: ϵ-pseudospectra for generalised eigenvalue problems
If $\mathbf{A}$, $\mathbf{B}$ *are square matrices, and* $\mathbf{B}$ *is non singular, then the* ϵ*-pseudospectra for the matrix pencil* $\mathbf{A} - \lambda\mathbf{B}$ *is* $\Lambda_\epsilon(\mathbf{A}, \mathbf{B}) = \Lambda_\epsilon(\mathbf{B^{-1}A})$.

Definition 4: spectral abscissa, ϵ-pseudospectral abscissa
The spectral abscissa of $\mathbf{A} \in \mathbb{C}^{N\times N}$, $\alpha(\mathbf{A}) = \sup_{\lambda\in\Lambda(\mathbf{A})} \Re(\lambda)$.
The ϵ*-pseudospectral abscissa of* $\mathbf{A} \in \mathbb{C}^{NxN}$, $\alpha(\mathbf{A}) = \sup_{\lambda\in\Lambda_\epsilon(\mathbf{A})} \Re(\lambda)$.

Definition 5: spectral radius, ϵ-pseudospectral radius
The spectral radius of $\mathbf{A} \in \mathbb{C}^{N\times N}$, $\rho(\mathbf{A}) = \sup_{\lambda\in\Lambda(\mathbf{A})} abs(\lambda)$.
The ϵ*-pseudospectral radius of* $\mathbf{A} \in \mathbb{C}^{N\times N}$, $\rho(\mathbf{A}) = \sup_{\lambda\in\Lambda_\epsilon(\mathbf{A})} abs(\lambda)$.

Definition 6: numerical range
The numerical range, also called the field of values, of $\mathbf{A} \in \mathbb{C}^{N\times N}$ *is the set of Rayleigh quotients,* $W(\mathbf{A}) = \left\{\mathbf{x}^*\mathbf{A}\mathbf{x} : \mathbf{x} \in \mathbb{C}^N, ||\mathbf{x}|| = 1\right\}$.

The numerical range is the closed, convex subset of $\mathbb{C}^N$ containing the convex hull of the spectrum $\Lambda(\mathbf{A})$. Further, if $\mathbf{A}$ is normal, then the numerical range is exactly equal to the convex hull of the spectrum.

Definition 7: numerical abscissa

The numerical abscissa of $\mathbf{A} \in \mathbb{C}^{N\times N}$, $\omega(\mathbf{A}) = \sup_{z\in W(\mathbf{A})} \Re(z)$

Definitions four to seven are useful in estimating the behaviour of the norm of the matrix exponential, $||\exp\{t\mathbf{A}\}||$, which will be very convenient when we consider the transient problem. The initial, transient and asymptotic behaviour of $||\exp\{t\mathbf{A}\}||$ are quite different. Furthermore, it can be shown that the numerical abscissa, pseudospectra and spectral abscissa determine the initial, transient and asymptotic behaviour respectively.

More specifically, imagine a discretised operator, $\mathbf{A}$, describing the dynamics of some vector, $\mathbf{u}$, such that $\frac{\partial \mathbf{u}}{\partial t} = \mathbf{A}\mathbf{u}$, and hence $\mathbf{u}(t) = \exp\{\mathbf{A}t\}\,\mathbf{u}(0)$. Then $\frac{||\mathbf{u}(t)||}{||\mathbf{u}(0)||} = ||\exp\{t\mathbf{A}\}||$ tells us something about the growth of the solution. Taking the limit, $t \to \infty$, one ordinarily expects the spectrum to be the decisive factor. In fact,

$$\lim_{t\to\infty} t^{-1} \log ||\exp\{t\mathbf{A}\}|| = \alpha(\mathbf{A}), \tag{3.76}$$

holds for any matrix, and it is thus the spectral abscissa that determines the asymptotic behaviour.

Conversely, one may consider the limit, $t \to 0$, and find that,

$$\frac{d}{dt}||\exp\{t\mathbf{A}\}||_{|t=0} = \lim_{t\downarrow 0} t^{-1} \log ||\exp\{t\mathbf{A}\}|| = \omega(\mathbf{A}). \tag{3.77}$$

That is, the numerical abscissa determines the initial response, or more specifically the slope.

The degree of normality of a matrix is related to the degree of linear independence of its eigenvectors. A matrix , $\mathbf{A}$, is normal if it is unitarily diagonalizable, $\mathbf{A} = \mathbf{U}\mathbf{D}\mathbf{U}^*$, where $\mathbf{U}$ is a unitary matrix whose columns are the orthonormal eigenvectors of $\mathbf{A}$ and $\mathbf{D}$ is a diagonal matrix of eigenvalues. The following two theorems are taken from the review of Trefethen [86].

Theorem 1: pseudospectra of a normal matrix
Let Δ_ϵ *be an open ball of radius* ϵ*, then for any* $\mathbf{A} \in \mathbb{C}^{N\times N}$,
$\Lambda_\epsilon(\mathbf{A}) \supseteq \Lambda(\mathbf{A}) + \Delta_\epsilon$.
If $\mathbf{A}$ *is normal (unitary diagonalizable), and* $||.|| = ||.||_2$*, then*
$\Lambda_\epsilon(\mathbf{A}) = \Lambda(\mathbf{A}) + \Delta_\epsilon$.

For a normal matrix, the ϵ-pseudospectra is just the union of ϵ balls about the eigenvalues. Normal matrices are rather insensitive to perturbations, and the degree of normality is thus an indicator of sensitivity. Suppose that $\mathbf{A}$ is not necessarily normal, but has a set of linearly independent eigenvectors and is thus diagonalizable, $\mathbf{A} = \mathbf{V}\mathbf{D}\mathbf{V}^{-1}$, then the condition number of the basis of eigenvectors, $K(\mathbf{A}) = ||\mathbf{V}||_2||\mathbf{V}^{-1}||_2$, characterises the degree of non normality. Denoting the largest and smallest singular values as $s_{max}(\mathbf{V})$ and $s_{min}(\mathbf{V})$, the condition number can be restated, $K(\mathbf{A}) = \frac{s_{max}(\mathbf{V})}{s_{min}(\mathbf{V})} \in [1, \infty)$. The condition number for $\mathbf{V}$ upper bounds the condition number of the individual eigenvalues of $\mathbf{A}$, as described by the Bauer-Fike theorem.

Theorem 2: Bauer-Fike theorem
Suppose $\mathbf{A} \in \mathbb{C}^{N\times N}$ *is diagonalizable,* $\mathbf{A} = \mathbf{V}\mathbf{D}\mathbf{V}^{-1}$. *Then for each* $\epsilon > 0$, *with* $||.|| = ||.||_2$,
$\Lambda(\mathbf{A}) + \Delta_\epsilon \subseteq \Lambda_\epsilon(\mathbf{A}) \subseteq \Lambda(\mathbf{A}) + \Delta_{\epsilon K(\mathbf{V})}$.

We have established that the ϵ-pseudospectra of a matrix is the subset of complex numbers which are eigenvalues of all complex matrices within a distance ϵ of the matrix. If the matrix has a certain structure, such as being symmetric, it is fitting to allow only perturbed matrices with the same structure. That is, if the original matrix has a certain structure, the perturbation must preserve the structure such that the new matrix has the same structure as the original. In such a case, it follows that the structured ϵ-pseudospectra is the subset of complex numbers which are eigenvalues of all complex structured matrices within a distance ϵ of the matrix. When making a structured perturbation one may expect the spectrum to respond differently. If we let *struct* denote some matrix structure, such as being symmetric or Hermitian, it can be shown that the ϵ-pseudospectra associated with a structured perturbation is a subset of the unstructured ϵ-pseudospectra. To be more precise, let us define the structured ϵ-pseudospectra.

Definition 8: structured ϵ-pseudospectra
Letting M_C^{struct} *denote a complex matrix with a particular structure, struct, the structured* ϵ*-pseudospectra of* $\mathbf{A} \in M_C^{struct}$ *is the set* $\Lambda_\epsilon^{struct}(\mathbf{A})$, *such that*
$\Lambda_\epsilon^{struct}(\mathbf{A}) = \Lambda(\mathbf{A} + \mathbf{E}),\ \forall\ \mathbf{E}$ *with* $||\mathbf{E}|| < \epsilon$ *and* $\mathbf{A} + \mathbf{E} \in M_C^{struct}$.

Importantly, it can be shown that $\Lambda_\epsilon^{struct}(\mathbf{A}) \subseteq \Lambda_\epsilon(\mathbf{A})$ [71]. Furthermore, when the structure is symmetric, $struct = sym$, $\Lambda_\epsilon^{sym}(\mathbf{A}) = \Lambda_\epsilon(\mathbf{A})$ [71]. That is, the structured ϵ-pseudospectra of a symmetric matrix is equal to the ϵ-pseudospectra of

that matrix. To see this, it is convenient to make use of the distance to singularity.

Definition 9: distance to singularity
Given a non-singular matrix $\mathbf{A} \in \mathbb{C}^{N\times N}$*, the distance to singularity, denoted* $d(\mathbf{A})$*, is defined as* $d(\mathbf{A}) = min\left\{||\Delta\mathbf{A}||; det(\mathbf{A}+\Delta\mathbf{A}) = 0, \Delta\mathbf{A} \in \mathbb{C}^{N\times N}\right\}$.

Similarly,

Definition 10: structured distance to singularity
Letting M_C^{struct} *denote a complex matrix with a particular structure, struct, then given a non-singular matrix* $\mathbf{A} \in M_C^{struct}$*, the structured distance to singularity, denoted* $d^{struct}(\mathbf{A})$*, is defined as* $d^{struct}(\mathbf{A}) = min\left\{||\Delta\mathbf{A}||; det(\mathbf{A}+\Delta\mathbf{A}) = 0, \Delta\mathbf{A} \in M_C^{struct}\right\}$.

Noting that $d(\mathbf{A}) = s_{min}(\mathbf{A})$ [28], and appealing to our Definition 2.iii, we see that the ϵ-pseudospectra may be written as

$$\Lambda_\epsilon(\mathbf{A}) = \left\{z \in \mathbb{C}, d(z-\mathbf{A}) < \epsilon\right\}. \tag{3.78}$$

Similarly,

$$\Lambda_\epsilon^{struct}(\mathbf{A}) = \left\{z \in \mathbb{C}, d^{struct}(z-\mathbf{A}) < \epsilon\right\}. \tag{3.79}$$

If $\mathbf{A} \in M_C^{sym}$, then $(z-\mathbf{A}) \in M_C^{sym}$ preserves the symmetric structure. In order to show that $\Lambda_\epsilon^{sym}(\mathbf{A}) = \Lambda_\epsilon(\mathbf{A})$, it suffices to show that $d^{sym}(\mathbf{A}) = d(\mathbf{A})$. That is, it is sufficient to show that $(\mathbf{A}+\Delta\mathbf{A})x = 0$ for some $x \neq 0$ with $\Delta\mathbf{A}$ symmetric and $d(\mathbf{A}) = s_{min}(\mathbf{A})$. Following Graillat [28], we show this to be true.

Let $\mathbf{A} \in M_C^{sym}$, then in accordance with the Takagi factorisation [35], we may write $\mathbf{A} = \mathbf{U}\mathbf{\Sigma}\mathbf{U}^T$, where $\mathbf{U}$ is a unitary matrix and $\mathbf{\Sigma}$ a diagonal matrix of the singular values of $\mathbf{A}$. If y is the column of $\mathbf{U}$ corresponding to the smallest singular value of $\mathbf{A}$, then $\mathbf{A}y^* = s_{min}(\mathbf{A})y$, where y^* denotes the complex conjugate of y. Furthermore, there exists a symmetric matrix $\mathbf{S}$ with $\mathbf{S}y^* = y$ and $||\mathbf{S}|| = 1$ [70]. We can construct a symmetric matrix by letting $\Delta\mathbf{A} = -s_{min}(\mathbf{A})\mathbf{S}$. Then

$$(\mathbf{A}+\Delta\mathbf{A})y^* = \mathbf{A}y^* + \Delta\mathbf{A}y^* = s_{min}(\mathbf{A})y - s_{min}(\mathbf{A})y = 0. \tag{3.80}$$

That is we have $\mathbf{A}+\Delta\mathbf{A}$ is singular where $\mathbf{A} \in M_C^{sym}$ and $\Delta\mathbf{A} \in M_C^{sym}$. Hence $\Lambda_\epsilon^{sym}(\mathbf{A}) = \Lambda_\epsilon(\mathbf{A})$.

Whilst eigenvalues are able to locate normal matrices in the complex plane, non-normal matrices cannot be pinned down so easily, and one must therefore appeal

to the family of ϵ-pseudospectra, $\{\Lambda_\epsilon(\mathbf{A})\}_\epsilon$, to not only bound their location, but indicate the sensitivity of their eigenvalues to perturbations. Having set forth the fundamentals of pseudospectra, we next make the connection to hydrodynamic stability theory.

3.2.5.4 Pseudospectra of the Orr-Sommerfeld Operator

The central question in modal stability analysis has always been, do the eigenvalues have positive imaginary part? If so, at least one exponentially growing perturbation exists, and the flow is thus deemed asymptotically unstable. As already alluded to, at sufficiently large Reynolds number many shear flows do indeed have eigenvalues which protrude into the unstable region of the complex half plane. In particular, we have seen that plane Poiseuille flow becomes asymptotically unstable at a Reynolds number of 5772, at a stream-wise wave-number of around 1.02. At any Reynolds number below this critical level, and any wave-number the flow is predicted eigenvalue stable. However, this is where eigenvalue analysis breaks down as it has long been known that plane Poiseuille flow can transition to instability at Reynolds numbers far below the theoretical critical limit of 5772. If one considers plane Poiseuille flow, at stream-wise wave-number 1.02 and Reynolds number 10000 (far exceeding the critical Reynolds number), one finds that modal analysis predicts an instability growing at a rate $\approx \exp(0.0037t)$, an exceptionally slow rate at such a large Reynolds number. A perturbation growing at this rate would need to travel many hundreds of channel widths downstream before growing by a mere factor of ten. Whilst such a channel has likely never been created, transition to turbulence at this Reynolds number is commonly observed in experiments. Clearly, the spectrum alone is not sufficient to explain the behaviour of real fluid flows.

The pseudospectra of the Orr-Sommerfeld operator, studied at length by Reddy, Schmid and Henningson [67], helps us to understand such phenomenon a little better. Below, in figure 3.3, we plot the pseudospectra of plane Poiseuille flow at the critical condition, that is $Re = 5772$ and $\alpha = 1.02$.

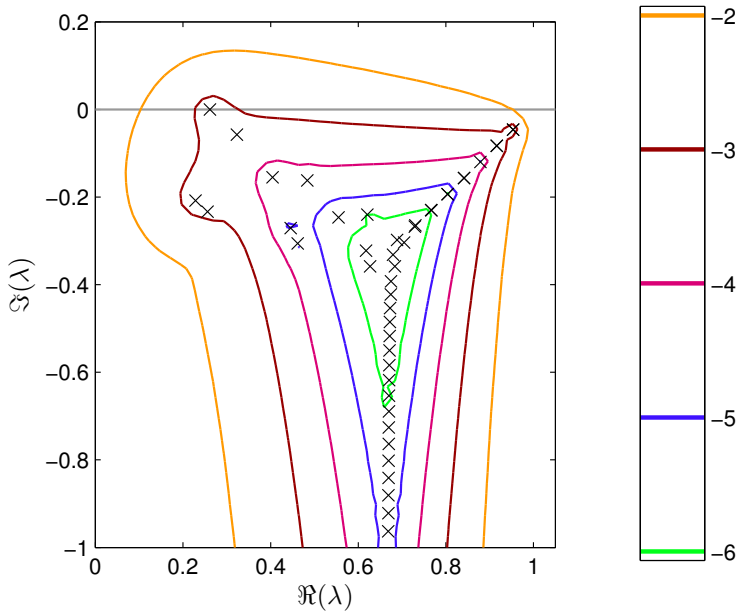

Figure 3.3: ϵ-pseudospectra of plane Poiseuille flow with log resolvent norm contours (contours of $\log_{10}\epsilon$), $\alpha = 1.02$, $\beta = 0.0$, $Re = 5772$.

The most striking feature of the spectrum is the non-normality, which one observes at the intersection of the Y branch. In this region, the eigenvalue problem is extremely ill conditioned where the resolvent norm can reach values of 10^6. We have already seen that the condition number (in the 2-norm) at this Reynolds number is exceptionally large and the eigenvalues are thus difficult to accurately compute. They are deep inside the spectrum and the ill conditioning has little physical relevance.

We note that the above definitions, outlined in this section, are dependent on a particular choice of norm $||.||$. It is convenient to compute the 2-norm, we therefore require a means of transforming the norm of interest into the 2-norm, and such tools will be outlined in 3.3.3.1.

3.3 Transient Analysis of the Viscous Problem

3.3.1 Introduction

In this section we return to the equations governing the evolution of small perturbations. Rather than focus on the eigenvalue formulation, the equations are assessed from the perspective of an initial value problem. Whilst this may appear, at first, to

be a trivial matter of formalism, it actually significantly alters the way we characterise the behaviour of disturbances. As previously alluded to by the pseudospectra, such phenomenon are rooted in linear algebra. To be more precise, differences between modal and transient analysis are a consequence of a discretised operators normality, or lack thereof.

To motivate the topic, we follow Schmid and Henningson [75]. Appealing to a model problem, we aim to highlight the differences between a modal and non modal analysis. Consider the problem

$$\frac{d}{dt}\begin{pmatrix} u_2 \\ \eta \end{pmatrix} = \begin{pmatrix} -\frac{1}{Re} & 0 \\ 1 & -\frac{2}{Re} \end{pmatrix}\begin{pmatrix} u_2 \\ \eta \end{pmatrix}, \tag{3.81}$$

with the initial conditions, $u_2(0) = u_2^0$ and $\eta(0) = \eta^0$. The important feature here is the non zero off diagonal term, which signifies that η is driven by u_2. Noting the eigenvalues of the system, $\left\{-\frac{1}{Re}, -\frac{2}{Re}\right\}$, we have the analytic solution

$$\begin{pmatrix} u_2 \\ \eta \end{pmatrix} = \begin{pmatrix} 1 \\ Re \end{pmatrix} u_2^0 \exp\left\{-\frac{t}{Re}\right\} + \begin{pmatrix} 0 \\ 1 \end{pmatrix}(\eta^0 - u_2^0 Re)\exp\left\{-\frac{2t}{Re}\right\}. \tag{3.82}$$

The eigenvalues alone suggest a time decaying solution, and would thus predict an eigenvalue stable system. This is certainly true of the wall normal velocity, but one must be a little more cautious when considering the vorticity component.

$$\eta(t) = \eta^0 \exp\left\{-\frac{2t}{Re}\right\} + u_2^0 Re\left\{\exp\left\{-\frac{t}{Re}\right\} - \exp\left\{-\frac{2t}{Re}\right\}\right\}. \tag{3.83}$$

Clearly, the evolution of the initial condition, η^0, decays in time. However, the second term, which represents the response due to driving by u_2, can be shown to exhibit transient growth. To see this, consider the Taylor expansion

$$\begin{aligned} u_2^0 Re\left\{\exp\left\{-\frac{t}{Re}\right\} - \exp\left\{-\frac{2t}{Re}\right\}\right\} &= u_2^0 Re\left\{\sum_{i=0}^{\infty}\left\{\frac{(-t)^i}{Re^i} - \frac{(-2t)^i}{Re^i}\right\}\right\} \\ &= u_2^0 t - \frac{3u_2^0}{Re}t^2 + \ldots, \end{aligned}$$

which, for small values of $t < \mathcal{O}(Re)$, can exhibit algebraic growth. We thus see that the superposition of decaying exponentials can generate short time algebraic, or transient growth. This phenomenon is a consequence of normality, the governing

matrix has non orthogonal eigenvectors,

$$\mathbf{q}_1 = \frac{1}{\sqrt{1+Re^2}} \begin{pmatrix} 1 \\ Re \end{pmatrix}, \tag{3.84}$$

$$\mathbf{q}_2 = \begin{pmatrix} 0 \\ 1 \end{pmatrix}. \tag{3.85}$$

As the Reynolds number increases, eigenvectors one and two will align. Geometrically, a general initial condition is represented by a superposition of the two eigenvectors, and the solution at all times is the vector superposition of these evolved modes. Whilst the length of each mode decays, at high Reynolds number the angle between the modes is very small and their superposition can actually increase in length, before decaying exponentially, thus giving rise to the transient growth phenomenon.

The preceding example should make it clear that eigenvalues, on their own, are insufficient, and eigenvectors, or the angle between them, are of equal importance. Spectral analysis alone cannot capture the full dynamics of a system governed by a non-normal discretised operator. In what follows, we set forth a system of alternative tools, allowing one to detect transient effects and quantify short-time behaviour.

3.3.2 Viscous Initial Value Problem

3.3.2.1 Discrete Formulation

Returning to the Orr-Sommerfeld and Squire equations and, contrary to previous explorations, making no assumption about the time dependency of solutions, we have

$$\left\{ (\frac{\partial}{\partial t} + i\alpha U)(D^2 - k^2) - i\alpha U'' - \frac{1}{Re}(D^2 - k^2)^2 \right\} \hat{u_2} = 0, \tag{3.86}$$

$$\left\{ (\frac{\partial}{\partial t} + i\alpha U) - \frac{1}{Re}(D^2 - k^2) \right\} \hat{\eta} = -i\beta U' \hat{u_2}, \tag{3.87}$$

with the boundary conditions, at solid walls and in the far field, $\hat{u_2} = D\hat{u_2} = \hat{\eta} = 0$.

To quantify the size of disturbances, we use the perturbation kinetic energy. Using Parseval's equality, this can be written in terms of the Fourier coefficients [29],

$$E_V = \int_\alpha \int_\beta E d\alpha d\beta, \tag{3.88}$$

where E is the energy density in Fourier space,

$$E = \int_{-1}^{1} |\hat{u_1}|^2 + |\hat{u_2}|^2 + |\hat{u_3}|^2 dx_2. \tag{3.89}$$

Noting that we may map from primitive to wall normal variables,

$$\begin{pmatrix} \hat{u_1} \\ \hat{u_2} \\ \hat{u_3} \end{pmatrix} = \begin{pmatrix} \frac{i\alpha D}{k^2} & -\beta I \\ I & 0 \\ \frac{i\beta D}{k^2} & -\alpha I \end{pmatrix} \begin{pmatrix} \hat{u_2} \\ \hat{\eta} \end{pmatrix}. \tag{3.90}$$

We therefore have

$$E = \frac{1}{2k^2} \int_{-1}^{1} \begin{pmatrix} \hat{u_2} \\ \hat{\eta} \end{pmatrix}^H \begin{pmatrix} (k^2 - D^2) & 0 \\ 0 & I \end{pmatrix} \begin{pmatrix} \hat{u_2} \\ \hat{\eta} \end{pmatrix} dx_2, \tag{3.91}$$

which is effectively a weighted inner product. We hence have

$$E_V = \int_\alpha \int_\beta \frac{1}{2k^2} \int_{-1}^{1} \left\{ |D\hat{u_2}|^2 + k^2 |\hat{u_2}|^2 + |\hat{\eta}|^2 \right\} dx_2 d\alpha d\beta. \tag{3.92}$$

3.3.3 Transient Growth

The eigen-modes of the Orr-Sommerfeld and Squire system form a complete set, and they can therefore be used to expand a general solution to the initial value problem,

$$\mathbf{L} \frac{\partial \mathbf{q}}{\partial t} = \mathbf{R}\mathbf{q}. \tag{3.93}$$

Or equivalently,

$$\frac{\partial \mathbf{q}}{\partial t} = \mathbf{L}^{-1}\mathbf{R}\mathbf{q} = \mathbf{L_1}\mathbf{q}. \tag{3.94}$$

In general, the solution to the Orr-Sommerfeld and Squire equations can be written as $\mathbf{q}(x_2, t) = \exp(-i\mathbf{L_1}t)\mathbf{q}(x_2, 0)$. Since the eigenfunctions form a complete set, we may expand the general solution, $\mathbf{q}(x_2, t) = \sum_{n=1}^{\infty} k_n(0) \exp(-i\lambda_n t)\tilde{\mathbf{q}}_n(x_2) = \sum_{n=1}^{\infty} k_n(t)\tilde{\mathbf{q}}_n(x_2)$, where $\tilde{\mathbf{q}}_n(x_2)$ denotes the nth eigenfunction. Further, if we order eigenvalues in descending imaginary part it is clear that terms for large n will be negligible and we may approximate the solution with the k eigenfunctions with

largest imaginary part, $\mathbf{q}(x_2,t) \approx \sum_{n=1}^{k} k_n(t)\tilde{\mathbf{q}}_n(x_2)$. More formally, let $\mathbb{S}^k$ denote the space spanned by the k eigenmodes with largest imaginary part,

$$\mathbb{S}^k = span\left\{\tilde{\mathbf{q}}_1(x_2), ..., \tilde{\mathbf{q}}_k(x_2)\right\}. \tag{3.95}$$

Then we can expand $\mathbf{q} \in \mathbb{S}^k$ in the basis $\{\tilde{\mathbf{q}}_1(x_2), ..., \tilde{\mathbf{q}}_k(x_2)\}$,

$$\mathbf{q}(x_2,t) = \sum_{n=1}^{k} k_n(t)\tilde{\mathbf{q}}_n(x_2), \forall \mathbf{q} \in \mathbb{S}^k. \tag{3.96}$$

Letting $\mathbf{k}(t)$ be the vector of coefficients, we can reformulate the initial value problem,

$$\frac{d\mathbf{k}}{dt} = -i\mathbf{\Lambda}\mathbf{k}, \forall \mathbf{\Lambda} \in \mathbb{C}^{k\times k}, \mathbf{k} \in \mathbb{C}^k. \tag{3.97}$$

And we then have $\mathbf{k}(t) = \exp(-i\mathbf{\Lambda}t)\mathbf{k}(0)$. The operator $\mathbf{\Lambda}$ is the projection of the evolution operator, $\mathbf{L_1}$, onto the space $\mathbb{S}^k$, which is effectively the diagonal matrix whose elements are the k eigenvalues with largest imaginary part. Henceforth, we can focus on the simplified initial value problem, describing the evolution of the expansion coefficients in $\mathbf{k}$, which are associated with both the Orr-Sommerfeld and Squire modes.

It should be noted that this simplified version of the initial value problem assumes both discrete eigenvalues and complete eigenvectors. The eigenvalue assumption is, in fact, only true for flows whose domain is bounded in the wall normal direction. For unbounded flows, such as the Blasius boundary layer, the spectrum comprises both a continuous and a discrete component. However, for computational purposes, it is often sufficient to use a discretised approximation to the continuous spectrum when solutions to the initial value problem are required. Whilst the eigenvalues of the discrete approximation may differ from their exact representation (especially as the decay rate increases), Butler and Farrell [37] show that their sum correctly describes the solution to the initial value problem.

However, one should ensure that computed results are independent of the continuous approximation. To this end, one should compute the spectrum at various levels of wall normal discretization, and ensure that the result does not depend on the discretization parameter.

3.3.3.1 Energy Norm

To complete the transformation, from $\mathbf{q}$ to $\mathbf{k}$, we must reformulate the scalar product and its associated norm. For $\mathbf{q_1}, \mathbf{q_2} \in \mathbb{S}^k$,

$$
\begin{aligned}
< \mathbf{q_1}, \mathbf{q_2} >_E &= \frac{1}{k^2} \int_{-1}^{1} \mathbf{q_2}^H \mathbf{L} \mathbf{q_1} dx_2 \\
&= \frac{1}{k^2} \int_{-1}^{1} \sum_{n_2=1}^{k} (k_{n_2} \tilde{\mathbf{q}}_{\mathbf{2}}^{n_2}(x_2))^H \mathbf{L} \sum_{n_1=1}^{k} k_{n_1} \tilde{\mathbf{q}}_{\mathbf{1}}^{n_1}(x_2) dx_2 \\
&= \frac{1}{k^2} \sum_{n_1=1}^{k} \sum_{n_2=1}^{k} k_{n_2}^H k_{n_1} \int_{-1}^{1} \tilde{\mathbf{q}}_{\mathbf{2}}^{n_2}(x_2)^H \mathbf{L} \tilde{\mathbf{q}}_{\mathbf{1}}{}^{n_1}(x_2) dx_2 \\
&= \mathbf{k_2}^H \mathbf{M} \mathbf{k_1},
\end{aligned}
$$

where weight matrix $\mathbf{M}$ is both Hermitian and positive definite, with components,

$$
M_{ij} = \frac{1}{k^2} \int_{-1}^{1} \mathbf{q_j}^H \mathbf{L} \mathbf{q_i} dx_2. \tag{3.98}
$$

We can therefore factor $\mathbf{M} = \mathbf{F}^H \mathbf{F}$, and we have the inner product

$$
< \mathbf{q_1}, \mathbf{q_2} >_E = \mathbf{k_2}^H \mathbf{M} \mathbf{k_1} = \mathbf{k_2}^H \mathbf{F}^H \mathbf{F} \mathbf{k_1} = < \mathbf{F} \mathbf{k_1}, \mathbf{F} \mathbf{k_2} >_2 . \tag{3.99}
$$

The energy norm of $\mathbf{q} \in \mathbb{S}^k$, then follows

$$
< \mathbf{q}, \mathbf{q} >_E = ||\mathbf{q}||_E^2 = ||\mathbf{F}\mathbf{k}||_2^2. \tag{3.100}
$$

And for matrices, $\mathbf{B}$, the energy norm is induced by the vector norm,

$$
\begin{aligned}
||\mathbf{B}||_E &= \sup_{\mathbf{q} \neq 0} \frac{||\mathbf{B}\mathbf{q}||_E}{||\mathbf{q}||_E} = \sup_{\mathbf{q} \neq 0} \frac{||\mathbf{F}\mathbf{B}\mathbf{q}||_2}{||\mathbf{F}\mathbf{q}||_2} \\
&= \sup_{\mathbf{q} \neq 0} \frac{||\mathbf{F}\mathbf{B}\mathbf{F}^{-1}\mathbf{F}\mathbf{q}||_2}{||\mathbf{F}\mathbf{q}||_2} = ||\mathbf{F}\mathbf{B}\mathbf{F}^{-1}||_2.
\end{aligned}
$$

3.3.3.2 Optimal Growth

We now have the necessary tools to formulate the maximum amplification of initial energy density, which we denote $G(t)$. To do so, at each time step, we search for the initial perturbation that maximises the short term, or transient, growth. More formally,

$$
\begin{aligned}
G(t) &= \sup_{\mathbf{q}\neq 0} \frac{||\mathbf{q}(t)||_E^2}{||\mathbf{q}(0)||_E^2} = \sup_{\mathbf{k}(0)\neq 0} \frac{||\mathbf{F}\mathbf{k}(t)||_2^2}{||\mathbf{F}\mathbf{k}(0)||_2^2} \\
&= \sup_{\mathbf{k}(0)\neq 0} \frac{||\mathbf{F}exp\left\{-i\mathbf{\Lambda}t\right\}\mathbf{k}(0)||_2^2}{||\mathbf{F}\mathbf{k}(0)||_2^2} = \sup_{\mathbf{F}\mathbf{k}(0)\neq 0} \frac{||\mathbf{F}exp\left\{-i\mathbf{\Lambda}t\right\}\mathbf{F}^{-1}\mathbf{F}\mathbf{k}(0)||_2^2}{||\mathbf{F}\mathbf{k}(0)||_2^2} \\
&= ||\mathbf{F}exp\left\{-i\mathbf{\Lambda}t\right\}\mathbf{F}^{-1}||_2^2 \\
&= S_{max}^2(\mathbf{F}exp\left\{-i\mathbf{\Lambda}t\right\}\mathbf{F}^{-1}),
\end{aligned}
$$

which is simply the square of the largest (principal) singular value of the matrix $\mathbf{F}exp\left\{-i\mathbf{\Lambda}t\right\}\mathbf{F}^{-1}$. The time series, $G(t)$, represents the maximum energy amplification at each time, optimised over all possible initial conditions with unit energy norm. It is worth noting that the initial condition that optimises the growth function may be different for different times. The curve should therefore be considered as an envelope which upper bounds the energy amplification at all times. We plot examples of such curves below, in figure 3.4, for plane Poiseuille flow at wave numbers $\alpha = 1.02$, $\beta = 0.0$, and varying Reynolds numbers.

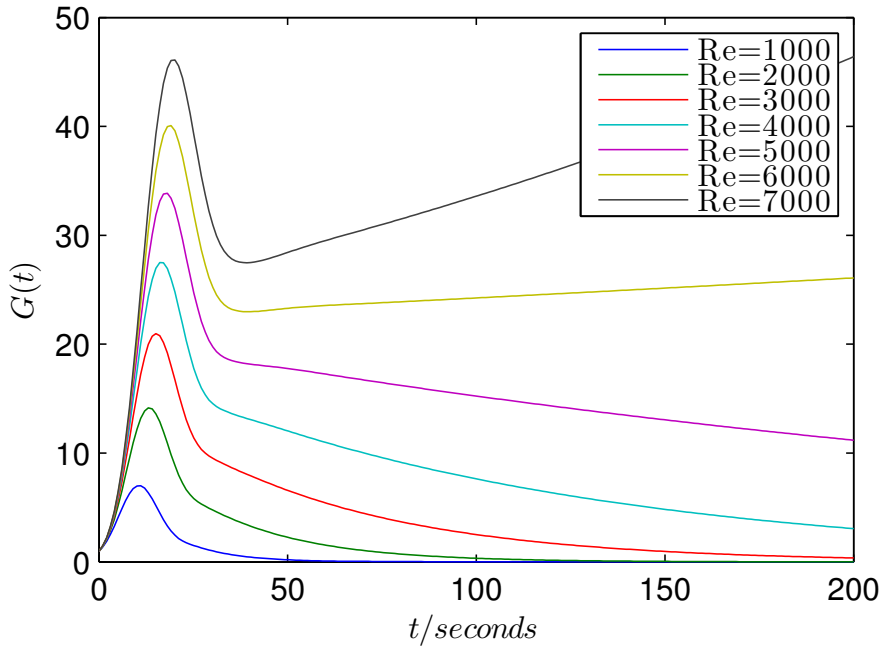

Figure 3.4: Transient growth of plane Poiseuille flow, $\alpha = 1.02$, $\beta = 0.0$.

As can be seen, transient growth is exhibited at all Reynolds numbers, but only flows at Reynolds numbers of six and seven thousand show asymptotic instability, as they continue to grow in time. This is expected as we know that the plane Poiseuille flow is asymptotically unstable at Reynolds numbers exceeding 5772, at

this particular wave-number combination.

Chapter 4

Numerical Implementation and Justification of Stochastic Model

4.1 Introduction and Assumptions

In this section we set out the deterministic formulation, introduce and justify our source of stochasticity, and extend the deterministic equations to give the stochastic formulation. There is a brief discussion on the formation of Latin Hypercubes, which we will use in later chapters. In addition, we discuss the numerical implementation and use a number of case studies to illustrate the identification of suitable levels of discretization for both the physical and stochastic domains, along with a suitable choice of polynomial chaos order. The case studies are naturally dependent on the choice of flow type, wave-number pair and Reynolds number, and are only presented as examples to demonstrate the process of selecting appropriate discretization levels.

To summarise, before going into the details, we select 200 collocation points for the discretization of the physical domain, and this is selected for sufficient resolution of the spectral modes as discussed in section 4.1.1.1. We select 4 and 12 dimensions for discretization of the stochastic domain for processes with correlation lengths of 0.50 and 0.10 respectively, and these are selected to give an error of less than 5 percent in the reconstruction of the correlation kernel, as discussed in section 4.3. In accordance with the case study in section 4.5, we select a polynomial chaos order of 7. Finally, we note that it is optimal to use a tensor grid in low stochastic dimension, a sparse grid in intermediate stochastic dimensions and an LHS grid in high stochastic dimensions.

4.1.1 Deterministic Formulation

We assume viscid, uniform, steady and incompressible 2D flow between parallel rigid and impermeable plates, where we apply appropriate no-slip and no-penetration conditions. We further assume an infinite plate length and span, both thus much greater than the distance separating the plates. Although in general all fluids flow three-dimensionally, with flow properties varying in all directions, the greatest changes in this case are confined to two directions. The driving forces cause flow in the down-stream direction, whilst variations in the cross-stream direction are a consequence of the boundary conditions at the plates. In comparison, changes in the span-wise direction are minimal and can be neglected, thus justifying the simplifying assumption of 2D flow. Further, a constant cross-section justifies our uniform flow assumption, whilst pressure changes are insufficient to induce variations in density, thus justifying the incompressibility assumption.

We will be considering two channel flows, plane Poiseuille and plane Couette, as described in the previous paragraph. We will also consider a Blasius boundary layer later. The Poiseuille flow is driven by a pressure gradient in the direction of the flow, and is retarded by viscous drag along both plates, such that these forces are in balance. Such a flow could be created by a constant velocity profile at the entrance, and we assume that we are sufficiently far downstream for the formation of a steady uniform parabolic base profile. Conversely, the Couette flow is driven by viscous forces, induced by tangential relative motion of the plates in the downstream direction. Again, we assume we are sufficient far downstream to establish a uniform steady linear base flow profile. With an infinite domain in the stream-wise and span-wise directions, x_1 and x_3, and $x_2 \in [-1, 1]$ bounded by the plates, we have the deterministic Poiseuille base flow, $U_i(x_2) = (1 - x_2^2)\delta_{1i} \; \forall \; x_2 \in [-1, 1]$, and the deterministic Couette flow $U_i(x_2) = x_2\delta_{1i} \; \forall \; x_2 \in [-1, 1]$. The base flow profile of the Blasius boundary layer is not known explicitly, but can be found from the solution of a non-linear ordinary differential equation.

An infinitesimal three-dimensional perturbation is added, of the from $\epsilon(x_2, t) \exp(i\alpha x_1 + i\beta x_3)$, and the governing Navier-Stokes equations are linearized about the base flow. If one further assumes an exponential dependency on time, $\epsilon(x_2, t) = \epsilon(x_2) \exp(-i\lambda t)$, the system is then reduced to the well known Orr-Sommerfeld and Squire (OSSQ) equations for the wall normal velocity vorticity amplitudes,

$$-i\lambda \begin{pmatrix} (K^2 - D^2) & 0 \\ 0 & I \end{pmatrix} \begin{pmatrix} \hat{u_2} \\ \hat{\eta} \end{pmatrix} + \begin{pmatrix} L_{OS} & 0 \\ i\beta U' & L_{SQ} \end{pmatrix} \begin{pmatrix} \hat{u_2} \\ \hat{\eta} \end{pmatrix} = 0, \tag{4.1}$$

where $L_{OS} = i\alpha U(K^2 - D^2) + i\alpha U'' + \frac{1}{Re}(K^2 - D^2)^2$ is the fourth order Orr-Sommerfeld operator, $L_{SQ} = i\alpha U - \frac{1}{Re}(D^2 - K^2)$ is the second order Squire operator, and $i\beta U'$ the coupling operator. In more compact form, the equations read

$$(\mathbf{L}^{-1}\mathbf{R} - i\lambda\mathbf{I})\hat{\boldsymbol{q}} = (\mathbf{L_1} - i\lambda\mathbf{I})\hat{\boldsymbol{q}} = 0, \tag{4.2}$$

where $\mathbf{L}$ and $\mathbf{R}$ are the left and right matrices of the above formulation. The Orr-Sommerfeld operator is fourth order and requires four boundary conditions, whilst the Squire operator is second order and requires two. No penetration at the solid boundaries implies that the wall normal velocity perturbation be zero, $\hat{u_2} = 0$ at $x_2 = \pm 1$. Furthermore, no slip at the solid boundaries implies that the stream-wise and span-wise velocities also be zero, $\hat{u_1} = \hat{u_3} = 0$ at $x_2 = \pm 1$, which in turn implies that the wall normal vorticity is zero, $\hat{\eta} = \frac{\partial \hat{u_1}}{\partial x_3} - \frac{\partial \hat{u_3}}{\partial x_1} = 0$ at $x_2 = \pm 1$. Finally, coupling zero span-wise and stream-wise velocity perturbations at the wall with the continuity condition gives $\frac{\partial \hat{u_2}}{\partial x_2} = 0$. The wall normal velocity $\hat{u_2}$ and vorticity amplitude $\hat{\eta}$ therefore satisfy the boundary conditions $\hat{u_2} = \frac{\partial \hat{u_2}}{\partial x_2} = \hat{\eta} = 0$ at $x_2 = \pm 1$.

4.1.1.1 Unresolved Modes and Discretization

Before proceeding with the stochastic formulation, one must first choose a suitable discretization level for the physical domain. It can be observed that eigenfunctions corresponding to eigenvalues along the S branch (figure 3.1) of the spectrum become increasingly oscillatory with decreasing imaginary part. These highly oscillatory eigenfunctions can be resolved at one discretization level but not another, and naturally require a greater level of discretization. Below, in figure 4.1, we plot the spectrum of a deterministic plane Poiseuille flow, at $\alpha = 1$, $\beta = 0$, $R_e = 12000$ and varying levels of discretization.

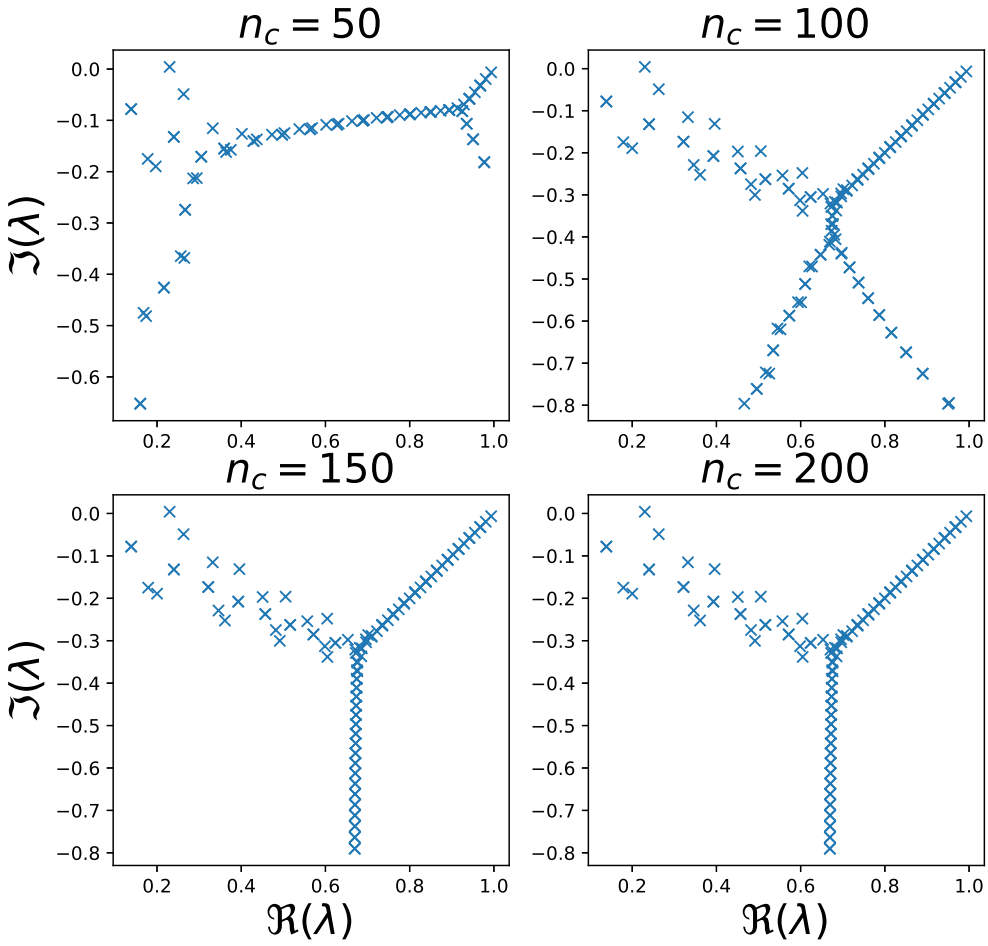

Figure 4.1: Insufficiently resolved Orr-Sommerfeld spectrum for deterministic plane Poiseuille flow, $\alpha = 1.00$, $\beta = 0.00$, $Re = 12000$, at discretization levels of 50 (top left), 100 (top right), 150 (bottom left) and 200 (bottom right).

Inspecting the S branch, and observing with decreasing imaginary part, it can be seen that the numerical resolution eventually becomes insufficient with the eigenvalues deviating from the straight line which they usually follow. Increasing the resolution helps to alleviate the issue and becomes sufficient at around 150 points in this case. At an extremely low resolution of 50 points, it is further observed that modes from the A and P branch are also insufficiently resolved. We therefore conclude that 200 spectral collocation points should be sufficient to resolve modes with $\Im(\lambda) > -0.8$, and this is the number adopted in numerical experiments.

4.1.2 Stochastic Formulation

Recent work [67] [66] [87] has focused on the non-normality of the underlying differential operator, applying an external unstructured random perturbation of magnitude ε, giving

$$(\mathbf{L_1} + \mathbf{E} - i\lambda\mathbf{I})\hat{\boldsymbol{q}} = 0, \tag{4.3}$$

where $||\mathbf{E}|| < \varepsilon$. The sensitivity of the eigen-solutions are highly dependent on the condition number of operator $\mathbf{L_1}$ and the magnitude of the structured perturbation, ε. Highly non-normal operators, such as the operator for Couette flow, have large condition numbers and a very small modification is thus sufficient to introduce non-negligible variations in the eigen-solutions. However, the physical meaning of such external perturbations is not clear and, furthermore, may introduce artificial coupling between the wall-normal velocity and vorticity components. Conversely, an internal structured perturbation makes more physical sense, and may represent some defects in the base flow by modifying the profile. We therefore adopt the latter approach, modifying the deterministic base flow profile with a truncated KLE representing the randomness in the solution, giving the formulation

$$(\boldsymbol{L_1}^* - i\lambda\boldsymbol{I})\,\hat{\boldsymbol{q}} = 0, \tag{4.4}$$

where the matrix $\boldsymbol{L_1}^*$ is the stochastic equivalent to $\boldsymbol{L_1}$, and follows by replacing the deterministic base flow with the Karhunen-Loève representation of the stochastic counterpart. Such randomness is characterised by the choice of correlation kernel.

4.1.3 Choice of Correlation Kernel and Stochastic Base Flow

In order to motivate our choice of stochasticity we inspect experimental shear flow data for a Blasius boundary layer. This data was kindly provided by Professor Michael Gaster's lab at City University, and previously used in experimental investigations by Barry Crowley [14]. It should be emphasised that the following results hold, with certainty, only for the Blasius boundary layer, and they do not necessarily apply to the general class of shear flows including the plane Poiseuille and Couette flow.

Whilst we are primarily interested in an unforced flow we inspect two sets of data, corresponding to both a forced and unforced case for comparison. The experimental data is taken from a wind tunnel with a turbulence intensity of 0.014 percent (with

the model placed), and consists of multiple observations of the mean flow at different downstream locations. Forcing is provided by a loudspeaker placed inside a cavity with a small hole, and measurements taken via a hot wire. Shown below, in figure 4.2, is the model used in the wind tunnel tests.

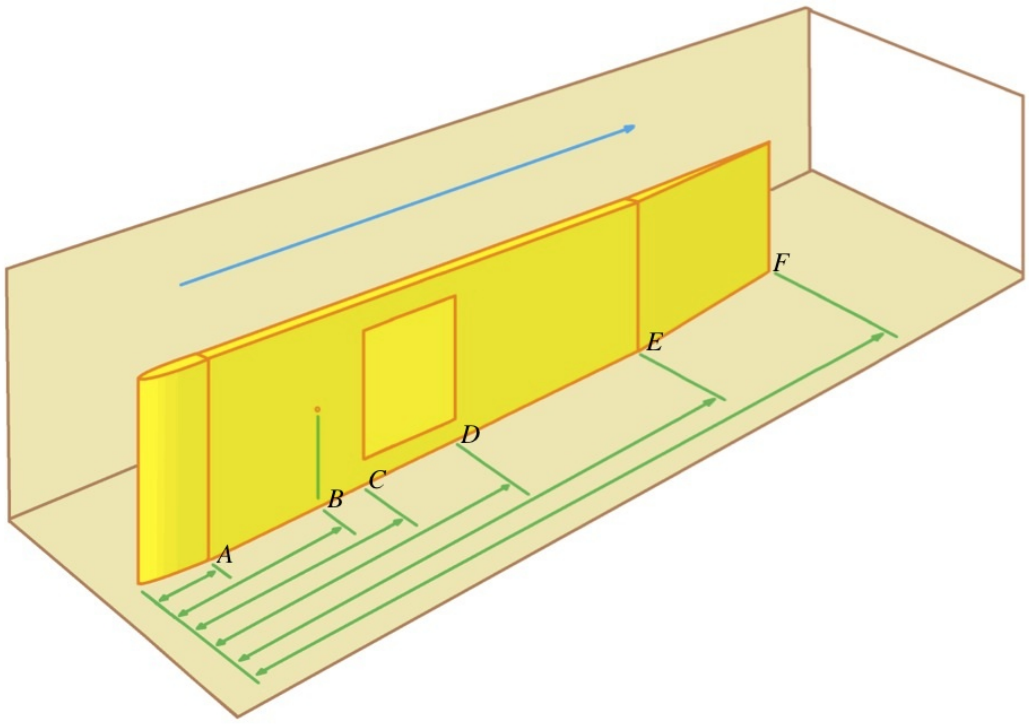

Figure 4.2: Diagram of the wind tunnel used for the Blasius boundary layer experiments.

The leading edge ends at 63.5mm (point A). A point exciter is located at 375mm (point B) from the leading edge. An insert panel is located between 500mm (point C) and 800mm (point D) from the leading edge, and the flap begins 1650mm (point E) from the leading edge. Measurements were taken at downstream locations every 50mm, starting at 550mm from the leading edge and ending at 1200mm in the unforced case, and every 20mm between 480mm and 1200mm from the leading edge in the forced case. It is known that the Blasius boundary layer thickness grows as the square root of the downstream distance, and it is therefore inappropriate to compare flows at different downstream locations when deep inside the boundary layer where the flow velocity is growing rapidly. We therefore focus our attention on the outer regions of the boundary layer. Below, in figures 4.3 and 4.4, we plot the experimental mean flow data.

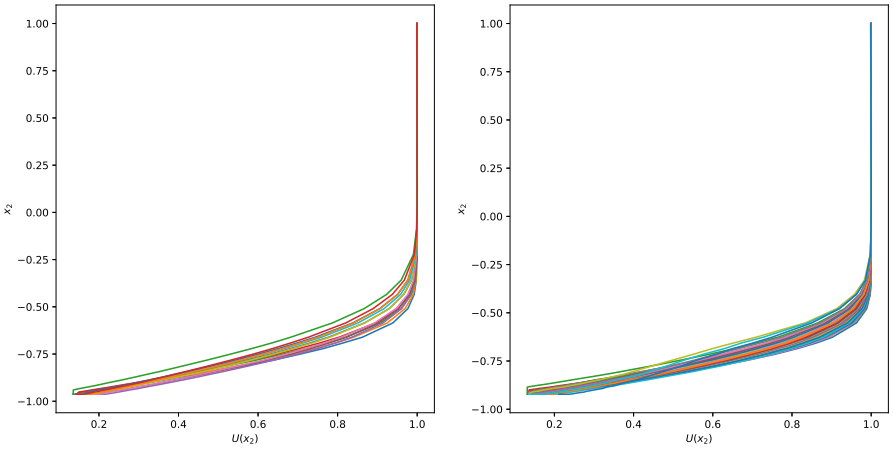

Figure 4.3: Experimental mean flow data for an unforced (left) and forced (right) Blasius boundary layer at different downstream locations (wall at $x_2 = -1$).

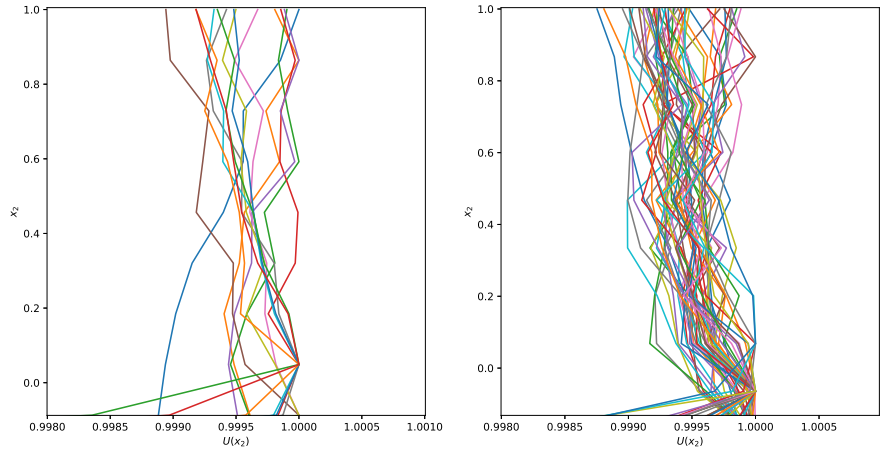

Figure 4.4: Experimental mean flow data in the outer region of the boundary layer, for an unforced (left) and forced (right) Blasius boundary layer at different downstream locations (wall at $x_2 = -1$).

It is worth recalling that the data is mean flow, meaning that each measurement (at a specific down-stream/cross-stream location) is averaged over many different times. We will therefore attempt to fit a mean model, that is a model of the steady base flow. The randomness in the base flow is therefore assumed steady, and the time dependent components will be captured by the perturbations which are commonly assumed in linear stability analysis. Furthermore, the data is only $2D$ and we are therefore restricted to fitting a $2D$ stochastic model. If we assume that stochasticity

will be induced by physical means, such as the down-stream driving forces (for example, variations in the pressure gradient) then it is reasonable to assume that the greatest stochastic modifications will be orientated in this direction and vary in the cross-stream direction (in accordance with the boundary conditions), as the deterministic base flow does. One may argue that such modified flows do not satisfy the Navier-Stokes equations. However, there is no steady, incompressible, inviscid, unidirectional base flow that does not satisfying the Euler equations. An arbitrary profile is therefore in convective equilibrium, slowly diffusing at a rate which is inversely proportional to the Reynolds number. If the growth rate of the instability is faster than such diffusion, then the velocity profile can effectively be frozen for stability analysis.

As can be seen, the experimental observations support these ideas. However, the profiles are very different close to the wall, say $x_2 < 0$, and this is a consequence of the flow growing in the downstream direction. We therefore focus on the region $x_2 > 0$ and use the experimental data to construct the correlation kernels,

$$\frac{K_u(x_2, x_2')}{\sigma^2} = \frac{\mathrm{E}[(U(x_2) - \mathrm{E}[U(x_2)])(U(x_2') - \mathrm{E}[U(x_2')])]}{\sigma^2}, \tag{4.5}$$

where σ^2 is the variance of the process, which are plotted below in figure 4.5.

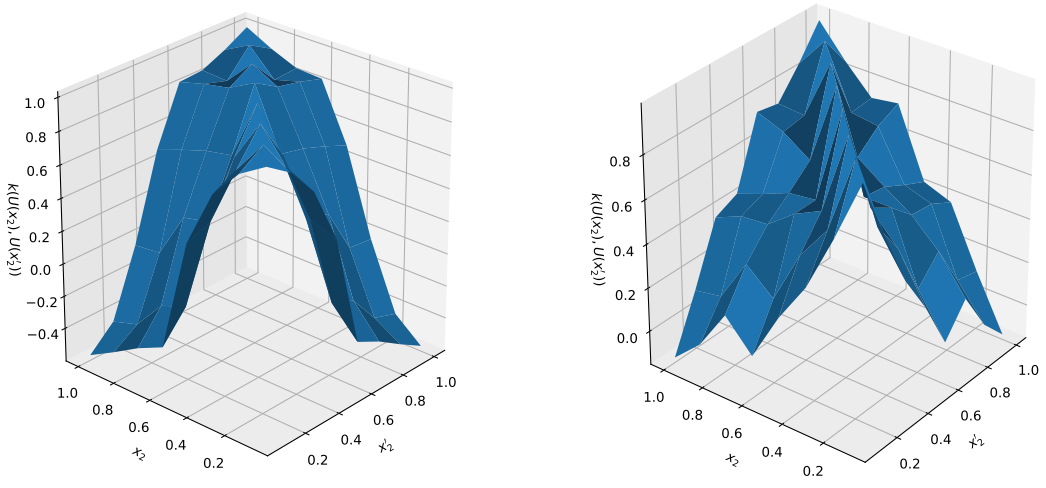

Figure 4.5: Correlation kernel, $\frac{K_u(x_2,x_2')}{\sigma^2} = \frac{\mathrm{E}[(U(x_2)-\mathrm{E}[U(x_2)])(U(x_2')-\mathrm{E}[U(x_2')])]}{\sigma^2}$, based upon experimental mean flow data for an unforced (left) and forced (right) Blasius boundary layer.

It is clear that the kernels exhibit a stationary behaviour, that is $K_u(x_2, x_2') = K_u(x_2 - x_2')$. Furthermore, the unforced kernel bears resemblance to a squared exponential kernel ($K_u(x_2, x_2') = \exp(-c(x_2 - x_2')^2)$), exhibiting a Gaussian shape, whilst the forced case exhibits the behaviour of an exponential kernel ($K_u(x_2, x_2') = \exp(-c|x_2 - x_2'|)$).

We shall therefore model the base flow defect as a stationary ($K_u(x_2, x_2') = K_u(x_2 - x_2')$), second-order ($\mathrm{E}[\hat{u_2}^*(x_2, \boldsymbol{\zeta}(\omega))^2] < \infty$) Gaussian process. We assume a zero mean and constant variance process, and therefore do not favour a priori any specific region of the channel. This kernel is parameterized by two variables, a standard deviation, σ, and a correlation length, c_l, controlling the size and noise of the process respectively. Lower values of c_l indicate a more noisy process, and hence a more wobbly base flow which should naturally lead to a greater number of inflection points, which may in turn increase the likelihood of instability. The kernel is defined

$$K_u(x_2, x_2') = \sigma^2 \exp\left(-\left(\frac{x_2 - x_2'}{2c_l}\right)^2\right) \forall\, x_2, x_2' \in [-1, 1]. \tag{4.6}$$

In order to identify a suitable size for the correlation length parameter, we take the experimental kernel and use an optimisation procedure, based upon the Broyden Fletcher Goldfarb Shanno (BFGS) algorithm [23], to fit a Gaussian kernel such that the Frobenius norm of the kernel differences is minimised. We plot the experimental correlation kernel and the fitted Gaussian model below in figure 4.6.

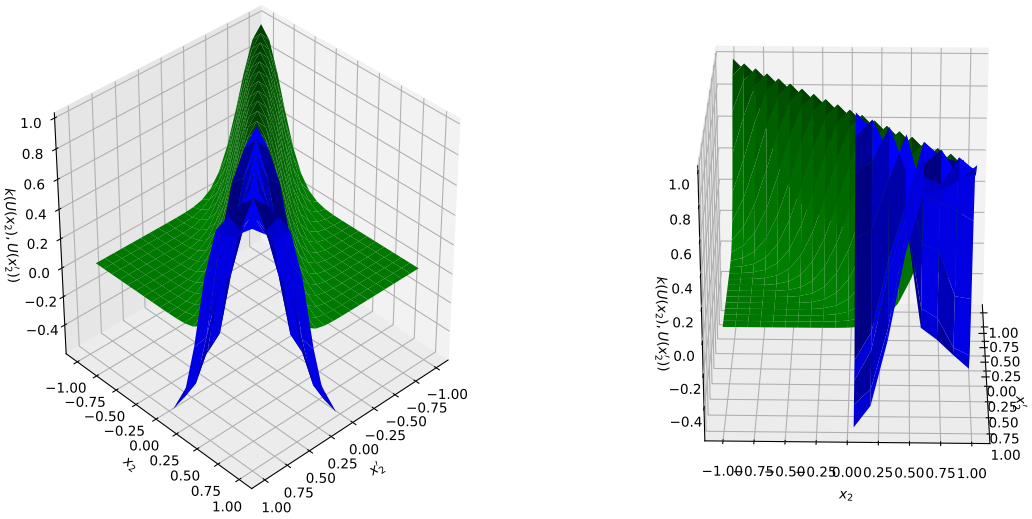

Figure 4.6: Correlation kernel based upon experimental mean flow data for an unforced Blasius boundary layer (blue) and fitted Gaussian kernel with $c_l = 0.18$ (green), at different viewing angles.

The optimisation procedure reveals a correlation length $c_l = 0.18$, and there appears to be a reasonable agreement between the Gaussian model and the experimental data. To better visualise the fit, below in figure 4.7 we plot slices of the experimental kernel as a function of $x_2 - x_2'$ at different x_2. In addition, we plot the fitted kernel at correlation length 0.18, as well as kernels with correlation lengths of 0.10 and 0.50.

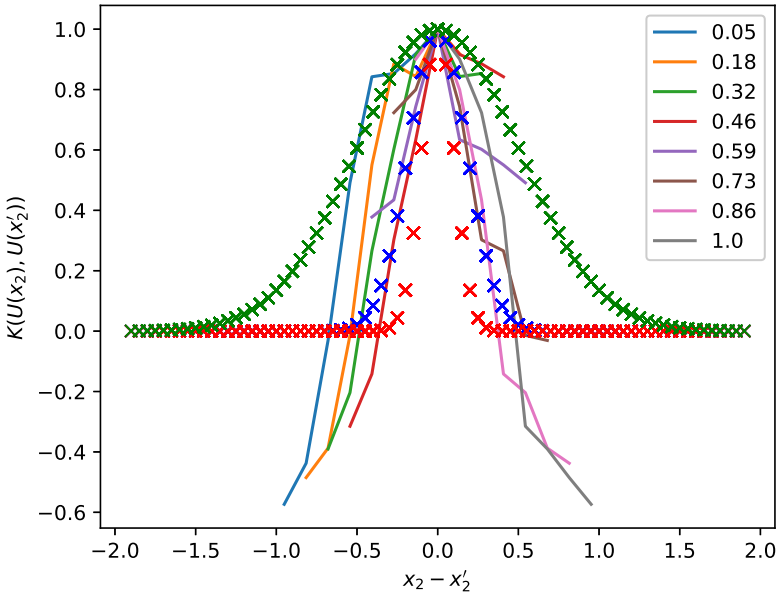

Figure 4.7: Slices of the Correlation kernel based upon experimental mean flow data (solid lines) for an unforced Blasius boundary layer, sliced at different x_2 in accordance with the plot legend, and fitted Gaussian kernels with $c_l = 0.10$ (red crossed), $c_l = 0.18$ (blue crosses) and $c_l = 0.50$ (green crosses).

It appears that the correlation length of 0.18 was fitted as a compromise between minimising the error corresponding to those points sitting above and those sitting below the horizontal zero line. The points falling below the horizontal axis correspond to those points where either x_2 or x_2' are approaching zero, and as noted the correlations at these points may be impacted by the boundary layer growing in the downstream direction. If we were to neglect these points falling below the horizontal axis, then it is clear that a larger correlation length, taking a value between 0.2 and 0.5, would be more appropriate choice.

Further, we compute the standard deviation of the base flows and find a value of the order 0.01 percent. Noting that the data is taken from a carefully controlled experiment, we expect this to be a lower bound on the typical size of noise present in more natural instances. We therefore adopt a Gaussian auto-covariance with correlation length of the order 0.1 and consider a range of standard deviations of the order 0.01 to 1 percent.

As discussed, the KLE expands a stochastic process with the eigenfunctions of its correlation kernel. There are actually infinitely many second-order processes with the same correlation kernel and thus the same set of expanding eigenfunctions. Such

processes, sharing the same auto-covariance, are distinguished by the joint probability of the random variables. By construction, these random variables are zero mean, unit variance and mutually orthogonal. In many instances, the random process is (assumed to be) Gaussian, leading to significant simplifications. The KLE of a Gaussian process involves random variables which are not only uncorrelated but independent, which allows the joint density of the random variables to be factored into a product of individual densities (which is extremely useful in sampling and numerical integration). We therefore select zero mean, unit variance Gaussian random variables, $\zeta_i(\omega) \sim \mathcal{N}(0,1)$. The stochastic base flow then follows by adding a truncated KLE, based upon the eigenvectors of the chosen correlation kernel, to the deterministic profiles aforementioned,

$$U^*(x_2,\omega) = U(x_2) + \sigma(x_2)\sum_{i=1}^{d}\sqrt{\gamma_i}e_i(x_2)\zeta_i(\omega), \tag{4.7}$$

where $U(x_2)$ is the deterministic profile, and

$$\sigma(x_2) = 2\sigma||U(x_2)||_2\frac{1}{\int_{-1}^{1}U(x_2)dx_2}U(x_2) = \bar{\sigma}U(x_2) \tag{4.8}$$

is chosen such that each stochastic mode $\sigma(x_2)e_i(x_2)$ is a continuous function satisfying the boundary conditions whose average standard deviation across the channel is σ.

4.2 Governing Equations: The Stochastic Expansion of the Orr-Sommerfeld and Squire Equations

Following the notation introduced previously, the stochastic base flow can be constructed with a truncated KLE,

$$U^*(x_2,\omega) = U(x_2) + \sigma(x_2)\sum_{i=1}^{d}\sqrt{\gamma_i}e_i(x_2)\zeta_i(\omega), \tag{4.9}$$

where $U(x_2)$ is the deterministic profile, and

$$\sigma(x_2) = 2\sigma||U(x_2)||_2\frac{1}{\int_{-1}^{1}U(x_2)dx_2}U(x_2) = \bar{\sigma}U(x_2), \tag{4.10}$$

is chosen such that each stochastic mode $\sigma(x_2)e_i(x_2)$ is a continuous function satisfying the boundary conditions whose average standard deviation across the channel is σ.

This expression is substituted into operator $\mathbf{R}$, leading to the modified operator $\boldsymbol{R}^*$. Stochastic solutions can then be accommodated by taking a WCE of the eigenvalues and eigenvectors,

$$\lambda^*(\boldsymbol{\zeta}(\omega)) = \sum_{i=0}^{N} \lambda^*_{\alpha^i} H_{\alpha^i}(\boldsymbol{\zeta}(\omega)), \tag{4.11}$$

$$\boldsymbol{q}^*(x_2, \boldsymbol{\zeta}(\omega)) = \sum_{i=0}^{N} \boldsymbol{q}_{\alpha^i}(x_2) H_{\alpha^i}(\boldsymbol{\zeta}(\omega)). \tag{4.12}$$

More specifically, each Chebyshev coefficient in the expansion of the physical domain becomes stochastic and must be expanded with Wick products in d-dimensions,

$$\hat{u_2}^*(x_2, \boldsymbol{\zeta}(\omega)) = \sum_{n=0}^{N_c} a_n(\boldsymbol{\zeta}(\omega)) T_n(x_2) = \sum_{n=0}^{N_c} \sum_{i=0}^{N} a_n^{\alpha^i} H_{\alpha^i}(\boldsymbol{\zeta}(\omega)) T_n(x_2). \tag{4.13}$$

Similarly,

$$\hat{\eta}^*(x_2, \boldsymbol{\zeta}(\omega)) = \sum_{n=0}^{N_c} b_n(\boldsymbol{\zeta}(\omega)) T_n(x_2) = \sum_{n=0}^{N_c} \sum_{i=0}^{N} b_n^{\alpha^i} H_{\alpha^i}(\boldsymbol{\zeta}(\omega)) T_n(x_2). \tag{4.14}$$

The OS formulation reads

$$\begin{aligned}
&\left\{ i\lambda k^2 - i\alpha k^2 U(x_2)(1 + \bar{\sigma} \sum_{n_1=1}^{d} \sqrt{\gamma_{n_1}} \zeta_{n_1}(\omega) e_{n_1}(x_2)) - \right. \\
&\left. i\alpha (U''(x_2) + \bar{\sigma} \sum_{n_1=1}^{d} \sqrt{\gamma_{n_1}} \zeta_{n_1}(\omega)(U''(x_2) e_{n_1}(x_2) + 2U'(x_2) e'_{n_1}(x_2) + U(x_2) e''_{n_1}(x_2))) - \frac{k^4}{Re} \right\} \\
&\sum_{n_2=0}^{N_c} \sum_{n_3=0}^{N} a_{n_2}^{\alpha^{n_3}} H_{\alpha^{n_3}}(\boldsymbol{\zeta}(\omega)) T_{n_2}(x_2) \\
&+ \left\{ -i\lambda + i\alpha U(x_2)(1 + \bar{\sigma} \sum_{n_1=1}^{d} \sqrt{\gamma_{n_1}} \zeta_{n_1}(\omega) e_{n_1}(x_2)) + \frac{2k^2}{Re} \right\} \sum_{n_2=0}^{N_c} \sum_{n_3=0}^{N} a_{n_2}^{\alpha^{n_3}} H_{\alpha^{n_3}}(\boldsymbol{\zeta}(\omega)) T''_{n_2}(x_2) \\
&- \frac{1}{Re} \sum_{n_2=0}^{N_c} \sum_{n_3=0}^{N} a_{n_2}^{\alpha^{n_3}} H_{\alpha^{n_3}}(\boldsymbol{\zeta}(\omega)) T''''_{n_2}(x_2) = 0,
\end{aligned}$$

and a similar formulation follows for the SQ equation,

$$\left\{-i\lambda + i\alpha U(x_2)(1+\bar{\sigma}\sum_{n_1=1}^{d}\sqrt{\gamma_{n_1}}\zeta_{n_1}(\omega)e_{n_1}(x_2)) + \frac{k^2}{Re}\right\}\sum_{n_1=0}^{N}\sum_{n_2=0}^{N_c} b_{n_2}^{\alpha_{n_1}} H_{\alpha^{n_1}}(\boldsymbol{\zeta}(\omega))T_{n_2}(x_2)$$
$$-\frac{1}{Re}\sum_{n_1=0}^{N}\sum_{n_2=0}^{N_c} b_{n_2}^{\alpha_{n_1}} H_{\alpha^{n_1}}(\boldsymbol{\zeta}(\omega))T''_{n_2}(x_2)$$
$$+i\beta\left\{U'(x_2)+\bar{\sigma}\sum_{n_1=1}^{d}\sqrt{\gamma_{n_1}}\zeta_{n_1}(\omega)(U'(x_2)e_{n_1}(x_2)+U(x_2)e'_{n_1}(x_2))\right\}$$
$$\sum_{n_1=0}^{N}\sum_{n_2=0}^{N_c} b_{n_2}^{\alpha_{n_1}} H_{\alpha^{n_1}}(\boldsymbol{\zeta}(\omega))T_{n_2}(x_2) = 0.$$

When vectorised the equations lead to a stochastic eigenvalue problem,

$$(\boldsymbol{L_1}^* - i\lambda^* \boldsymbol{I})\,\boldsymbol{q}^* = 0, \tag{4.15}$$

where the matrix $\boldsymbol{L_1}^*$ is the stochastic equivalent to $\boldsymbol{L_1}$, and follows by replacing the deterministic base flow with the Karhunen-Loève representation of the stochastic counterpart.

4.3 Numerical Method

We model the base flow defect as a stationary ($K_u(x_2, x_2') = K_u(x_2 - x_2')$), second-order ($\mathrm{E}[\hat{u_2}^*(x_2, \boldsymbol{\zeta}(\omega))^2] < \infty$) Gaussian process. We assume a zero mean and constant variance process, and therefore do not favour a priori any specific region of the channel. Analysis is conducted with a squared exponential covariance kernel, which does not admit an analytic decomposition. We also employ an exponential kernel, for which an analytic decomposition does exist, to verify the procedure. The squared exponential kernel must be decomposed numerically, but, being infinitely differentiable, symmetric, stationary and isotropic, has many desirable characteristics enabling fast convergence of its numerical representation [63]. This kernel is parameterized by two variables, a standard deviation, σ, determining the average distance of the function from its mean, and a correlation length, c_l, which determines the rate at which the correlation decays between points of the process. Lower values of c_l indicate a more noisy process, and hence a more wobbly base flow which should naturally lead to a greater number of inflection points, which may in turn

increase the likelihood of instability. The kernel is defined

$$K_u(x_2, x_2') = \mathrm{E}[(U(x_2) - \mathrm{E}[U(x_2)])(U(x_2') - \mathrm{E}[U(x_2')])] = \sigma^2 \exp\left(-\left(\frac{x_2 - x_2'}{2c_l}\right)^2\right) \forall x_2, x_2' \in [-1, 1]. \tag{4.16}$$

The kernel's eigenvalues, γ_j, and eigenfunctions, $e_j(x_2)$, solve the Fredholm integral equation of the second kind,

$$\int_{-1}^{1} K_u(x_2, x_2') e_j(x_2') dx_2' = \sigma^2 \gamma_j e_j(x_2). \tag{4.17}$$

This is solved numerically via a projection method [2]. The integral equation is reformulated as $P_Z(\sigma^2\gamma - K_u)e_Z = 0$, where P_Z is a projection operator, projecting onto the Lagrange basis, and Z denotes a Z point discretization. We require a d term KLE, and therefore select $Z > 2d+2$ collocation points, based on the Lagrange abscissa, to ensure accuracy of the first d eigen-solutions.

More formally, letting $\{h_n(x_2); n = 1, ..., Z\}$ form a complete basis in the Hilbert space $L^2([-1, 1])$, we approximate each eigenfunction as a truncated expansion in this basis,

$$e_i(x_2) = \sum_{k=1}^{Z} d_k^i h_k(x_2), i = 1, ..., Z, \tag{4.18}$$

where d_k^i are constant coefficients for the ith eigenfunction. Introducing the expansion gives a residual error,

$$\varepsilon_d = \sum_{k=1}^{Z} d_k^i \left(\int_{-1}^{1} K_u(x_2, x_2') h_k(x_2') dx_2' - \sigma^2 \gamma_i h_k(x_2)\right). \tag{4.19}$$

We then seek the coefficients d_k^i such that the residual is orthogonal to the space spanned by the approximating basis, $< \varepsilon_d, h_j(x_2) >= 0, \forall j = 1, ..., Z$. Enforcement of the constraint yields a system of equations,

$$\sum_{k=1}^{d} d_k^i \left(\int_{-1}^{1}\int_{-1}^{1} K_u(x_2, x_2') h_k(x_2') h_j(x_2)) dx_2 dx_2' - \sigma^2 \gamma_i \int_{-1}^{1} h_k(x_2) h_j(x_2) dx_2\right) = 0, \tag{4.20}$$

which, omitting the index of the eigenfunction, can be written in matrix form as a

generalised eigenvalue problem,

$$[\mathbf{K} - \gamma\mathbf{M}]\mathbf{d} = 0, \tag{4.21}$$

where $K_{ij} = \int_{-1}^{1}\int_{-1}^{1} K_u(x_2, x_2')h_i(x_2)h_j(x_2')dx_2dx_2'$, and $M_{ij} = \sigma^2\int_{-1}^{1} h_i(x_2)h_j(x_2)dx_2$. This is solved numerically for Z eigen-pairs, and the first d used to construct the base flow with a truncated KLE,

$$U^*(x_2, \boldsymbol{\zeta}(\omega)) = U(x_2) + \sigma\sum_{i=1}^{d}\sqrt{\gamma_i}e_i(x_2)\zeta_i(\omega). \tag{4.22}$$

KLEs of increasing dimensions (number of retained terms) are considered, and their convergence assessed for different correlation lengths, $c_l \in \{0.01, 0.05, 0.10, 0.25, 0.50, 1.00\}$. The L^1-norm percentage error for kernel reconstruction,

$$E_K^1(d) = \frac{\int_{-1}^{1}\int_{-1}^{1}|\ K_u(x_2, x_2') - \sigma^2\sum_{i=1}^{d}\gamma_i e_i(x_2)e_i(x_2')|\ dx_2dx_2'}{\int_{-1}^{1}\int_{-1}^{1}|\ K_u(x_2, x_2')|dx_2, dx_2'} \tag{4.23}$$

is used to study convergence, and $ln(E_K^1(d))$ is plotted (for the Gaussian kernel) for various correlation lengths in figure 4.8 below.

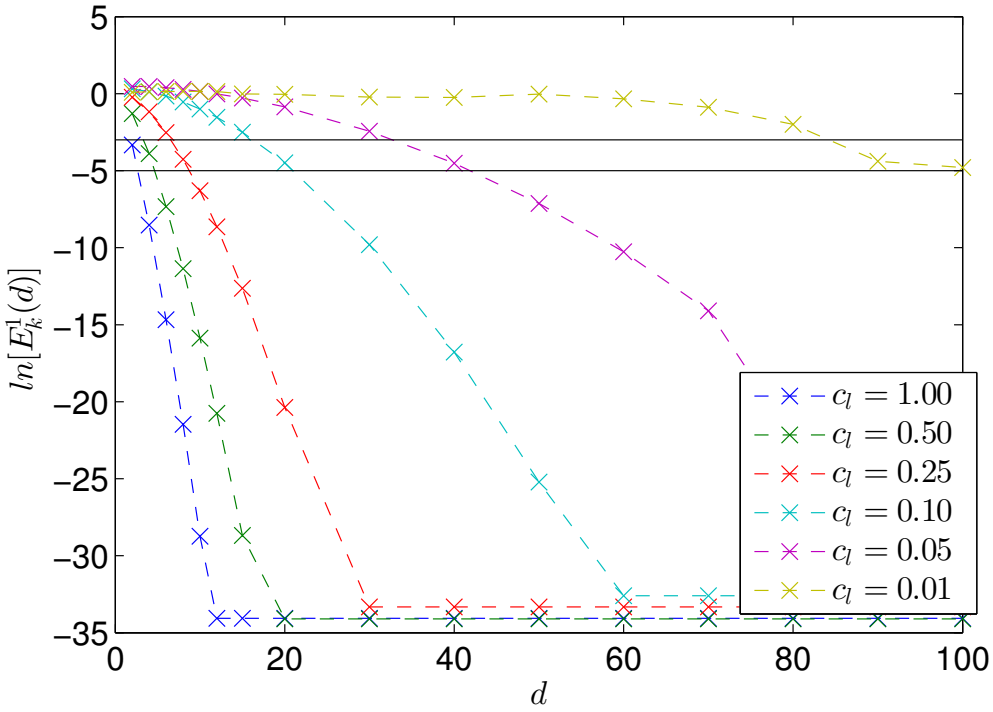

Figure 4.8: Logarithmic values of the $1-norm$ percentage error in Mercer's reconstruction of the Gaussian auto-covariance, reconstructed with a d term KLE at various correlation lengths, c_l. Horizontal black lines at -3 and -5 are indicative of percentage errors of five and one respectively.

The horizontal black lines at -3 and -5 are indicative of percentage errors of five and one respectively. The convergence analysis shows that the squared exponential kernel can be reconstructed to a high degree of accuracy with only a few terms. Errors are far greater in the case of the exponential kernel, and this can be attributed to the fact that it is non differentiable at the origin. We therefore only use the exponential kernel as a means of verifying the numerical algorithm, and restrict stability analysis to the squared exponential case, for which errors, $E_K^1(d)$, less than 5% are achieved with with 2, 4, 8, 15, 40 and 80 retained terms at correlation lengths of 1.00, 0.50, 0.25, 0.10, 0.05 and 0.01 respectively. Similarly, errors of less than 1% are achieved with 4, 6, 10, 30, 50 and 100 retained terms at correlation lengths of 1.00, 0.50, 0.25, 0.10, 0.05 and 0.01 respectively. Considering the trade off between computational efficiency and accuracy, we will reference the above figure when later selecting appropriate stochastic dimensions.

As an example we plot the modal decay and the eigen-modes, for the case $c_l = 1.0$ (figure 4.9), 0.5 (figure 4.10), 0.1 (figure 4.11), and $\sigma = 1.0$.

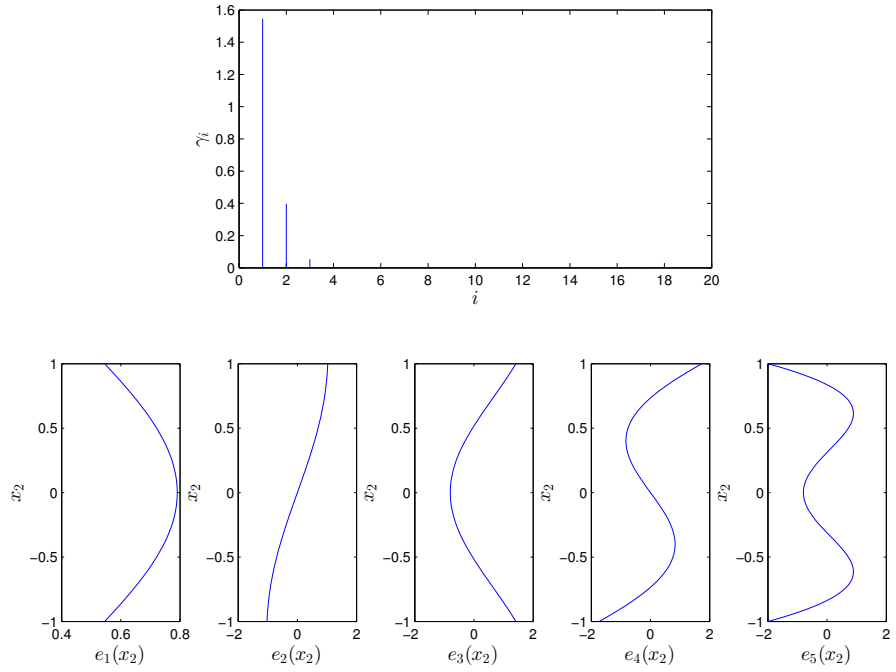

Figure 4.9: Decomposition of Gaussian auto-covariance: decay of eigenvalues (top) and eigenvectors (bottom). $c_l = 1.00$ and $\sigma = 1.00$.

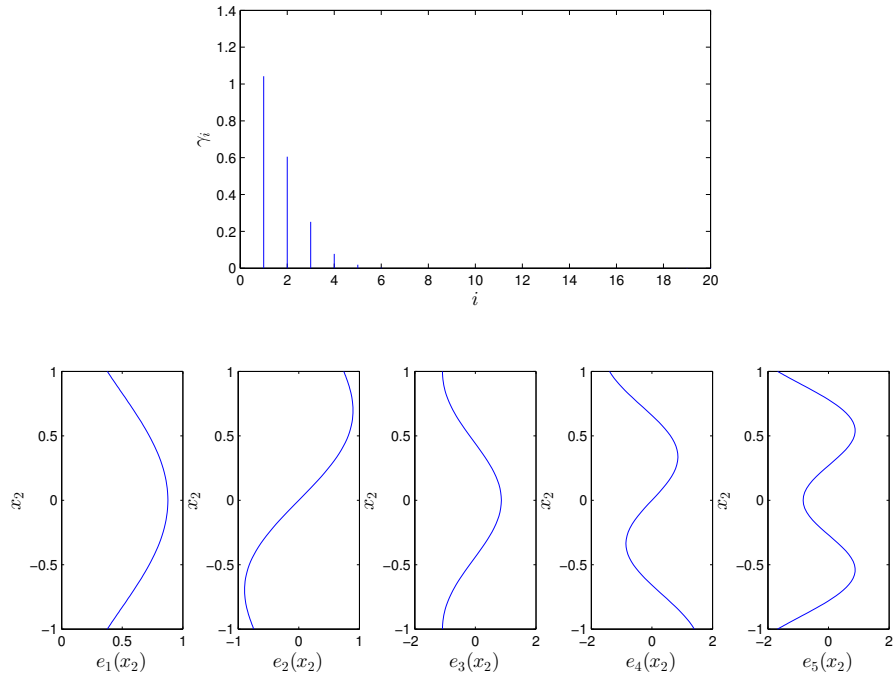

Figure 4.10: Decomposition of Gaussian auto-covariance: decay of eigenvalues (top) and eigenvectors (bottom). $c_l = 0.50$ and $\sigma = 1.00$.

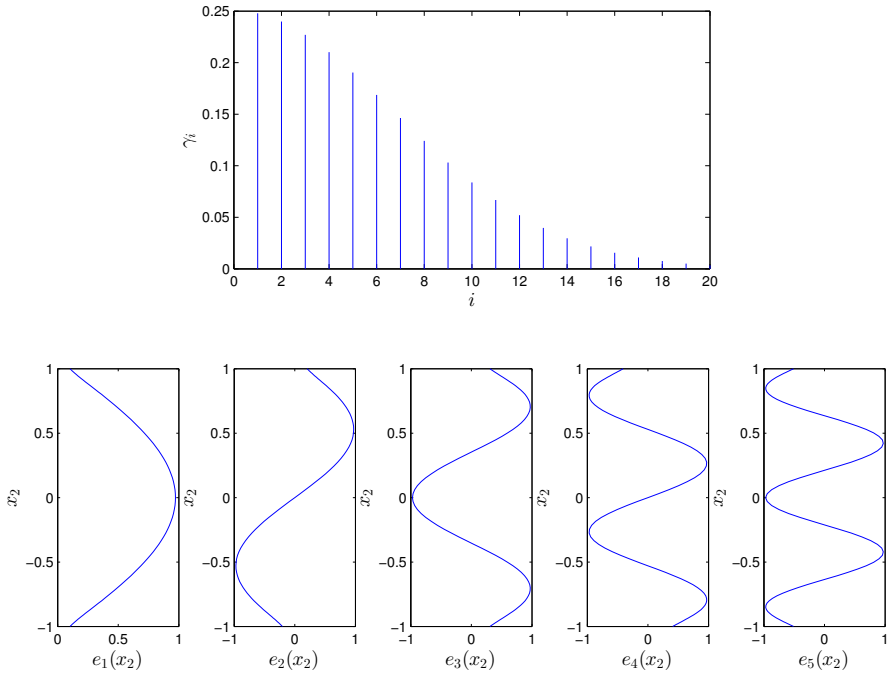

Figure 4.11: Decomposition of Gaussian auto-covariance: decay of eigenvalues (top) and eigenvectors (bottom). $c_l = 0.10$ and $\sigma = 1.00$.

Referring to the upper sub-plots, it is seen that modal amplitudes decay fast for large correlation lengths, and few terms are thus required to accurately approximate the process. For example, the first four modes would be more than sufficient to capture the variance of the unit correlation length process. The lower sub-plots depict the stochastic modes. The first mode is a level shift, where stochastic variable one effectively increases all velocities across the channel. The second mode could be described as a skew effect, where an increase in stochastic variable two increases flow velocities towards the upper boundary whilst simultaneously having the opposing effect on velocities near the lower boundary. The third mode is a convexity effect, increasing flow velocities towards channel boundaries whilst decreasing those in the central region.

A vertical inspection of the sub-plots shows that higher order modes become more important as the correlation length decreases. Furthermore, eigenvectors become more curved and, in general, modal shapes become increasingly complicated.

We also plot (figure 4.12) the Mercer's [50] reconstruction of the Gaussian kernel, based upon an appropriate d term expansion, for varying correlation lengths. That is, $K_u(x_2, x_2') \approx \sigma^2 \sum_{i=1}^{d} \gamma_i e_i(x_2) e_i(x_2')$.

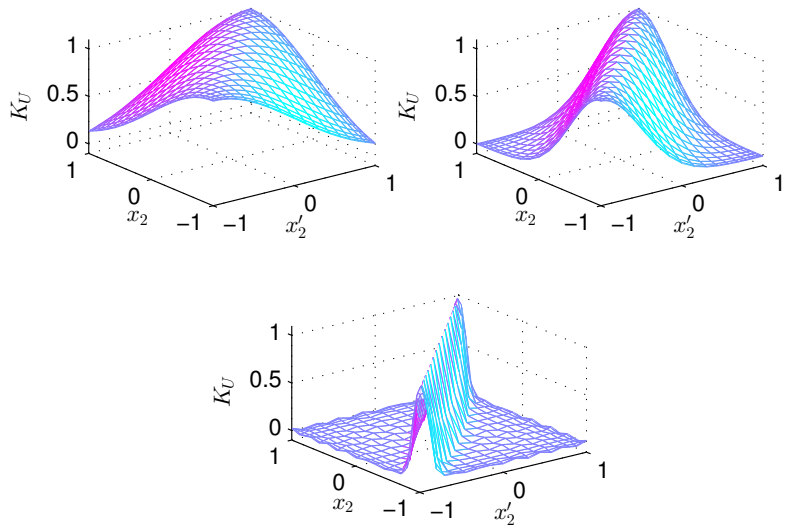

Figure 4.12: Mercer's reconstruction of Gaussian auto-covariance with a d term KLE, $c_l = 1.00$ and $d = 4$ (top left), $c_l = 0.50$ and $d = 6$ (top right), $c_l = 0.10$ and $d = 15$ (bottom).

In addition, to visualise convergence, we reconstruct the auto-covariance at the reasonably low correlation length of 0.1, for increasing retained terms, d, and plot in figure 4.13:

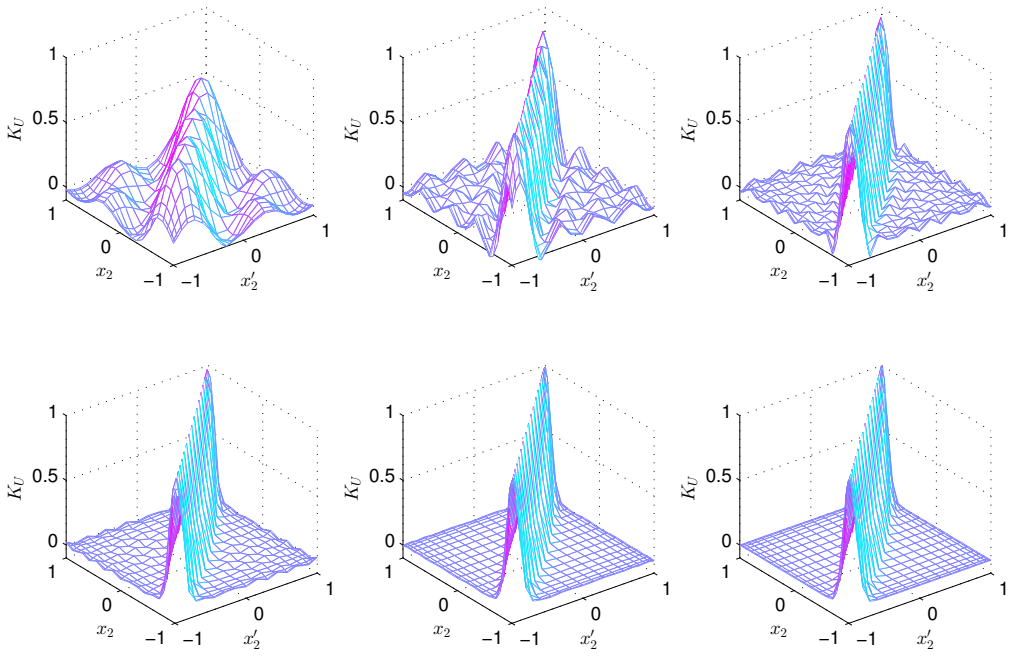

Figure 4.13: Mercer's reconstruction of Gaussian auto-covariance, $c_l = 0.1$ and $d = 4$ (top left), $c_l = 0.10$ and $d = 8$ (top centre), $c_l = 0.10$ and $d = 12$ (top right), $c_l = 0.10$ and $d = 15$ (bottom left), $c_l = 0.10$ and $d = 20$ (bottom centre), $c_l = 0.10$ and actual auto-covariance (bottom right). $\sigma = 1.0$.

As can be seen, Mercer's approximation of the auto-covariance converges to the actual Gaussian kernel as we increase the number of retained terms, d.

To illustrate the resulting base flows, $U^*(x_2, \omega) = U(x_2) + \sigma(x_2) \sum_{i=1}^{d} \sqrt{\gamma_i} e_i(x_2) \zeta_i(\omega)$, we plot (in figure 4.14) ten random realisations of a Poiseuille, where $\zeta_i(\omega) \sim N(0, 1)$, for a range of input standard deviations and correlation lengths below.

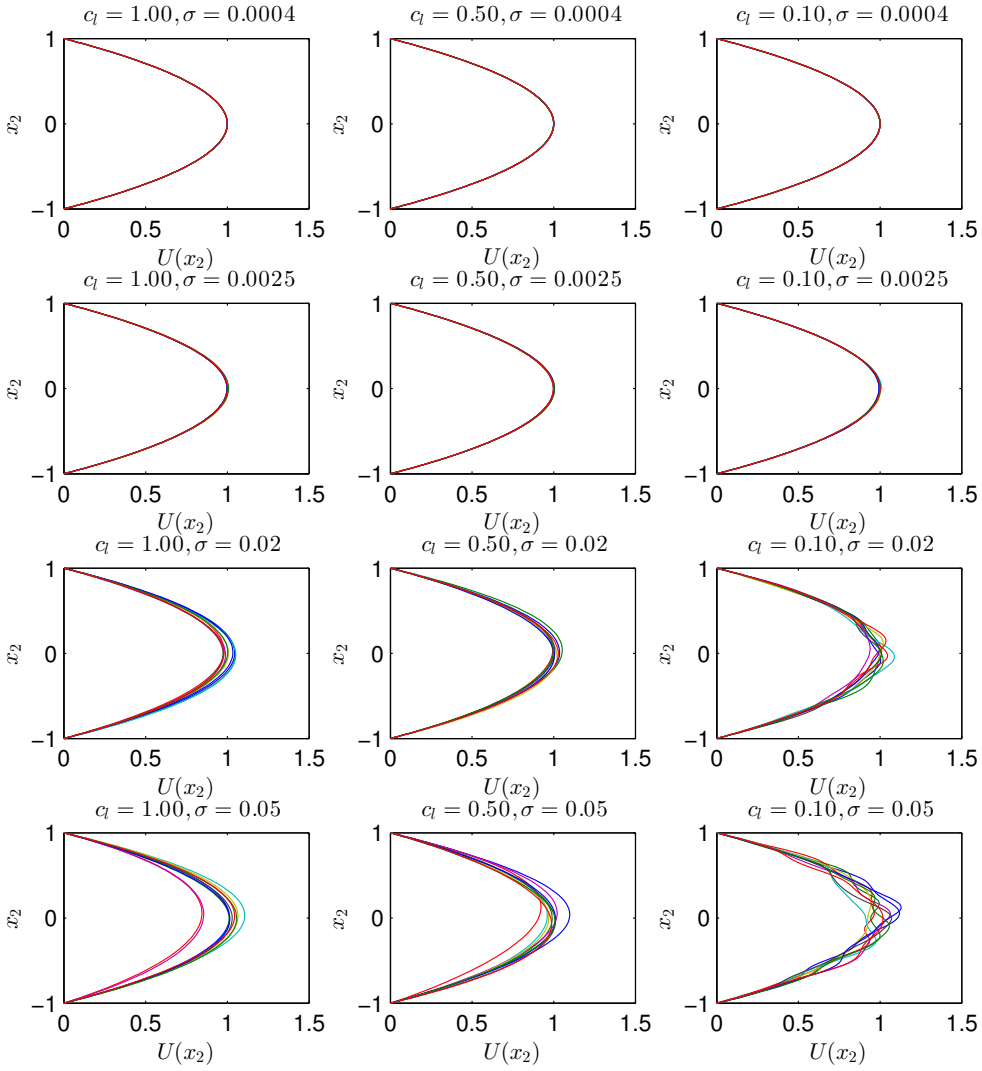

Figure 4.14: Random realisations of a plane Poiseuille flow with input standard deviation varying row-wise, $\sigma = 0.0004, 0.0025, 0.02, 0.05$ top to bottom, and input correlation length varying column-wise, $c_l = 1.00, 0.50, 0.10$ from left to right.

Row-wise the input standard deviations take values of 0.04, 0.25, 2 and 5 percent, and the correlation length varies column-wise, as 1.00, 0.50 and 0.10. As can be seen, all realisations satisfy the boundary conditions and the stochasticity is greatest at the channel centre-line, where the flow field has the greatest magnitude. If one considers the discretised flow, then we have in effect added stochasticity of σ percent of the deterministic base flow at each individual point. Hence, there is no stochasticity at the walls and the boundary conditions are satisfied exactly. Evidently, the size of the base flow deviation is proportional to the input standard

deviation. Furthermore, the base flow is indeed seen to become more erratic as the correlation length of the process is decreased.

We pick four combinations of input standard deviation and correlation length as canonical examples, namely $\{\sigma, c_l\} = \{0.0004, 0.10\}, \{0.02, 0.10\}, \{0.02, 0.50\}, \{0.05, 0.50\}$. We therefore investigate the effects of both low magnitude, highly irregular stochasticity, and moderate magnitude smooth stochasticity, across the channel. Owing to the curse of dimensionality, we rely upon LHS and sparse grid WCEs to study the lower correlation lengths, whilst full tensor chaos expansions will suffice for the moderate correlation length of 0.50.

4.4 Latin Hypercube Sampling

Before proceeding with numerical experiments, we briefly review the construction of Latin Hypercube Sampling grids, which will be very useful for making comparisons with the results of the WCE.

Latin Hypercube Sampling (LHS) offers an alternative and more efficient approach to random Monte Carlo sampling. Consider a variable, y, that depends on stochastic variables, ζ_1, ζ_2, ... ζ_d. One may like to know how y varies when the ζs vary according to some assumed joint probability distribution, or other statistics such as the expected value, or the 99th percentile. Developed by McKay, Conover, and Beckman [48], LHS selects n different values from each of the d variables, ζ_1, ζ_2, ... ζ_d, in the following manner. First, the range of each variable is divided into n non overlapping intervals of equal probability, and one value from each interval is selected at random with respect to the probability density in the interval. The n values obtained for ζ_1 are paired in a random manner with the n values of ζ_2. These n pairs are then randomly combined with the n values of ζ_3 to form triplets, and the process repeats until n tuplets of length d are finally formed. This is the Latin Hypercube sample, forming an n by d matrix of inputs whose ith row contains the d input variables for the ith simulation.

To help clarify the situation, consider the example of generating a Latin Hypercube with $n = 10$ samples, in $d = 2$ variables, which we assume are each zero mean and unit variance, $\zeta_i \sim \mathcal{N}(0, 1)$. Each ζ_i is divided into ten intervals, with each interval corresponding to a 10 percent probability. The Gaussian intervals are constructed by mapping uniform intervals via the inverse cumulative distribution function for the random variable. Next, a sample is picked from each interval, sampling randomly with respect to the density within the interval. That is, a specific value of ζ_1 and ζ_2 is picked from each of the ten intervals, so we have one value for ζ_1 in each

interval, and one value for ζ_2 in each interval, giving two column vectors of length ten. The uniform samples are mapped to Gaussian samples in exactly the same way the intervals were mapped, via the inverse cumulative distribution function. As an example, figure 4.15 below depicts the mapping for ζ_1.

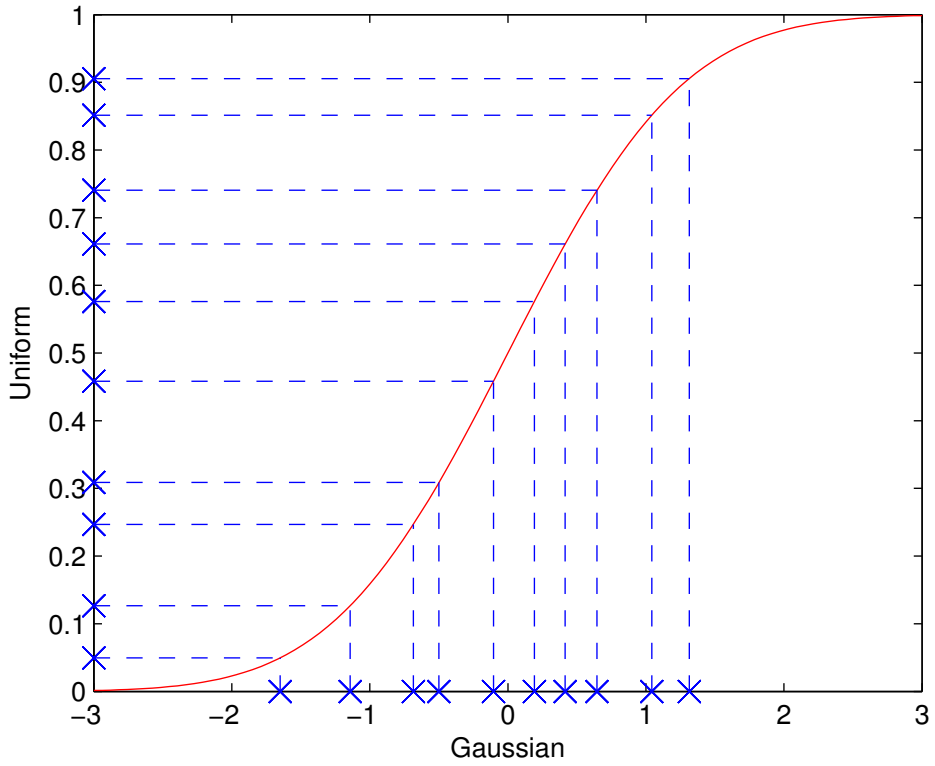

Figure 4.15: Mapping uniform samples to Gaussian samples.

These two vectors are then placed to form the columns of a matrix, and each column is randomly shuffled to give the final Latin Hypercube sample, where each row of the matrix forms a sample. The algorithm, written in Python, is given below.

```
grid = numpy.zeros((n,d))
binsize = 1/n
for i in range(n):
        grid[i,:] = (i + numpy.random.uniform(0,1,d))*binsize
for j in range(d):
        numpy.random.shuffle(result[:,j])
grid = scipy.stats.norm.ppf(grid)
```

Scipy and numpy are standard Python libraries. Finally, we plot the Latin Hyper-

cube for the pre-mapped uniform random variables and the final mapped Gaussian random variables below in figure 4.16.

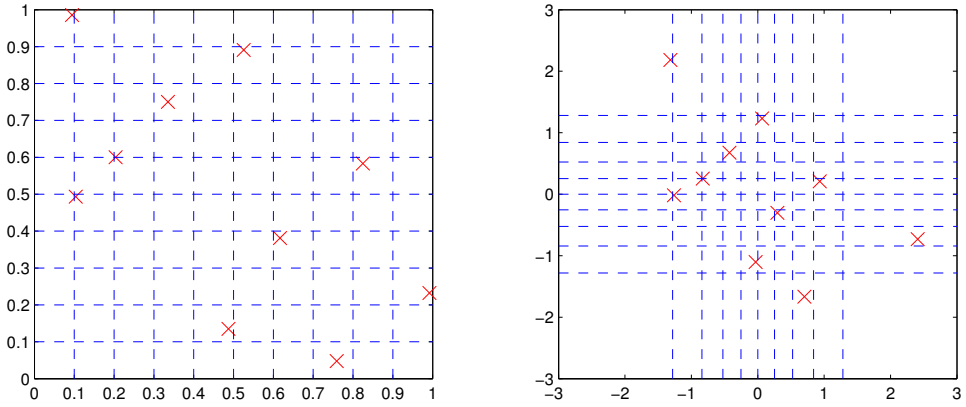

Figure 4.16: 2D Uniform Latin Hypercube samples (left) and corresponding Gaussian Latin Hypercube samples (right).

We also compute the time taken to construct the Gaussian Latin Hypercubes for different sample sizes, n, and number of stochastic variables, d. It is useful to note that there is always some variation in execution time. The machine will be performing other tasks while running the code, such as accessing the network, disk, or RAM, and these factors can cause variations in the execution time of a program. It is possible to incorrectly attribute a random variation in execution time to an improvement in the algorithm, and one must therefore observe this normal variation when timing the execution of code. We repeat the computations 100 times at each (n, d) pair, from which both the mean (figure 4.17) and standard deviation (figure 4.18) of the computation time is calculated. The code is executed with a 2.5 GHz Intel Core i5 processor and 4 GB of RAM, running Mac OS X Lion 10.7.5.

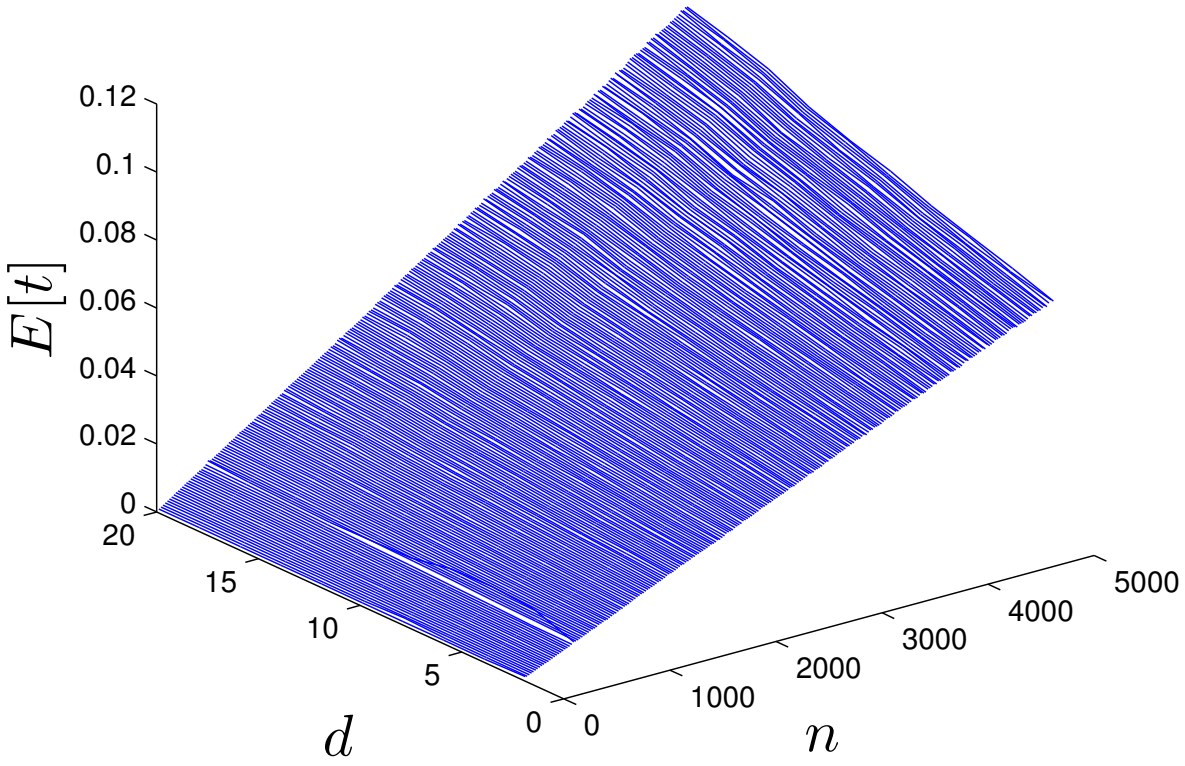

Figure 4.17: Mean of LHS grid computation times (in seconds) for varying grid size n and dimension d.

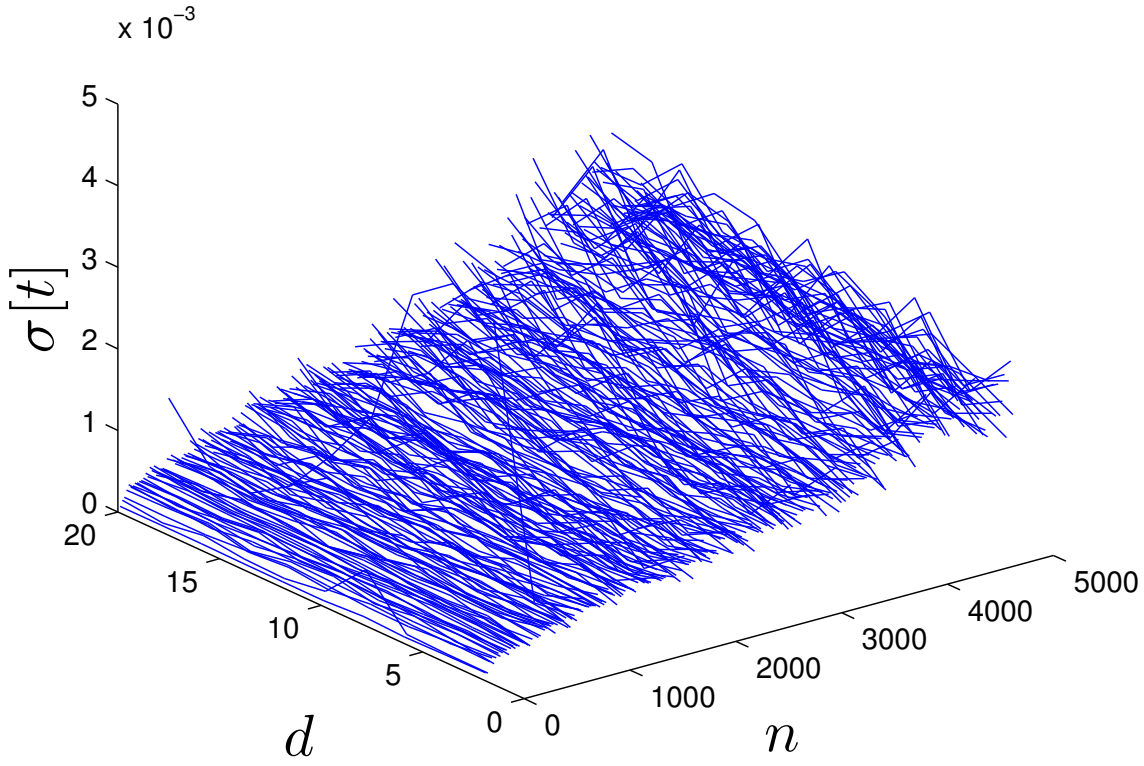

Figure 4.18: Standard deviation of LHS grid computation times (in seconds) for varying grid size n and dimension d.

As can be seen, the computational time increases linearly with both the dimension of the problem and the number of samples. Both the mean and standard deviation exhibit this linear growth, with the standard deviation sitting around two percent of the mean. The maximum computational time, for the grid $(n = 5000, d = 20)$, is less than 0.11 seconds. The computational times of the grids we will be considering will therefore be quite negligible.

4.5 Choice of Polynomial Chaos Order

As outlined in section 4.3, four and 12 term KLEs are sufficient for accurate reconstruction of the correlation kernel at correlation lengths of 0.50 and 0.10 respectively, and these are the expansions which we adopt in modelling the input process. The output process is expanded via the WCE, to four and 12 terms as dictated by the input process, and a convergence study is used to determine the appropriate polynomial order. Chaos coefficients are to be determined via numerical integration and

we therefore select n collocation points, based upon the Gauss-Hermite rules, for integration of polynomials of order $2n - 1$.

In order to identify a suitable choice of polynomial order, and hence the number of collocation points in each stochastic dimension, we choose to study the transient growth of stochastic plane Poiseuille flow at $c_l = 0.50$, $\sigma = 0.02$, $Re = 4000$, $\alpha = 1.02$ and $\beta = 0.00$, for varying polynomial orders between two and 13. We study the convergence in both mean and variance, plotting the mean in figure 4.19 and variance in figure 4.20, as computed via the WCE at varying polynomial orders.

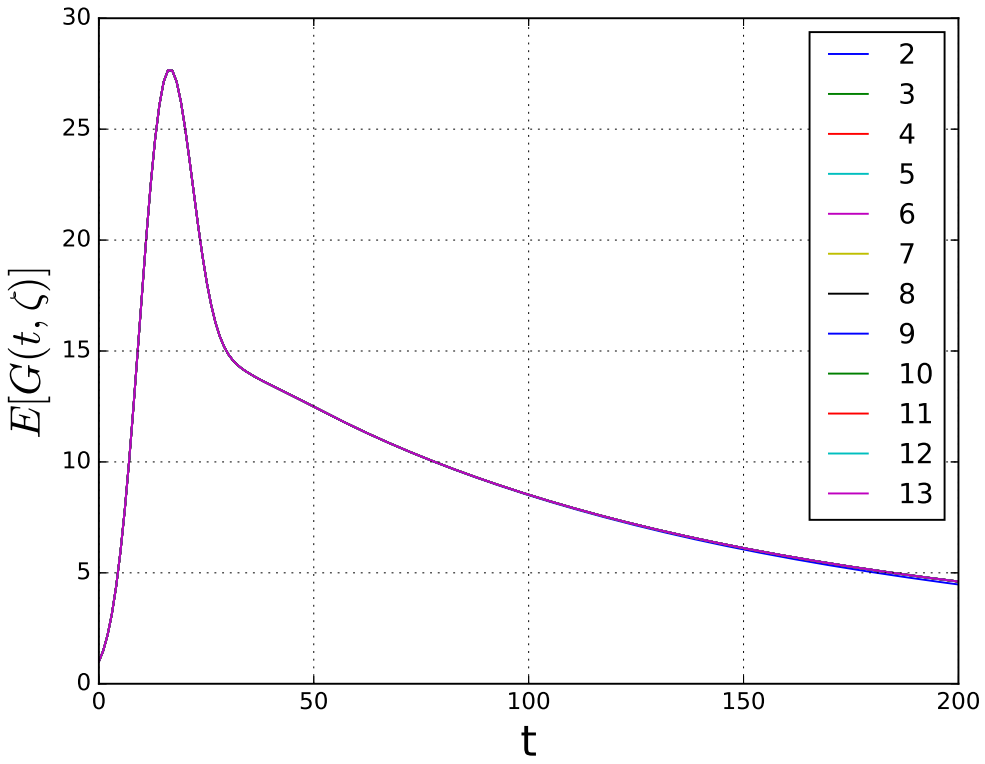

Figure 4.19: Mean transient growth, $E[G(t, \boldsymbol{\zeta})]$, for varying polynomial order. For input processes with $c_l = 0.50$ and $\sigma = 0.02$. Poiseuille flow at $Re = 4000$, $\alpha = 1.02$, $\beta = 0.00$.

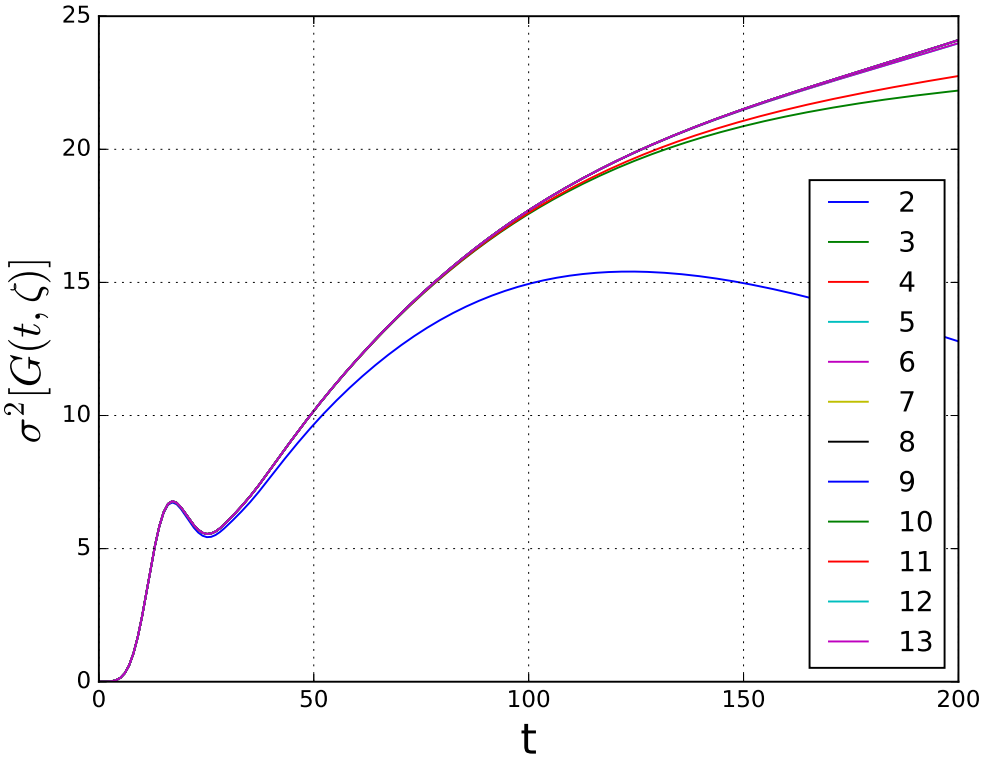

Figure 4.20: Variance of transient growth, $\sigma^2[G(t,\boldsymbol{\zeta})]$, for varying polynomial order. For input processes with $c_l = 0.50$ and $\sigma = 0.02$. Poiseuille flow at $Re = 4000$, $\alpha = 1.02$, $\beta = 0.00$.

Further, we compute the convergence in expectation and variance. The expectation is computed via the WCE for increasing polynomial order, resulting in a time series for the growth function at each polynomial order. A scalar measure is obtained by taking the mean of the time series. We plot the percentage difference as the order is increased below in figure 4.21.

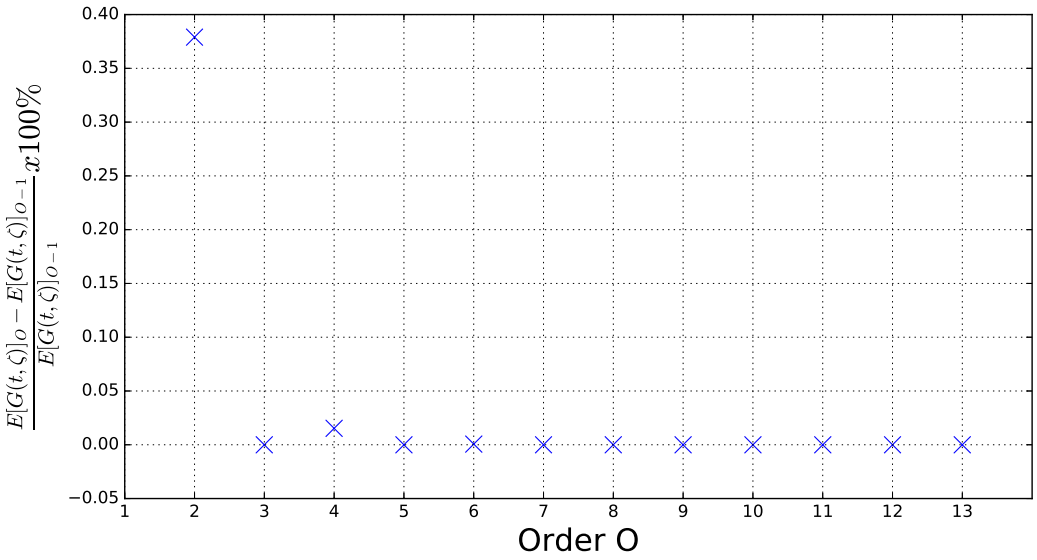

Figure 4.21: Convergence of the WCE computation of $E[G(t,\boldsymbol{\zeta})]$ for increasing polynomial order. Poiseuille flow at $Re = 4000$, $\alpha = 1.02$, $\beta = 0.00$, $c_l = 0.50$ and $\sigma = 0.02$.

A similar procedure is adopted for the variance, and depicted below in figure 4.22.

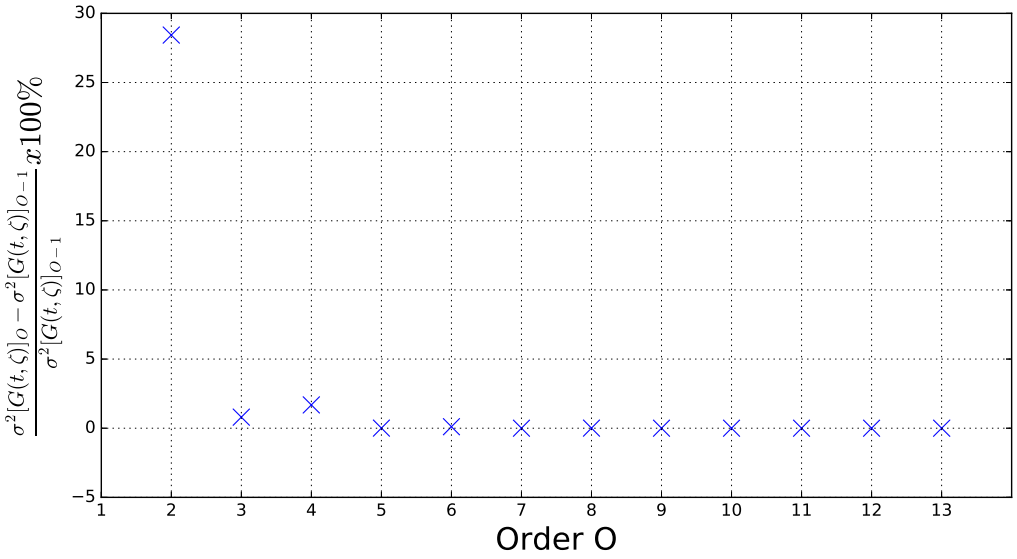

Figure 4.22: Convergence of the WCE computation of $\sigma^2[G(t,\boldsymbol{\zeta})]$ for increasing polynomial order. Poiseuille flow at $Re = 4000$, $\alpha = 1.02$, $\beta = 0.00$, $c_l = 0.50$ and $\sigma = 0.02$.

As can be seen, the expectation of the transient growth converges much faster than the variance (which depends on higher WCE coefficients). However, it is clear that convergence in both the expectation and variance is almost achieved by polynomial

order five, and most definitely by polynomial order seven. A small increase in variance is observed when going from order five to six and a monotonic decrease can be observed from this this point on. We therefore adopt a polynomial order of seven for future computations, which in turn requires four collocation points in each stochastic dimension.

4.6 Comparison of Numerical Grids

4.6.1 Moderate Correlation Length

Finally, having identified a suitable polynomial order, we compare the computational efficiency of the LHS, tensor and sparse WCE. For this study we select our canonical example of stochastic plane Poiseuille flow at $Re = 4000$, $\alpha = 1.02$, $\beta = 0.00$, $c_l = 0.50$ and $\sigma = 0.02$. We adopt six stochastic dimensions, as the performance of the sparse and tensor approach should be comparable at this point. With four collocation points in each direction, the tensor grid contains $4^6 = 4096$ points and thus requires 4096 function evaluations. The LHS based approach adopts a total of 10000 samples with the statistical moments being updated every 50 simulations. We compare these results to sparse grids, also with six dimensions and an increasing number of levels, including levels of two, three, four and five. Previous analyses suggests that the full tensor WCE converges by order seven, and we shall therefore use this full tensor WCE as our base case for comparison. In particular, we compute the root-mean-square error (RMSE) of the expectation and standard deviation of the transient growth. That is, we compute the root mean square deviation of the time series for $E[G(t, \boldsymbol{\zeta})]$ and $\sigma[G(t, \boldsymbol{\zeta})]$ with the corresponding expectation or standard deviation time series corresponding to the base case based upon the WCE tensor grid. Table 4.1, below, summarises the grid size, computational time and RMSE of the approaches considered. Figure 4.23 plots the expectation time series and figure 4.24 the standard deviation time series.

grid	points	computational time (s)	RMSE in $E[G(t,\boldsymbol{\zeta})]$	RMSE in $\sigma[G(t,\boldsymbol{\zeta})]$
LHS	2000	4340	0.013	0.399
LHS	5000	10558	0.001	0.119
LHS	10000	20991	0.000	0.040
Sparse (level 2)	85	470	0.000	24.969
Sparse (level 3)	389	2126	0.000	0.128
Sparse (level 4)	1433	7780	0.000	0.001
Sparse (level 5)	4541	24991	0.000	0.000
Tensor	4096	39309	0.000	0.000

Table 4.1: Comparison of computational times and root mean squared errors for LHS, tensor WCE and sparse WCE computations of transient growth. Stochastic plane Poiseuille flow, $c_l = 0.50$, $\sigma = 0.02$, $Re = 4000$, $\alpha = 1.02$, $\beta = 0.00$.

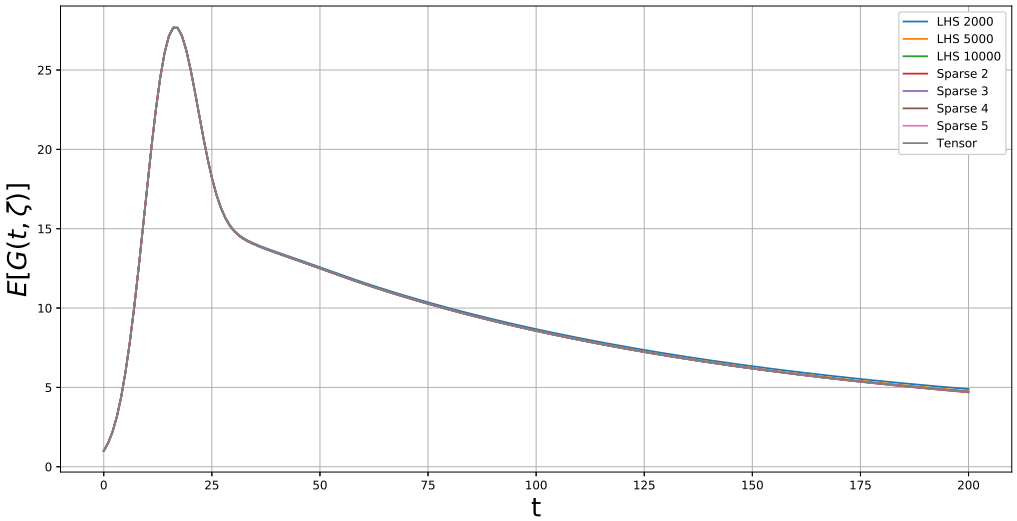

Figure 4.23: Comparison of computations of $E[G(t,\boldsymbol{\zeta})]$, for LHS, tensor WCE and sparse WCE based approaches. Stochastic plane Poiseuille flow, $c_l = 0.50$, $\sigma = 0.02$, $Re = 4000$, $\alpha = 1.02$, $\beta = 0.00$.

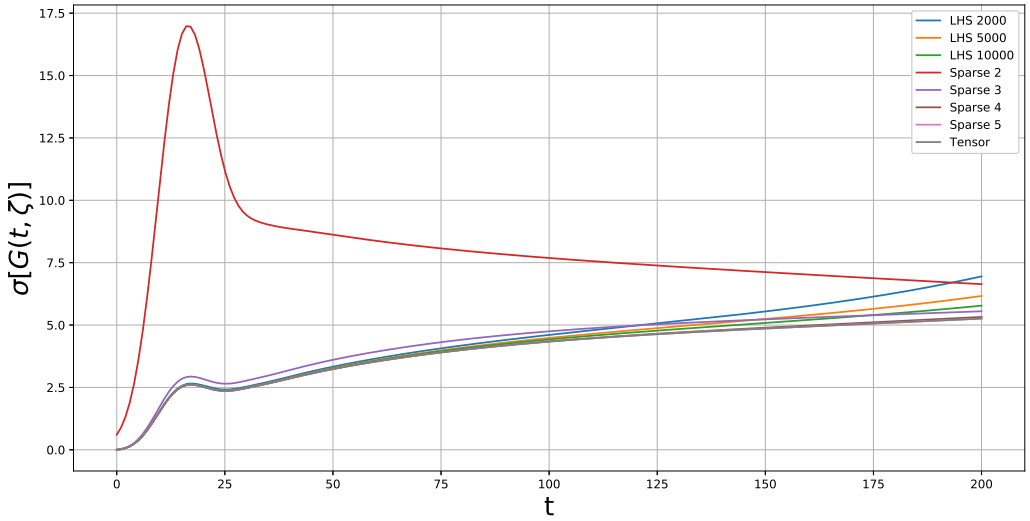

Figure 4.24: Comparison of computations of $\sigma[G(t, \boldsymbol{\zeta})]$, for LHS, tensor WCE and sparse WCE based approaches. Stochastic plane Poiseuille flow, $c_l = 0.50$, $\sigma = 0.02$, $Re = 4000$, $\alpha = 1.02$, $\beta = 0.00$.

As can be seen, all approaches are successful in computing the expectation, $E[G(t, \boldsymbol{\zeta})]$, to a high degree of accuracy. Even the level 2 sparse grid, with a mere 85 points, is sufficient for the computation of the expectation. Conversely, the computation of the second moment is more challenging, with a RMSE of 24.969 in standard deviation the level 2 sparse grid is clearly inadequate. However, the level 3 and most definitely the 4 sparse grid demonstrate their ability to achieve high accuracy at a reduced computational cost. The level 4 sparse grid, containing 35 percent of the points present in the full tensor grid and taking only 20 percent of the corresponding computational time, clearly illustrates the superiority of sparse grids in moderate to high stochastic dimensions. Furthermore, the LHS approach is also clearly inferior to the sparse grid in this case.

4.6.2 Low Correlation Length

The advantages of sparse grids only improve as the stochastic dimension increases and the computational savings in the case of 12 stochastic dimensions is much greater. Unfortunately, the tensor grid would contain 4^{12} points in this case and it is therefore infeasible to build. However, a sparse grid with 4 levels would contain only 17217 points. Such a grid would perform comparatively well with an LHS grid, which also does not suffer from the curse of dimensionality. Below, figures 4.25 (expectation) and 4.26 (standard deviation) depict such a comparison of the LHS

and sparse WCE for the transient growth of the same stochastic plane Poiseuille flow, but with a 12 dimensional stochastic input at $c_l = 0.10$ and $\sigma = 0.0025$.

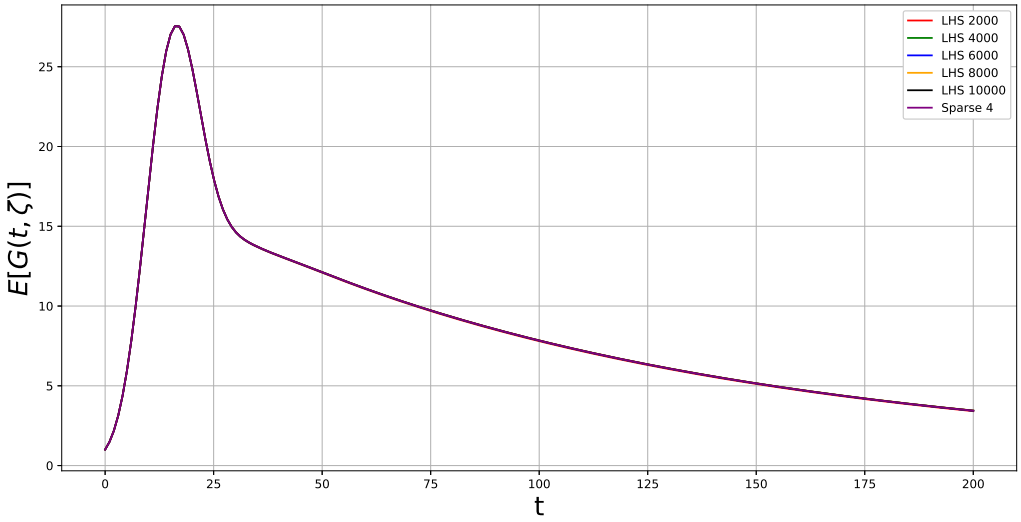

Figure 4.25: Comparison of computations of $E[G(t, \boldsymbol{\zeta})]$, for LHS and sparse WCE based approaches. Stochastic plane Poiseuille flow, $c_l = 0.10$, $\sigma = 0.0025$, $Re = 4000$, $\alpha = 1.02$, $\beta = 0.00$.

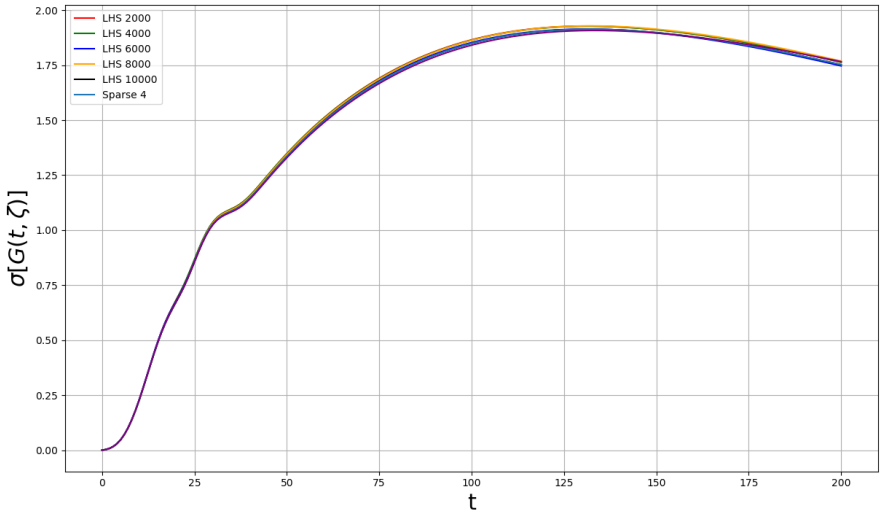

Figure 4.26: Comparison of computations of $\sigma[G(t, \boldsymbol{\zeta})]$, for LHS and sparse WCE based approaches. Stochastic plane Poiseuille flow, $c_l = 0.10$, $\sigma = 0.0025$, $Re = 4000$, $\alpha = 1.02$, $\beta = 0.00$.

As can be seen, the LHS based approach appears to have converged in both expecta-

tion and standard deviation by 10000 simulations. Furthermore, the 12 dimensional sparse grid with four levels agrees with these results. However, the sparse WCE approach results in WCE coefficients which would allow further analysis of variance based sensitivity that the LHS technique cannot. The tensor WCE approach would require around 1000 times as many simulations to achieve the same coefficients.

4.6.3 Summary

In summary, we can conclude that the optimal method for numerical integration depends on the number of stochastic dimensions. For low dimensional problems, involving say four or less stochastic variables, the tensor WCE offers the highest computational efficiency. In moderate dimensions, the tensor WCE begins to suffer from the curse of dimensionality and the sparse WCE should be favoured. Finally, problems involving a large number of stochastic random variables are best solved via LHS, where the number of grid points required is completely independent of the problem dimension.

4.7 Summary

In this chapter we set out the deterministic formulation, introduced and justified our source of stochasticity, and extended the deterministic equations to give the stochastic formulation. The numerical implementation was discussed, and a number of case studies were provided to illustrate the identification of suitable levels of discretization for both the physical and stochastic domain, along with a suitable choice of polynomial chaos order.

We conclude that 200 collocation points are sufficient for the discretization of the physical domain. Based upon experimental Blasius boundary layer data, we show a Gaussian kernel to be a suitable model and identify a suitable range of values for its parameterization, namely a correlation length $0.1 < c_l < 0.5$ and a standard deviation $0.0001 < \sigma < 0.05$. Further, we discretize the stochastic domain with zero mean, unit variance Gaussian random variables, and show that 4 and 12 variables are sufficient for processes with correlation lengths of 0.50 and 0.10 respectively, giving errors of less than 5 percent in the reconstruction of the correlation kernel. A convergence analysis indicates a sufficient polynomial chaos order of 7.

Finally, we show that the choice of the stochastic method is highly dependent upon the stochastic dimension, and hence the correlation length of the process. In low dimensions the Wiener chaos expansion on a tensor grid is the most computationally

efficient but suffers from the curse of dimensionality, rendering it inefficient in higher dimensions. In moderate stochastic dimensions the Wiener chaos expansion on a sparse grid is able to alleviate the problem and is shown to be more efficient than both tensor WCE and stratified Monte Carlo methods. Whilst the computational cost of the sparse WCE doesn't increase exponentially with the number of stochastic dimensions, it does still increase and in very high dimensions stratified Monte Carlo approaches prove to be more computationally efficient. The root mean square error (RMSE) of the sampling decays as the square root of the number of samples, Monte Carlo methods are thus effectively independent of the stochastic dimension. When the stochastic dimension becomes large, it becomes more efficient to pay for this decay than to integrate over a high dimensional space. However, WCE methods are far more efficient in moderate to low stochastic dimensions, and, furthermore, provide a much richer solution allowing for variance based sensitivity analysis.

Chapter 5

Stochastic Plane Poiseuille and Couette Flow

5.1 Introduction

In this section we study the stability of both plane Poiseuille and Couette flow with a stochastic base flow profile, focusing mostly on the stochastic Poiseuille flow.

5.2 Modal Analysis

5.2.1 Sensitivity of Individual Eigenvalues: Adjoints

In this section we will quantify the sensitivity of individual eigenvalues to stochastic base flow perturbations. These sensitivities will be stochastic themselves, and will be characterised by their statistical moments. We will use adjoint methods to achieve these results. We recap the direct eigenvalue problem

$$(\mathbf{L_1} - i\lambda_j \mathbf{I})\hat{\boldsymbol{q}}_{\boldsymbol{j}} = 0, \tag{5.1}$$

with eigen-pairs $(\lambda_j, \hat{\boldsymbol{q}}_{\boldsymbol{j}})$, and the adjoint problem

$$(\mathbf{L}_1^+ - i\lambda_j^+ \mathbf{I})\hat{\boldsymbol{q}}_{\boldsymbol{j}}{}^+ = 0, \tag{5.2}$$

with eigen-pairs $(\lambda_j^+, \hat{\boldsymbol{q}}_{\boldsymbol{j}}{}^+)$. The adjoint matrix $\mathbf{L}_\mathbf{1}^+$ can be derived from an inner

product and our choice of energy norm. That is

$$< \mathbf{L_1^+}\hat{\boldsymbol{q}}_j{}^+, \hat{\boldsymbol{q}}_j >_E = < \hat{\boldsymbol{q}}_j{}^+, \mathbf{L_1}\hat{\boldsymbol{q}}_j >_E . \tag{5.3}$$

Using the energy norm weight matrix, $\mathbf{M} = \mathbf{F}^H\mathbf{F}$, we have

$$(\mathbf{L_1^+}\hat{\boldsymbol{q}}_j{}^+)^H\mathbf{M}\hat{\boldsymbol{q}}_j = \hat{\boldsymbol{q}}_j{}^{+H}\mathbf{M}\mathbf{L_1}\hat{\boldsymbol{q}}_j, \tag{5.4}$$

from which it follows that the adjoint matrix may be written as

$$\mathbf{L_1^+} = \mathbf{M^{-1}}\mathbf{L_1^H}\mathbf{M}. \tag{5.5}$$

As outlined in section 3.2.5.1, the change $\delta\lambda_j$ induced by a modification operator $\delta\mathbf{L_1}$ of norm much less than one can be expressed as

$$\delta\lambda_j = \frac{< \hat{\boldsymbol{q}}_j{}^+, \delta\mathbf{L_1}\hat{\boldsymbol{q}}_j >_E}{< \hat{\boldsymbol{q}}_j{}^+, \hat{\boldsymbol{q}}_j >_E}. \tag{5.6}$$

Further, assuming the eigenvectors are appropriately scaled ($< \hat{\boldsymbol{q}}_j{}^+, \hat{\boldsymbol{q}}_j >_E = 1$), the expression can be bounded,

$$|\delta\lambda_j| \leq ||\hat{\boldsymbol{q}}_j{}^+||_E||\delta\mathbf{L_1}||_E||\hat{\boldsymbol{q}}_j||_E = ||\mathbf{F}\hat{\boldsymbol{q}}_j{}^+||_2||\mathbf{F}\delta\mathbf{L_1}\mathbf{F}^{-1}||_2||\mathbf{F}\hat{\boldsymbol{q}}_j||_2, \tag{5.7}$$

where subscript E and 2 denote the energy and two norm respectively. The quantity $||\hat{\boldsymbol{q}}_j{}^+||_E||\hat{\boldsymbol{q}}_j||_E$ appears as a proportionality constant between the norm of the perturbation and the size of the deviation in the eigenvalue, and is therefore interpreted as the sensitivity, which is a property of the stability operator. Below, in table 5.1, we list the sensitivity of selected eigenvalues, from the A, P and S branch, for a plane Poiseuille flow at $Re = 4000$, $\alpha = 1.02$ and $\beta = 0.00$. In addition, the modes are plotted in figure 5.1.

Eigenvalue	Branch	Sensitivity
$0.287 - 0.005i$	A	4.4
$0.453 - 0.178i$	A	56.1
$0.541 - 0.183i$	A	102.8
$0.941 - 0.079i$	P	5.9
$0.896 - 0.124i$	P	26.7
$0.805 - 0.215i$	P	679.4
$0.685 - 0.373i$	S	31318.5
$0.688 - 0.404i$	S	21318.3
$0.682 - 0.866i$	S	879.4

Table 5.1: Sensitivity of selected eigenvalues for plane Poiseuille flow at $Re = 4000$, $\alpha = 1.02$, $\beta = 0.00$.

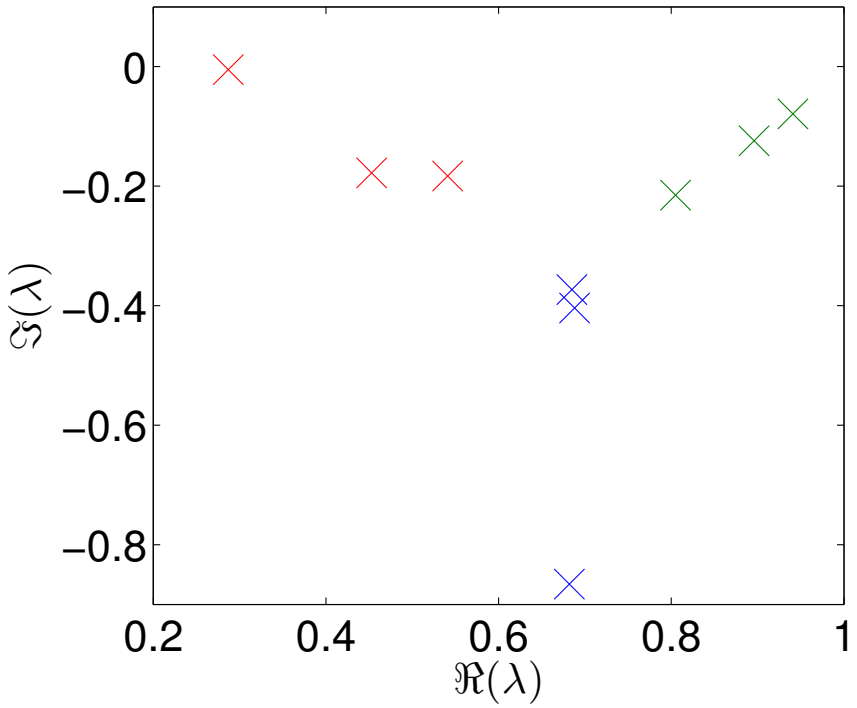

Figure 5.1: Selected eigenvalues for plane Poiseuille flow at $Re = 4000$, $\alpha = 1.02$, $\beta = 0.00$. Red, green and blue crosses from the A, P and S branches respectively.

It is well known that the eigenvalues at the junction of the three branches exhibit the highest sensitivity, and thus react significantly to small perturbations of the governing operator. Inspecting the table, this is indeed seen to be the case with the sensitivity of modes from both the A and P branch increasing as approaching

the junction, and the sensitivity of modes from the S branch decreasing as moving away.

We now extend this deterministic analysis by introducing our stochastic perturbation. Introducing the KLE of the stochastic base flow, we can formulate $\mathbf{L_1^*} = \mathbf{L_1} + \delta\mathbf{L_1}$ and hence formulate an expression for $\delta\mathbf{L_1}$. Noting $\hat{\mathbf{L_1}}^* = \mathbf{L}^{-1}\hat{\mathbf{R}}^*$, where

$$\hat{\mathbf{R}}^* = \begin{pmatrix} i\alpha U(x_2)(1+\bar{\sigma}\sum_{i=1}^{d}\sqrt{\gamma_i}\zeta_i(\omega)e_i(x_2))(K^2-D^2)+ & 0 \\ i\alpha(U''(x_2)+ & \\ \bar{\sigma}\sum_{i=1}^{d}\sqrt{\gamma_i}\zeta_i(\omega)(U''(x_2)e_i(x_2)+2U'(x_2)e_i'(x_2)+ & \\ U(x_2)e_i''(x_2))) + \frac{1}{Re}(K^2-D^2)^2 & \\ & \\ i\beta(U'(x_2)+ & \\ \bar{\sigma}\sum_{i=1}^{d}\sqrt{\gamma_i}\zeta_i(\omega)(U'(x_2)e_i(x_2)+U(x_2)e_i'(x_2))) & i\alpha U(x_2)(1+\bar{\sigma}\sum_{i=1}^{d}\sqrt{\gamma_i}\zeta_i(\omega)e_i(x_2))- \\ & \frac{1}{Re}(D^2-K^2) \end{pmatrix}$$

$$= \mathbf{R} + \bar{\sigma}\sum_{i=1}^{d}\sqrt{\gamma_i}\zeta_i(\omega)\hat{\mathbf{R}}_\mathbf{i},$$

it is clear that

$$\hat{\mathbf{L_1}}^* = \mathbf{L_1} + \bar{\sigma}\sum_{i=1}^{d}\sqrt{\gamma_i}\zeta_i(\omega)\mathbf{L^{-1}}\hat{\mathbf{R}}_\mathbf{i} = \mathbf{L_1} + \bar{\sigma}\sum_{i=1}^{d}\sqrt{\gamma_i}\zeta_i(\omega)\mathbf{P}_i = \mathbf{L_1} + \delta\mathbf{L_1}. \tag{5.8}$$

We hence have an expression for $\delta\mathbf{L_1}$,

$$\delta\mathbf{L_1} = \bar{\sigma}\sum_{i=1}^{d}\sqrt{\gamma_i}\zeta_i(\omega)\mathbf{P}_i. \tag{5.9}$$

Using this expression we can formulate the stochastically perturbed eigenvalue as

$$\delta\lambda_j = \frac{1}{\phi_j}\bar{\sigma}\sum_{i=1}^{d}\sqrt{\gamma_i}\zeta_i(\omega) < \hat{\boldsymbol{q}}_\boldsymbol{j}^{+}, \mathbf{P}_i\hat{\boldsymbol{q}}_\boldsymbol{j} >_E, \tag{5.10}$$

where $\phi_j =< \hat{\boldsymbol{q}}_\boldsymbol{j}^{+}, \hat{\boldsymbol{q}}_\boldsymbol{j} >_E$. From this we can compute the statistical moments; the mean,

$$\mathrm{E}[\delta\lambda_j] = \frac{1}{\phi_j}\bar{\sigma}\sum_{i=1}^{d}\sqrt{\gamma_i}\mathrm{E}[\zeta_i(\omega)] < \hat{\boldsymbol{q}}_\boldsymbol{j}^{+}, \mathbf{P}_i\hat{\boldsymbol{q}}_\boldsymbol{j} >_E = 0, \tag{5.11}$$

and variance,

$$\mathrm{Var}[\delta\lambda_j] = \frac{1}{\phi_j}\bar{\sigma}\sum_{i=1}^{d}\sqrt{\gamma_i}\mathrm{Var}[\zeta_i(\omega)] < \hat{\boldsymbol{q}}_{\boldsymbol{j}}{}^{+}, \mathbf{P}_i\hat{\boldsymbol{q}}_{\boldsymbol{j}} >_E = \frac{1}{\phi_j}\bar{\sigma}\sum_{i=1}^{d}\sqrt{\gamma_i} < \hat{\boldsymbol{q}}_{\boldsymbol{j}}{}^{+}, \mathbf{P}_i\hat{\boldsymbol{q}}_{\boldsymbol{j}} >_E . \tag{5.12}$$

Using these expressions, we study the stochastic spectrum of plane Poiseuille flow. We consider Poiseuille flow at $Re = 4000$, $\alpha = 1.02$ and $\beta = 0.00$, for stochastic input processes characterised as $\{\sigma = 0.0004, c_l = 0.10\}$, $\{\sigma = 0.0025, c_l = 0.10\}$, $\{\sigma = 0.02, c_l = 0.50\}$ and $\{\sigma = 0.05, c_l = 0.50\}$. Figure 5.2 depicts the results.

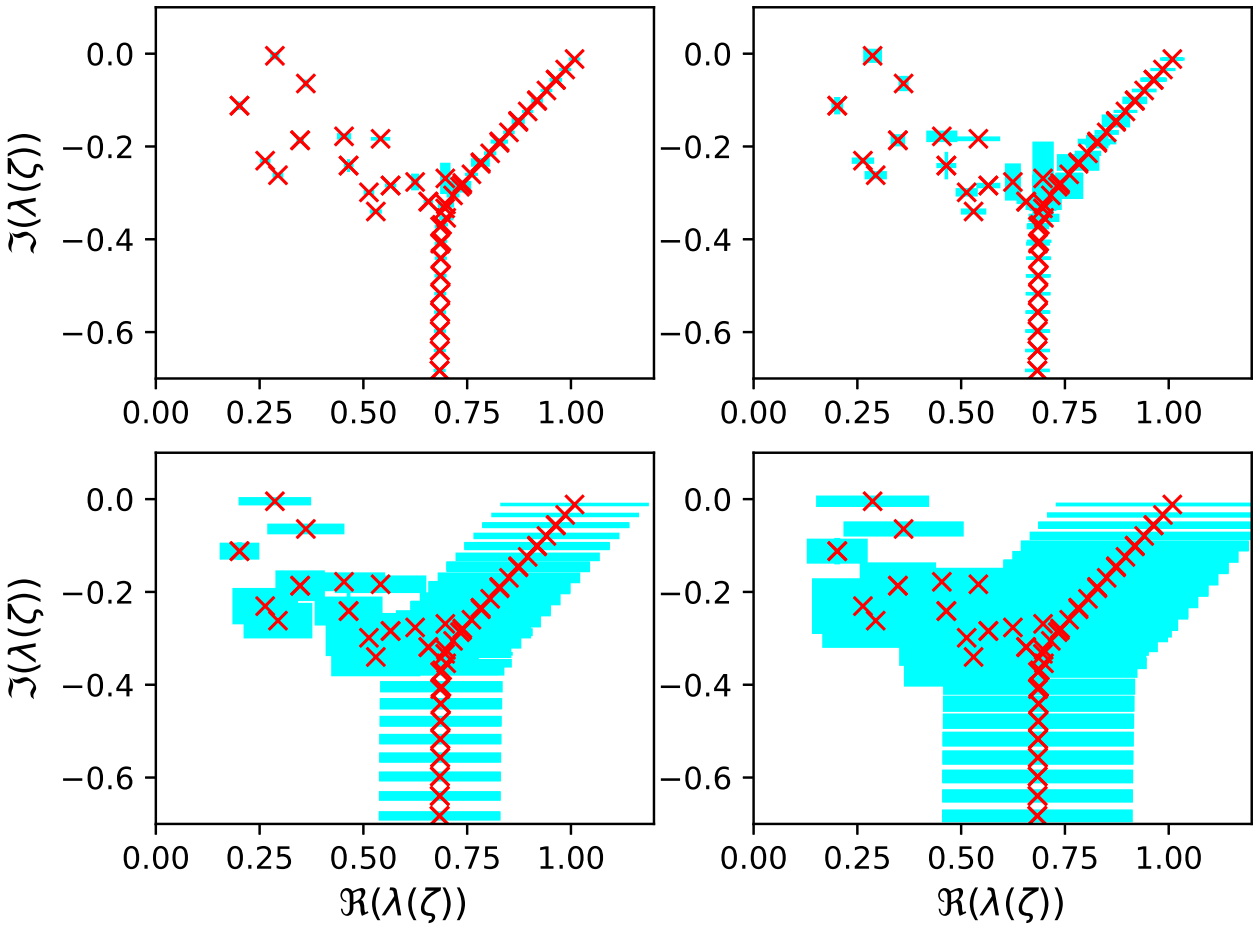

Figure 5.2: Spectrum (red crosses) for stochastic plane Poiseuille flow with standard deviation bars (blue rectangles) for $c_l = 0.10$ and $\sigma = 0.0004$ (top left), $c_l = 0.10$ and $\sigma = 0.0025$ (top right), $c_l = 0.50$ and $\sigma = 0.02$ (bottom left), $c_l = 0.50$ and $\sigma = 0.05$ (bottom right), $Re = 4000$, $\alpha = 1.02$, $\beta = 0.00$.

The eigenvalues are depicted with red crosses, each centred on a blue rectangle whose width and height represent the real and imaginary part of the standard deviation. That is, the blue bars extend one standard deviation to the left and one standard deviation to the right of the mean of the eigenvalue, as well as a standard deviation above and below.

In general, sensitivity can be seen to be greatest in the vicinity of the Y branch. A reduction in correlation length is seen to have a significant effect on modes in the vicinity of the Y-branch, whilst having little impact on those further away. Conversely, an increase in the input standard deviation is observed to have a more homogeneous impact on the spectrum. The eigenvalues show most variability along the real axis with the rectangles elongated in this direction. The phase speed is thus far more sensitive to stochasticity than the asymptotic growth rate associated with a mode.

To extend the deterministic results listed in table 5.1, we further list the standard deviation of each of the selected modes for the case $c_l = 0.50$ and $\sigma = 0.02$ (bottom left subplot of figure 5.2) in table 5.2.

Eigenvalue	Branch	Sensitivity	Standard deviation
$0.287 - 0.005i$	A	4.4	$0.084 + 0.006i$
$0.453 - 0.178i$	A	56.1	$0.095 - 0.017i$
$0.541 - 0.183i$	A	102.8	$0.107 - 0.016i$
$0.941 - 0.079i$	P	5.9	$0.172 - 0.004i$
$0.896 - 0.124i$	P	26.7	$0.170 - 0.006i$
$0.805 - 0.215i$	P	679.4	$0.166 - 0.011i$
$0.685 - 0.373i$	S	31318.5	$0.137 + 0.004i$
$0.688 - 0.404i$	S	21318.3	$0.144 + 0.009i$
$0.682 - 0.866i$	S	879.4	$0.142 + 0.005i$

Table 5.2: Sensitivity and standard deviation of selected eigenvalues for plane Poiseuille flow at $Re = 4000$, $\alpha = 1.02$, $\beta = 0.00$, $c_l = 0.50$ and $\sigma = 0.02$.

It is interesting to note that there does not appear to be a direct correlation between the sensitivity of a mode and its standard deviation. The sensitivity is a measure of mobility for a general perturbation, whilst the standard deviation measures the mobility for our particular structured perturbation. Inspecting the first eigenvalue in the table, $0.287 - 0.005i$, we see that a bump of size $0.005i$ or greater would be sufficient to push it into the unstable region of the spectrum. This eigenvalue has a standard deviation with imaginary part $0.006i$, and a one standard deviation

move would be more than sufficient for asymptotic instability. In fact, a move of 0.83 standard deviations or more would suffice. Noting that a linear combination of mutually independent normal random variables is itself normally distributed (see appendix C.1 Linear Combinations of Independent Normal Random Variables), we can say that a move of plus 0.83 standard deviation or more occurs with a probability of around 20 percent. That is, at these flow conditions, with this stochastic input process, asymptotic instability arises with a 20 percent probability. We can make similar claims for other modes, such as mode $0.941 - 0.079i$ from the P branch, requiring a 20 standard deviation move for asymptotic instability, which is extremely unlikely with probability of 3×10^{-87} percent.

5.2.2 Sensitivity of the Whole Spectrum: ϵ-Pseudospectra

An alternative approach to analysing the behaviour and sensitivity of a matrix is to consider the ϵ-pseudospectra [86]. Appealing to definition 2.2 (section 3.2.5.3) of the ϵ-pseudospectra, $\Lambda_\epsilon(\mathbf{A}) = \Lambda(\mathbf{A} + \delta\mathbf{L_1}),\ \forall\ \delta\mathbf{L_1} \in \mathbb{C}^{NxN}$ with $||\delta\mathbf{L_1}|| < \epsilon$, we write the KLE of the discretised Orr-Sommerfeld and Squire equations in such a way that we can identify the perturbation matrix $\delta\mathbf{L_1}$, which we have established as

$$\delta\mathbf{L_1} = \bar{\sigma} \sum_{i=1}^{d} \sqrt{\gamma_i}\zeta_i(\omega)\mathbf{P}_i. \tag{5.13}$$

We see that the perturbation matrix, $\delta\mathbf{L_1}$, exhibits a certain structure which is defined by the base flow, and we should therefore consider the structured ϵ-pseudospectra (definition 8, section 3.2.5.3). Importantly, it can be shown that $\Lambda_\epsilon^{struct}(\mathbf{A}) \subseteq \Lambda_\epsilon(\mathbf{A})$ [71]. Furthermore, when the structured matrix is a symmetric one, it can be shown that the structured and unstructured ϵ-pseudospectra are equal, $\Lambda_\epsilon^{sym}(\mathbf{A}) = \Lambda_\epsilon(\mathbf{A})$ [71].

In the case $\beta = 0$, each matrix $\hat{\mathbf{R}}_\mathbf{i}$ (equation 5.8) would appear to become symmetric. In such a case we would have a complex symmetric matrix to which we add a symmetric perturbation, preserving the structure. However, application of the boundary conditions and numerical discretization destroy the symmetry. We therefore cannot claim that $\Lambda_\epsilon^{struct}(\mathbf{A}) = \Lambda_\epsilon(\mathbf{A})$ (as discussed in section 3.2.5.3), but only that $\Lambda_\epsilon^{struct}(\mathbf{A}) \subseteq \Lambda_\epsilon(\mathbf{A})$. **We therefore do not attempt to make a direct comparison between our structured perturbations and the unstructured ones of the ϵ-pseudospectra, but simply note that as a subset our results should be bounded by those of the more general case.**

To proceed, we bound the norm of the random matrix from above,

$$||\delta \mathbf{L_1}||_2 = ||\bar{\sigma} \sum_{i=1}^{d} \sqrt{\gamma_i}\zeta_i(\omega)\mathbf{L^{-1}}\hat{\mathbf{R}}_\mathbf{i}||_2 \leq \bar{\sigma} \sum_{i=1}^{d} |\sqrt{\gamma_i}||\zeta_i(\omega)|||\mathbf{L^{-1}}\hat{\mathbf{R}}_\mathbf{i}||_2. \tag{5.14}$$

For instance, at $Re = 4000$, $c_l = 0.10$, and $\sigma = 0.0004$, we can bound the perturbation matrix via a summation of random variables truncated to 15 terms,

$$||\delta \mathbf{L_1}||_2 \leq \sigma \sum_{i=1}^{15} |\sqrt{\gamma_i}||\zeta_i(\omega)|||\mathbf{L^{-1}}\hat{\mathbf{R}}_\mathbf{i}||_2 =$$

$$0.0004|\zeta_1(\omega)| + 0.0004|\zeta_2(\omega)| + 0.0005|\zeta_3(\omega)| + 0.0006|\zeta_4(\omega)| +$$

$$0.0007|\zeta_5(\omega)| + 0.0007|\zeta_6(\omega)| + 0.0007|\zeta_7(\omega)| + 0.0007|\zeta_8(\omega)| +$$

$$0.0007|\zeta_9(\omega)| + 0.0006|\zeta_{10}(\omega)| + 0.0005|\zeta_{11}(\omega)| + 0.0005|\zeta_{12}(\omega)| +$$

$$0.0004|\zeta_{13}(\omega)| + 0.0003|\zeta_{14}(\omega)| + 0.0002|\zeta_{15}(\omega)|,$$

which has an expectation of zero and a standard deviation of 0.0022, and whose corresponding log resolvent norm is $\log_{10}(0.0022) \approx -2.7$. Similarly, for $\{\sigma = 0.0025, c_l = 0.10\}$ we get a standard deviation of 0.0135, $\{\sigma = 0.02, c_l = 0.50\}$ we get a standard deviation of 0.0410, and $\{\sigma = 0.05, c_l = 0.50\}$ we get a standard deviation of 0.1018, with corresponding log values of -1.9, -1.4 and -1.0 respectively.

In figure 5.3, below, we plot stochastic eigenvalues and pseudospectral log resolvent norm contours, corresponding to these cases. We emphasise that the pseudospectral log resolvent norm contours correspond to the fully deterministic base flow.

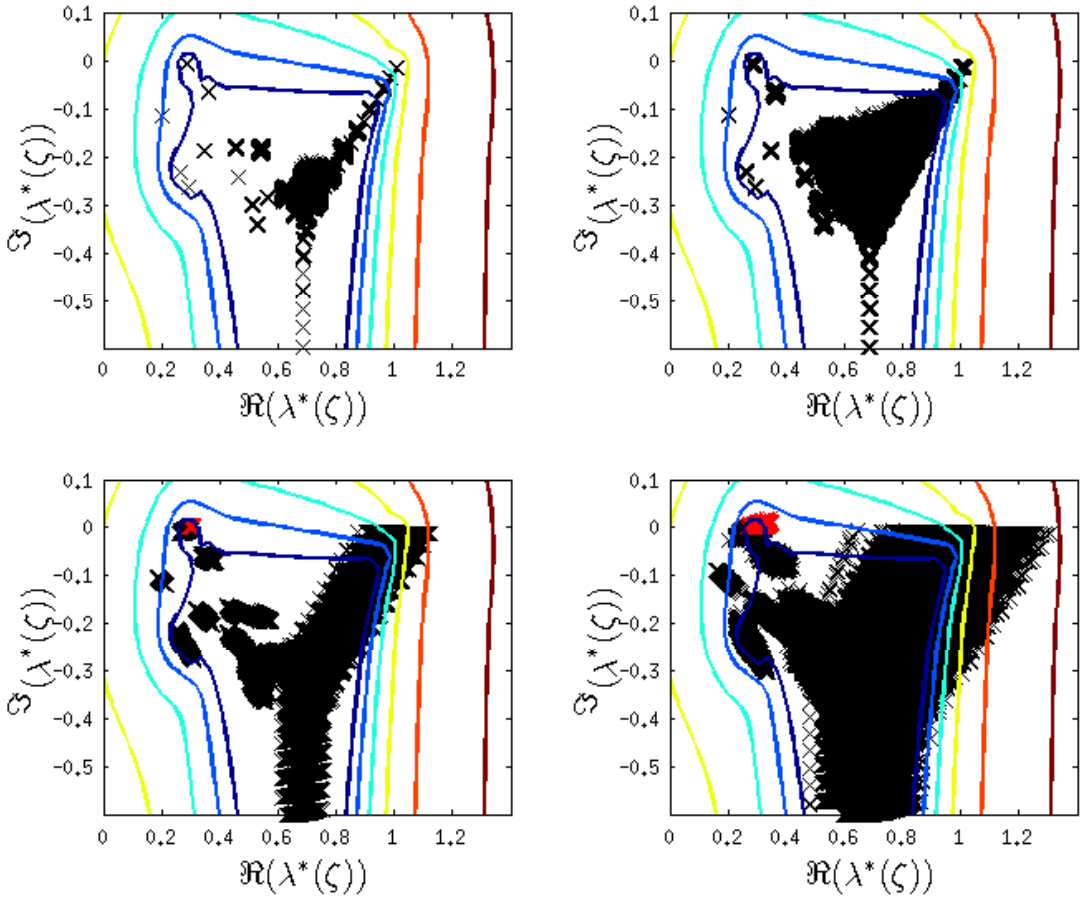

Figure 5.3: Stochastic eigenvalues (5000 Monte Carlo simulations) and pseudo-spectral log resolvent norm contours ($\log_{10}\epsilon$=-3,-2.5,-2,-1.5,-1,-0.5 from inner to outer) of a plane Poiseuille flow, $c_l = 0.10$ and $\sigma = 0.0004$ (top left), $c_l = 0.10$ and $\sigma = 0.0025$ (top right), $c_l = 0.50$ and $\sigma = 0.02$ (bottom left), $c_l = 0.50$ and $\sigma = 0.05$ (bottom right), $Re = 4000$, $\alpha = 1.02$, $\beta = 0.00$.

As was seen with the adjoint approach, a reduction in correlation length has most impact on modes in the vicinity of the Y-branch, whilst an increase in the input standard deviation is observed to have a more homogeneous effect on all modes. The real part of the eigenvalues have far greater mobility than the imaginary part (which determines the asymptotic stability). Those modes with positive imaginary part, deemed asymptotically unstable and plotted in red, are mostly confined to the cases involving the larger input standard deviations.

Recalling that ζ_i are mutually independent normal random variables, we see that $\delta\mathbf{L_1}$ is simply a linear combination of such variables. Furthermore, a linear combination of mutually independent normal random variables is itself normally distributed

(see appendix C.1 Linear Combinations of Independent Normal Random Variables) and $\delta\mathbf{L_1}$ is therefore normally distributed. For a normal random variable, we expect around 67% of observations to fall within one standard deviation of the mean, which corresponds to the log resolvent norm contour of -1 in the case of the lower right sub-plot. Furthermore, we expect 99% of observations to fall within three standard deviations of the mean, which for the lower right sub-plot corresponds to a log resolvent norm of -0.5. Clearly, the above figure is consistent with both of these results. In fact, all observations are seen to sit within the -0.5 contour, and this is to be expected as our estimate of the norm of the perturbation matrix was actually an upper bound.

In addition, we repeat the analysis for a Couette flow at the same wave number pair but at a lower Reynolds number. We restrict the Reynolds number to a value of 2000 due to the greater mobility of eigenvalues in the vicinity of the Y-branch. The figure below, 5.4, depicts the results.

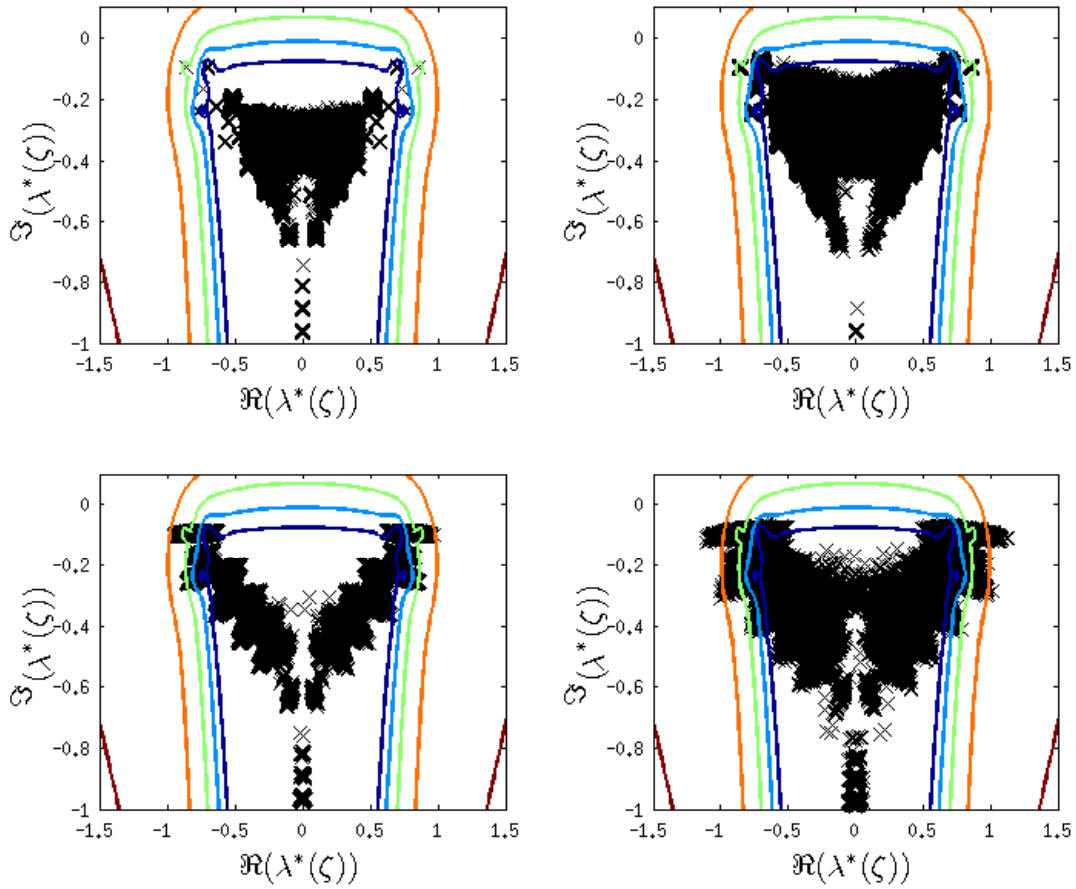

Figure 5.4: Stochastic eigenvalues (5000 Monte Carlo simulations) and pseudo-spectral log resolvent norm contours ($\log_{10}\epsilon$=-3,-2.5,-2,-1.5,-1 from inner to outer) of a plane Couette flow, $c_l = 0.10$ and $\sigma = 0.0004$ (top left), $c_l = 0.10$ and $\sigma = 0.0025$ (top right), $c_l = 0.50$ and $\sigma = 0.02$ (bottom left),$c_l = 0.50$ and $\sigma = 0.05$ (bottom right), $Re = 2000$, $\alpha = 1.02$, $\beta = 0.00$.

As can be seen, all eigenvalues have negative imaginary part and all realisations are therefore asymptotically stable. As observed with the Poiseuille flow, a reduction in correlation length is observed to increase the mobility of eigenvalues in the vicinity of Y-branch, whilst an increase in the input standard deviation is observed to effect all eigenvalues to a similar degree. Again, it can be shown that the pseudospectra are consistent with the stochastic realisations, which all sit within the three standard deviation log resolvent norm contour, with values of -1.17, -0.38, 0.33 and 0.73 corresponding to the figures running clockwise from the upper left sub-plot. Finally in this subsection we wish to emphasise again that one must be careful when interpreting the pseudospectra. In particular, we repeat that the structured pseudospectra, resulting from the structured perturbations, is only a subset of the more general unstructured full pseudospectra.

5.2.3 Neutral Curves

The curve that defines the boundary between those perturbations which grow exponentially and those which do not, in $\alpha - Re$ parameter space ($\beta = 0.00$), is termed the neutral curve. One typically computes the neutral curve by selecting a discrete grid in the parameter space, and computing the maximum asymptotic growth rate for each $\alpha - Re$ combination before finally forming contours of constant growth rate. The neutral curve is then the contour with a growth rate of exactly zero. Furthermore, exponentially growing and decaying waves can be identified from the positive and negative growth contours respectively. The leftmost tip of the neutral curve defines the lowest Reynolds number for which an exponentially growing perturbation exists, and the corresponding Reynolds number is the critical Reynolds number. As already seen in the spectra, in the deterministic setting the critical Reynolds number for Poiseuille flow is about 5772, occurring at a stream-wise wave-number of $\alpha = 1.02$.

We here extend the typical deterministic analysis, and form a stochastic picture of the neutral curve. As previously stated, one forms the neutral curve from a maximum growth rate contour plot in a discretised parameter space. In the deterministic setting alone this is a computationally expensive procedure. To produce accurate and smooth contours one may need to discretize both the Reynolds number and the stream-wise wave-number with around fifty points, which amounts to computing the spectra and identifying the most unstable wave 2500 times. In the stochastic case we would need to compute the neutral curve for each stochastic base flow and therefore repeat those 2500 calculations many times, thus accentuating the computational complexity of the problem. We therefore do not attempt to form a full picture of the stochastic neutral curve but select specific growth rate contours which we compute to high accuracy. We adopt LHS and form growth rate contours with rates of -0.005, -0.002, 0.000 (neutral curve) and 0.002, the figures below, 5.5, depict the mean contours plus or minus one standard deviation.

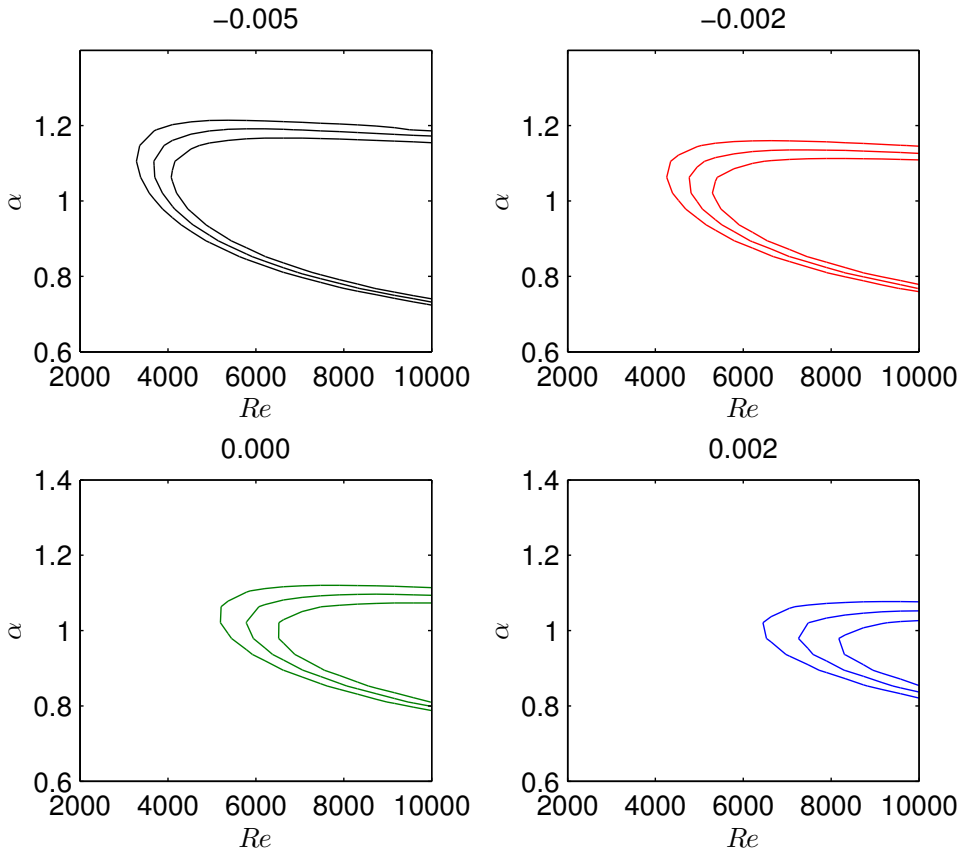

Figure 5.5: Selected growth rate contours (mean ± one standard deviation) from neutral curve for Stochastic plane Poiseuille flow, $c_l = 0.10$, $\sigma = 0.0004$. Growth rate contours of -0.005 (top left), -0.002 (top right), 0.000 (bottom left), 0.002 (bottom right).

Comparing the sub-plots, it is evident that the variability in parameter space, of a given growth rate contour, increases with the growth rate such that stochastic defects have a greater influence on perturbations which grow faster. Considering the variability in the critical Reynolds number, or the leftmost point for the non zero growth rates, we tabulate the standard deviations below, in figure 5.3.

Max Growth Rate	E[α_{crit}]	$\sigma[\alpha_{crit}]$	E[Re_{crit}]	$\sigma[Re_{crit}]$
-0.005	1.09	0.03 (2.8%)	3670	637 (17.4%)
-0.002	1.04	0.04 (3.8%)	4752	871 (18.3%)
0.000	1.02	0.04 (3.9%)	5770	1124 (19.5%)
0.002	0.99	0.03 (3.0%)	7234	1492 (20.5%)

Table 5.3: Expectation and standard deviation of leftmost perturbation in parameter space. Percentages of mean in brackets.

The table shows that variability in Reynolds number is much greater than that in stream-wise wave number. Furthermore, as the graphs suggest, the relative standard deviation does indeed increases with growth rate. Focusing on the neutral curve only, we see that mean values for the critical Reynolds and stream-wise wave numbers agree reasonably well with the deterministic case, and the small percentage differences are most likely due to a slight inadequacy in discretization of the parameter space, rather than rooted in the physics. The variability in critical Reynolds number is evidently of a significant magnitude, at around 19.5%. We use 10000 MC simulations to plot the empirical distribution for Re_{crit} in figure 5.6, and also fit a normal curve to the observations.

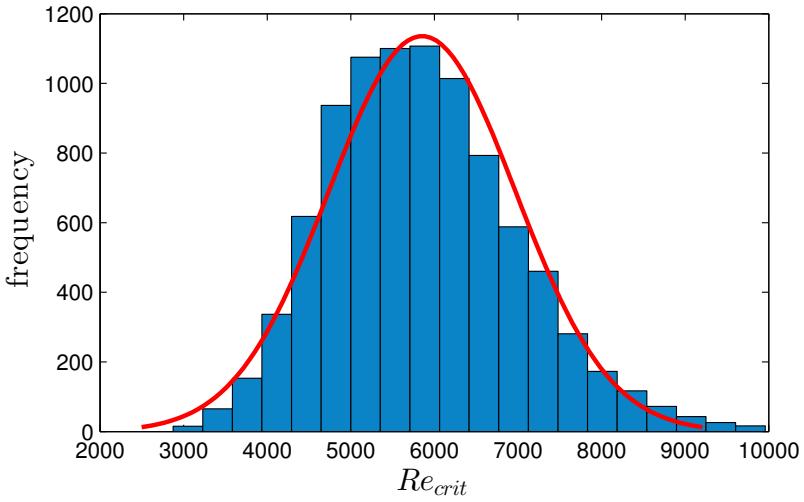

Figure 5.6: Histogram of Re_{crit} and fitted normal distribution.

In addition, we compute the higher statistical moments, finding a skew of 0.45 and a kurtosis of 3.17 (0.17 excess kurtosis). The slight excess kurtosis suggests that extreme events are slightly more likely than the normal case, and the positive skew is indicative of the longer right tail. The mass of the distribution is thus concentrated to the left, implying that the critical Reynolds number frequently makes small downside deviations from the mean value of 5770, and infrequently makes large upside deviations. Nevertheless, the distribution is reasonably well approximated as normal. If we therefore assume this parameter is normally distributed, then one would expect the critical Reynolds number to fall within the range $4646 - 6894$ with 67% probability, thus suggesting that the critical Reynolds number could take values less than 4646 with a probability of around 16%, and values below 2398 with probability of around 0.5 percent.

As previously stated, experimental instabilities have been observed at Reynolds numbers far below the deterministic critical value of 5772. We also know that

there is inherent uncertainty in the flow properties of such systems. Combining this knowledge with the above analysis, it does not seem too unreasonable to postulate that stochastic defects could at least partially explain the deviations between theory and experiment.

5.3 Transient Analysis

5.3.1 The Stochastic Expansion of the Perturbation Energy Growth Function

Recalling the definition of the energy norm, we here reformulate the stochastic equivalent, which we will use in formulating the stochastic perturbation energy growth function. The energy norm reads

$$||\mathbf{q}(x_2,\boldsymbol{\zeta}(\omega))||_E^2 = \int_{-1}^{1}(k^2|u_2(x_2,\boldsymbol{\zeta}(\omega))|^2+|\eta(x_2,\boldsymbol{\zeta}(\omega))|^2+|u_2'(x_2,\boldsymbol{\zeta}(\omega))|^2)dx_2. \quad (5.15)$$

We approximate the spatial dimension with Chebyshev polynomials and the stochastic dimension with Wick products. $u_2(x_2,\boldsymbol{\zeta}(\omega)) = \sum_{i=1}^{n_c}\sum_{\alpha=0}^{N} v_\alpha^i H_\alpha(\boldsymbol{\zeta}(\omega))T_i(x_2)$, $\eta(x_2,\boldsymbol{\zeta}(\omega)) = \sum_{i=1}^{n_c}\sum_{\alpha=0}^{N}\eta_\alpha^i H_\alpha(\boldsymbol{\zeta}(\omega))T_i(x_2)$ and $u_2'(x_2,\boldsymbol{\zeta}(\omega)) = \sum_{k=1}^{n_c}\sum_{i=1}^{n_c}\sum_{\alpha=0}^{N} D_{ik}v_\alpha^k H_\alpha(\boldsymbol{\zeta}(\omega))T_i(x_2)$, where $T_i(x_2)$ are Chebyshev polynomials, $H_\alpha(\boldsymbol{\zeta}(\omega))$ are Wick products, v_α^i are WCE coefficients for the ith spectral Chebyshev coefficient, $\sum_{k=1}^{n_c} D_{ik}v_\alpha^k$ is the WCE coefficient for the ith spectral Chebyshev coefficient in the expansion of the spatial derivative, and D_{ik} are the elements of the first order Chebyshev derivative matrix. Substituting the expansions into the energy norm, we have

$$||\mathbf{q}(x_2,\boldsymbol{\zeta}(\omega))||_E^2 = \sum_{\alpha=0}^{N}\sum_{\beta=0}^{N} H_\alpha(\boldsymbol{\zeta}(\omega))H_\beta(\boldsymbol{\zeta}(\omega))\sum_{i=1}^{n_c}\sum_{j=1}^{n_c}\int_{-1}^{1} T_i(x_2)T_j(x_2)dx_2$$
$$\left\{k^2 v_\alpha^i v_\beta^j + \eta_\alpha^i\eta_\beta^j + \sum_{m=1}^{n_c}\sum_{n=1}^{n_c} D_{im}v_\alpha^m D_{jn}v_\beta^n\right\}.$$

Let $C_{ij} = \int_{-1}^{1} T_i(x_2)T_j(x_2)dx_2$, $\mathbf{v}^\alpha = (v_\alpha^1,...,v_\alpha^{n_c})^T$, $\boldsymbol{\eta}^\alpha = (\eta_\alpha^1,...,\eta_\alpha^{n_c})^T$, $\hat{\mathbf{v}} = \sum_{\alpha=0}^{N} H_\alpha(\boldsymbol{\zeta}(\omega))\mathbf{v}^\alpha$, and $\hat{\boldsymbol{\eta}} = \sum_{\alpha=0}^{N} H_\alpha(\boldsymbol{\zeta}(\omega))\boldsymbol{\eta}^\alpha$, then $\hat{\mathbf{v}}$ and $\hat{\boldsymbol{\eta}}$ are chaos expansions of the Chebyshev spectral coefficients associated with the wall normal velocity and vorticity, we can

then define the energy norm in matrix form,

$$||\mathbf{q}(x_2, \boldsymbol{\zeta}(\omega))||_E^2 = \hat{\mathbf{v}}^*(\mathbf{D}^*\mathbf{C}\mathbf{D} + k^2\mathbf{C})\hat{\mathbf{v}} + \hat{\boldsymbol{\eta}}^*\mathbf{C}\hat{\boldsymbol{\eta}} = \hat{\mathbf{v}}^*{\mathbf{E_v}}^*\mathbf{E_v}\hat{\mathbf{v}} + \hat{\boldsymbol{\eta}}^*{\mathbf{E}_\eta}^*\mathbf{E}_\eta\hat{\boldsymbol{\eta}}, \quad (5.16)$$

where the last equality holds since the matrices are Hermitian. Matrices $\mathbf{E_v}$ and $\mathbf{E_n}$ can be computed from a singular value decomposition (SVD) of $\mathbf{D}^*\mathbf{C}\mathbf{D} + k^2\mathbf{C}$ and $\mathbf{C}$ respectively. For instance, noting $\mathbf{C}$ is positive definite we can compute the SVD, $\mathbf{C} = \mathbf{U}\mathbf{S}\mathbf{V}^*$, where $\mathbf{U}$ and $\mathbf{V}$ contain the right and left singular vectors, and $\mathbf{S}$ is the diagonal matrix of singular values. Further, since $\mathbf{C}$ is symmetric we must have $\mathbf{U} = \mathbf{V}$, hence $\mathbf{C} = \mathbf{U}\mathbf{S}\mathbf{U}^* = \mathbf{U}\sqrt{\mathbf{S}^*}\sqrt{\mathbf{S}}\mathbf{U}^* = (\sqrt{\mathbf{S}}\mathbf{U}^*)^*(\sqrt{\mathbf{S}}\mathbf{U}^*) = {\mathbf{E}_\eta}^*\mathbf{E}_\eta$. Let $\mathbf{E} = \begin{pmatrix} \mathbf{E_v} & 0 \\ 0 & \mathbf{E}_\eta \end{pmatrix}$, and $\hat{\mathbf{a}} = \begin{pmatrix} \hat{\mathbf{v}} \\ \hat{\boldsymbol{\eta}} \end{pmatrix}$, then

$$||\mathbf{q}(x_2, \boldsymbol{\zeta}(\omega))||_E^2 = ||\mathbf{E}\hat{\mathbf{a}}||_2^2, \quad (5.17)$$

from which it is clear that $\mathbf{E}$ is an energy weight matrix, which can be used to formulate the energy growth function,

$$\begin{aligned} G(t, \boldsymbol{\zeta}(\omega)) &= \sup_{\mathbf{q}(t=0,\boldsymbol{\zeta}(\omega))} \frac{\|\mathbf{q}(t, \boldsymbol{\zeta}(\omega))\|_E^2}{\|\mathbf{q}(t=0, \boldsymbol{\zeta}(\omega))\|_E^2} = \sup_{\hat{\mathbf{a}}(0)} \frac{\|\mathbf{E}\hat{\mathbf{a}}(t)\|_2^2}{\|\mathbf{E}\hat{\mathbf{a}}(0)\|_2^2} = \sup_{\mathbf{E}\hat{\mathbf{a}}(0)} \frac{||\mathbf{E}\exp(-i\hat{\boldsymbol{\Lambda}}t)\mathbf{E^{-1}}\mathbf{E}\hat{\mathbf{a}}(0)||_2^2}{||\mathbf{E}\hat{\mathbf{a}}(0)||_2^2} \\ &= ||\mathbf{E}\exp(-i\hat{\boldsymbol{\Lambda}}t)\mathbf{E}^{-1}||_2^2 = S_{max}^2(\mathbf{E}\exp(-i\hat{\boldsymbol{\Lambda}}t)\mathbf{E}^{-1}), \end{aligned}$$

where $S_{max}^2(\mathbf{E}\exp(-i\hat{\boldsymbol{\Lambda}}t)\mathbf{E}^{-1})$ is the square of the largest singular value of the matrix $\mathbf{E}\exp(-i\hat{\boldsymbol{\Lambda}}t)\mathbf{E}^{-1}$, and $\hat{\boldsymbol{\Lambda}} = \hat{\boldsymbol{\Lambda}}(\boldsymbol{\zeta}(\omega))$ is the WCE of the diagonal matrix with the k stochastic eigenvalues of largest imaginary part along the diagonal. By taking the WCE of the discretised operator $\mathbf{L_1}(\boldsymbol{\zeta}(\omega))$ and performing an eigen-decomposition we generate the matrix $\hat{\boldsymbol{\Lambda}}(\boldsymbol{\zeta}(\omega))$, which facilitates computation of the statistical moments of the energy growth function.

5.3.2 Stochastic Poiseuille and Couette Flow at a Moderate Correlation Length

Having set forth the mathematics of the problem, we proceed with numerical experiments. We first use 5000 MC simulations, adopting LHS to speed convergence, to compute the transient growth of both Poiseuille and Couette flows at a Reynolds number of 4000, with stochastic base flows parameterized with both

$\{\sigma = 0.02, c_l = 0.50\}$ and $\{\sigma = 0.0004, c_l = 0.10\}$. We pick wave-numbers $\{\alpha = 0.000, \beta = 2.040\}$ and $\left\{\alpha = \frac{35}{Re} \approx 0.009, \beta = 1.60\right\}$ for Poiseuille and Couette flow respectively. These wave-number pairs are known to produce the greatest transient growth in the deterministic case, and should hence provide interesting tests for the stochastic case. In addition, we investigate the effects of stochasticity on a plane Poiseuille flow at $\{\alpha = 1.02, \beta = 0.00\}$, corresponding to the perturbation which first becomes asymptotically unstable at the critical Reynolds number.

For simplicity, a constant Reynolds number, based upon the channel centre-line velocity, is assumed in all computations. However, the stochastic defects which we introduce will cause slight fluctuations in the centre-line velocity which in turn cause variations in the Reynolds number. We argue that these fluctuations are negligible and can safely be neglected. To this end, we record both the flux (integral of velocity across channel) and the Reynolds number for each of the 5000 stochastic base flow realisations. We find that the Reynolds number takes a value no greater than 4037 with a mean of 4000 and a standard deviation of around 10. The maximum deviation in Reynolds number is thus less than one percent and the standard deviation is around 0.25 percent. Furthermore, we find that the velocity flux takes values no greater than 1.341, with a mean of 1.33 (agreeing with the deterministic case) and a standard deviation less than 0.01. We therefore conclude that stochastic base flow variations have a negligible impact on both the flux and Reynolds number, and can therefore, for simplicity, be neglected in stochastic analysis.

At the correlation length of 0.50 we also compare the Monte Carlo results to those obtained via the WCE, accommodating terms up to order seven. Adopting a full tensor grid with four collocation points in each stochastic dimension, we require $4^4 = 256$ function evaluations to numerically integrate the chaos coefficients. In contrast, the computational expense of the low correlation length case is far greater. Using tensor grids, the WCE suffers from the curse of dimensionality, which LHS does not, where the number of function evaluations increases exponentially with the dimension of the stochastic space. For this reason, it would be infeasible to compute the WCE at the low correlation length of 0.10, where we require 12 stochastic dimensions to accurately build the auto-covariance. Recovery of the chaos coefficients would consequently require 4^{12} function evaluations. This is clearly impractical and we therefore adopt a sparse grid in favour of the traditional tensor approach.

Figure 5.7, below, shows the convergence, in mean and variance, of the LHS computations.

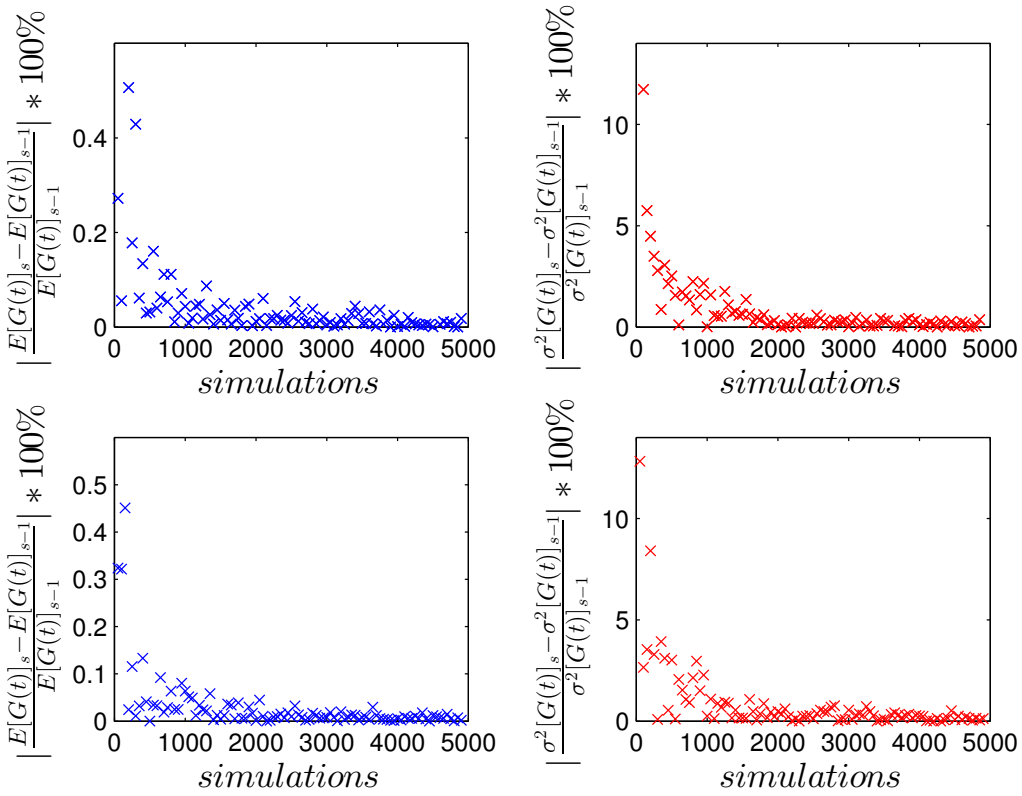

Figure 5.7: Convergence of LHS computations of $G(t, \boldsymbol{\zeta})$, convergence in mean (left) and variance (right). For input processes with $c_l = 0.50$ and $\sigma = 0.02$. Poiseuille flow (upper) at $Re = 4000$, $\alpha = 0.00$, $\beta = 2.04$. Couette flow (lower) at $Re = 4000$, $\alpha = 0.009$, $\beta = 1.60$.

The expectation after n simulations is computed by first computing the empirical average of the growth function over the n realisations, thus resulting in a time series, then taking the mean of this time series to acquire a scalar measure. A similar procedure is adopted for the variance. We plot the percentage difference every additional 50 simulations and, as depicted, convergence in mean occurs much more rapidly than that in variance. The Poiseuille and Couette flow appear to converge at a similar rate. As seen, a few hundred simulations are sufficient to achieve percentage differences of less than one percent for the mean. Conversely, it takes around 2000 simulations to achieve a similar convergence in variance. We are interested in both statistical moments and the variance is thus the limiting case.

Although a little superfluous, we adopt the full 5000 simulations in all cases, to ensure sufficient accuracy. Figure 5.8, below, compares the LHS and WCE results for the Poiseuille flow at the moderate correlation length, that is $c_l = 0.50$ and $\sigma = 0.02$.

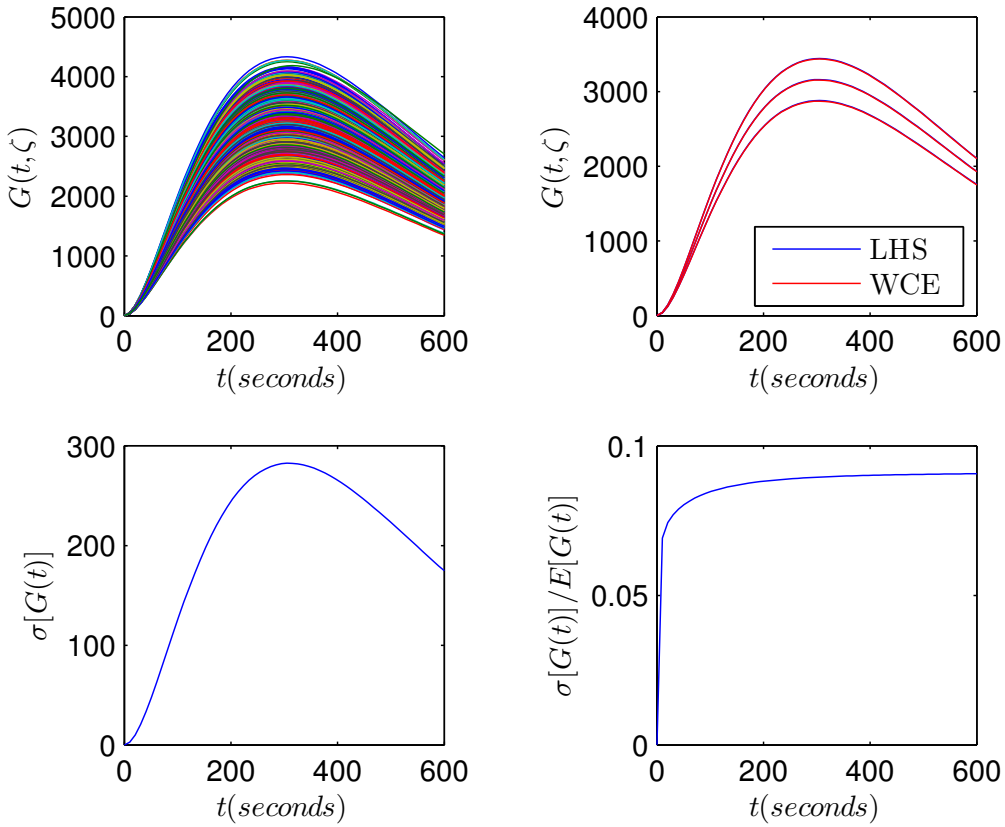

Figure 5.8: Transient growth of stochastic plane Poiseuille flow, $c_l = 0.50$, $\sigma = 0.02$, $Re = 4000$, $\alpha = 0.00$, $\beta = 2.04$, 5000 Monte Carlo simulations of $G(t, \boldsymbol{\zeta})$ (top left), $E[G(t, \boldsymbol{\zeta})] \pm \sigma[G(t, \boldsymbol{\zeta})]$ (top right), $\sigma[G(t, \boldsymbol{\zeta})]$ (bottom left), $\sigma[G(t, \boldsymbol{\zeta})]/E[G(t, \boldsymbol{\zeta})]$ (bottom right).

The upper left sub-plot indicates the 5000 LHS realisations of the growth function, and the right sub-plot depicts the mean plus or minus one standard deviation, computed via LHS (blue) and WCE (red). The results are seen to agree very well with curves overlapping. Requiring only 625 function evaluations to reproduce the LHS result with a stochastic dimension of four, we see the superior efficiency of the WCE in low stochastic dimensions. However, owing to the curse of dimensionality, this efficiency decays rapidly. The lower left sub-plot depicts the standard deviation, and the lower right normalises this by the mean. Whilst there is considerable variability in transient growth, all realisations decay asymptotically and thus remain stable, in a modal sense. Furthermore, the variability is seen to grow with time in a similar fashion to the mean. In fact, all transient growth realisations are identical (zero variance) at small times, the variability then grows rapidly to reach a constant ratio with the mean of about 0.08. It would therefore seem that stochasticity is not that influential in this case, the standard deviation remains small and the mean, or

deterministic part, is the most significant.

Turning attention to the Couette flow and considering the same stochastic parameters, $c_l = 0.50$ and $\sigma = 0.02$, figure 5.9 illustrate a similar situation.

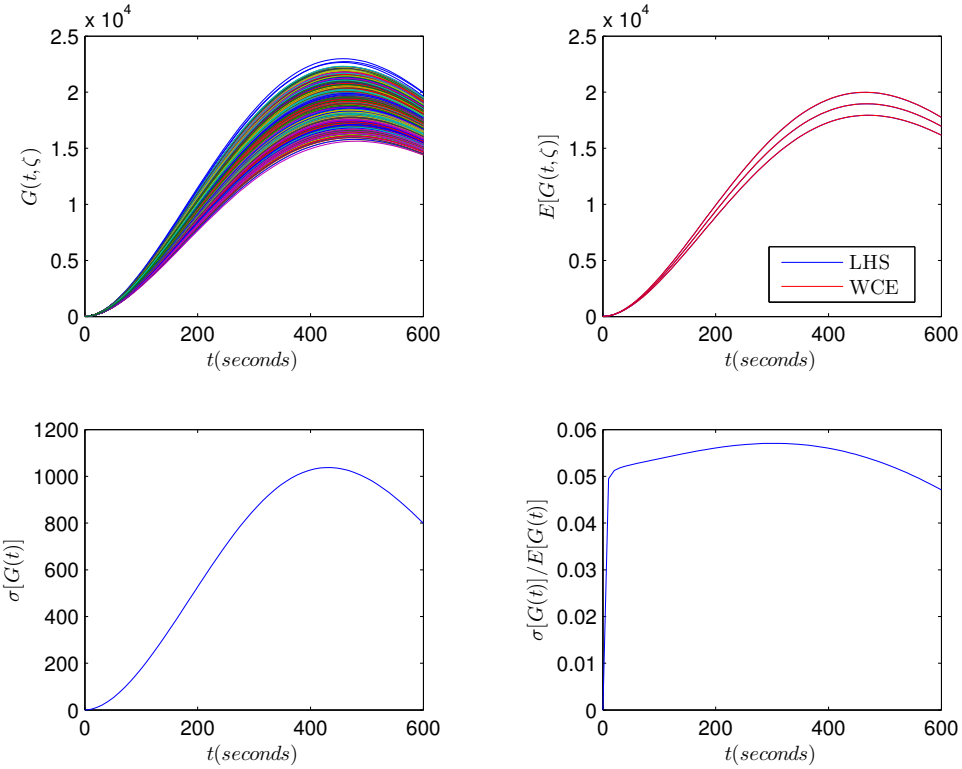

Figure 5.9: Transient growth of stochastic plane Couette flow, $c_l = 0.50$, $\sigma = 0.02$, $Re = 4000$, $\alpha = 0.009$, $\beta = 1.60$, 5000 Monte Carlo simulations of $G(t, \boldsymbol{\zeta})$ (top left), $E[G(t, \boldsymbol{\zeta})] \pm \sigma[G(t, \boldsymbol{\zeta})]$ (top right), $\sigma[G(t, \boldsymbol{\zeta})]$ (bottom left), $\sigma[G(t, \boldsymbol{\zeta})]/E[G(t, \boldsymbol{\zeta})]$ (bottom right).

Again, all realisations are asymptotically stable (decaying), and the standard deviation remains small in comparison to the mean. Whilst significant transient growth is clearly observed, stochasticity does not contribute much at these wave numbers, $\alpha \approx 0$. For this reason, we investigate the Poiseuille flow at the wave-number pair $\{\alpha = 1.02, \beta = 0.00\}$. At the critical Reynolds number of 5772, this is the first wave to transition. We conduct experiments at $Re = 4000$, $c_l = 0.50$ and $\sigma = 0.02$, adopt the WCE and plot the results in figure 5.10

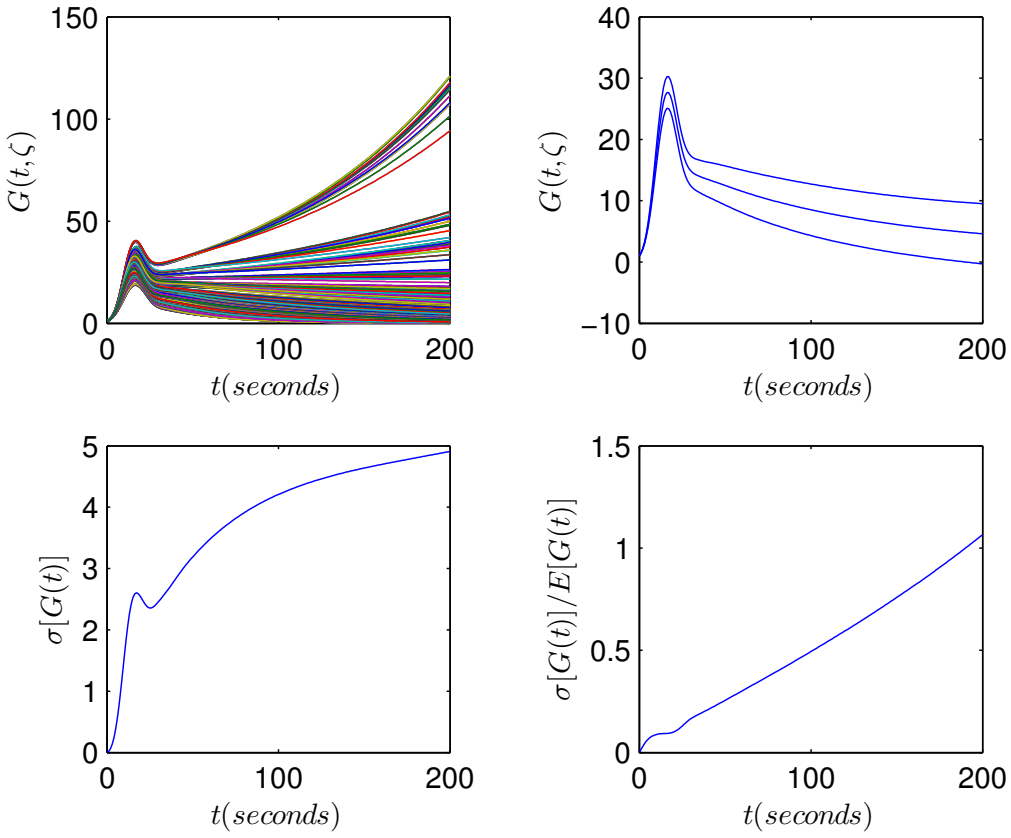

Figure 5.10: Transient growth of stochastic plane Poiseuille flow, $c_l = 0.50$, $\sigma = 0.02$, $Re = 4000$, $\alpha = 1.02$, $\beta = 0.00$, 625 WCE realisations of $G(t, \boldsymbol{\zeta})$ (top left), $E[G(t, \boldsymbol{\zeta})] \pm \sigma[G(t, \boldsymbol{\zeta})]$ (top right), $\sigma[G(t, \boldsymbol{\zeta})]$ (bottom left), $\sigma[G(t, \boldsymbol{\zeta})]/E[G(t, \boldsymbol{\zeta})]$ (bottom right).

From a physical perspective, the results for this case are far more interesting. The top left sub-plot shows the growth function for each of the 625 simulations used to integrate the chaos coefficients, and indicates that whilst transient behaviour is qualitatively the same for all base flows at early times, differences become apparent at larger times, where, under some realisations of the base flow, asymptotic instability occurs.

The top right sub-plot depicts the mean energy amplification, plus or minus one standard deviation, and the bottom sub-plots illustrates the evolution of standard deviation. The standard deviation is shown to grow linearly with respect to the mean result, and given sufficient time can actually grow larger than the mean component. As time passes, stochasticity becomes increasingly important and small defects can have fundamental effects on solutions. This was, conversely, not the case for waves with $\alpha \approx 0.0$ (long stream-wise waves), and it therefore seems that defects have a greater effect on the shorter stream-wise waves.

Investigating the physical significance further, we compute the stochastic spectral abscissa, $\chi(\mathbf{L_1^*}(\boldsymbol{\zeta})) = \sup_{\lambda \in \Lambda(\mathbf{L_1^*}(\boldsymbol{\zeta}))} \Re(\lambda)$, and the stochastic numerical abscissa, $\psi(\mathbf{L_1^*}(\boldsymbol{\zeta})) = \sup_{z \in W(\mathbf{L_1^*}(\boldsymbol{\zeta}))} \Re(z)$, where $W(\mathbf{L_1^*}(\boldsymbol{\zeta})) = \left\{\mathbf{x}^* \mathbf{L_1^*}(\boldsymbol{\zeta})\mathbf{x} : \mathbf{x} \in \mathbb{C}^N, ||\mathbf{x}|| = 1\right\}$ is the numerical range of $\mathbf{L_1^*}(\boldsymbol{\zeta})$. Using the WCE, we find that the spectral abscissa has a mean of -0.005 and a standard deviation of 0.001, whilst the numerical abscissa takes values of 0.664 and 0.028, for the mean and standard deviation respectively. The mean values are in excellent agreement with deterministic results at the same flow conditions, for which we find a spectral abscissa of -0.005 and a numerical abscissa of 0.662. Furthermore, the standard deviation of the spectral abscissa is in clear agreement with the above figure. As previously stated, $\frac{d}{dt}||exp\left\{t\mathbf{L_1^*}(\boldsymbol{\zeta})\right\}||_{|t=0} = \lim_{t \downarrow 0} t^{-1} log||exp\left\{t\mathbf{L_1^*}(\boldsymbol{\zeta})\right\}|| = \psi(\mathbf{L_1^*}(\boldsymbol{\zeta}))$, and the spectral abscissa is thus the initial slope of the growth function. If one observes the stochastic realisations, above, it is evident that they all have the same initial slope and it therefore follows that the standard deviation of the numerical abscissa be approximately zero, as is the case. Clearly, stochasticity has no initial impact, but its significance increases with time. It can also be shown that the spectral and numerical abscissa bound the perturbation energy growth,

$$\exp\left\{t\chi(\mathbf{L_1^*}(\boldsymbol{\zeta}))\right\} \leq ||\exp\left\{t\mathbf{L_1^*}(\boldsymbol{\zeta})\right\}|| \leq \exp\left\{t\psi(\mathbf{L_1^*}(\boldsymbol{\zeta}))\right\}, \tag{5.18}$$

which implies that stochastic defects have very little impact on the lower bound, yet can significantly alter the upper bound, especially at large times. In order to further inspect those realisations which exhibit asymptotic growth, we plot the maximum asymptotic growth rate of each of the 625 realisations used in computing the chaos coefficients. The results are presented below, in figure 5.11, where we plot the realisations on the spectrum and highlight those exhibiting instability in red.

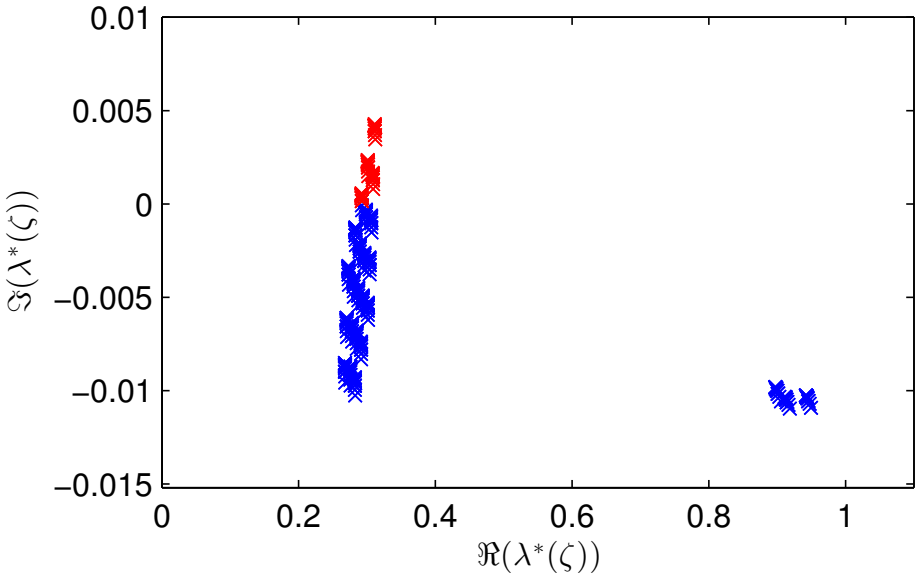

Figure 5.11: Fastest growing perturbations of 625 WCE realisations of plane Poiseuille flow, $c_l = 0.50$, $\sigma = 0.02$, $Re = 4000$, $\alpha = 1.02$, $\beta = 0.00$.

And we plot the corresponding modes, in wall normal velocity-vorticity form, in figure 5.12:

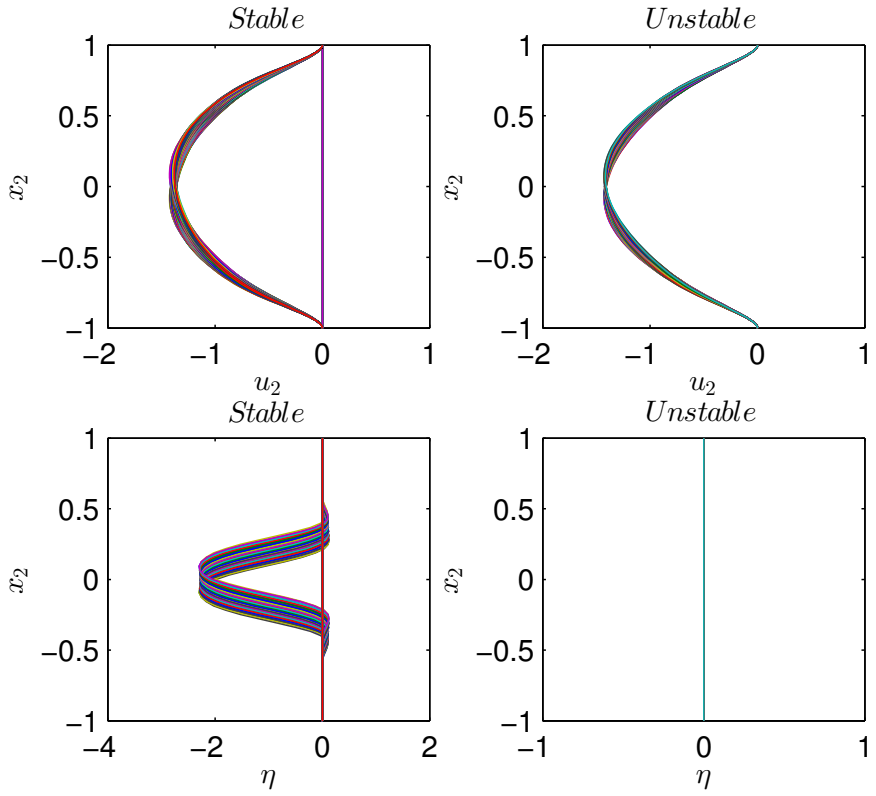

Figure 5.12: Fastest growing perturbations, wall normal velocity-vorticity modes of 625 WCE realisations of plane Poiseuille flow, $c_l = 0.50$, $\sigma = 0.02$, $Re = 4000$, $\alpha = 1.02$, $\beta = 0.00$.

Clearly, it is the Orr-Sommerfeld modes which are unstable. That is, the wall normal velocity. Further, the unstable modes are characteristic wall modes, with large variations in the vicinity of the solid boundaries.

5.3.2.1 Variance Based Sensitivity Analysis

The WCE lends itself nicely to variance analysis, which LHS does not. That is, we can use the WCE to decompose the variance of the output process amongst the random input sources, or KLE modes in this case. We recall, from chapter two, that the variance based sensitivity indices can be computed directly from the WCE coefficients, and we use the formula outlined earlier to decompose the variance.

If we consider a simplified formulation of the stochastic perturbation energy amplification WCE,

$$G(t, \boldsymbol{\zeta}(\omega)) = \sum_{\boldsymbol{\alpha_i} \in I_O} g_{\alpha^i}(t) H_{\alpha^i}(\boldsymbol{\zeta}(\omega)) = \sum_{i=0}^{N} g_{\alpha^i}(t) H_{\alpha^i}(\boldsymbol{\zeta}(\omega)), \tag{5.19}$$

where the chaos coefficients are explicitly functions of time, $g_{\alpha^i}(t)$, we may then proceed to compute the total sensitivity index,

$$S_i^{tot}(t) = \frac{\sum_{k\in\left\{1,\ldots,N;\alpha_i^k>0\right\}} g^2_{\alpha^k}(t)}{\sum_{k=1}^{N} g^2_{\alpha^k}(t)}, \forall i \in \{1,2,...,d\}\,, \tag{5.20}$$

and the first order sensitivity index,

$$S_i(t) = \frac{\sum_{k\in\left\{1,\ldots,N;\alpha_i^k>0,\alpha_j^k=0\forall j\neq i\right\}} g^2_{\alpha^k}(t)}{\sum_{k=1}^{N} g^2_{\alpha^k}(t)}, \forall i \in \{1,2,...,d\}\,. \tag{5.21}$$

We recall that the first order variance based sensitivity indices measure the sole contribution of the ith stochastic variable, $\zeta_i(\omega)$, to the variance of the output process. The second order variance based sensitivity indices measure the contribution of the interaction of stochastic input variables to the variance of the output process, and the total variance based sensitivity indices measure the total contribution of an input to the output variance.

We would ideally like a scalar measure of sensitivity, and we therefore take the average of the time series indices, that is average in time. The time averaged indices are depicted below in figure 5.13.

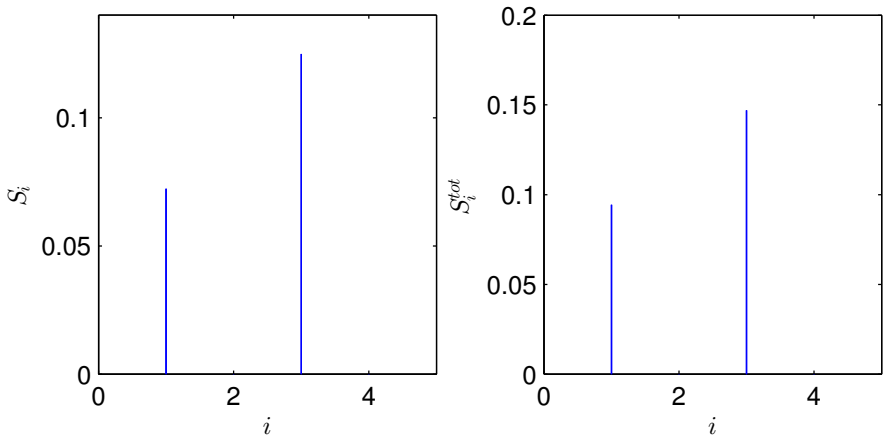

Figure 5.13: Total (left) and first order (right) variance based sensitivity indices, for $G(t,\boldsymbol{\zeta})$, stochastic Poiseuille flow, $c_l = 0.50$, $\sigma = 0.02$, $Re = 4000$, $\alpha = 1.02$, $\beta = 0.00$.

Clearly, stochastic inputs of odd mode number contribute significantly more to the output variance than even modes (which are small but non-zero). Further, if one inspects the KLE decomposition of the 625 base flows used in the WCE, one finds no general pattern in the realisations of $\zeta_i(\omega)$ in the stable cases, whilst $\zeta_1(\omega)$ is strictly positive and $\zeta_3(\omega)$ strictly negative in all unstable realisations. We plot

the actual stochastic modes, $\sqrt{\gamma_i}\sigma(x_2)e_i(x_2)$, and their ensuing curvatures below, in figure 5.14.

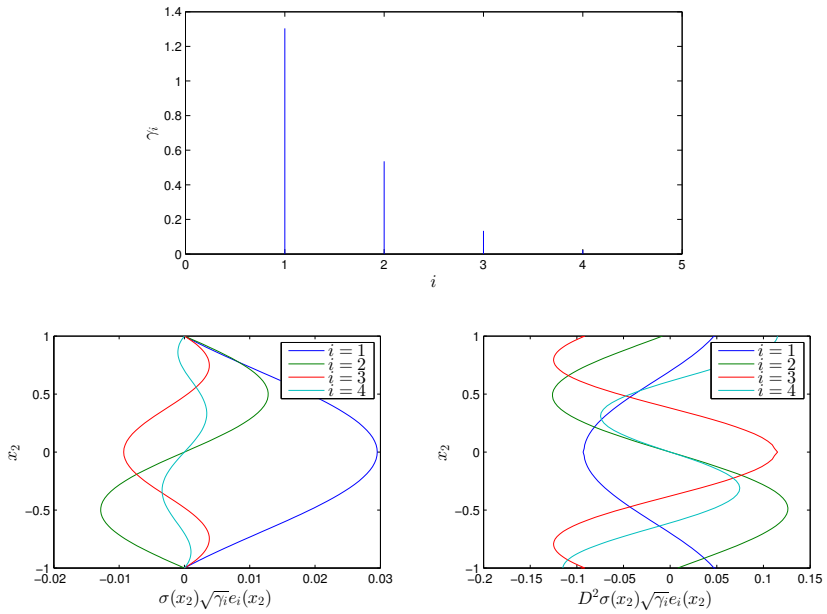

Figure 5.14: Stochastic KLE Inputs. Eigenvalues (top), eigenvectors (left) and curvature of eigenvectors (right).

We see that the odd modes are symmetrical about the channel centre, and modify the centre-line velocity. Furthermore, mode one acts to increase the centre-line velocity whilst mode three acts to decrease it. Strictly positive and negative realisations of random variable one and three would suggest an increase in the centre-line velocity, in the asymptotically unstable cases.

It would also seem plausible to expect the first order variance based sensitivity indices to be proportional to the number of inflection points in the stochastic mode. We entertain such ideas by inspecting the curvatures, $D^2\left\{\sqrt{\gamma_i}\sigma(x_2)e_i(x_2)\right\}$. Noting that an inflection point is simply a change in curvature sign, we see that there is no obvious pattern between the number of inflection points and the stochastic mode number. We might expect the first order variance based sensitivity indices to increase with the number of modal inflection points, but no such relationship is observed. In fact, if one notes the small amplitude of the KLE curvatures and also notes that a deterministic plane Poiseuille has a constant curvature of -2, then it is clear that only a very large random realisation of a $\zeta_i(\omega)$ would be sufficient to induce an inflection point in the net flow. For instance, even if we consider the largest KLE mode, mode one, then we would only observe a net inflectional flow if $|\zeta_1(\omega)| >$

20, which is extremely improbable. To be more specific, we actually adopted a tensor grid $\boldsymbol{\zeta} \in [-3, 3]^d$ for numerical computation of the chaos coefficients, and can therefore most certainly rule out instabilities of an inflectional nature.

One may also expect the output variability attributed to a given mode to be proportional to the variability in the input attributed to that same mode. To test this hypothesis, we plot the input variance attributed to each stochastic KLE input below, which is simply its eigenvalue, γ_i (see the upper subplot of figure 5.14). The attributed input variance is seen to decay with mode number whilst the output variance attributed to each mode showed no such relationship. Oddly, there does not appear to be a significant relationship between the magnitude of input and output variance attributed to a given KLE mode. In fact, there seems to be no correlation between the two.

The above analysis suggests that it is neither the number of inflection points in a mode, nor the size of that mode that determines the first order variance based sensitivity indices, but the symmetry of a mode. The modal shape appears to determine the relative contribution of a mode to the total output variance. Further, it is the odd modes, exhibiting a symmetry about the channel centre-line, which contribute most. The deterministic Poiseuille profile is itself symmetric about the channel centre-line, and these symmetric stochastic defects are thus ones which preserve symmetry. Furthermore, all symmetric modes modify the centre-line velocity. In contrast, the anti-symmetric modes have no impact at the centre of the channel and act to break the symmetry of the net flow. Clearly, the modification of the centre-line velocity modifies the Reynolds number, but as previously explained this modification is relatively small such that a deterministic Poiseuille flow at such modified Reynolds numbers are asymptotically stable.

5.3.2.2 Optimal Stochastic Defect

In this section, we seek to determine the stochastic defect which causes the greatest deviation from the deterministic growth function. We formulate this problem as a constrained optimisation. To this end, we seek the stochastic coefficients in the KLE which maximise the root mean squared deviation between the stochastic and deterministic growth functions, where the mean is computed across the time series, that is

$$\boldsymbol{\zeta}^* = argmin_{\boldsymbol{\zeta}} \left\{ -\frac{1}{n_T} \sum_{j=1}^{n_T} (G(t_j, 0) - G(t_j, \boldsymbol{\zeta}))^2 \right\}$$
$$\forall \zeta_i \in [-3, 3], i = 1, 2, ...d,$$

where we have discretised the time domain with n_T points and we have confined the stochastic search space to the hypercube $[-3, 3]^d$, which is a justified simplification since the random variables are Gaussian and therefore fall, with 99% probability, within three standard deviations of their zero mean. It is also worth noting that we negate the objective function and seek a minimum, which is equivalent to the maximum of the non-negated objective function which we seek. We solve the problem with the simplex method. We conduct three optimisations, one in which we constrain odd KLE coefficients to zero, one in which we constrain the even coefficients to zero and one in which we allow both odd and even coefficients to take non zero values. The optimal stochastic coefficients, growth function and KLE are plotted below in figure 5.15.

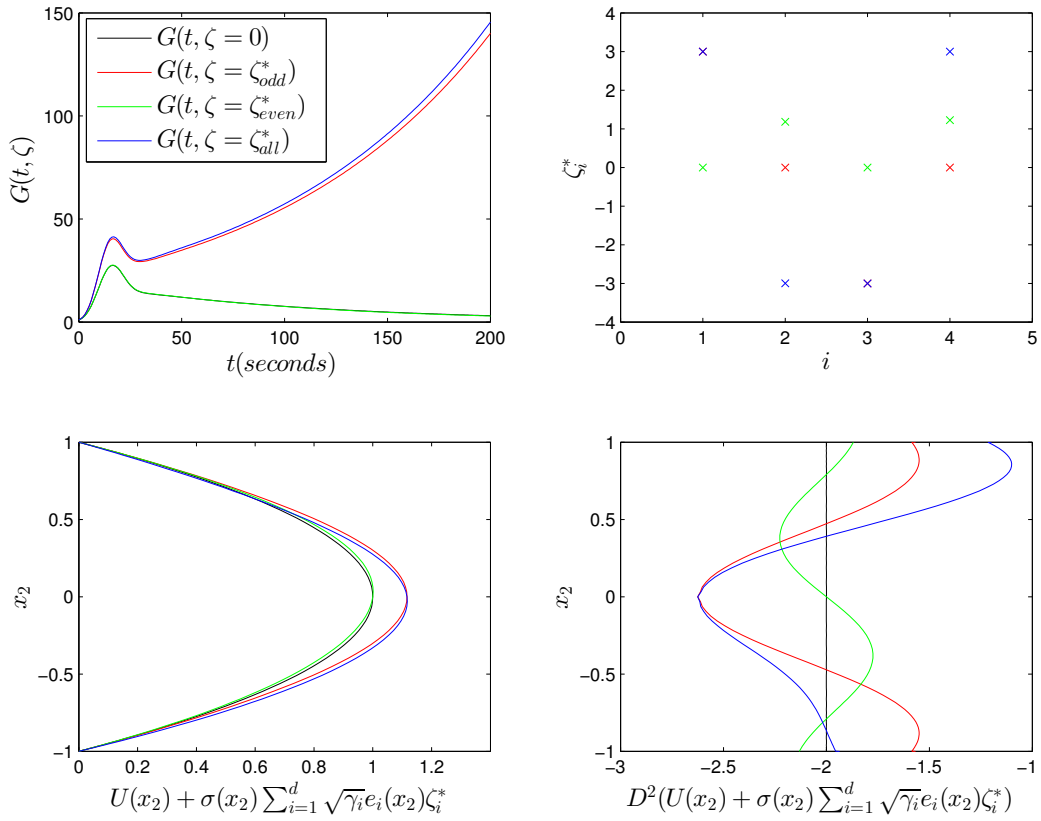

Figure 5.15: Optimal stochastic perturbation energy growth function (top left), optimal stochastic KLE coefficients (top right), optimal stochastic base flow (bottom left) and curvatures (bottom right), stochastic Poiseuille flow (bottom right), for $G(t,\boldsymbol{\zeta})$, $c_l = 0.50$, $\sigma = 0.02$, $Re = 4000$, $\alpha = 1.02$, $\beta = 0.00$.

As can be seen, the optimal even-only stochastic defect has negligible impact, which is evident from the upper left sub-plot of growth functions where the deterministic ($G(t,\boldsymbol{\zeta}=0)$) and optimal even ($G(t,\boldsymbol{\zeta}=\boldsymbol{\zeta}^*_{even})$) growth functions overlap. Conversely, the odd (or symmetric) stochastic defects can cause significant transient growth. In fact, optimising over both odd and even stochastic modes is almost synonymous with optimising over odd only. This is clearly consistent with the variance based sensitivity indices, which suggested that it was only the odd modes which effected perturbation energy amplification. In addition, we see that random variable one takes the maximum possible positive value of 3 whilst random variable three takes -3. Again, this observation is consistent with previous analyses which suggested that defects that increased the channel centre-line velocity where most detrimental. Even considering this optimised (highly improbable) flow, the channel centre-line velocity is not augmented by more than about 10%, which in turn im-

plies a Reynolds number of no more than 4400, for which a deterministic Poiseuille flow is certainly stable.

Inspecting curvatures (bottom right sub-plot of figure 5.15), it is clear that instabilities cannot be of an inflectional nature. The curvatures are strictly negative and do not change sign at any point across the channel. The superposition of an optimised defect is thus unable to cause a change in curvature sign, and the net profiles are inflexionless. It is thus clear that any instability created by stochasticity is not inflectional in origin but due to viscous effects.

5.3.2.3 Reynolds-Orr Analysis

In what follows, we investigate how stochasticity impacts the transfer of energy between the base flow and the perturbations. We therefore turn our attention to the Reynolds-Orr equation, firstly consider the non-linear evolution equation,

$$\frac{\partial u_i}{\partial t} = -U_j \frac{\partial u_i}{\partial x_j} - u_j \frac{\partial U_i}{\partial x_j} - \frac{\partial p}{\partial x_i} + \frac{1}{Re}\frac{\partial^2}{\partial x_j^2} u_i - u_j \frac{\partial u_i}{\partial x_j}. \tag{5.22}$$

Multiplying by the perturbation velocity, u_i, noting that $u_i \frac{\partial^2}{\partial x_j^2} u_i = \frac{\partial}{\partial x_j} u_i \frac{\partial u_i}{\partial x_j} - \frac{\partial u_i}{\partial x_j}\frac{\partial u_i}{\partial x_j}$, and integrating over volume V, we have

$$\frac{\partial}{\partial t}\int_V \frac{1}{2} u_i u_i dV = -\int_V \frac{\partial U_i}{\partial x_j} u_i u_j dV - \frac{1}{Re}\int_V \frac{\partial u_i}{\partial x_j}\frac{\partial u_i}{\partial x_j} dV - \int_V \frac{\partial u_i}{\partial x_j} U_j u_i + \frac{\partial u_i}{\partial x_j} u_j u_i - \frac{1}{Re}\frac{\partial}{\partial x_j}\frac{\partial u_i}{\partial x_j} u_i dV. \tag{5.23}$$

Further, one may re-write the last integral as

$$\int_V \frac{\partial u_i}{\partial x_j} U_j u_i + \frac{\partial u_i}{\partial x_j} u_j u_i - \frac{1}{Re}\frac{\partial}{\partial x_j}\frac{\partial u_i}{\partial x_j} u_i dV = \int_V \frac{\partial}{\partial x_j}\frac{1}{2} u_i u_i U_j - \frac{1}{2} u_i u_i \frac{\partial}{\partial x_j} U_j + \frac{\partial}{\partial x_j}\frac{1}{2} u_i u_i u_j - \frac{1}{2} u_i u_i \frac{\partial}{\partial x_j} u_j - \frac{1}{Re}\frac{\partial}{\partial x_j} u_i \frac{\partial u_i}{\partial x_j} dV,$$

where each term is clearly of the form $\int_V \frac{\partial}{\partial x_i} f_i dV$, which according to the divergence theorem is equivalent to a surface integral,

$$\int_V \frac{\partial f_i}{\partial x_i} dV = \int_{x_i}\int_{x_j}\int_{x_k} \frac{\partial f_i}{\partial x_i} |\frac{\epsilon_{ijk}}{2}| dx_i dx_j dx_k = \int_{x_j}\int_{x_k} f_i |\frac{\epsilon_{ijk}}{2}| dx_j dx_k. \tag{5.24}$$

However, all perturbations are zero at solid boundaries, hence surface terms f_i vanish at the boundaries and we are simply left with

$$\frac{\partial}{\partial t}\int_V \frac{1}{2}u_i u_i dV = -\int_V \frac{\partial U_i}{\partial x_j}u_i u_j dV - \frac{1}{Re}\int_V \frac{\partial u_i}{\partial x_j}\frac{\partial u_i}{\partial x_j}dV, \tag{5.25}$$

which we simplify further, for the case of 2D perturbations, $U = (U(x_2), 0)$, $u = (u_1(x_2), u_2(x_2))exp(i\alpha x_1)exp((\Im(\lambda) - i\Re(\lambda))t)$. Substituting these parameters, integrating over a single stream-wise wave length, cancelling and taking the time derivative, we have

$$\Im(\lambda)\int_{-1}^{1} u_1^2(x_2) + u_2^2(x_2)dx_2 = -\int_{-1}^{1} U'(x_2)u_1(x_2)u_2(x_2)dx_2$$
$$-\frac{1}{Re}\int_{-1}^{1} u_1'^2(x_2) + u_2'^2(x_2) + \alpha^2 u_1^2(x_2) + \alpha^2 u_2^2(x_2)dx_2.$$

The term on the left hand side is the rate of perturbation energy growth, the integral is strictly positive, and we see that asymptotic growth occurs when the the wave number, λ, has positive imaginary part (which is consistent with spectral analysis). The first term on the right describes the transfer of energy between the base flow and the perturbations, and can be positive or negative. The last term describes the dissipation of perturbation energy, and is non positive.

Considering the optimised stochastic base flow of the previous sub-section, that is $\{\zeta_1(\omega) = 3, \zeta_2(\omega) = 0, \zeta_3(\omega) = -3, \zeta_4(\omega) = 0\}$, and using the Reynolds-Orr formulation, we further investigate the impact of stochasticity. Firstly, we plot the fastest growing mode, as shown below in figure 5.16.

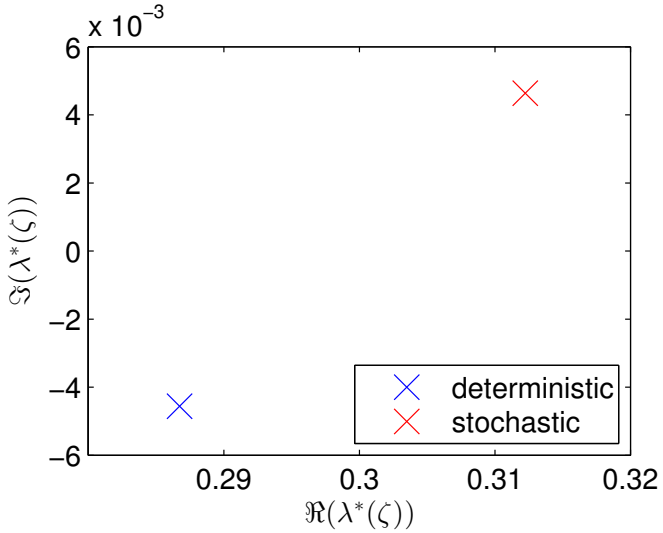

Figure 5.16: Spectrum of fastest growing stochastic mode (red) and deterministic mode (blue), for plane Poiseuille flow, at $c_l = 0.50$, $\sigma = 0.02$, $Re = 4000$, $\alpha = 1.02$, $\beta = 0.00$.

As expected, the fastest growing deterministic mode has negative imaginary part and is thus asymptotically stable. Conversely, the fastest growing stochastic mode is asymptotically unstable, with positive imaginary part. This is all consistent with the transient analyses we have considered.

To understand the origin of these observations, we plot the parameters in the Reynolds-Orr formulation, namely the velocities, the velocity gradients and the actual energy terms. Again, blue is representative of the deterministic case and red the optimised stochastic flow. Below, figure 5.17 depicts the results.

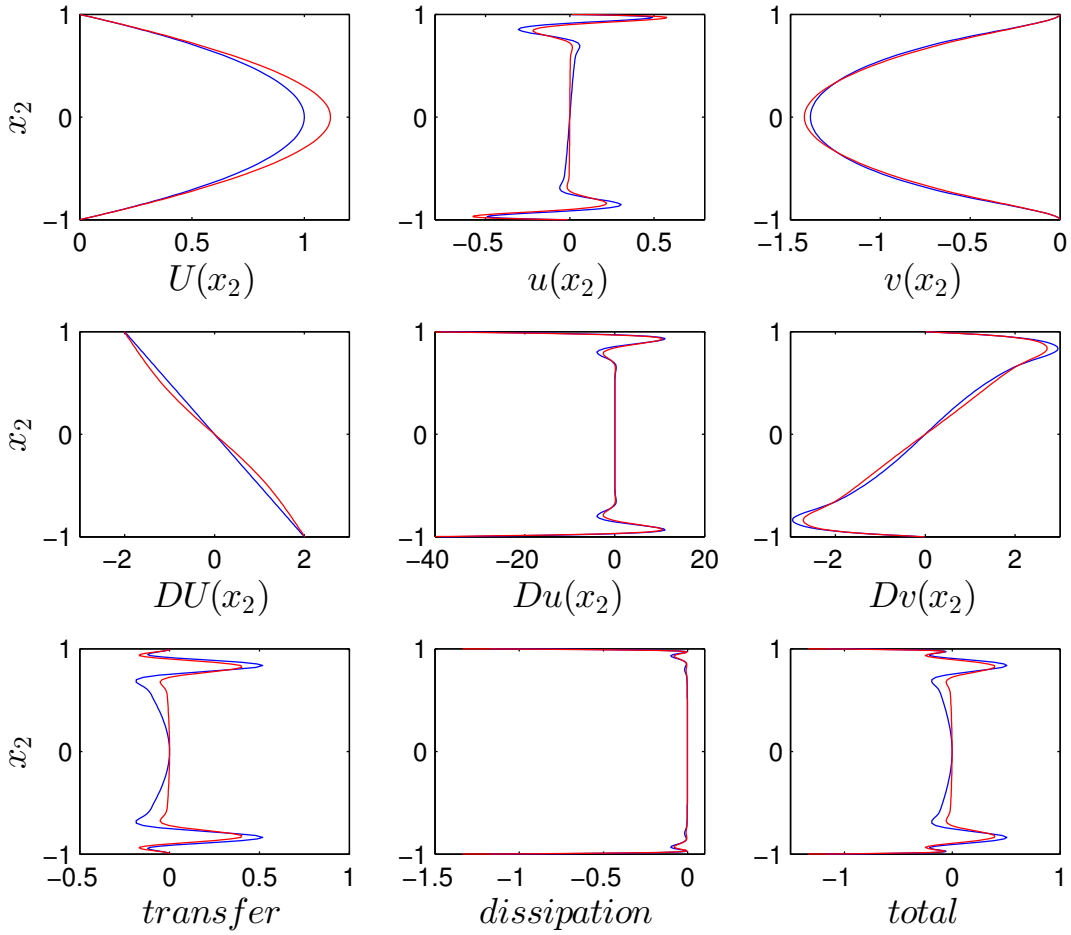

Figure 5.17: Comparison of fastest growing stochastic mode (red) and deterministic mode (blue), via the Reynolds-Orr Equation, for plane Poiseuille flow, at $c_l = 0.50$, $\sigma = 0.02$, $Re = 4000$, $\alpha = 1.02$, $\beta = 0.00$. Base flow and perturbations (top row), first derivative of base flow and perturbations (middle row), and terms in the Reynolds-Orr formulation (bottom row).

As seen, stochasticity increases the base flow, augmenting the centre-line velocity

by about 10%, which corresponds to a modified Reynolds number of around 4400 (which in the deterministic case would be stable up to 5772). Furthermore, stochasticity is seen to increase the gradient of the base flow, which in turn results in an increase in the transfer of energy between the base flow and the perturbations. The perturbations seem to change very little, with a slight increase in shearing in the immediate vicinity of the wall and a slight decrease a little further away, resulting in slight increases and decreases in dissipation respectively. The end result is a clear increase in the transfer of energy to the perturbed flow, and little change in dissipation. To visualise this more clearly, we plot the energy term differences in figure 5.18, that is the stochastic energy terms less the deterministic.

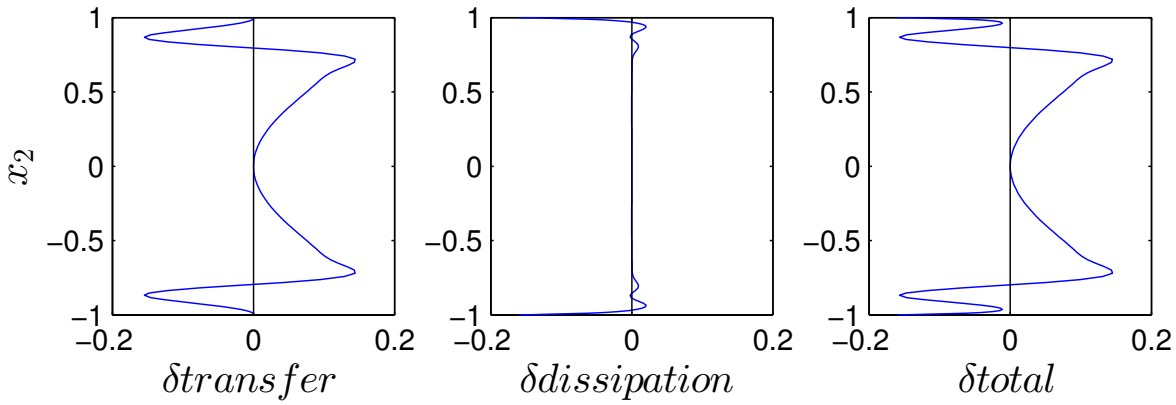

Figure 5.18: Comparison of fastest growing stochastic mode (red) and deterministic mode (blue), via the Reynolds-Orr Equation, for plane Poiseuille flow, at $c_l = 0.50$, $\sigma = 0.02$, $Re = 4000$, $\alpha = 1.02$, $\beta = 0.00$. Differences (stochastic minus deterministic) in the terms in the Reynolds-Orr formulation.

Clearly, stochasticity has had little impact on the dissipation of perturbation energy and a much stronger effect on energy transfer. We argue that it is not the increased magnitude of the base flow centre-line velocity, or equivalently the Reynolds number, that causes the stable flow to transition to an unstable one, but the increased velocity gradient. After all, it is the velocity gradient which is present in the Reynolds-Orr formulation, not the base flow itself. By stretching the centre-line velocity, we implicitly increase the velocity gradient, which in turn allows more transfer of energy from the base flow to the perturbations. If one integrates and sums the dissipation and transfer terms, then one finds negative and positive values for the deterministic and stochastic cases respectively, indicating that the stochasticity has indeed transformed the asymptotically stable flow into an unstable one, as eigenvalue analysis had previously suggested. However, the benefit of this energy

analysis is that we can observe the effects of the terms in the equations and thus postulate an explanation for the origin of this transition.

With this insight, it is interesting to go back and evaluate the impact of the even (anti-symmetric) stochastic modes via the Reynolds-Orr formulation. To this end, we consider the same problem with stochastic base flow, described with random variables $\{\zeta_1(\omega) = 0, \zeta_2(\omega) = 3, \zeta_3(\omega) = 0, \zeta_4(\omega) = 3\}$, and produce the same set of plots. Figure 5.19 depicts the perturbations, their derivatives and terms in the Reynolds-Orr formulation, and figure 5.20 depicts the difference (between deterministic and stochastic) in the Reynolds-Orr energy terms.

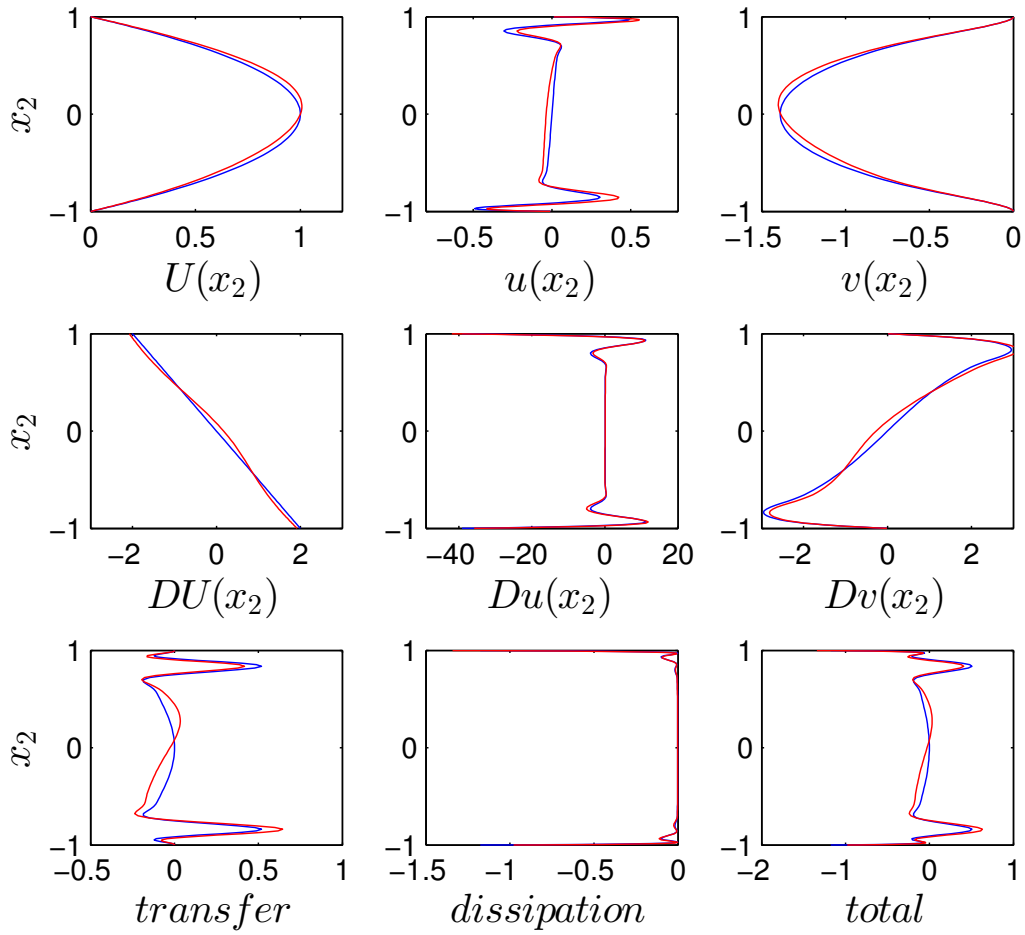

Figure 5.19: Comparison of even growing stochastic mode (red) and deterministic mode (blue), via the Reynolds-Orr Equation, for plane Poiseuille flow, at $c_l = 0.50$, $\sigma = 0.02$, $Re = 4000$, $\alpha = 1.02$, $\beta = 0.00$. Base flow and perturbations (top row), first derivative of base flow and perturbations (middle row), and terms in the Reynolds-Orr formulation (bottom row).

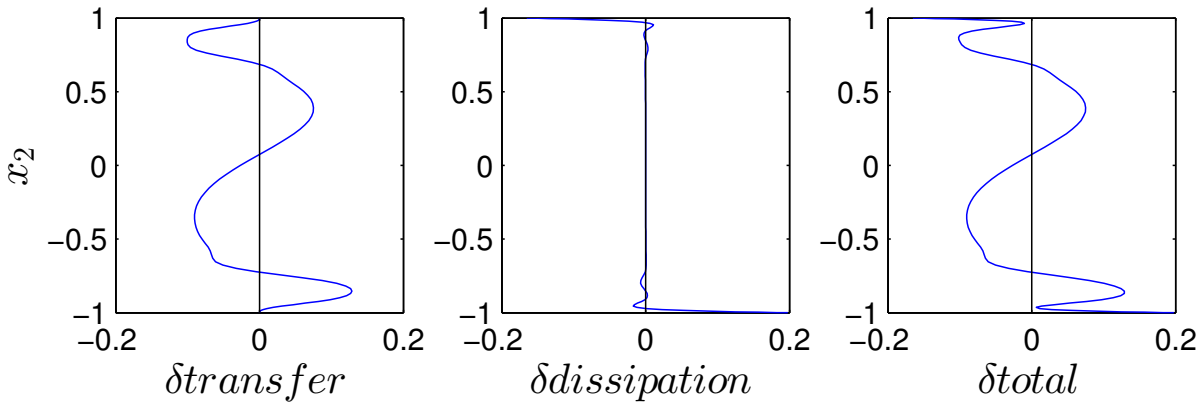

Figure 5.20: Comparison of even stochastic mode (red) and deterministic mode (blue), via the Reynolds-Orr Equation, for plane Poiseuille flow, at $c_l = 0.50$, $\sigma = 0.02$, $Re = 4000$, $\alpha = 1.02$, $\beta = 0.00$. Differences (stochastic minus deterministic) in the terms in the Reynolds-Orr formulation.

From these plots it is now very clear why the even modes do not impact stability. They are anti-symmetric about the channel centre-line and therefore have anti-symmetric effects on the base flow and its gradient. We know, from the previous analysis, that it is the gradient of the base flow that impacts the transfer of energy to the perturbations, and, furthermore, it is the transfer term which dominates the total change in perturbation energy. Since the changes to the gradient are now in opposition about the channel centre-line, we see that the increase in transfer in one region of the channel is cancelled out by a decrease in the other, giving little to no net impact.

5.3.2.4 Critical Reynolds Number

We extend the analysis of the previous section, by seeking the critical Reynolds number. That is, for a given set of stochastic parameters, we aim to find the lowest Reynolds number at which at least one mode has a growth rate of zero. We fix the correlation length at $c_l = 0.5$ and seek the critical Reynolds number of the stochastic Poiseuille flow, at $\alpha = 1.02$ and $\beta = 0.00$, for input standard deviations $\sigma = 0.000, 0.010, ..., 0.050$. As the input standard deviation does not change the shape of the flow, only its size, we retain the same four optimised stochastic variables used previously, $\{\zeta_1(\omega) = 3, \zeta_2(\omega) = 0, \zeta_3(\omega) = -3, \zeta_4(\omega) = 0\}$. For each of the base flows, we use interval reduction to find the Reynolds number with an asymptotic growth of zero. This is the critical Reynolds number assuming that stochasticity does not modify the centre-line velocity, which it obviously does. We therefore

correct the Reynolds number, scaling it up by multiplying by the channel centre-line velocity, and then scaling the base flow down (uniformly) such that it has a velocity of unity at the centre-line. We finally check that this modified flow, at the corrected critical Reynolds number, has an asymptotic growth rate of zero, which it does. Below, in figure 5.21, we plot the resulting base flows.

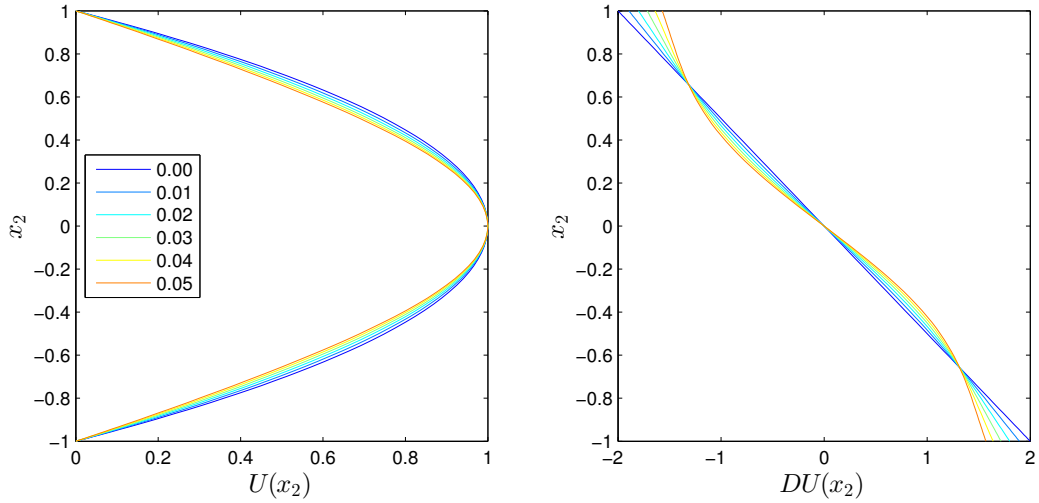

Figure 5.21: Optimised base flows (left) and gradients (right), for varying input standard deviations, $\sigma = 0.00, 0.01, 0.02, 0.03, 0.04$ and 0.05 from right to left, for plane Poiseuille flow, at $c_l = 0.50$, $\alpha = 1.02$, $\beta = 0.00$.

As can be seen, all flows have a maximum velocity of unity (by construction), and a very similar shape. As the input standard deviation is increased, the flux of the flows is observed to gradually decreases with steeper gradients in the middle half of the channel, and slightly lower in the upper and lower quarters. We know, from the Reynolds-Orr formulation, that these steeper gradients generally promote the transfer of energy from the base flow to the perturbations, and we therefore expect to see a corresponding decrease in the critical Reynolds number. Observing figure 5.22, we see that this is indeed the case.

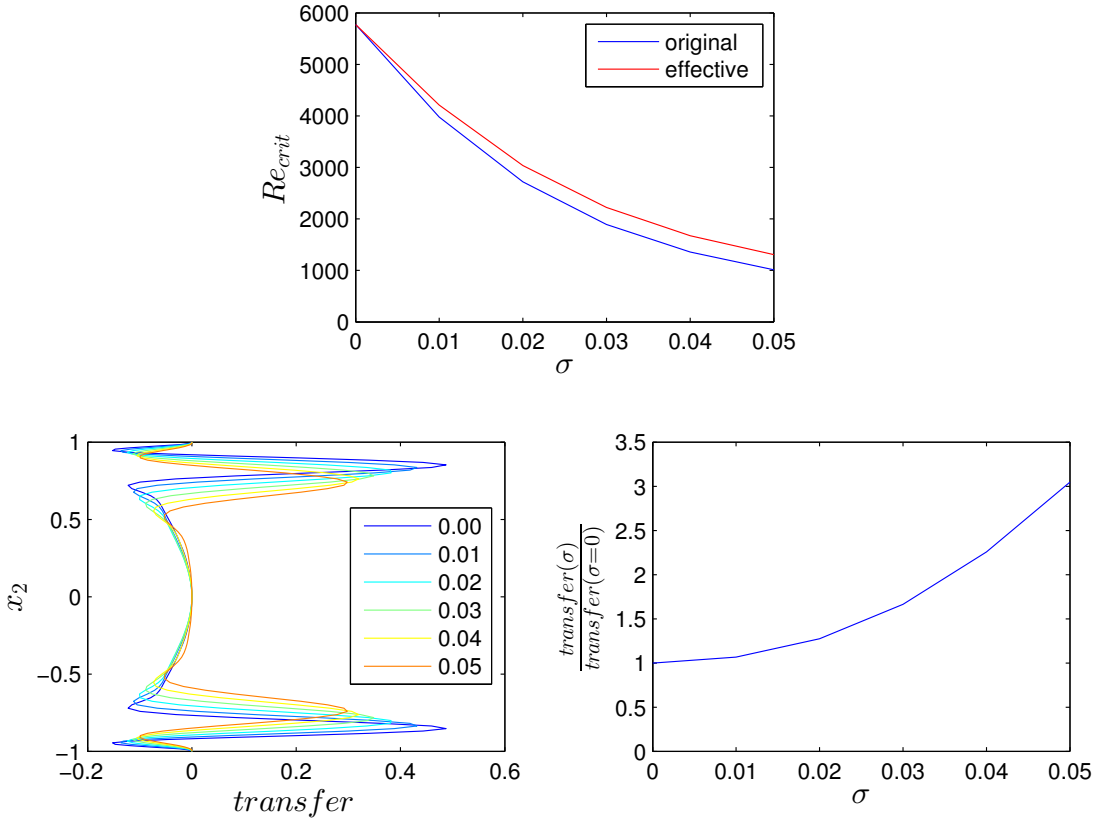

Figure 5.22: Critical Reynolds number as a function of input standard deviation (top left), Reynolds-Orr transfer terms (bottom left), increase in the integral of the Reynolds-Orr transfer term as a function of input standard deviation (bottom right), for plane Poiseuille flow, at $c_l = 0.50$, $\alpha = 1.02$, $\beta = 0.00$.

Referring first to the upper sub-plot of figure 5.22, the blue curve represents the critical Reynolds number, assuming that stochasticity does not modify the channel centre-line velocity, whilst the red curve depicts the corrected critical Reynolds number, when the base flow is scaled back to unity at the channel centre. We see that a reasonably modest modification to the base flow can cause dramatic reductions in the critical Reynolds number. For instance, the rather small difference in base flows at $\sigma = 0.00$ (deterministic case) and $\sigma = 0.05$ results in a large drop in the critical Reynolds number, of about 77 percent, from 5772 to 1306. Turning our attention to the lower two sub-plots, we see why this is so. The leftmost plot shows the distribution of the transfer of energy from the base flow to the perturbations, and the right shows the integral of this function (normalised by the deterministic case). All flows are seen to have very similar transfer in the central regions of the channel,

leaving the upper and lower quarters responsible for the differences observed. It seems that, whilst the absolute velocities of the flows are not too dissimilar, those flows with steeper gradients facilitate increased energy transfer to the perturbations. Referring back to the previous plot of the base flow velocity gradient, we see that, in general, the regions of the channel where the magnitude of the velocity gradient is increased also correspond to the regions where the transfer of energy is increased. This increased energy transfer, in turn, results in a significant reduction in the critical Reynolds number. It should be remembered that the dissipation scales inversely with Reynolds number, and at the critical Reynolds number the transfer and dissipation cancel exactly. A significant increase in transfer therefore allows a much higher dissipation and thus a lower critical Reynolds number, as we observe here.

5.3.3 Stochastic Poiseuille-Couette Flow at a Low Correlation Length

We finally consider the case of highly erratic stochasticity at a low correlation length. As previously noted, we retain 12 terms in the KLE and adopt a sparse grid for efficient computation of the WCE. To get an overview of the sensitivity in wave-number space, we compute maximum energy amplification contours, in a stochastic sense. We restrict analysis to a Reynolds number of 1000, and limit the input standard deviation to only 0.0004, such that the input stochasticity is parameterized as $\{\sigma = 0.0004, c_l = 0.10\}$. We restrict both the Reynolds number and input standard deviation as many realisations of the base flow with larger input parameters lead to asymptotic growth, thus giving a maximum energy amplification of infinity, which naturally leads to an infinite value when computing statistical moments by empirical averaging. This limited analysis is merely adopted to identify the relative sensitivity across wave-number space. We discretize the $\alpha - \beta$ plane with a 20 by 20 grid, and compute the maximum energy amplification for each of the 400 wave-number pairs. We repeat this process for many LHS realisations of the base flow, and, appealing to the central limit theorem, compute the statistical moments via empirical averaging. To this end, we construct the mean and standard deviation of the maximum energy amplification contours, and plot below in figure 5.23.

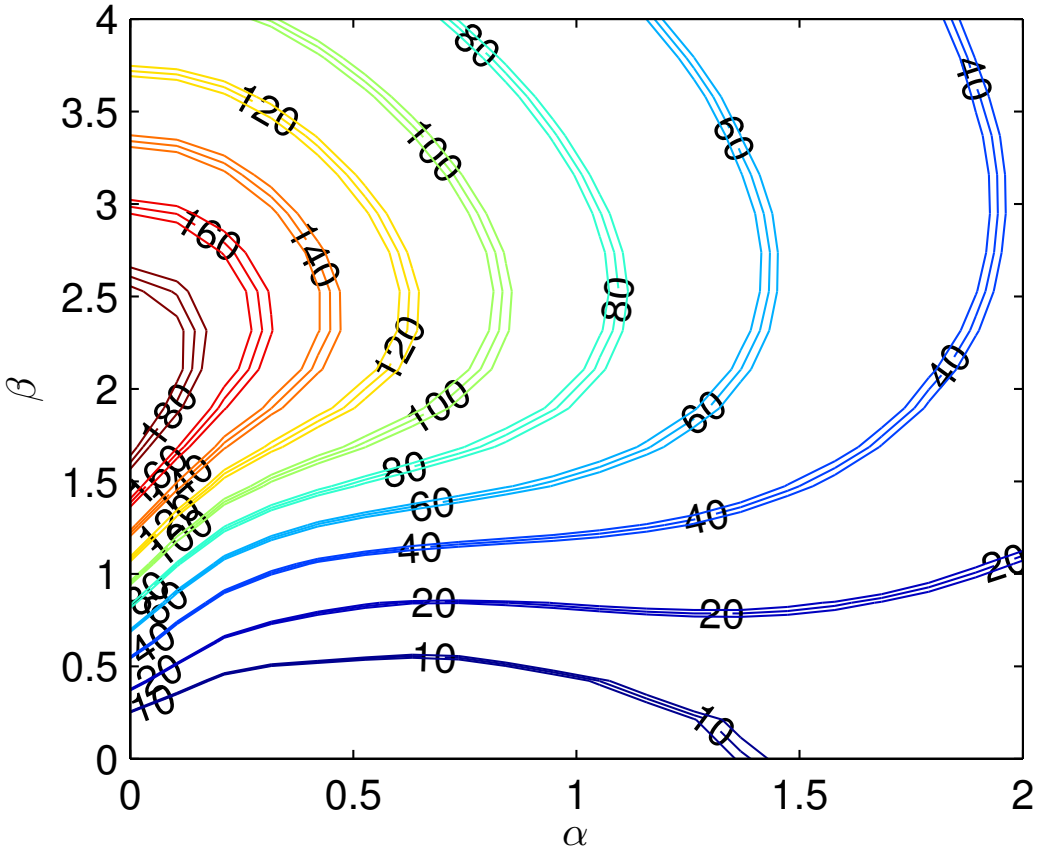

Figure 5.23: Contours of maximum energy amplification, mean plus/minus one standard deviation, for stochastic plane Poiseuille flow, at $c_l = 0.10$, $\sigma = 0.0004$, $Re = 1000$.

As depicted, the shorter span-wise (larger β) waves exhibit more aggressive transient growth, whilst variability, and hence the impact of stochasticity, increases with stream-wise wave-number, α. That is, shorter span-wise waves exhibit more growth but shorter stream-wise waves are more sensitive to the impact of stochasticity.

We also investigate the transient growth at the wave-number pair $\alpha = 1.02$ and $\beta = 0.00$, with $c_l = 0.10$ and $\sigma = 0.0025$. The expectation and standard deviation are plotted below, in figure 5.24.

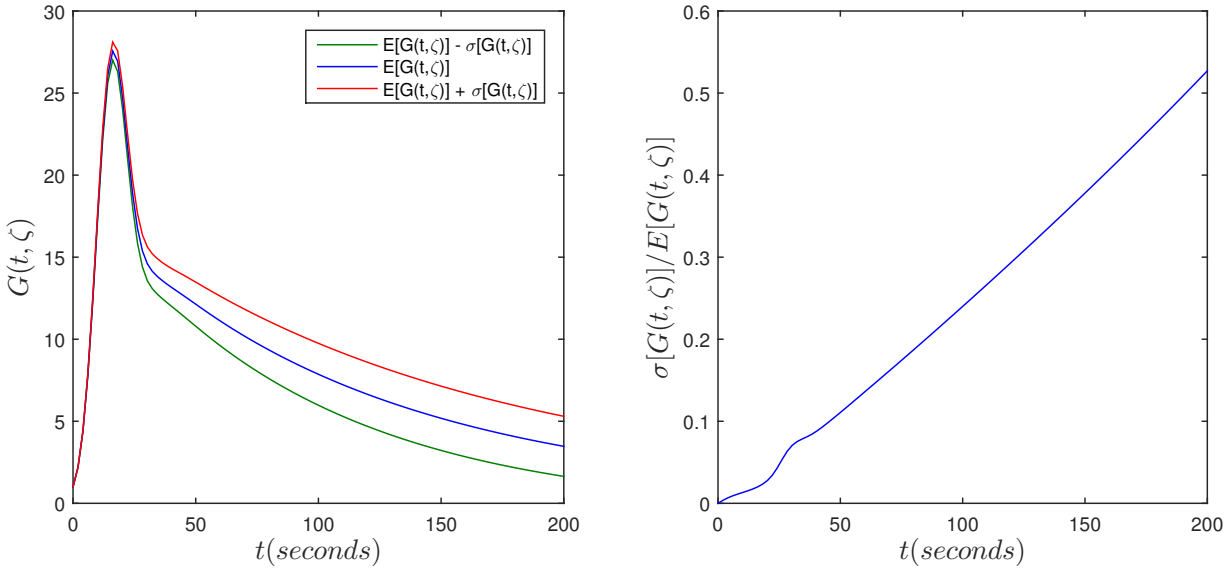

Figure 5.24: Transient growth of stochastic plane Poiseuille flow, $c_l = 0.10$, $\sigma = 0.0025$, $Re = 4000$, $\alpha = 1.02$, $\beta = 0.00$. $E[G(t, \boldsymbol{\zeta})] \pm \sigma[G(t, \boldsymbol{\zeta})]$ (left), $\sigma[G(t, \boldsymbol{\zeta})]/E[G(t, \boldsymbol{\zeta})]$ (right).

As with all previous test cases at these wave numbers, the effects of stochasticity accumulate with time and the ratio of standard deviation to mean (or the deterministic solution) grows linearly in time. Thus given sufficient time, an extremely small amplitude, highly erratic defect can dominate the behaviour of the flow.

5.4 Summary

In this chapter, we have studied the stability of stochastic Poiseuille and Couette type flows. We conducted a number of numerical experiments, involving both modal and non modal analyses. In general, from a physical perspective, we have seen that all flows become more sensitive to stochastic defects as the correlation length of the stochastic base flow is decreased, and the profile thus becomes more erratic. From a numerical perspective, we have seen the superior efficiency offered by the WCE in low stochastic dimensions. However, the curse of dimensionality renders chaos expansions inefficient in higher stochastic dimensions. Whilst sparse grids were able to partially relieve the problem, the Monte Carlo approach proved much more efficient in very high stochastic dimensions.

Through spectral analysis, we have shown that modes in the vicinity of the Y-branch are much more sensitive to stochastic defects than those further away. Furthermore, we showed that our structured perturbations are bounded by the log resolvent norm contours of the more general unstructured perturbations of the ϵ-pseudospectra. We have also seen that neutral curves can be highly sensitive to stochastic defects, which can significantly reduce the critical Reynolds number and may partially explain the deviations between theory and experiment, which are commonly observed.

Our transient analyses revealed that stochastic defects have no initial impact on perturbation energy growth and, in general, the effects of stochasticity accumulate with time. We showed that variability (standard deviation) in the perturbation energy growth increased almost linearly, relative to the mean, with time, in the case of Poiseuille flow, whilst variability in the Couette flow remained of a negligible magnitude at all times. Given sufficient time, the standard deviation, in perturbation energy amplification of a Poiseuille flow, can exceed the mean value, thus rendering stochasticity non negligible. Finally, we showed that neither the number of inflection points in a defect, nor the input variance attributed to a defect, had the capacity to significantly influence the variance in perturbation energy growth attributed to that defect. Instability, arising from stochastic imperfections, must therefore not be inflectional in nature but viscous instead. Furthermore, only modes symmetric about the channel centre-line were deemed to be responsible for the variance in the output process. Reynolds-Orr analyses explain these observations. Anti-symmetric defects lead to an increase in energy transfer (from the base flow to the perturbations) in one region of the channel which is cancelled by a decrease in the opposite half of the channel. Conversely, symmetric defects can lead to an increase in the energy transfer across the whole channel, thus allowing sooner transition and reducing the critical Reynolds number.

Chapter 6

Stochastic Blasius Boundary Layer

6.1 Introduction

Boundary layers, or thin regions of shear, can be unstable to small amplitude disturbances. When the Reynolds number increases sufficiently, and exceeds the critical value (Re_{crit}), boundary layers become convectively unstable, small amplitude disturbances grow and, when large enough, trigger non-linear mechanisms that rapidly generate turbulence. Recent work by Healey [32] suggests inflectional modifications to a boundary layer profile have the capacity to both increase and decrease stability. In addition, there are other transition mechanisms, which do not depend on the Reynolds number, such as non-modal transient growth and by-pass transition. We here investigate these ideas using our stochastic framework. We briefly review boundary layer stability theory before presenting numerical results for the stochastic Blasius boundary layer.

6.2 Boundary Layer Stability Theory

Here, we briefly review the classical results of boundary layer stability theory, indicating how they suggest potentially stabilising/destabilising modifications. Rayleigh [65] described the evolution of linearized disturbances in the inviscid limit and showed that inviscid solutions are stable in the absence of an inflection point. The base flow profile, or more specifically its curvature, is thus an important characteristic in the inviscid case. Later, Tollmien [84] extended these ideas and showed that it is the curvature at the critical point, x_2^c, where $U(x_2^c) = c = \frac{\Re(\lambda)}{\alpha}$, that is most important in controlling inviscid stability.

Orr [54] and Sommerfeld [82] introduced viscous effects, giving rise to the well known Orr Sommerfeld equation. Tollmien [84] demonstrated the destabilising influence of viscosity in boundary layers without an inflection point. At Reynolds numbers exceeding the critical value, he showed that an unstable band of wave-numbers forms, bounded by two neutral wave-numbers which define the zero growth contour in the neutral curve. The smallest neutral wave-numbers are termed the lower branch, whilst the upper branch refers to the higher neutral wave-numbers [32].

Squire showed that two dimensional waves were the first to become unstable, thus directing early studies towards two-dimensional perturbations. The stability of the eigen-modes, of the Orr-Sommerfeld problem, depend on their wavelength, frequency, and on the Reynolds number, defined for a boundary layer as $R_e = \frac{U_\infty \delta}{\nu}$, where U_∞ and ν are the free-stream velocity and kinematic viscosity respectively, and $\delta = \sqrt{\frac{\nu x_1}{U_\infty}}$ is the boundary layer thickness, growing with the square root of the downstream distance. δ, and therefore the Reynolds number, increases in the downstream direction and evaluating the stability of a disturbance at different Reynolds numbers is thus synonymous with evaluation at different downstream locations [20].

The growth rates of the viscous instability mechanism are known to be weaker than those of inviscidly unstable inflectional profiles. This suggests that a modification to an inflexionless profile which introduces an inflection point will be destabilising. However, Healey [32] showed this to be a common misconception, demonstrating that inflectional modifications can, in fact, be strongly stabilising. Although the creation of an inflection point will certainly make an inflexionless profile more unstable in the limit, $Re \to \infty$, one cannot generalise such a result to finite Reynolds numbers. In general, curvature has a strong influence on shorter waves (those near the upper branch of the neutral curve), and only a weak influence on longer waves (near the lower branch of the neutral curve). At large but finite Reynolds number it can be shown that, to leading order, curvature only affects the upper branch of the neutral curve [19]. Furthermore, a flow modification with negative curvature at x_2^c will stabilise the flow by lowering the upper branch and thus reducing the unstable range of wave-numbers. Conversely, a flow modification with positive curvature at x_2^c will generally destabilise the flow. We will not derive such results here but the interested reader may refer to section 28.2 of Drazin and Reid [19].

Transition originating from exponentially growing eigenfunctions is usually called classical or natural transition, observable in natural flows only if the background turbulence is very small, around one percent of the free-stream velocity. For higher values, disturbances are sufficient to trigger other mechanisms which bypass the natural scenario. Morkovin [51] coined the expression bypass transition in 1969,

stating that the natural mechanism could by bypassed altogether. In fact, many experiments have shown transition in boundary layers at Reynolds numbers far below those predicted by eigenvalue analysis. Landahl [43] proposed a physical mechanism for these observations, which is now commonly known as the lift-up effect. The idea is that cross-stream disturbances may amplify stream-wise velocity perturbations. That is, weak pairs of counter rotating vortices are able to lift up fluid with low velocity, from the wall, and simultaneously bring higher speed fluid elements towards the wall. This often results in streaks of high and low stream-wise velocity, which alternate in the span-wise direction. An inspection of Squire's equation, describing the interaction between the wall normal velocity and the wall normal vorticity perturbations, provides some insight. If one was to integrate this equation, for the wall normal vorticity, the result would be an advection term representing the growth of the initial vorticity, and a second term representing the integrated effect of the wall normal velocity. This second term represents the generation of horizontal velocity by the lifting up of fluid elements in the presence of mean shear, and is hence aptly termed the lift up effect.

Such mechanisms are often responsible for the transient growth of boundary layers. Mathematically, we know that the Orr-Sommerfeld operator for a Blasius boundary layer is non normal with a condition number far greater than one, and we therefore expect transient behaviour before a possible exponential growth. Such transient growth is generally larger for long stream-wise waves ($\alpha \approx 0$). Furthermore, it exists at sub-critical Reynolds numbers and is generally perceived to be the underlying mechanism in bypass transition.

In practice, free-stream turbulence is often responsible for the development of disturbances, leading to non-modal growth and transition. Within a boundary layer, turbulence is highly damped, but low frequency oscillations, associated with long streaky structures, appear. Klebanof [62] was the first to experimentally study these disturbances, showing that, for moderate levels of free-stream turbulence, the dominant disturbances within a boundary layer were not Tollmien-Schlichting waves but characterised by low frequencies. Kendall [40] later denoted these disturbances as Klebanof modes. As these streaks grow downstream, they breakdown into regions of intense randomised flow, termed turbulent spots. The leading edge of these spots travels much faster than the trailing, the spots grow and merge until the flow is fully turbulent. Later, Westin [7] showed how different experiments with apparently similar conditions can disagree on the location and extent of transition. Transition to turbulence may follow different routes, depending upon the disturbance environment, but generally begins with the presence of stream-wise vortices, which generate strong stream-wise streaks, in turn growing and eventually breaking

down into turbulence.

The two main linear growth mechanisms encountered in flat plate boundary layers are the exponential growth of Tollmien-Schlichting waves, and the transient growth of stream-wise elongated streaks. When the amplification of either disturbance is sufficient, nonlinear effects become relevant, the primary perturbations saturate and take the flow into a new state. The linear stability of these new, more complicated laminar flow configurations is the subject of secondary instability.

6.3 Base Flow

A natural application for stability analysis is the boundary layer over an aerofoil, that is the thin region of shear between the wing where the flow velocity vanishes, satisfying the no slip condition, and the free-stream where the flow is at the uniform speed of the aircraft. One can model this problem as a thin wing at zero angle of attack, or equivalently a flat plate.

6.3.1 Parallel Flow Assumption

More specifically, we shall consider a stationary, uniform $2D$ flow impinging tangentially upon a flat plate of semi-infinite length. We assume this flow is moving at a constant velocity, U_∞, in the stream-wise direction, x_1, for $x_1 < 0$ with the plate placed along the half-plane $x_2 = 0$, $x_1 > 0$. The flow impinges the plate at $x_1 = 0$, where it interacts taking the value zero at $x_2 = 0$ and growing to the previous uniform velocity U_∞ at the edge of the boundary layer and in the free-stream. Figure 6.1 depicts a sketch of such a flow.

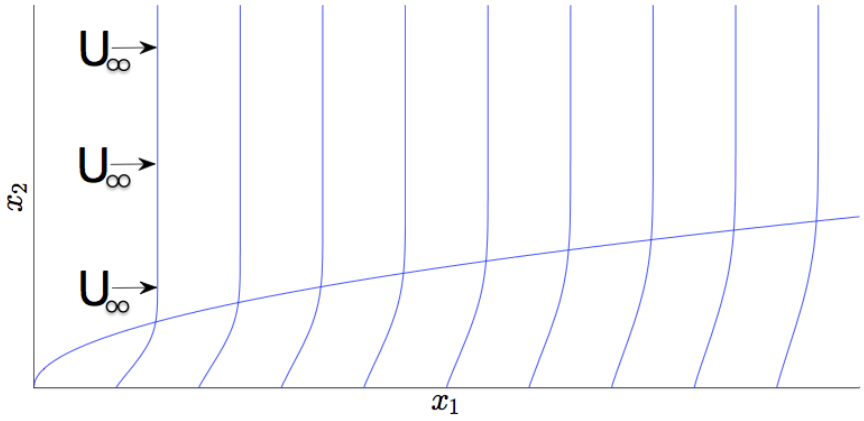

Figure 6.1: Sketch of the Blasius boundary layer.

The boundary layer, born at the plate leading edge, grows in thickness as the square root of the spatial distance progressing towards the trailing edge, thus inducing an increase in the local length scale, in turn increasing the local Reynolds number. We assume we are sufficiently far downstream that the behaviour of the flow is independent of the behaviour at the leading edge of the plate. The growth of the boundary layer thickness is slow and the transverse velocity is comparatively small. Neglecting the weak stream-wise growth and the small transverse velocity of the flow, the basic assumption of a mean flow with parallel streamlines is made.

To justify this, consider a rectangular control volume including the boundary layer with a long side resting on the plate and a short side in the transverse direction. It is clear that the flux entering the control volume, in the horizontal direction, from the side closest to the edge ($x_1 = 0$) is greater than that exiting from the other short side. As the flow moves far from the origin, the plate effectively manifests its presence by reducing the mean stream-wise velocity inside the control volume. Consequently, continuity implies that there must be a flow in the cross-stream direction, flowing out through the long side of the control volume which is not in contact with the plate. These cross-stream velocities must start from zero at the plate and increase with the distance from it. However, the length of control volume through which the cross-stream velocities pass is far greater than the length through which the stream-wise velocities pass, and it thus follows that they are far smaller in magnitude. In fact, the ratio between the mean cross-stream velocity and the mean stream-wise velocity is of the order of the ratio between the thickness of the boundary layer and the distance from the origin, and is therefore very small. It is therefore argued that this transverse flow is of secondary importance, it may be neglected and the flow assumed parallel. Further, the control volume analysis holds for both the deterministic and stochastic cases, with the arguments thus carrying over to the case of a stochastic base flow.

6.3.2 Shooting for the Base Flow Profile

An approximate solution for this base flow can be formed from the boundary layer equations, giving a self-similar flow field, which is commonly termed the Blasius profile. The flow depends only on the wall-normal direction, and the dynamics of small perturbations to the Blasius profile are once more described by the Orr-Sommerfeld and Squire equations. The flat plate is located at $x_2 = 0$ ($x_2 = -1$ when mapped onto the Chebyshev grid), and the reference length for non-dimensionalisation of

the problem is given by the displacement thickness,

$$\delta^* = \int_0^\infty 1 - \frac{U(x_2)}{U_\infty} dx_2, \tag{6.1}$$

where U_∞ is the free-stream velocity.

The displacement thickness is the perpendicular distance by which a surface would have to be moved from the reference plane in an inviscid flow to give the same flow rate as occurs between the surface and the reference plane in the real viscous fluid. In practical terms, the displacement thickness modifies the shape of a body immersed in a fluid to allow an inviscid solution. This is commonly used in aerodynamics to overcome the difficulty inherent in the fact that fluid in a boundary layer asymptotically approaches the free stream velocity as distance from the wall increases, at any steam-wise location.

We are therefore tasked with solving the Orr-Sommerfeld and Squire system on the domain $x_2 \in [0, \infty]$ with the Blasius base flow profile, which we introduce later, and the no slip boundary conditions $u_2(x_2 = 0) = u_2'(x_2 = 0) = \eta(x_2 = 0) = 0$ at the wall, and $u_2(x_2 = \infty) = u_2'(x_2 = \infty) = \eta(x_2 = \infty) = 0$ in the free-stream.

The base flow profile for the Blasius boundary layer is not known explicitly, but may be found from the solution of a non-linear ordinary differential equation (ODE), in some function f, where the profile is given by $U(x_2) = U_\infty f'(x_2^*)$. Using a similarity transformation Blasius [6] arrived at a third order non-linear ordinary differential in the function f,

$$2f''' + ff'' = 0, \tag{6.2}$$

subject to the boundary conditions $f(0) = f'(0) = 0$ and $f'(\infty) = 1$, where $x_2^* = Re_{\delta^*}\sqrt{\frac{v}{U_\infty x_1}}x_2$ is a similarity variable, and Re_{δ^*} is the Reynolds number based upon the boundary layer thickness.

We must therefore solve a third order non-linear ODE. Being third order, the ODE requires three boundary conditions. However, only two boundary conditions can be specified at $x_2^* = 0$, namely $f(0) = f'(0) = 0$. We therefore proceed with a shooting method, we take an initial guess for the second derivative, $f''(0) = g_0^*$, integrate over the domain and check to see if the solution obtained satisfies the boundary condition at the far end of the domain, that is $f'(\infty) = 1$. If the value obtained is not within an acceptable error, we use the magnitude of the error to update the guess and shoot once more, repeating the process until converging to the correct solution. Noting that the value of the function f' at the far end of the domain is an

implicit function of the guess, g_i^*, the procedure can be formalised with Newton's method, to solve

$$f'(\infty, g_i^*) - 1 = 0. \tag{6.3}$$

Below, we outline an adaptive Newton shooting method for the solution to the problem.

First, one writes the third order ODE as a system of three first order equations,

$$f' = g, \tag{6.4}$$

$$g' = h, \tag{6.5}$$

$$h' = -\frac{1}{2} fh, \tag{6.6}$$

with the boundary conditions at $x_2^* = 0$, $f(0) = 0$, $g(0) = 0$, $h(0) = g_0$, where g_0 is the initial guess.

Next, Newton's method is applied to find the value of the guess satisfying the boundary condition at the far end of the domain. Let $N(g_i^*) = g(\infty, g_i^*) - 1$. The updated guess is then

$$g_{i+1}^* = g_i^* - \frac{N(g_i^*)}{\frac{\partial N}{\partial g^*}_{|g^*(i)}}. \tag{6.7}$$

An efficient way to evaluate the derivative $\frac{\partial N}{\partial g^*}_{|g^*(i)}$ is to solve, in parallel, the variational system

$$F' = G, \tag{6.8}$$

$$G' = H, \tag{6.9}$$

$$H' = -\frac{1}{2}(Fh + fH), \tag{6.10}$$

where $F = \frac{\partial f}{\partial g^*}$, $G = \frac{\partial g}{\partial g^*}$ and $H = \frac{\partial h}{\partial g^*}$, and the boundary conditions at the wall are $F(0) = G(0) = 0$, $H(0) = 1$.

Grouping the coupled equations involving the unknown functions, f, g, h, F, G, H, into a vector, the solution is easily computed with a standard ODE solver. Once converged, we have the Blasius base flow profile

$$U(x_2) = U_\infty f'(x_2^*) = U_\infty g(x_2^*). \tag{6.11}$$

6.3.3 The Stochastic Base Flow Profile

As with the Poiseuille/Couette flow, we assume a Gaussian auto-covariance for the stochastic component of the flow, once more characterised by a standard deviation and a correlation length. We then employ a truncated Karhunen-Loève expansion, based upon the assumed auto-covariance, resulting in the flow field

$$U^*(x_2, \omega) = U(x_2) + \sigma(x_2) \sum_{i=1}^{d} \sqrt{\gamma_i} e_i(x_2) \zeta_i(\omega). \tag{6.12}$$

For further details, the reader is referred back to §4.2 and §4.3. As an example, we plot the first few KLE modes in figure 6.2, $\sigma(x_2)\sqrt{\gamma_i}e_i(x_2)$, for the case $c_l = 0.50$ and $\sigma = 0.02$.

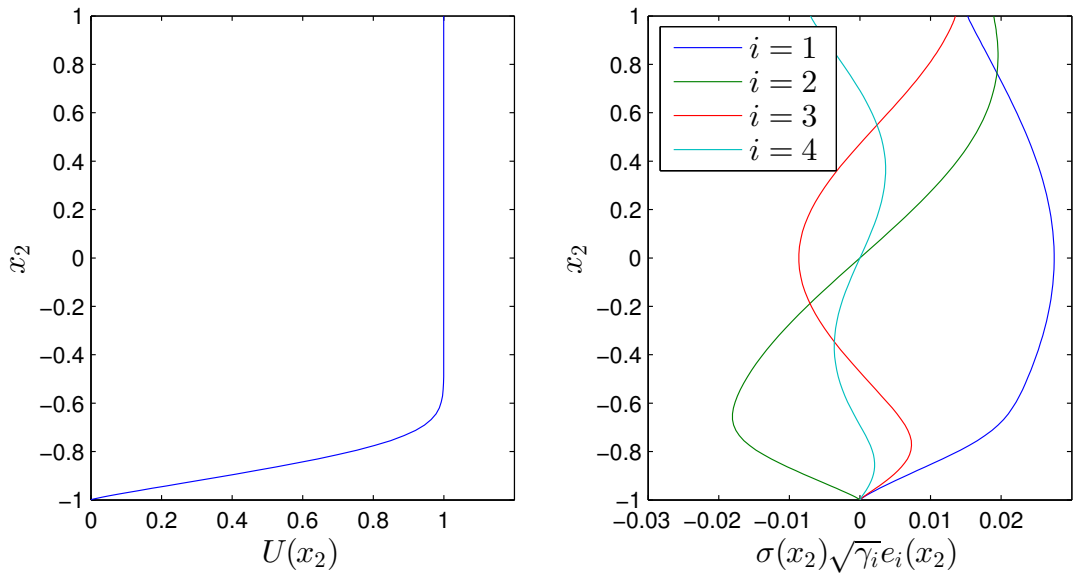

Figure 6.2: Deterministic Blasius boundary layer profile (left). Blasius KLE modes (right) for $c_l = 0.50$, $\sigma = 0.02$.

Examples of stochastic base flow realisations are given in figure 6.3.

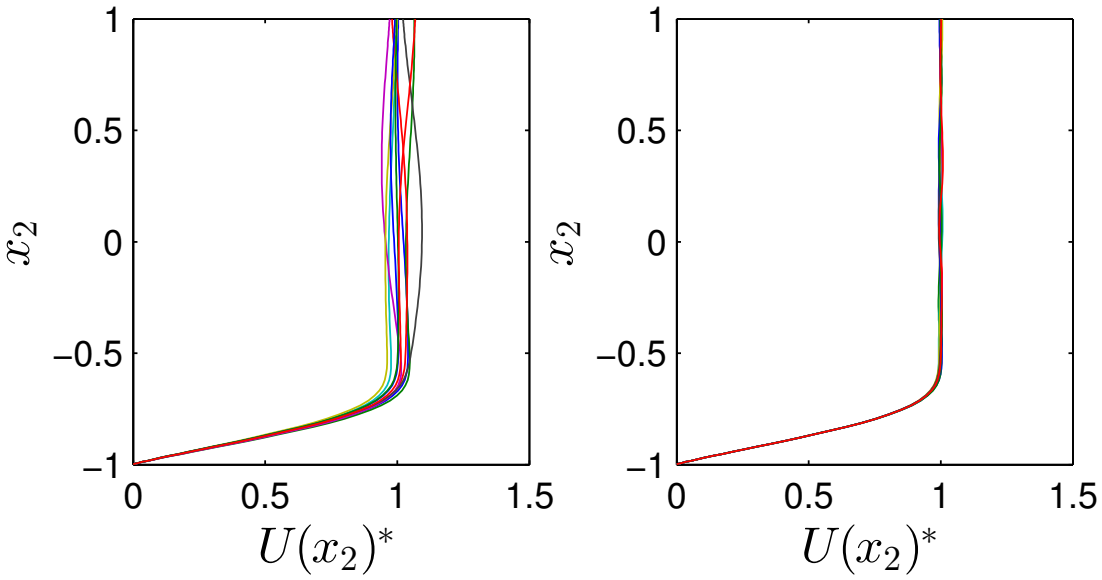

Figure 6.3: Examples of stochastic base flow realisations for $c_l = 0.50$ and $\sigma = 0.02$ (left), and $c_l = 0.10$ and $\sigma = 0.0025$ (right).

As can be seen, all additive stochastic defects satisfy the boundary conditions at the wall. However, we have not forced the defects to zero at the upper end of the domain, and the total stochastic flow is therefore allowed to take values which differ from unity at this point. Instead, we allow the non-dimensional base flow to take a value which differs from unity and rescale the Reynolds number to account for the difference. Recalling that the true solution to the Navier-Stokes equations is $\overline{U}(x_2) = U_\infty U(x_2)$, where U_∞ is the free-stream velocity and $U(x_2)$ is the non-dimensional solution we employ in our non-dimensional equations, and that the Reynolds number is $R_e = \frac{U_\infty \delta}{\nu}$, we see that the true solution, $\overline{U}(x_2)$, is unchanged when we scale U_∞ by a constant factor $1+\epsilon$ and the non-dimensional solution, $U(x_2)$, by the inverse factor $\frac{1}{1+\epsilon}$. Further, scaling the free-stream velocity is synonymous with scaling the Reynolds number. We therefore employ the following procedure; we add stochasticity to our non-dimensional base flow and compute its maximum value across the domain, say $1 + \epsilon$, we then scale the whole non-dimensional base flow by the factor $\frac{1}{1+\epsilon}$ so that it takes a maximum value of unity, and rescale the Reynolds number by a factor $1 + \epsilon$ to take into account this change. This way, the modifications to the size of the base flow are encapsulated in the Reynolds number. In the deterministic case the Reynolds number is based upon the far field velocity, which in turn is the maximum velocity of a deterministic Blasius boundary layer. By basing the stochastic Reynolds number on the maximum flow velocity we remain consistent with this approach, as well as maintaining a consistency with the Reynolds number adopted in similar flows, such as jets.

6.4 Modal Analysis

Here, we present a numerical study of the temporal eigenvalue spectrum of the Orr-Sommerfeld equation, for the stochastic Blasius boundary layer. We modify the deterministic Blasius boundary layer profile with a truncated KLE, as was done for the Poiseuille-Couette flow. We consider processes with a range of correlation lengths and input standard deviations, retaining an appropriate number of terms in the KLE (for accurate representation of the stochastic process), and use 5000 LHS based simulations to verify the results of the WCE.

6.4.1 Deterministic Spectra

As an example, we first consider a deterministic Blasius boundary layer, with wave-numbers $\alpha = 0.303$, $\beta = 0.00$, at Reynolds numbers of both 400 and 600. The wave-number pair is chosen to correspond to the first wave to transition at the critical Reynolds number of about 519, and the Reynolds numbers are chosen as examples of sub and super critical flows respectively. The figure below, 6.4, depicts the spectra for these cases.

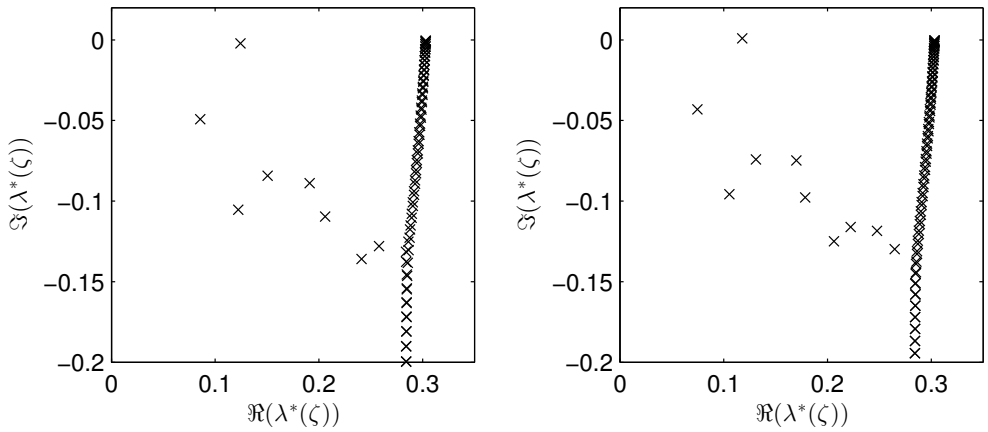

Figure 6.4: Spectra of the deterministic Blasius boundary layer, $Re = 400$ (left) and $Re = 600$ (right), $\alpha = 0.303$, $\beta = 0.00$.

As seen above, the spectra for the Blasius base flow is very different from the other parallel shear flows considered in this thesis, comprising of both a continuous and a discrete portion. There are a rather small number of scattered eigenvalues, accounting for the discrete portion of the spectrum, and an almost vertical line of modes at unity phase speed ($\frac{\Re(\lambda^*(\zeta))}{\alpha}$), which are an approximation to the continuous part of the spectrum, arising as a consequence of the unbounded domain. The

Blasius boundary layer has at most one unstable mode, and becomes asymptotically unstable at a Reynolds number of 519.4, at the wave-number pair considered here. This Tollmien-Schlichting wave is therefore present in the rightmost figure, at the super-critical Reynolds number of 600, but not the left, and corresponds to the mode with positive imaginary part. This mode is seen to have a rather small real part and thus a slow phase speed, which explains why its maximum amplitude is typically very close to the wall.

6.4.2 Stochastic Spectra and ϵ-pseudospectra

We use 5000 LHS based simulations of the stochastic Blasius boundary layer base flow, compute the spectra for each flow and finally add pseudo-spectral log resolvent norm contours. We consider four cases, and parameterise the stochasticity with an input standard deviation and a correlation length. The cases considered are $\{\sigma = 0.0004, c_l = 0.10\}$, $\{\sigma = 0.0025, c_l = 0.10\}$, $\{\sigma = 0.02, c_l = 0.50\}$ and $\{\sigma = 0.05, c_l = 0.50\}$. We first set forth the mathematics, then present the numerical results.

Appealing to definition 2.2 (section 3.2.5.3) of the ϵ-pseudospectra, we write the KLE of the discretised Orr-Sommerfeld and Squire equations in such a way that we can identify the perturbation matrix $\delta\mathbf{L_1}$. Recalling that $\hat{\mathbf{L_1}}^* = \mathbf{L}^{-1}\hat{\mathbf{R}}^*$, where

$$\hat{\mathbf{R}}^* = \begin{pmatrix} i\alpha u(x_2)(1+\bar{\sigma}\sum_{i=1}^{d}\sqrt{\gamma_i}\zeta_i(\omega)e_i(x_2))(K^2-D^2)+ & 0 \\ i\alpha(u''(x_2)+ & \\ \bar{\sigma}\sum_{i=1}^{d}\sqrt{\gamma_i}\zeta_i(\omega)(u''(x_2)e_i(x_2)+2u'(x_2)e_i'(x_2)+ & \\ u(x_2)e_i''(x_2)))+\frac{1}{Re}(K^2-D^2)^2 & \\ & \\ i\beta(u'(x_2)+ & \\ \bar{\sigma}\sum_{i=1}^{d}\sqrt{\gamma_i}\zeta_i(\omega)(u'(x_2)e_i(x_2)+u(x_2)e_i'(x_2))) & i\alpha u(x_2)(1+\bar{\sigma}\sum_{i=1}^{d}\sqrt{\gamma_i}\zeta_i(\omega)e_i(x_2))- \\ & \frac{1}{Re}(D^2-K^2) \end{pmatrix}$$

$$= \mathbf{R} + \bar{\sigma}\sum_{i=1}^{d}\sqrt{\gamma_i}\zeta_i(\omega)\hat{\mathbf{R}}_\mathbf{i},$$

we hence have $\hat{\mathbf{L_1}}^* = \mathbf{L_1} + \bar{\sigma}\sum_{i=1}^{d}\sqrt{\gamma_i}\zeta_i(\omega)\mathbf{L^{-1}}\hat{\mathbf{R}}_\mathbf{i} = \mathbf{L_1} + \delta\mathbf{L_1}$. Once again, we see that the perturbation matrix, $\delta\mathbf{L_1} = \bar{\sigma}\sum_{i=1}^{d}\sqrt{\gamma_i}\zeta_i(\omega)\mathbf{L^{-1}}\hat{\mathbf{R}}_\mathbf{i}$, is structured, and we should therefore consider the structured ϵ-pseudospectra (definition 8, section 3.2.5.3). However, in the case $\beta = 0$, each matrix $\hat{\mathbf{R}}_\mathbf{i}$ would appear to become symmetric. In such a case we would have a complex symmetric matrix to which

we add a symmetric perturbation, preserving the structure. However, application of the boundary conditions and numerical discretization destroy the symmetry. We therefore cannot claim that $\Lambda_\epsilon^{struct}(\mathbf{A}) = \Lambda_\epsilon(\mathbf{A})$ (as discussed in section 3.2.5.3), but only that $\Lambda_\epsilon^{struct}(\mathbf{A}) \subseteq \Lambda_\epsilon(\mathbf{A})$. **We therefore do not attempt to make a direct comparison between our structured perturbations and the unstructured ones of the ϵ-pseudospectra, but simply note that as a subset our results should be bounded by those of the more general case.** We can bound the norm of the random matrix from above,

$$||\delta\mathbf{L_1}||_2 = ||\bar{\sigma}\sum_{i=1}^{d}\sqrt{\gamma_i}\zeta_i(\omega)\mathbf{L^{-1}}\hat{\mathbf{R}}_\mathbf{i}||_2 \leq \bar{\sigma}\sum_{i=1}^{d}|\sqrt{\gamma_i}||\zeta_i(\omega)|||\mathbf{L^{-1}}\hat{\mathbf{R}}_\mathbf{i}||_2. \tag{6.13}$$

Below, in figure 6.5, we plot the stochastic eigenvalues and pseudospectral log resolvent norm contours, corresponding to these cases.

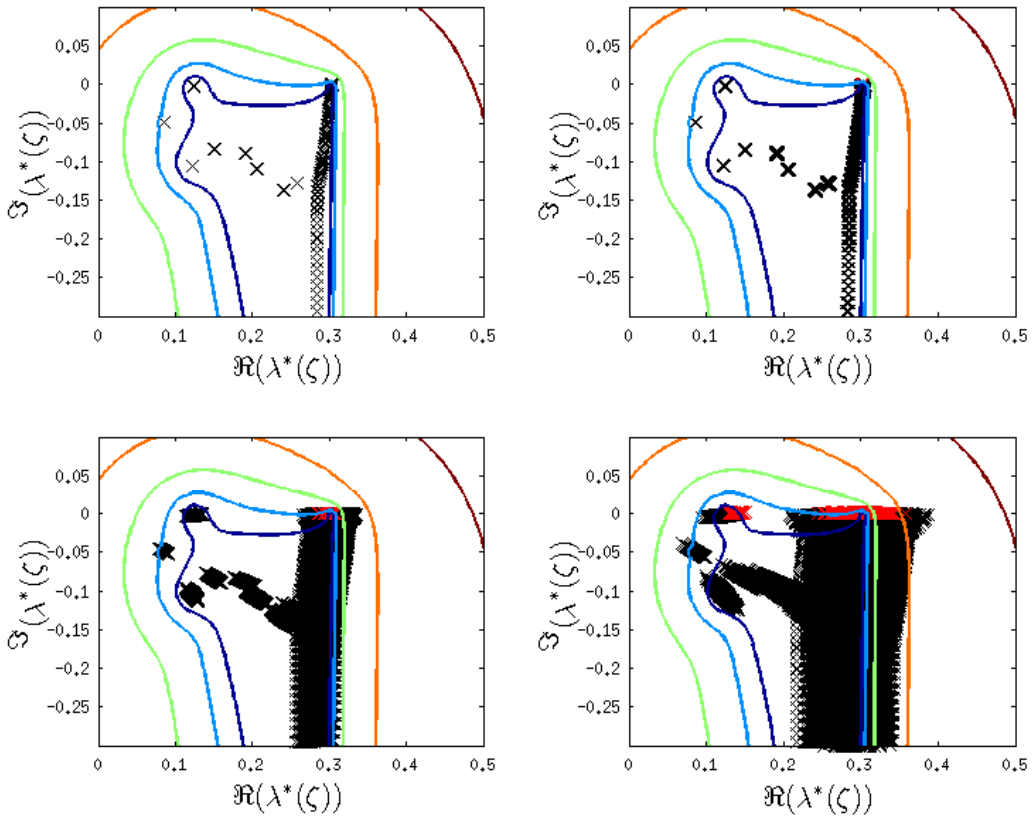

Figure 6.5: Stochastic eigenvalues (5000 Monte Carlo simulations) and pseudo-spectral log resolvent norm contours ($\log_{10}\epsilon$=-3,-2.5,-2,-1.5,-1 from inner to outer) of a Blasius boundary layer, $c_l = 0.10$ and $\sigma = 0.0004$ (top left), $c_l = 0.10$ and $\sigma = 0.0025$ (top right), $c_l = 0.50$ and $\sigma = 0.02$ (bottom left), $c_l = 0.50$ and $\sigma = 0.05$ (bottom right), $Re = 400$, $\alpha = 0.303$, $\beta = 0.00$.

In contrast to the Poiseuille-Couette flows, the correlation length of the input flow appears to have far less impact on the spectrum, with the upper sub-plots showing little eigenvalue mobility. The lower sub-plots suggest that the input standard deviation has much more influence. Furthermore, as observed with the Poiseuille-Couette flows, the input standard deviation appears to affect eigenvalue mobility uniformly throughout the spectrum. This mobility is mostly confined to the real axis, thus not affecting asymptotic stability much. Those eigenvalues with positive imaginary part are plotted in red, and correspond to asymptotically growing unstable modes. As can be seen, all realisations at the low correlation length and low input standard deviation combinations remain stable. However, there are a few realisations at $\{\sigma = 0.02, c_l = 0.50\}$ exhibiting instability, and many more at $\{\sigma = 0.05, c_l = 0.50\}$. It is also interesting to note that the unstable mode is not always located in the same location as the unstable deterministic case. In the deterministic case, the unstable

mode was located in the upper left region of the spectrum, but we now see, in the stochastic case, that we sometimes get unstable modes in the upper right region of the spectrum. These modes have far greater phase speed and will therefore be less localised to the wall region of the flow.

For a normal random variable, we expect around 67% of observations to fall within one standard deviation of the mean, which corresponds to log resolvent norm contours of around -1.42, -0.32, -0.44 and -0.04, in the case of the upper left, upper right, lower left and lower right sub-plots respectively. Clearly, the above figure is consistent with these results, as one would expect as our estimate of the norm of the perturbation matrix was in fact an upper bound.

6.5 Transient Analysis

Here, we investigate the transient behaviour of the stochastic Blasius boundary layer. We start by reviewing the deterministic case, and comparing the maximum amplification of perturbation energy growth (growth functions) for $\alpha = 0.303$, $\beta = 0.000$, at different Reynolds numbers. We know that the Blasius boundary layer is asymptotically stable up to a Reynolds number of around 519, and we therefore expect the energy amplification of perturbations below such Reynolds number to exhibit a long term decay. Below, figure 6.6 depicts the growth functions at varying Reynolds number.

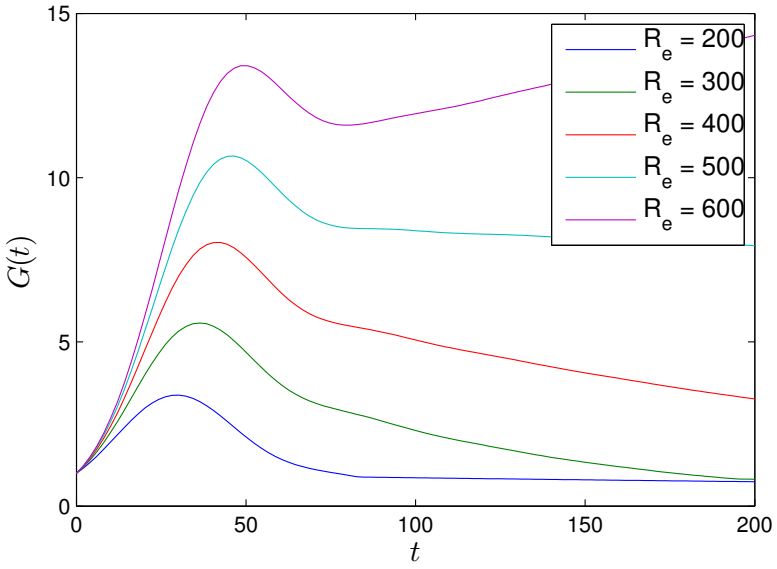

Figure 6.6: Transient growth of a deterministic Blasius boundary layer at varying Reynolds number, $\alpha = 0.303$, $\beta = 0.00$.

As expected, those with Reynolds numbers less than 519.4 do indeed exhibit a decaying behaviour, whilst those with a super-critical Reynolds number are seen to continuously grow at large times. Having reviewed the deterministic case, we now turn our attention to the case of a stochastic base flow. We consider a stochastic flow at a moderate correlation length, parameterized as $\{\sigma = 0.02, c_l = 0.50\}$ with $d = 4$ terms retained in the KLE. We solve the problems with the WCE on a tensor grid, adopting 5000 LHS simulations to verify all WCE results.

6.5.1 Stochastic Blasius Boundary Layer at a Moderate Correlation Length

At the moderate correlation length of 0.50, we retain only four stochastic dimensions and discretize each dimension with only four points, resulting in a tensor grid of size 256, again highlighting the superior efficiency of the WCE in low dimensions. Adopting this grid, we compute the WCE coefficients for the energy amplification, at $Re = 400$, $\alpha = 0.303$, $\beta = 0.000$, from which we compute the statistical moments. The formulation is identical to that in §4.5.3, we do not repeat the derivation here but, for convenience, restate the result

$$G(t, \boldsymbol{\zeta}(\omega)) = S^2_{max}(\mathbf{E} \exp(-i\hat{\mathbf{\Lambda}}t)\mathbf{E}^{-1}), \tag{6.14}$$

where $S^2_{max}(\mathbf{E} \exp(-i\hat{\mathbf{\Lambda}}t)\mathbf{E}^{-1})$ is the square of the largest singular value of the matrix $\mathbf{E} \exp(-i\hat{\mathbf{\Lambda}}t)\mathbf{E}^{-1}$, $\hat{\mathbf{\Lambda}} = \hat{\mathbf{\Lambda}}(\boldsymbol{\zeta}(\omega))$ is the WCE of the diagonal matrix with the k stochastic eigenvalues of largest imaginary part along the diagonal, and $\mathbf{E}$ is the energy weight matrix.

The results are illustrated in figure 6.7 below.

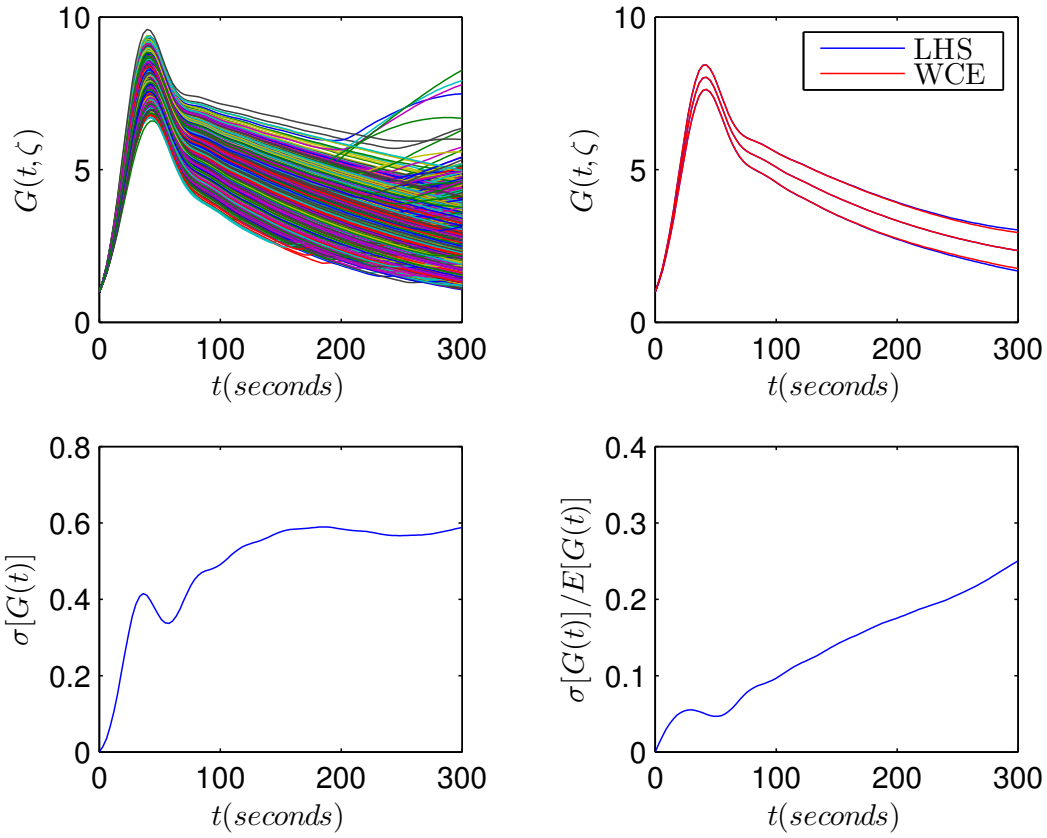

Figure 6.7: Transient growth of the stochastic Blasius boundary layer, $c_l = 0.50$, $\sigma = 0.02$, $Re = 400$, $\alpha = 0.303$, $\beta = 0.00$, 5000 Monte Carlo simulations of $G(t, \boldsymbol{\zeta})$ (top left), $E[G(t, \boldsymbol{\zeta})] \pm \sigma[G(t, \boldsymbol{\zeta})]$ (top right), $\sigma[G(t, \boldsymbol{\zeta})]$ (bottom left), $\sigma[G(t, \boldsymbol{\zeta})]/E[G(t, \boldsymbol{\zeta})]$ (bottom right).

The upper left sub-plot depicts the energy amplification for each of 5000 LHS simulations, which we use to verify the WCE. The upper right sub-plot displays the mean growth, plus or minus one standard deviation. The blue curves correspond to the LHS result and the red the WCE. As can be seen, the WCE accurately produces the LHS result with only 256 function evaluations, which is very efficient indeed. From a physical perspective, we see that there are some stochastic flows which demonstrate an asymptotic growth, even at this sub-critical Reynolds number. From the lower two sub-plots, we see that the effects of stochasticity accumulate with time (as they did for the Poiseuille flow at $\beta \approx 0$) and the standard deviation can grow large relative to the mean (deterministic) result.

6.5.1.1 Variance Based Sensitivity Analysis

We can use the WCE to decompose the variance of the output process amongst the random input sources, or KLE modes. The variance based sensitivity indices can

be computed directly from the WCE coefficients, and we use the formula outlined earlier, in chapter two, to decompose the variance.

Consider the simplified formulation of the stochastic perturbation energy amplification WCE,

$$G(t,\boldsymbol{\zeta}(\omega)) = \sum_{\boldsymbol{\alpha_i}\in I_O} g_{\alpha^i}(t) H_{\alpha^i}(\boldsymbol{\zeta}(\omega)) = \sum_{i=0}^{N} g_{\alpha^k}(t) H_{\alpha^i}(\boldsymbol{\zeta}(\omega)), \tag{6.15}$$

where the coefficients are explicitly functions of time, $g_{\alpha^i}(t)$. We have the total sensitivity index

$$S_i^{tot}(t) = \frac{\sum_{k\in\left\{1,\ldots,N;\alpha_i^k>0\right\}} g_{\alpha^k}^2(t)}{\sum_{k=1}^{N} g_{\alpha^k}^2(t)}, \forall i \in \{1,2,...,d\}\,, \tag{6.16}$$

and the first order sensitivity index,

$$S_i(t) = \frac{\sum_{k\in\left\{1,\ldots,N;\alpha_i^k>0,\alpha_j^k=0\forall j\neq i\right\}} g_{\alpha^k}^2(t)}{\sum_{k=1}^{N} g_{\alpha^k}^2(t)}, \forall i \in \{1,2,...,d\}\,. \tag{6.17}$$

We recall that the first order variance based sensitivity indices measure the sole contribution of the ith stochastic variable, $\zeta_i(\omega)$, to the variance of the output process, and the total variance based sensitivity indices measure the total contribution of an input to the output variance. We would like a scalar measure of sensitivity, and we therefore take the average of the time series indices, which we plot below in figure 6.8.

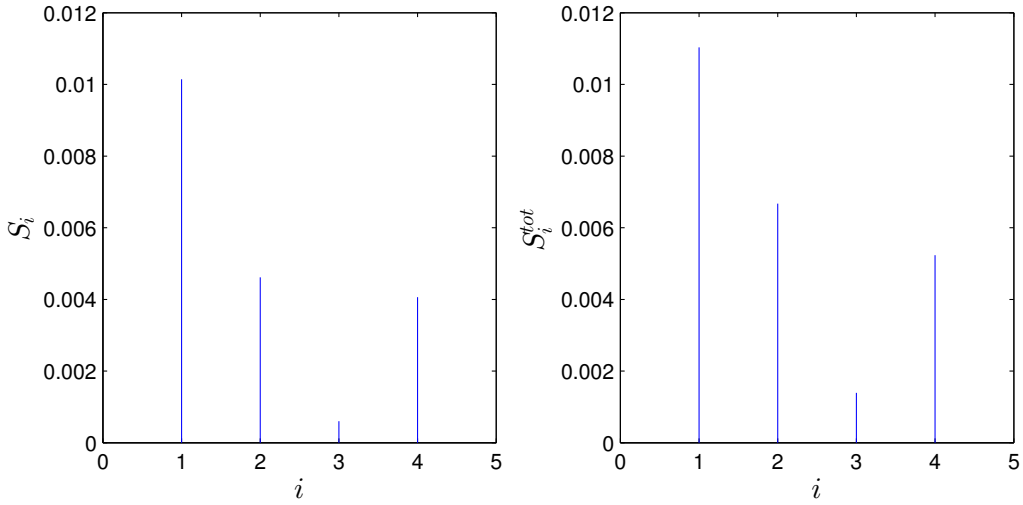

Figure 6.8: Total (right) and first order (left) variance based sensitivity indices, for $G(t,\boldsymbol{\zeta})$, stochastic Blasius boundary layer, $c_l = 0.50$, $\sigma = 0.02$, $Re = 400$, $\alpha = 0.303$, $\beta = 0.00$.

The results are very different to those obtained for the stochastic Poiseuille flow. With the exception of mode three to four, the output variance attributed to each stochastic input appears to decrease with mode number. Noting that the input variance attributed to a stochastic mode decreases monotonically with the mode number, it seems intuitive that the output variance also decrease. We will later postulate an explanation for the ineffectiveness of mode three, when we look at the instability from an energy perspective.

6.5.1.2 Optimal Stochastic Defect

In this section, we seek to determine the stochastic defect which causes the greatest deviation from the deterministic growth function. We formulate this problem as a constrained optimisation. To this end, we seek the coefficients in the KLE which maximise the root mean squared deviation between the stochastic and deterministic growth functions, where the mean is computed across the time series, that is

$$\boldsymbol{\zeta}^* = argmin_{\boldsymbol{\zeta}} \left\{ -\frac{1}{n_T} \sum_{j=1}^{n_T} (G(t_j, 0) - G(t_j, \boldsymbol{\zeta}))^2 \right\}$$
$$\forall \zeta_i \in [-3, 3], i = 1, 2, ...d,$$

where we have discretised the time domain with n_T points, and confined the search space to the hypercube $[-3, 3]^d$. For zero mean, unit variance Gaussian random variables, such as these, we know that 99 percent of observations fall within three standard deviations of the mean, thus justifying our simplified search space. We expect the resulting flow to be quite different to the deterministic Blasius boundary layer as we are optimising, but hope it will highlight the features of a defect which are responsible for deviations between theory and experiment. We solve the problem with the simplex method, and plot the optimal stochastic coefficients, the growth function, the resulting base flows and their curvatures in figure 6.9.

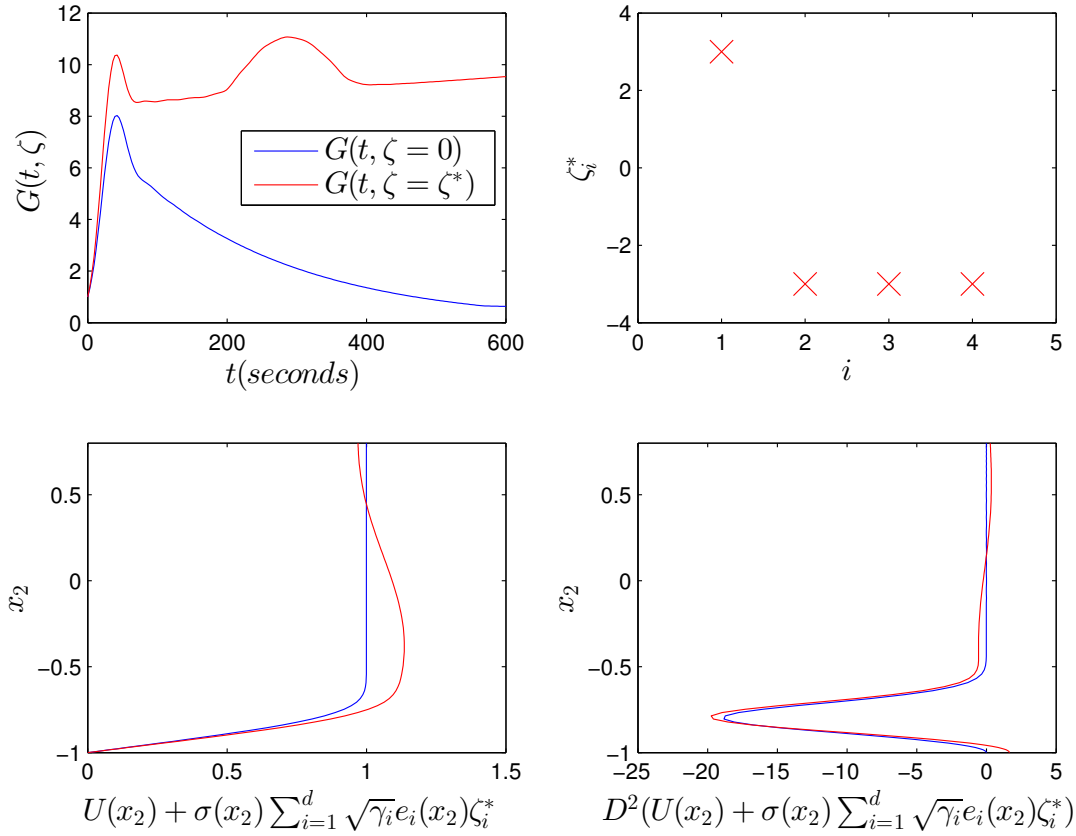

Figure 6.9: Optimal stochastic perturbation energy growth function (top left), optimal stochastic KLE coefficients (top right), optimal stochastic base flow (bottom left) and curvatures (bottom right), stochastic Blasius boundary layer, $c_l = 0.50$, $\sigma = 0.02$, $Re = 400$, $\alpha = 0.303$, $\beta = 0.00$. Deterministic in blue and stochastic in red.

We also plot the spectra, in figure 6.10, before discussing the plots.

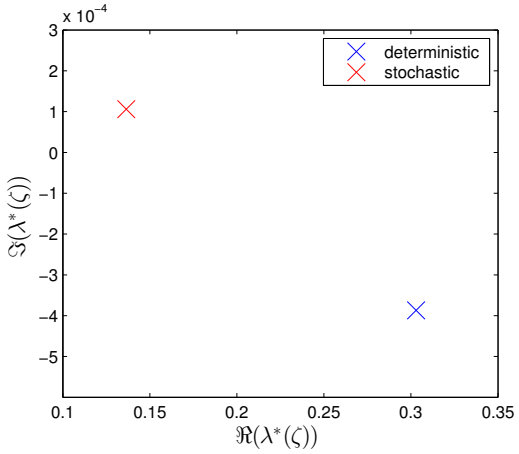

Figure 6.10: Spectra of fastest growing deterministic (blue) and optimised stochastic (red) mode, Blasius boundary layer, $c_l = 0.50$, $\sigma = 0.02$, $Re = 400$, $\alpha = 0.303$, $\beta = 0.00$.

We see, from the spectrum, that the actual fastest growing mode appears to change when stochasticity is added. Not only is the stochastic mode asymptotically unstable, but the phase speed of the fastest growing modes are very different, with $c = \frac{\Re(\lambda)}{\alpha} = 0.45$ and 1.00 in the stochastic and deterministic case respectively. We are essentially dealing with a completely different mode, which was conversely not the case for the Poiseuille flow under optimised stochasticity, where we saw that the phase speed of the fastest growing mode varied very little whilst its growth rate increased slightly. We argue that it was essentially the same mode, and things are therefore more complicated in this case.

We know that curvature at the critical point, x_2^c, where $U(x_2^c) = c$, is very important in controlling stability properties. In particular, in the long wave limit, the critical point produces a destabilising term in the dispersion relation whenever the curvature at that point is positive. At large Reynolds number, it can be shown [19] that the upper branch of the neutral curve for a favourable pressure gradient boundary layer lies at

$$\alpha_{upper} \sim \frac{(U_0')^{\frac{11}{6}}}{2^{\frac{1}{6}}\pi^{\frac{1}{3}}(-U_0'')^{\frac{1}{3}}} R_e^{-\frac{1}{6}}. \tag{6.18}$$

Whilst the lower branch lies at

$$\alpha_{lower} \sim 1.0005(U_0')^{\frac{5}{4}} R_e^{-\frac{1}{4}}, \tag{6.19}$$

where subscript 0 denotes a quantity evaluated at the wall. The expressions show that, to leading order, curvature only impacts the upper branch of the neutral

curve, and furthermore it is the curvature in the immediate vicinity of the wall, or near the lower critical point. Noting that the deterministic Blasius boundary layer has both zero curvature and a large positive gradient at the wall, and that curvature is negative in the immediate vicinity moving outwards from the wall, a flow modification with negative curvature in the vicinity of the wall will make the second derivative more negative and stabilise the flow by pulling α_{upper} down, thus reducing the range of unstable wave numbers. Conversely, positive curvature in the wall region will have the opposite effect, thus destabilising the flow. The wall gradient is clearly not as influential as curvature (owing to the already large positive gradient which the small modifications are simply adding to), but nevertheless a modification with a positive (negative) gradient at the wall will act to destabilise (stabilise) the flow.

When the flow is deterministic, the curvature is everywhere negative and the flow is therefore inviscidly stable. The instability in the deterministic case, occurring at $Re \approx 519$, is therefore due to viscous effects, and it therefore seems plausible that instability in the stochastic case is of an inflectional nature. Computing the critical point, we find a value, when mapped onto the Chebyshev grid (where $x_2 = -1$ is at the wall and $x_2 = 1$ is at infinity), of $x_2^c \approx -0.90$. We inspect the curvature of the flow in this region and plot a zoomed in view of this curvature, which is depicted below in figure 6.11.

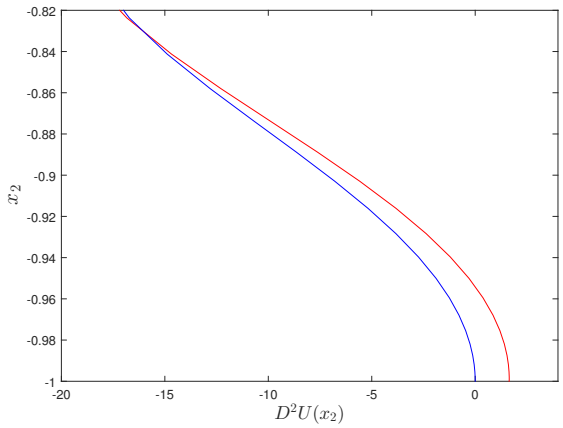

Figure 6.11: Blown up view of the curvature of the deterministic (blue) and optimised stochastic (red) Blasius boundary layer in the vicinity of the critical point, $c_l = 0.50$, $\sigma = 0.02$, $Re = 400$, $\alpha = 0.303$, $\beta = 0.00$.

Clearly, the optimised stochasticity has significantly increased curvature in the vicinity of the critical point. Inspecting curvature even further out from the wall, we observe that stochasticity does actually decrease curvature in some regions but these

are far from the critical point where the stability of the flow is insensitive to curvature. Furthermore, stochasticity introduces two inflection points which will only enhance the instability of the flow, at least in the large Reynolds number limit. If we inspect the curvature of the individual KLE modes, we see that the optimised coefficients, ζ_i^*, are such that each mode increases curvature in the wall region, in the vicinity of the critical point, as illustrated in figure 6.12.

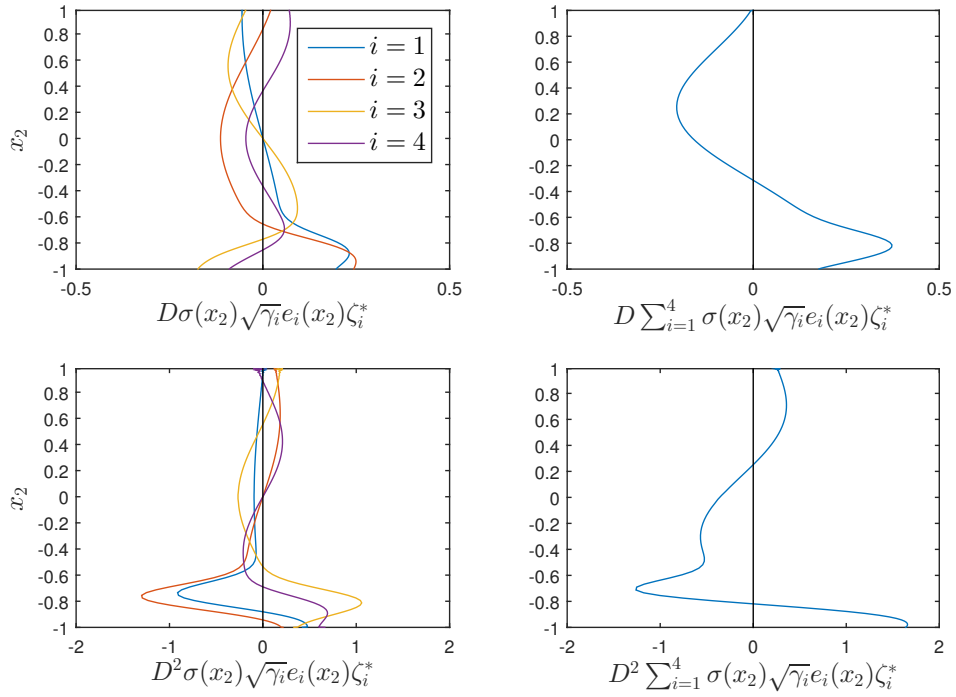

Figure 6.12: Gradient (upper) and curvature (lower) of the individual (left) and summed (right) KLE modes with optimised coefficients.

The lower leftmost sub-plot 6.12 illustrates the curvature of the individual KLE modes when scaled by the optimised coefficients, ζ_i^*. Clearly, the optimisation algorithm has chosen the coefficients such that each mode has positive curvature in the wall region and is thus destabilising. Inspecting the upper left subplot, we see that optimised modes one and two both increase the wall gradient, mode four has little effect and mode three acts to significantly reduce the wall gradients. Positive wall gradients and positive wall curvatures act to destabilise the flow, however, for a given mode shape, the algorithm simply has to pick a positive or negative scalar coefficient and can therefore not guarantee each modification increases both gradients and curvatures. We expected the curvature to be the more important factor and the algorithm has indeed made a selection consistent with this. The large negative contribution of mode three to wall gradients could partially explain

why it was attributed such a small variance based sensitivity index. That is, it destabilises through its effect on curvature whilst stabilising through its impact on wall gradients.

Referring back to the growth functions in figure 6.9, we see that, interestingly, the stochastic growth function depicts two distinct humps, as opposed to the one commonly observed in the deterministic setting. It is interesting to seek the initial conditions which cause these distinct bumps, at $t \approx 41$ seconds and $t \approx 287$ seconds. We recall that the perturbation energy growth function is an upper bound, which is optimised over all possible initial conditions (with unit energy norm) at each instance in time. The initial condition which maximises the energy amplification may therefore be different at different times. We therefore restrict our attention to the initial conditions which cause the maximum growth at $t \approx 41$, 287, corresponding to the two humps, and also the mode with largest imaginary part, responsible for the asymptotic instability.

Rather than conduct an optimisation, one may employ ideas from linear algebra, namely the SVD, to determine the optimal initial conditions of interest. Recall that

$$\begin{aligned} G(t,\boldsymbol{\zeta}(\omega)) &= \sup_{\mathbf{q}(t=0,\boldsymbol{\zeta}(\omega))} \frac{\|\mathbf{q}(t,\boldsymbol{\zeta}(\omega))\|_E^2}{\|\mathbf{q}(t=0,\boldsymbol{\zeta}(\omega))\|_E^2} = \sup_{\hat{\mathbf{a}}(0)} \frac{\|\mathbf{E}\hat{\mathbf{a}}(t)\|_2^2}{\|\mathbf{E}\hat{\mathbf{a}}(0)\|_2^2} = \sup_{\mathbf{E}\hat{\mathbf{a}}(0)} \frac{||\mathbf{E}\exp(-i\hat{\boldsymbol{\Lambda}}t)\mathbf{E}^{-1}\mathbf{E}\hat{\mathbf{a}}(0)||_2^2}{||\mathbf{E}\hat{\mathbf{a}}(0)||_2^2} \\ &= ||\mathbf{E}\exp(-i\hat{\boldsymbol{\Lambda}}t)\mathbf{E}^{-1}||_2^2 = S_{max}^2(\mathbf{E}\exp(-i\hat{\boldsymbol{\Lambda}}t)\mathbf{E}^{-1}), \end{aligned}$$

where $\mathbf{E}$ is the energy weight matrix, $\hat{\mathbf{a}} = \begin{pmatrix} \hat{\mathbf{v}} \\ \hat{\boldsymbol{\eta}} \end{pmatrix}$, $S_{max}^2(\mathbf{E}\exp(-i\hat{\boldsymbol{\Lambda}}t)\mathbf{E}^{-1})$ is the square of the largest singular value of the matrix $\mathbf{E}\exp(-i\hat{\boldsymbol{\Lambda}}t)\mathbf{E}^{-1}$, and $\hat{\boldsymbol{\Lambda}}$ is the diagonal matrix of eigenvalues. It follows that if the optimal initial condition is of unit energy norm and, by definition, possesses an energy of $||\mathbf{E}\exp(-i\hat{\boldsymbol{\Lambda}}t)\mathbf{E}^{-1}||_2$ at time t, then

$$\mathbf{E}\hat{\mathbf{a}}_\mathbf{t} = \frac{\mathbf{E}\exp(-i\hat{\boldsymbol{\Lambda}}t)\mathbf{E}^{-1}\mathbf{E}\hat{\mathbf{a}}_\mathbf{0}}{||\mathbf{E}\exp(-i\hat{\boldsymbol{\Lambda}}t)\mathbf{E}^{-1}||_2}, \tag{6.20}$$

where $\hat{\mathbf{a}}_\mathbf{t}$ is the normalised condition at time t. To simplify the mathematics, let $\hat{\mathbf{b}}_\mathbf{t} = \mathbf{E}\hat{\mathbf{a}}_\mathbf{t}$ and $\mathbf{M} = \mathbf{E}\exp -i\hat{\boldsymbol{\Lambda}}t\mathbf{E}^{-1}$. Now factorising the matrix via the SVD, we have that $\mathbf{M} = \mathbf{B_t}\boldsymbol{\Sigma}\mathbf{B_0}^*$, where $\mathbf{B_t}$ is a matrix whose columns are the left singular vectors, $\boldsymbol{\Sigma}$ is the diagonal matrix of singular values and $\mathbf{B_0}$ is the matrix whose columns are the right singular vectors of $\mathbf{M}$. Noting that $\mathbf{B_0}$ is unitary and rearranging we have that $\mathbf{M}\mathbf{B_0} = \mathbf{B_t}\boldsymbol{\Sigma}$. Selecting only the largest singular value,

Σ_{11}, we have that $\mathbf{MB_0^1} = \Sigma_{11}\mathbf{B_t^1}$, where $\mathbf{B_0^1}$ and $\mathbf{B_t^1}$ are the principle vectors. Finally, noting that the largest singular value is simply the 2-norm, rewriting $\mathbf{B_0^1} = \hat{\mathbf{b}}_\mathbf{0}$ and $\mathbf{B_t^1} = \hat{\mathbf{b}}_\mathbf{t}$, it follows that

$$||\mathbf{M}||_2\hat{\mathbf{b}}_\mathbf{t} = \mathbf{M}\hat{\mathbf{b}}_\mathbf{0}, \tag{6.21}$$

and the initial condition which maximises the energy amplification at time t can simply be found from the principal left singular vector of $\mathbf{E}\exp(-i\hat{\mathbf{\Lambda}}t)\mathbf{E}^{-1}$,

$$\hat{\mathbf{a}_0} = \begin{pmatrix} \hat{\mathbf{v}_0} \\ \hat{\boldsymbol{\eta}_0} \end{pmatrix} = \mathbf{E^{-1}}\hat{\mathbf{b}}_\mathbf{0}. \tag{6.22}$$

Following this procedure, we compute the initial and final conditions responsible for the distinct humps in the growth function. We find the exact times corresponding to the humps by performing an optimisation in their surrounding neighbourhood. We map the wall normal velocity-vorticity results into Cartesian form and plot below in figure 6.13.

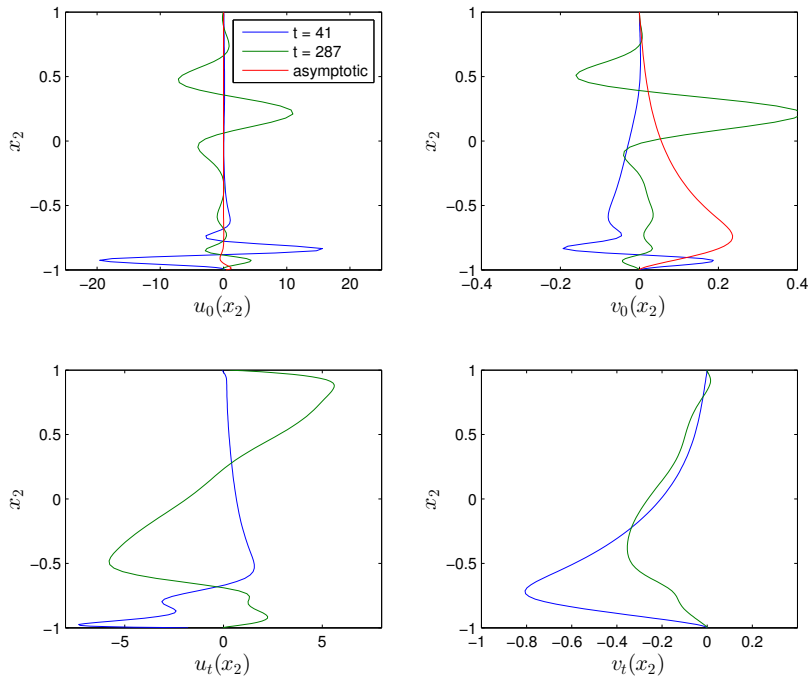

Figure 6.13: Optimal initial (top) and final (bottom) perturbations in primitive coordinates, u (left) and v (right), stochastic Blasius boundary layer, $c_l = 0.50$, $\sigma = 0.02$, $Re = 400$, $\alpha = 0.303$, $\beta = 0.00$.

We also map the results into streamlines. The following three plots in figures 6.14,

6.15 and 6.16 correspond to the three aforementioned times, with the upper sub-plot corresponding to the initial and the lower sub-plot corresponding to the ultimate flow state.

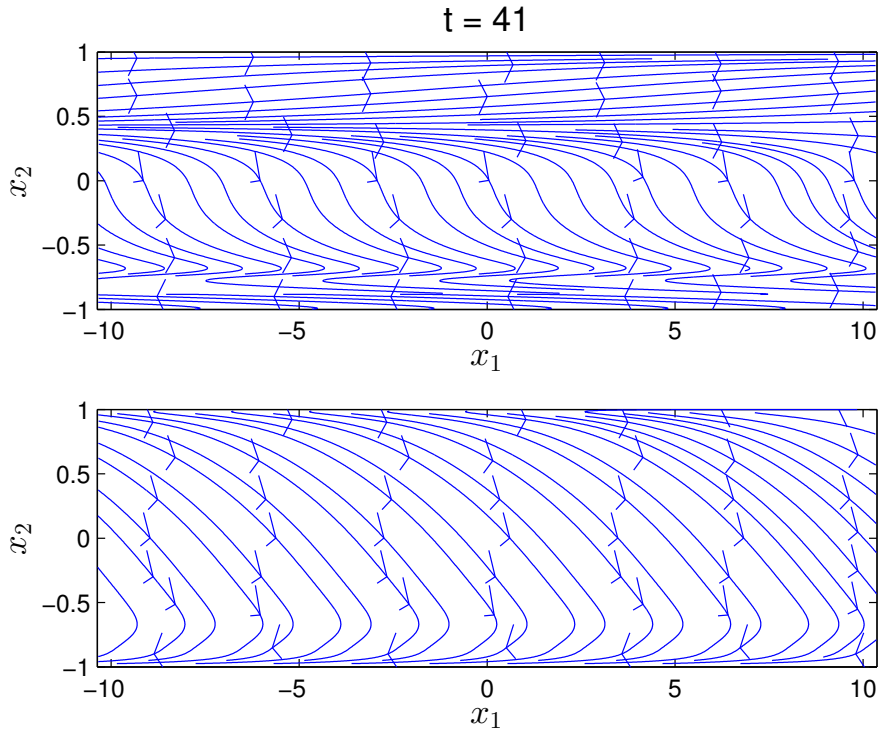

Figure 6.14: Streamlines for the optimal initial (top) and final (bottom) perturbation, optimising growth at $t = 41$ seconds, stochastic Blasius boundary layer, $c_l = 0.50$, $\sigma = 0.02$, $Re = 400$, $\alpha = 0.303$, $\beta = 0.00$.

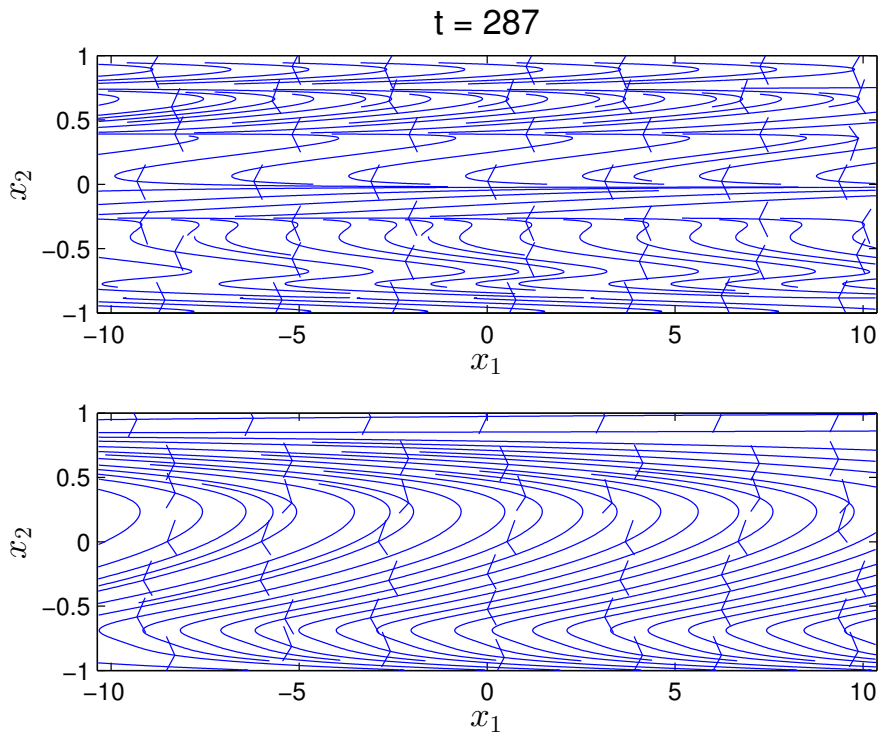

Figure 6.15: Streamlines for the optimal initial (top) and final (bottom) perturbation, optimising growth at $t = 287$ seconds, stochastic Blasius boundary layer, $c_l = 0.50$, $\sigma = 0.02$, $Re = 400$, $\alpha = 0.303$, $\beta = 0.00$.

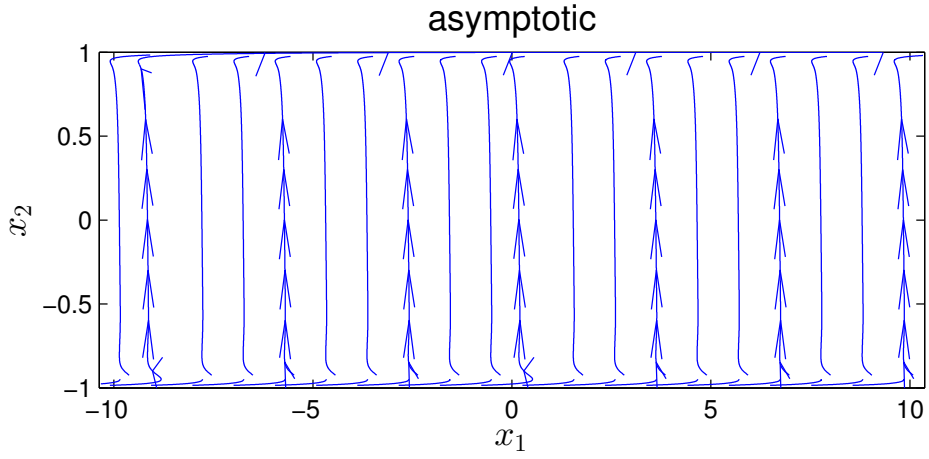

Figure 6.16: Streamlines for the initial perturbation with largest asymptotic growth rate, stochastic Blasius boundary layer, $c_l = 0.50$, $\sigma = 0.02$, $Re = 400$, $\alpha = 0.303$, $\beta = 0.00$.

The figures show that the modes responsible for the two distinct humps are rather different. The perturbation responsible for the first hump is clearly a wall mode, with large variations in the vicinity of the wall. Conversely, the mode responsible for the second hump is quite different with much larger variations in the central

channel region, making it more of a centre mode. In all cases, the perturbations appear to be dominated by the stream-wise velocity component, with much weaker cross-stream velocities.

6.5.1.3 Reynolds-Orr Analysis

In this section, we look at the problem from a different perspective. We look at the transfer of energy between the base flow and the perturbations, and use this energy based framework to help explain the impacts of stochasticity. We therefore turn our attention to the Reynolds-Orr equation, which we recall (from §4.5.3.3), for the case of 2D perturbations, $U = (U(x_2), 0)$, $u = (u(x_2), v(x_2))exp(i\alpha x_1)exp((\Im(\lambda) - i\Re(\lambda))t)$, as

$$\Im(\lambda)\int_{-1}^{1} u^2(x_2) + v^2(x_2)dx_2 = -\int_{-1}^{1} U'(x_2)u(x_2)v(x_2)dx_2$$
$$-\frac{1}{Re}\int_{-1}^{1} u'^2(x_2) + v'^2(x_2) + \alpha^2 u^2(x_2) + \alpha^2 v^2(x_2)dx_2,$$

where the first, second and third terms correspond to the total change in perturbation energy, the transfer of energy between the base flow and the perturbations, and the dissipation of perturbation energy respectively.

We consider the fastest growing modes corresponding to the stochastic test case considered throughout this chapter. We plot the base flows, the perturbations in primitive co-ordinates, the corresponding derivatives and the terms in the Reynolds-Orr formulations in figure 6.17. As usual, blue is representative of the deterministic flow and red the stochastic.

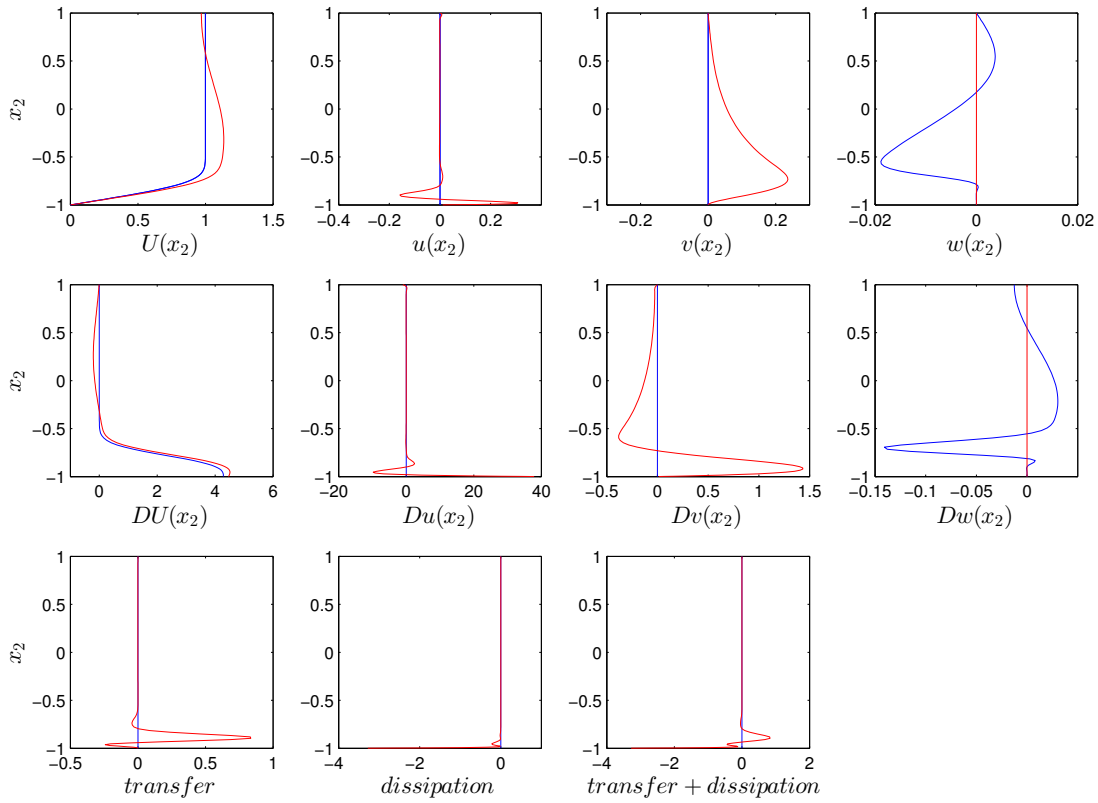

Figure 6.17: Velocities (top), velocity gradients (middle) and terms in the Reynolds-Orr formulation (bottom), stochastic Blasius boundary layer, $c_l = 0.50$, $\sigma = 0.02$, $Re = 400$, $\alpha = 0.303$, $\beta = 0.00$.

We see that the magnitude of the velocity gradients are generally larger for the optimised stochastic flow. Further, inspecting the perturbation velocities, we see that the deterministic flow produces perturbations constrained to the x_3 direction, and therefore does not enable energy transfer between the base flow and the perturbations. Conversely, the stochastic flow has non-zero perturbation velocities in the x_1 and x_2 direction, this coupled with steeper base flow gradients results in substantial energy transfer in the wall region of the flow, in turn leading to an asymptotically unstable flow. Such observations are clearly consistent with previous analyses, where it was determined that an increase in the base flow velocity gradient had the capacity to expand the range of unstable wave numbers for a given Reynolds number, and was therefore a destabilising factor.

Finally, in figure 6.18 we plot the differences, stochastic less deterministic, in the energy terms of the Reynolds-Orr formulation.

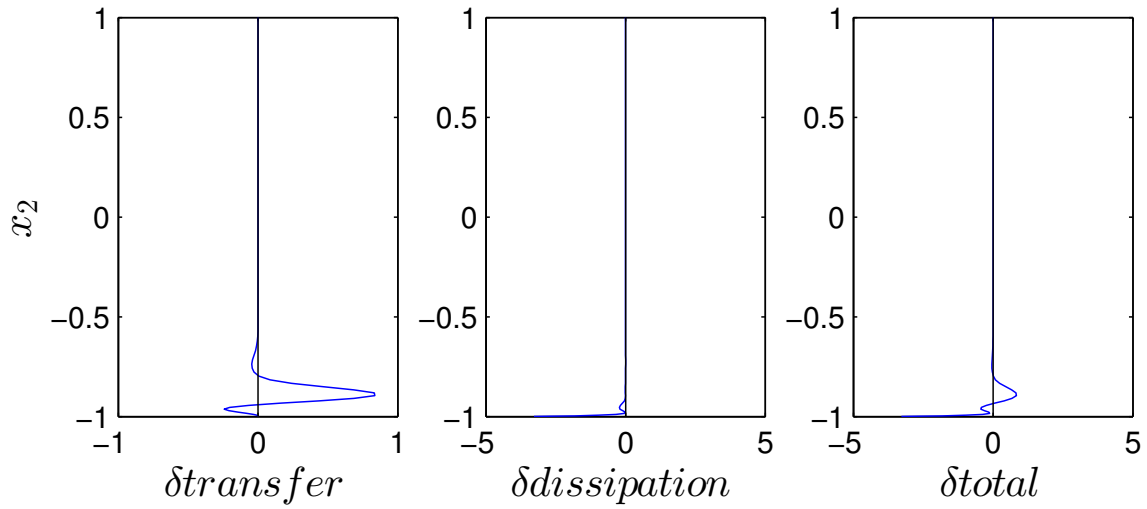

Figure 6.18: Differences (stochastic less deterministic) of terms in the Reynolds-Orr formulation, stochastic Blasius boundary layer, $c_l = 0.50$, $\sigma = 0.02$, $Re = 400$, $\alpha = 0.303$, $\beta = 0.00$.

From the figure, it is evident that the stochastic defects significantly enhance transfer whilst having negligible impact on dissipation, as was the case for the Poiseuille flow. Remembering that the dissipation term scales inversely with the Reynolds number, and that neutral stability is achieved when dissipation and transfer exactly balance, we see that the increased transfer allows the flow to reach neutral stability at lower Reynolds numbers, thus reducing the critical Reynolds number. We investigate these ideas further in the next subsection.

6.5.1.4 Critical Reynolds Number

We extend the analysis of the previous section, by seeking the critical Reynolds number. That is, for a given set of stochastic parameters, we aim to find the lowest Reynolds number at which the fastest growing mode has a growth rate of exactly zero. We fix the correlation length at $c_l = 0.50$ and seek the critical Reynolds number of the stochastic Blasius flow, at $\alpha = 0.303$ and $\beta = 0.000$, for input standard deviations $\sigma = 0.00, 0.01, ..., 0.05$. It should be noted that, by fixing the wave numbers, we are implicitly assuming that the shape of the neutral curve does not significantly change, but we later inspect the whole wave number space to verify these ideas.

As the input standard deviation does not change the shape of the flow, only its size, we retain the same four optimised stochastic variables used previously, $\{\zeta_1(\omega) = 3, \zeta_2(\omega) = -3, \zeta_3(\omega) = -3, \zeta_4(\omega) = -3\}$. For each of the base flows, we

use interval reduction to find the Reynolds number with an asymptotic growth of zero. This is the critical Reynolds number assuming that stochasticity does not modify the velocity used to define the Reynolds number, which it obviously does. We therefore correct the Reynolds number, scaling it up by multiplying by the maximum boundary layer velocity, and then scaling the base flow down (uniformly) such that it has a maximum velocity of unity. This is effectively the flow whose critical Reynolds number we solve. Clearly, there is some choice in how one defines the Reynolds number, and which velocity one uses. For instance, one could select the maximum flow velocity, or the average velocity of the flow beyond δ^*. Whilst these two methods produce identical results in the deterministic setting, they will certainly be different once stochasticity is introduced. We argue that the effective critical Reynolds number, obtained by scaling the flow back to have a maximum value of unity, provides an upper bound, whilst the original Reynolds number, of the unscaled flow, provides a lower bound. To see why this is so, we plot the scaled down base flows, and their derivatives, for each of the input standard deviations below, in figure 6.19.

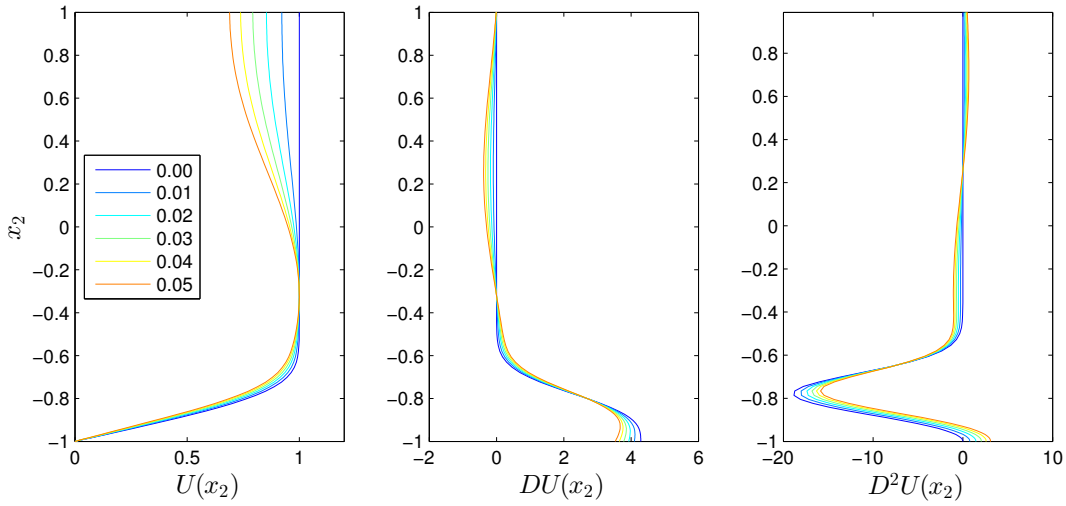

Figure 6.19: Optimised base flows (left), derivative (centre) and second derivative (right), for varying input standard deviations, $\sigma = 0.00, 0.01, 0.02, 0.03, 0.04$ and 0.05 from right to left, for plane Poiseuille flow, at $c_l = 0.50$, $\alpha = 0.303$, $\beta = 0.00$.

As can be seen, basing the Reynolds number upon the maximum flow velocity will indeed provide an upper bound, as we could have selected an alternative point across the channel (all of which having a smaller velocity). As the input standard deviation is increased, the flux of the flows is observed to decrease, especially in the upper regions. Inspecting the curvatures, the deterministic flow is seen to be inflexionless with a negative curvature across the boundary layer. Conversely, the

stochastic flows are seen to introduce inflection points, where the second derivative changes sign, both in the immediate vicinity of the wall and also in the upper half of the domain, at $x_2 \approx 0.2$. Furthermore, stochasticity is seen to increase curvature in the immediate vicinity of the wall. This is where the critical point, x_2^c, is located. As the standard deviation is increased, the curvature in this region also increases and we therefore expect the flow to become progressively less stable. It should be noted that the wall gradients actually appear to decrease with the size of the input standard deviation, and this is because the velocity profiles have been scaled back to have a maximum value of unity. It would therefore seem that it is curvature in the vicinity of the wall, not gradients, that are primarily responsible for pushing the neutral curve to the left.

Below, in figure 6.20, we plot the critical Reynolds number, corresponding to the above flows.

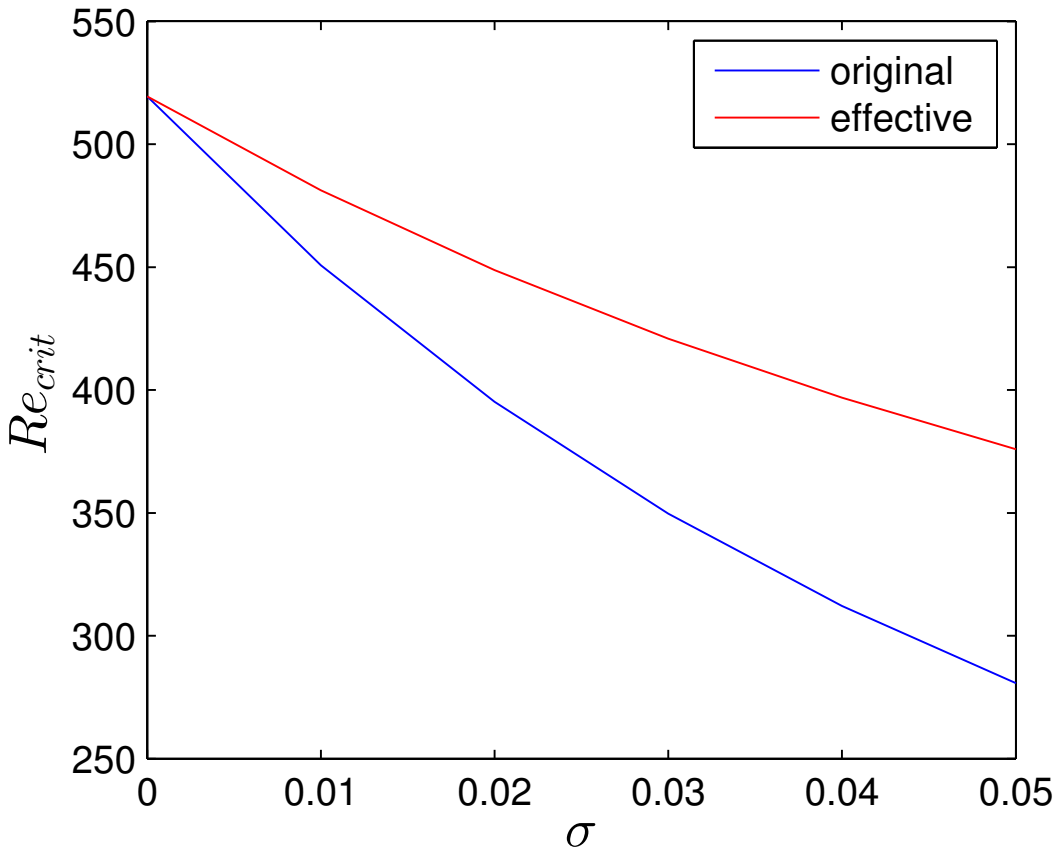

Figure 6.20: Critical Reynolds number as a function of input standard deviation, for the Blasius boundary layer, at $c_l = 0.50$, $\alpha = 0.303$, $\beta = 0.00$.

The blue curve represents the critical Reynolds number, assuming that stochasticity does not modify the free stream velocity, whilst the red curve depicts the corrected

critical Reynolds number, when the base flow is scaled back to a maximum value of unity. The true critical Reynolds number will sit somewhere between the two curves, depending upon the velocity used in its definition. Comparing the result to those obtained for the case of plane Poiseuille flow, it would seem that the asymptotic stability of the Blasius boundary layer is far less sensitive, at least for the type of stochasticity considered here.

6.5.1.5 Neutral Curves

However, it should be remembered that we assumed that the most unstable wave-number would not change as we increased the stochasticity and would therefore remain at $\alpha = 0.303$. It is interesting to actually test this assumption and construct the full neutral curve in $\alpha - R_e$ space, for the values of input standard deviation aforementioned. To this end, we present these neutral curves below, for both the actual (figure 6.21) and the effective (figure 6.22) Reynolds number.

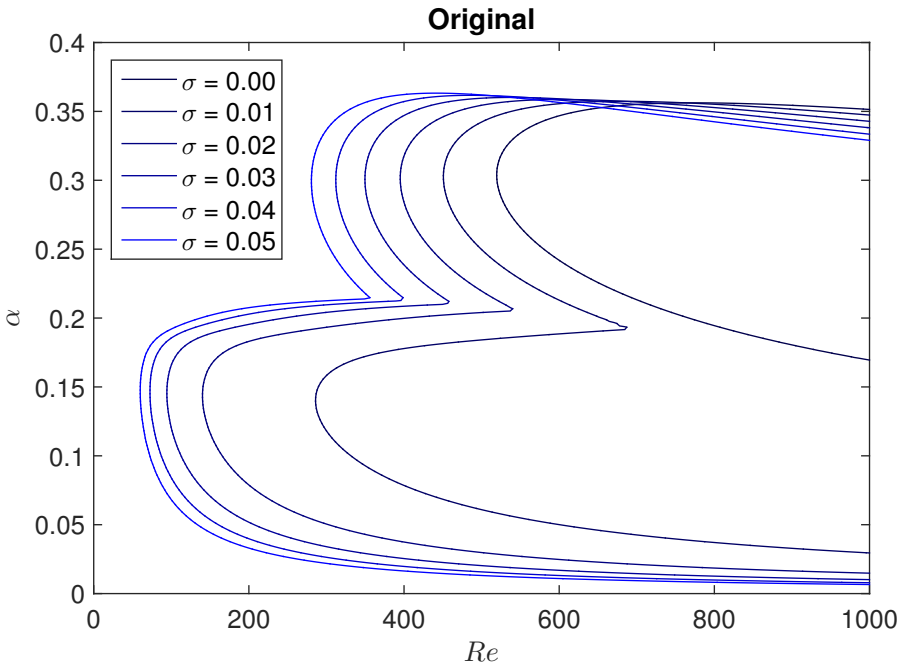

Figure 6.21: Neutral curves for the optimised stochastic Blasius boundary layer, at $c_l = 0.50$, $\sigma = 0.00, 0.01, 0.02, 0.03, 0.04, 0.05$, from inner to outer. Actual Reynolds number.

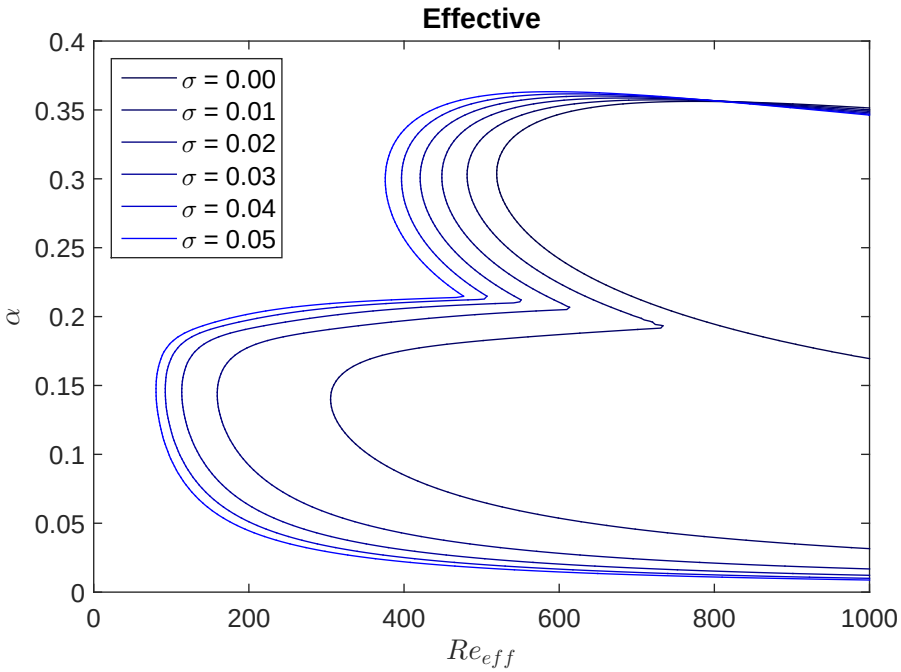

Figure 6.22: Neutral curves for the optimised stochastic Blasius boundary layer, at $c_l = 0.50$, $\sigma = 0.00, 0.01, 0.02, 0.03, 0.04, 0.05$, from inner to outer. Effective Reynolds number.

Clearly, stochasticity does not simply pull the neutral curve to the left, to lower Reynolds number, but significantly modifies the shape of the contour. More specifically, a second lobe appears to form beneath the original, at lower wave numbers. Furthermore, this lower lobe extends further to the left and therefore results in a more significant reduction in the critical Reynolds number than the previous analyses suggested. We list the critical points corresponding to the second lobe in the table 6.1 below, and plot the reduction in the critical Reynolds number as a function of the input standard deviation in figure 6.23.

σ	α_{crit}	R_{ecrit}
0.00	0.303	519.4
0.01	0.139	285.9
0.02	0.143	140.2
0.03	0.145	94.3
0.04	0.147	72.6
0.05	0.148	60.0

Table 6.1: Critical wave-number and Reynolds number for optimised stochastic Blasius boundary layer at varying levels of input standard deviation.

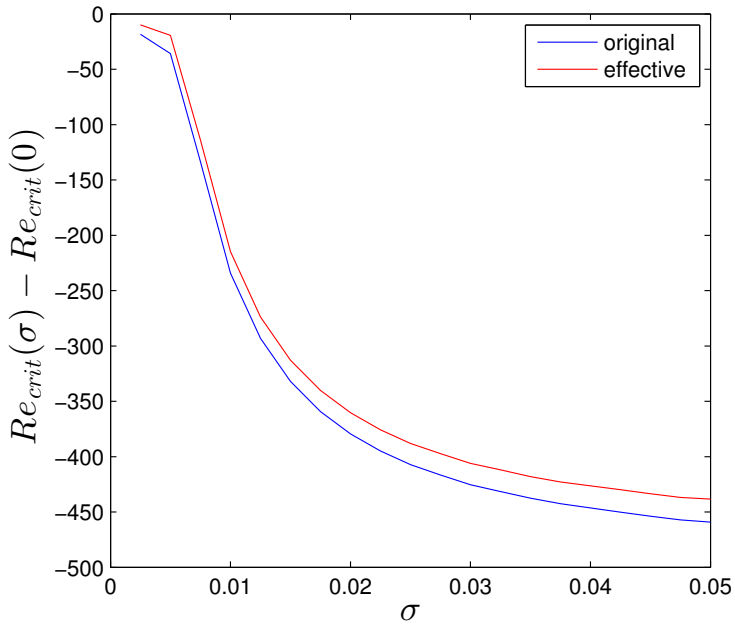

Figure 6.23: Reduction in critical Reynolds number for the optimised stochastic Blasius boundary layer at varying levels of input standard deviation.

Even with a rather conservative input standard deviation, of one percent, the critical Reynolds number has almost halved. Interestingly, the T-S waves are of a very different nature, having a much smaller wave number and therefore exhibiting a much greater stream-wise elongation. Below, in figure 6.24, we plot the modes in primitive co-ordinates.

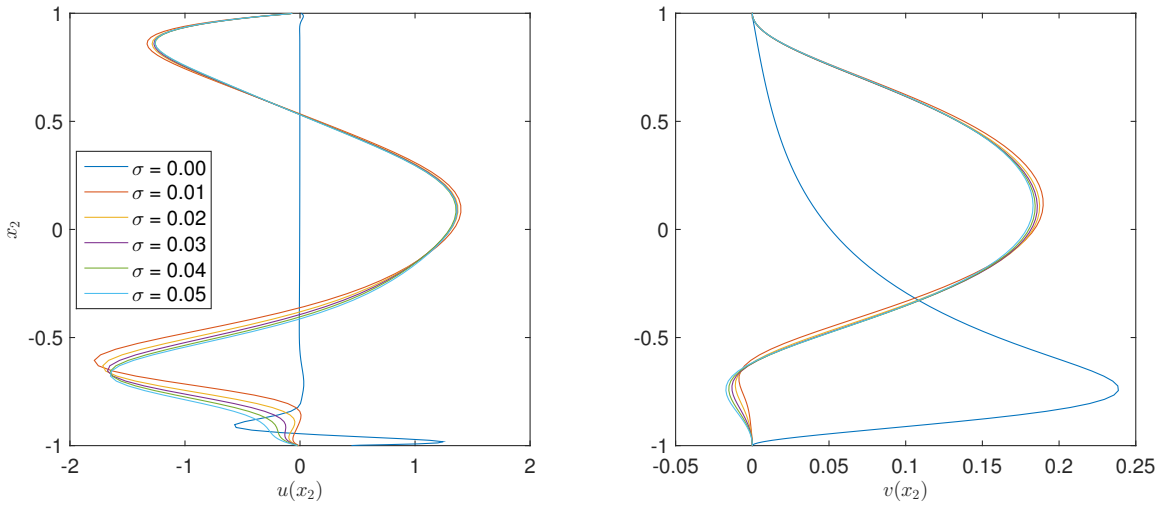

Figure 6.24: Modes (in primitive co-ordinates) corresponding to the critical Reynolds number for the optimised stochastic Blasius boundary layer, at $c_l = 0.50$, $\sigma = 0.00, 0.01, 0.02, 0.03, 0.04, 0.05$.

Clearly, the unstable mode is very different when $\sigma \neq 0$. There are two things at play, the modifications to the curvature of the base flow and the modifications to the gradient. We know that increasing wall curvature decreases stability by pulling the upper branch of the neutral curve down, and this is exactly what we observe with the upper lobe of the neutral curve. As the input standard deviation is increased, so is the wall curvature and the upper branch of the neutral curve moves downwards. It also appears to move towards the left, and in effect we have pulled the neutral curve at a Reynolds number where it originally sat at an infinite wave number to a finite one. The deterministic instability corresponding to this point is viscous in nature, and it therefore seems reasonable to assume the stochastic instabilities at this same wave number are also viscous. The more interesting observation, which we wish to explain, is the addition of a new lobe with unstable modes corresponding to those at $\alpha \approx 0.14$. The flow modifications not only increase wall curvature, but change gradients and introduce inflection points. There are therefore a number of factors to consider, making it hard to pin down a single explanation. To investigate further, it is useful to isolate the individual and combined effects of each of the KLE modes. We know that mode three has a negligible impact and we therefore discard it, leaving us with three modes to investigate. We allow each each stochastic coefficient, ζ_i^*, to take one of three values, namely -1, 0 or 1. So we have three variables, each taking one of three possible values, giving a total of 27 combinations. We plot the neutral curves corresponding to these 27 cases below, in figure 6.25.

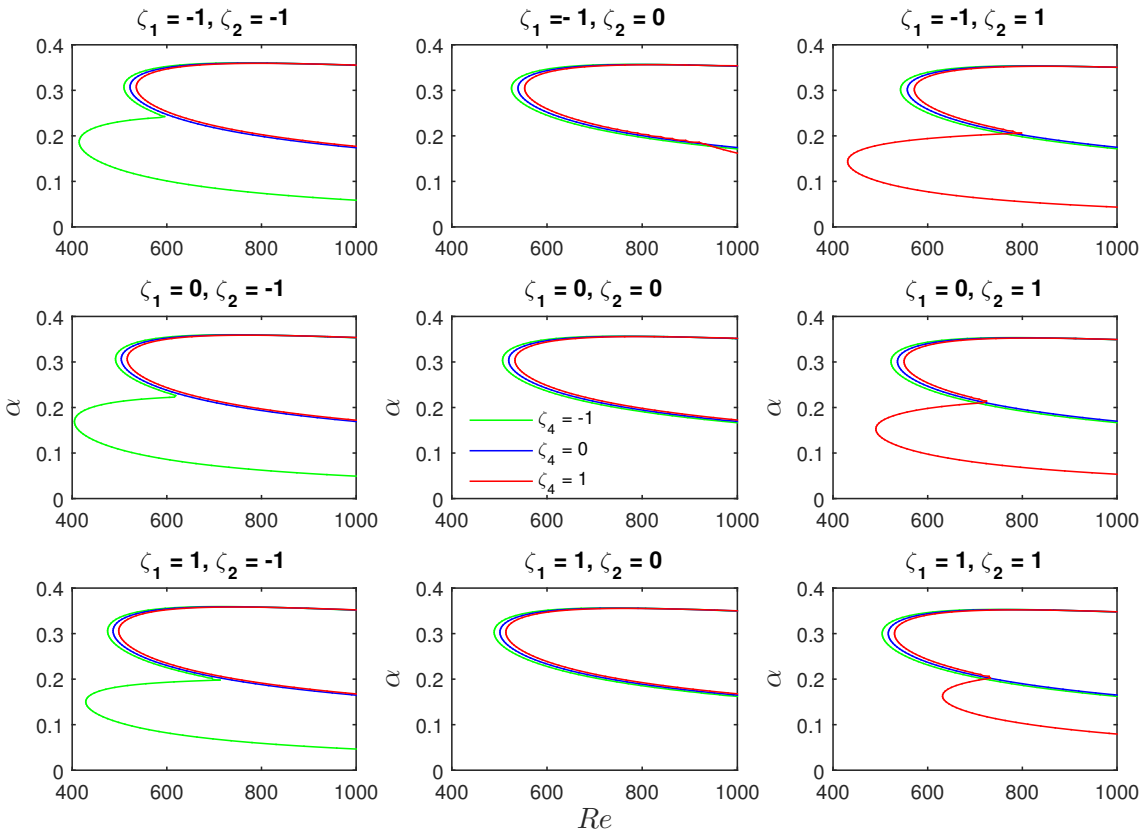

Figure 6.25: Neutral curves for the optimised stochastic Blasius boundary layer, at $c_l = 0.50$, $\sigma = 0.02$. $\zeta_1 = -1, 0, 1$ top to bottom, $\zeta_2 = -1, 0, 1$ left to right, $\zeta_4 = -1, 0, 1$ green, blue and red.

Observing the plot, there are two obvious patterns. The upper lobe shifts to the right as stochastic variable four is increased, and the additional second lobe only appears when stochastic variables two and four take the same sign. If we inspect the wall curvatures, as depicted in figure 6.26, we see the first observation is consistent with our previous analyses and is simply a consequence of the fact that mode four progressively decreases wall curvatures.

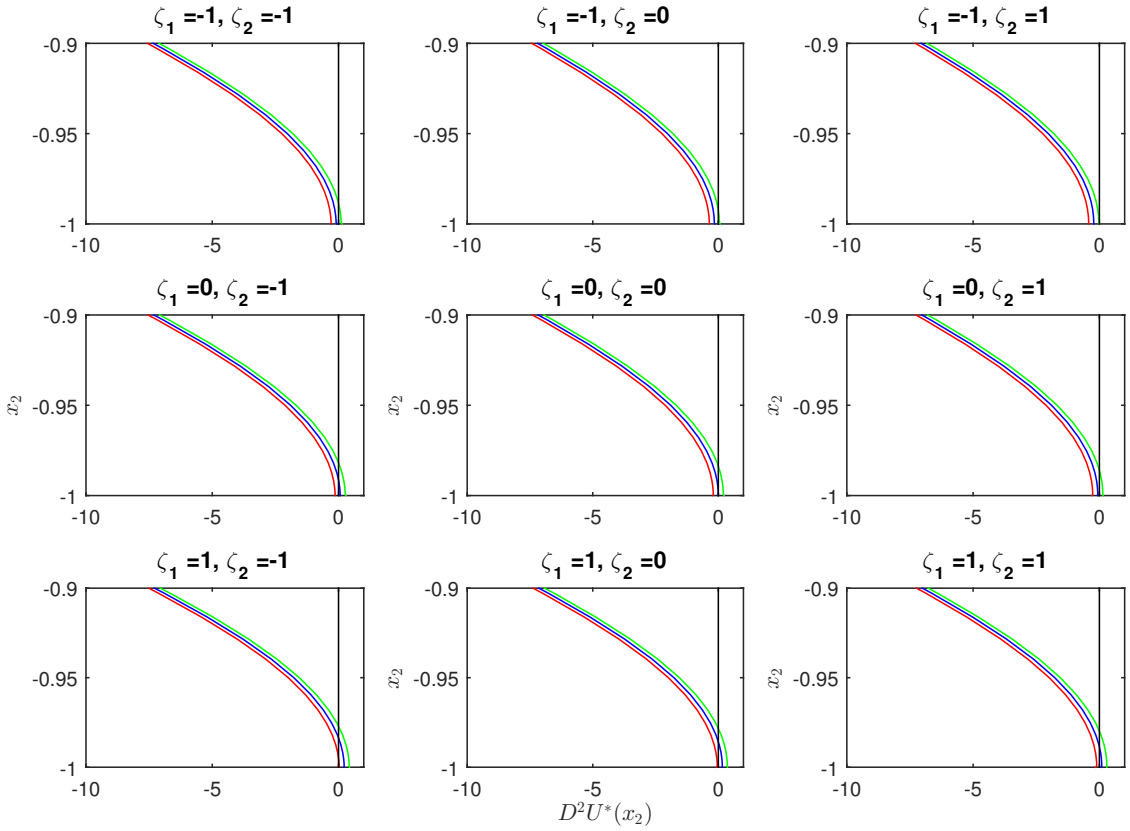

Figure 6.26: Wall curvatures for the optimised stochastic Blasius boundary layer, at $c_l = 0.50$, $\sigma = 0.02$. $\zeta_1 = -1, 0, 1$ top to bottom, $\zeta_2 = -1, 0, 1$ left to right, $\zeta_4 = -1, 0, 1$ green, blue and red.

The second observation is more challenging to explain. Inspecting curvatures and gradients across the channel there is no obvious patterns which emerge. Each of the 27 cases introduce a number of inflection points at various different locations across the channel, and it therefore does not appear to be a single inflection point which is responsible for the additional lobe. The only consistent observation is that in cases where the additional lobe appears, the magnitude of the gradients in the central channel regions are much increased, as depicted below in figure 6.27.

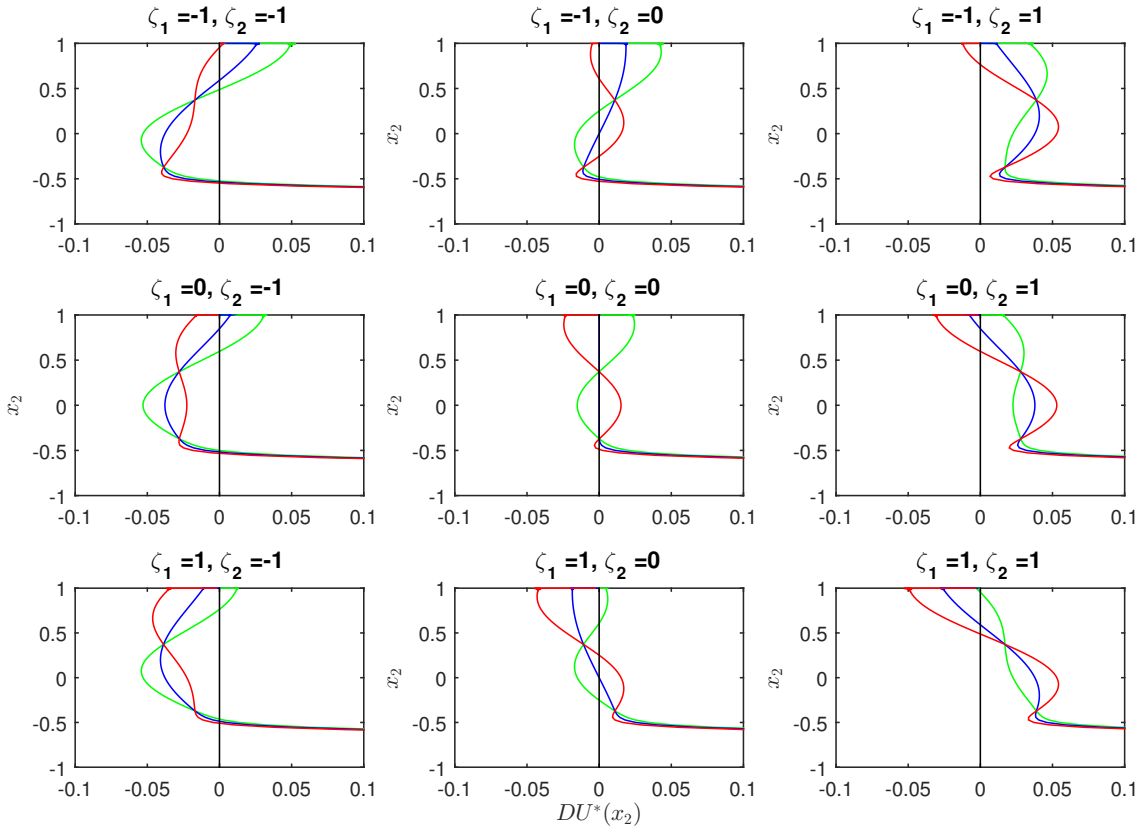

Figure 6.27: Base flow gradients of the optimised stochastic Blasius boundary layer, at $c_l = 0.50$, $\sigma = 0.02$. $\zeta_1 = -1, 0, 1$ top to bottom, $\zeta_2 = -1, 0, 1$ left to right, $\zeta_4 = -1, 0, 1$ green, blue and red.

It seems that these large central gradients, with a magnitude of around 5 percent of the maximum base flow, could be increasing energy transfer to the low wave-number disturbances, thus allowing them to grow into asymptotic instabilities. Whilst these modification appear significant in gradient space, they actually translate into quite minimal modifications to the base flow itself. To test this hypothesis further, we perform a Reynolds-Orr analysis of each of the flows, and plot the ensuing energy transfer below in figure 6.28

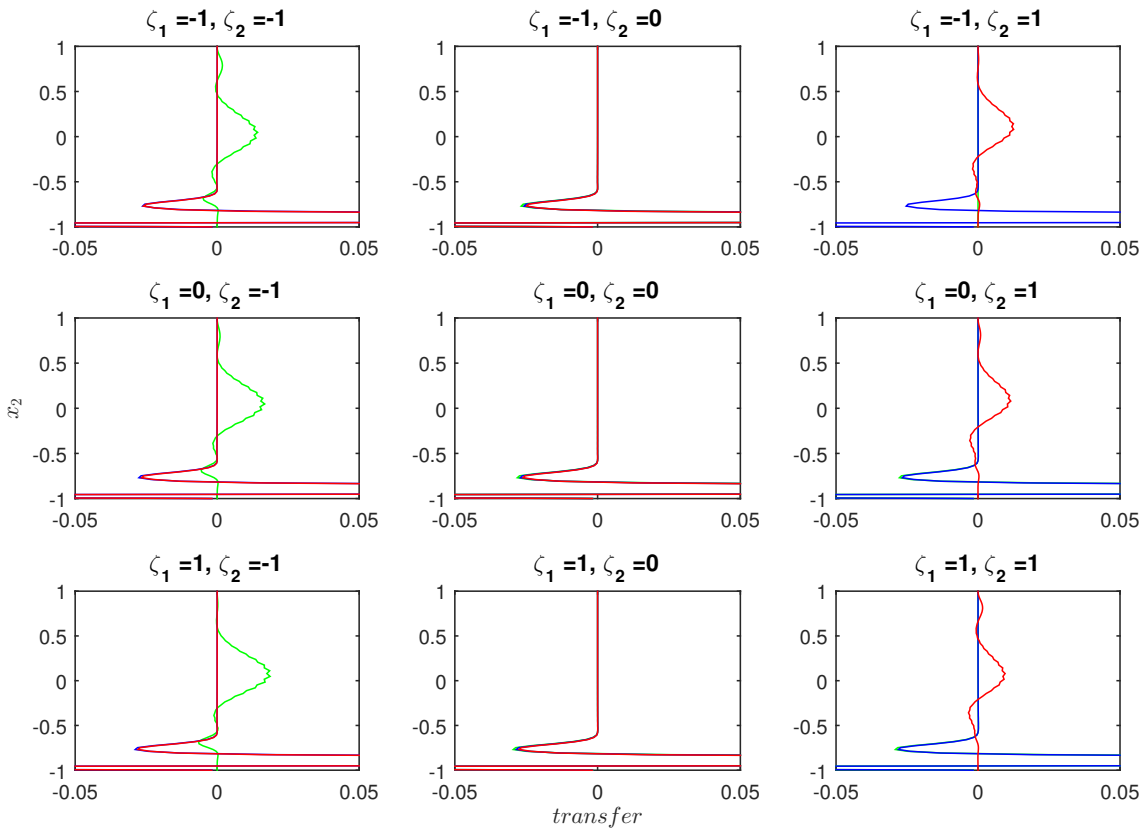

Figure 6.28: Energy transfer from the base flow to the left most perturbations for the optimised stochastic Blasius boundary layer, at $c_l = 0.50$, $\sigma = 0.02$. $\zeta_1 = -1, 0, 1$ top to bottom, $\zeta_2 = -1, 0, 1$ left to right, $\zeta_4 = -1, 0, 1$ green, blue and red.

The above figure would indeed appear to confirm our hypothesis. Firstly, when $\zeta_2 \neq \zeta_4$ there is a large energy transfer in the immediate vicinity of the wall. This is the primary region of energy transfer in these cases and gives rise to the usual upper lobe in the neutral curve. There are clearly large velocity gradients in the wall region which have a capacity to transfer energy to perturbations with large velocity values in this region. It is therefore natural to expect the perturbation corresponding to the critical mode to be a wall mode in these cases. Referring back to figure 6.24 and noting that the $\sigma = 0$ case corresponds to the typical upper lobe critical point at $\alpha \approx 0.3$, we see that this mode does indeed take large velocity values in the vicinity of the wall. More interestingly, in each of the cases where the additional lower lobe appears (when $\zeta_2 = \zeta_4 \neq 0$), there is no longer the dominant energy transfer in the vicinity of the wall, but a significant increase in energy transfer much further away in the exact same region as the increased base flow gradients. The large

central gradients are providing an additional source of energy transfer, transferring energy from the base flow to the low wave number perturbations. Remembering that we are looking at the energy transfer to the leftmost perturbation in the neutral curve, we see that the most unstable perturbations acquire a substantially increased transfer in the central region in all cases where the lower lobe appears. Since neutral stability is achieved when viscous dissipation balances energy transfer, we see that this additional energy source allows the perturbation to become neutrally stable at a lower Reynolds number (as viscous dissipation scales inversely with Reynolds number). In short, increased base flow gradients in the outer regions of a boundary layer are providing additional energy transfer to longer stream-wise perturbations, resulting in earlier transition. Referring once more to figure 6.24 and noting that the $\sigma = 0.01$ case corresponds to the typical lower lobe critical point at $\alpha \approx 0.14$, we see that the corresponding critical mode is now a centre mode taking large values in the outer boundary layer region. The large outer gradients have managed to excite these centre modes, transferring energy and leading to transition at a much reduced Reynolds number.

For completeness, in figure 6.29, we plot the actual base flows corresponding to the above cases. It should be noted that in this instance, we plot the unscaled flows, but as explained the stability results would be the same when scaling the flow back and the Reynolds number up.

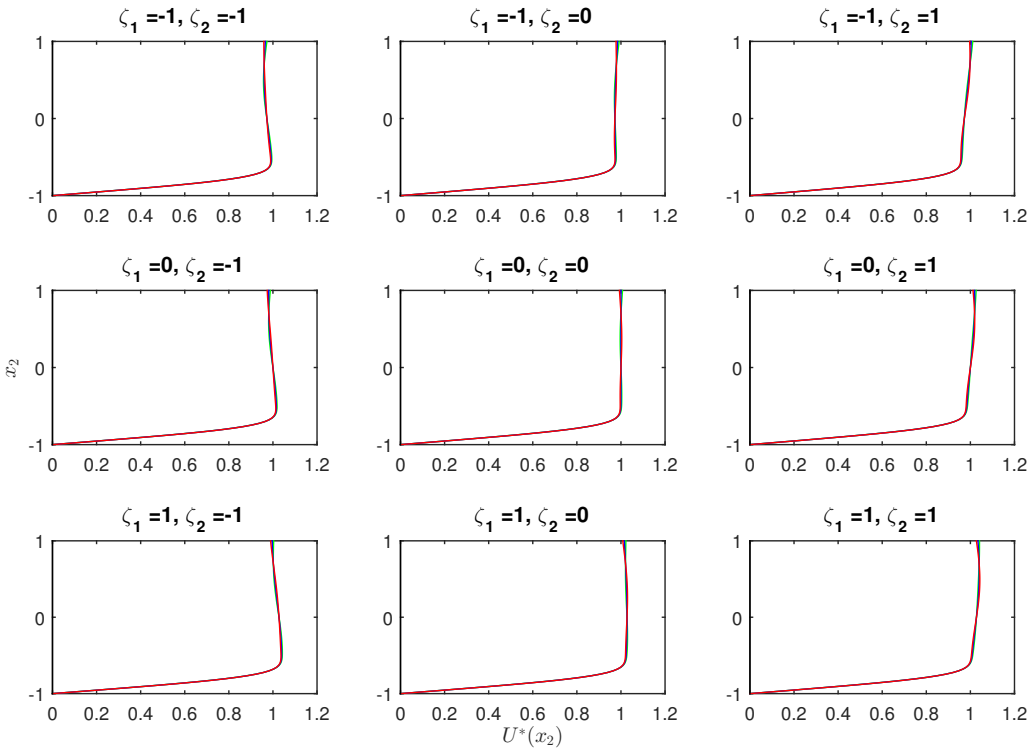

Figure 6.29: Base flows of the optimised stochastic Blasius boundary layer, at $c_l = 0.50$, $\sigma = 0.02$. $\zeta_1 = -1, 0, 1$ top to bottom, $\zeta_2 = -1, 0, 1$ left to right, $\zeta_4 = -1, 0, 1$ green, blue and red.

As can be seen, the modifications to the actual base flow, which translate into the increased gradients in the central boundary layer region, are actually quite minimal. The red, blue and green base flows are almost indistinguishable, yet the minor difference in velocities translate into a more significant difference in velocity gradient and, as we have seen, fundamentally alter the shape of the neutral curve. It would appear that a reasonably modest stochastic defect can therefore have a significant impact on stability. For instance, if one was designing an aerofoil assuming the base flow was deterministic, then it would be reasonable to assume critical flow conditions of $\alpha \approx 0.3$ and $R_e \approx 519$. However, in reality the base flow is not deterministic and it may have small deviations similar to those investigated above, and the whole design may be focusing on the wrong point in the neutral curve.

Referring back to figure 6.23, we see that the critical Reynolds number varies in inverse proportional to the input standard deviation. Bottaro [9] performed a similar investigation for Couette flow, investigating the sensitivity of the Orr-Sommerfeld operator's eigenvalues for non-infinitesimal variations in a plane Couette base flow. They showed that sufficiently large modifications to the base flow could induce

linear instability, with the critical Reynolds number varying as r^{-1} (where r is an energy based measure of the size of the modification $\delta U(x_2)$, $r^2 = \int_{x_2} \delta U^2(x_2) dx_2$). Noting that Bottaro's energy based measure of size is directly proportional to our measure of size, namely the input standard deviation, we see that the results are consistent. However, Bottaro used a variational framework to find the optimised flow which maximised the asymptotic growth rate for a given perturbation size. Our results extend these works as our disturbances are not only selected from a physically feasible set, but we are able to quantify the likelihood of such a base flow.

To achieve a clearer probabilistic picture we compute the critical Reynolds number as a function of the random variables. We have established that ζ_3 does not contribute to variability and we once again set this variable to zero. Further, observing the neutral curves in figure 6.25 we see that the additional lower lobe extends further to the left than the original upper lobe when $\zeta_2 > 1$, $\zeta_4 > 1$ and $\zeta_1 < 0$, or when $\zeta_2 < -1$, $\zeta_4 < -1$ and $\zeta_1 < 0$. We therefore set $\zeta_1 = -1$, and compute the critical Reynolds number as a function of random variables ζ_2 and ζ_4. Figure 6.30 depicts the critical Reynolds number and figure 6.31 depicts the corresponding stream-wise wave-number.

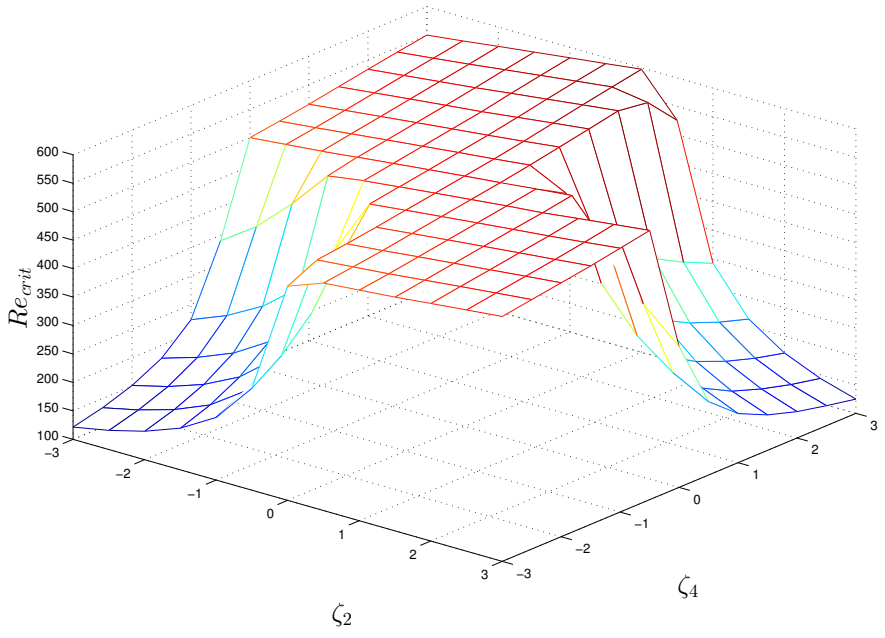

Figure 6.30: Critical Reynolds number ($\beta = 0$) for stochastic Blasius boundary layer, at $c_l = 0.50$, $\sigma = 0.02$. $\zeta_1 = -1$, $\zeta_3 = 0$, ζ_2 and ζ_4 varying.

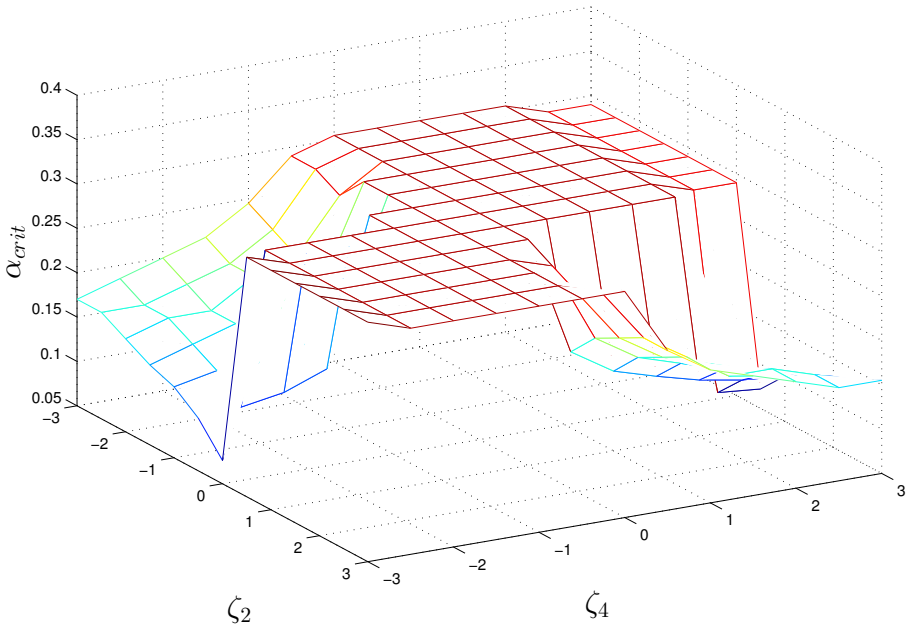

Figure 6.31: Critical wave-number number ($\beta = 0$) for stochastic Blasius boundary layer, at $c_l = 0.50$, $\sigma = 0.02$. $\zeta_1 = -1$, $\zeta_3 = 0$, ζ_2 and ζ_4 varying.

The figures are clearly consistent with previous analyses, with the critical Reynolds number decreasing rapidly and the lower lobe appearing only when random variables ζ_2 and ζ_4 take the same sign. Furthermore, since the random variables are standard normal random variables one may use standard z-tables to map the ζ values to probabilities and we effectively have a probability distribution for the critical Reynolds number. For instance, observing the neutral curves in figure 6.25 we see that the additional lower lobe extends further to the left than the original upper lobe when $\zeta_2 > 1$, $\zeta_4 > 1$ and $\zeta_1 < 0$, or when $\zeta_2 < -1$, $\zeta_4 < -1$ and $\zeta_1 < 0$. Since the random variables are independent, zero mean, unit variance and Gaussian distributed we can compute the probability of this event as $P(\zeta_2 > 1, \zeta_4 > 1, \zeta_1 < 0) + P(\zeta_2 < -1, \zeta_4 < -1, \zeta_1 < 0) = 2P(\zeta_2 > 1, \zeta_4 > 1, \zeta_1 < 0) = 2P(\zeta_2 > 1)P(\zeta_4 > 1)P(\zeta_1 < 0) = 0.025$. We can therefore see that the additional lower lobe occurs, with the critical Reynolds number shifting to this lower wave-number region, with a probability of around 2.5 percent. However, a much more extreme event would be required to achieve the critical Reynolds numbers presented in table 6.1. These critical Reynolds numbers, which vary in inverse proportional to the input standard deviation, required much larger realisations of the random variables and the resulting probability is far less than one percent.

6.5.1.6 Relation to Jet Flows

There have been numerous studies on the instability of a plane laminar wall jet [12] [88] [49], and it is known that such a jet has two modes of temporal instability. One is attributed to large scale disturbances (low frequencies) and associated with the outer inflection point in the mean flow, whilst the other is attributed to small scale disturbances evolving in the vicinity of the wall. The stream-wise velocity component of the eigenfunction associated with the large scale disturbance takes its maximum absolute value in the vicinity of the outer inflection point of the base flow. These disturbances are dominated by inertia and may be considered inviscidly unstable. Conversely, the stream-wise velocity component of the eigenfunction associated with the small scale disturbance takes its maximum absolute value in the vicinity of the wall, and this disturbance may be considered viscous. The instability of a wall jet is thus caused by both the inflection point in the base profile and by viscous effects in the inner wall region, with the large scale disturbances associated with the outer inflection point leading to the critical Reynolds number, which based upon the maximum velocity of the jet and its local half width (the point at which the local velocity is half its maximum) takes a value of around 56.68 (at stream-wise wave number 1.16) [49].

With these results in mind, we take our optimised stochastic base flow, with $\sigma = 0.01$ and $c_l = 0.50$, and inspect the relationship between the flow (and its gradients) and the mode corresponding to the critical point, that is the mode with wave-numbers $\beta = 0.000$ and $\alpha_{crit} = 0.139$. Figure 6.32, below, depicts the stream-wise velocity component of this mode along with the base flow, its first and second derivative.

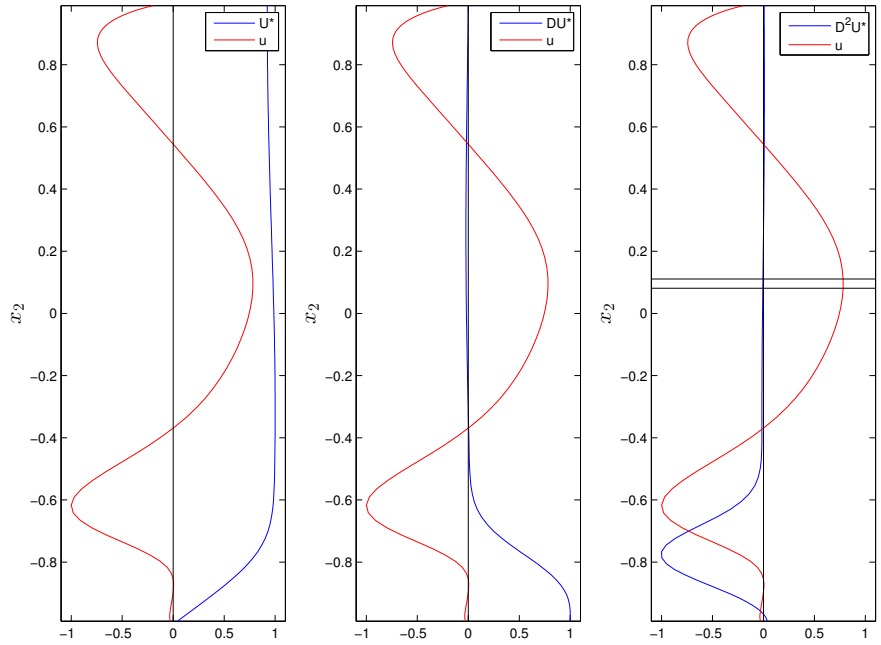

Figure 6.32: Stream-wise velocity of critical mode and optimal stochastic base flow (left), gradient (centre) and curvature (right) for the Blasius boundary layer. Horizontal lines in the right subplot corresponding to the maximum of the perturbation at $x_2 = 0.08$, and the inflection point in the base flow at $x_2^* = 0.11$. $\sigma = 0.01$, $c_l = 0.50$, $\beta = 0.000$ and $\alpha_{crit} = 0.139$. All scaled to a maximum absolute value of unity for visualisation.

Firstly, inspecting the base flow profile in the far left subplot, it could be argued that the boundary layer has acquired an almost jet like characteristic in the outer region. That is, it bows out to some maximum value before retarding slightly. This is obviously not as extreme as a typical jet flow but the general characteristic shape bears a resemblance. Turning attention to the centre and far right subplots, inspecting the gradient and the curvature of the base flow, we see that the flow locally satisfies Fjørtoft's criterion. Locally, the mean velocity profile is monotonically decreasing (the gradient is negative) with the inflection point being a local minima of the velocity gradient. Hence $D^2U(x_2)(U(x_2) - U(x_2^*)) < 0$ around x_2^*, where $D^2U(x_2^*) = 0$ and x_2^* is the inflection point. Further, inspecting the perturbation, we see that it takes a local maximum value (at $x_2 = 0.08$) in the vicinity of the outer inflection point of the base flow (at $x_2 = 0.11$). Just below the inflection point the vorticity (or velocity gradient) is increasing in amplitude (becoming more negative), and just above it is decreasing in amplitude. There is thus a local vorticity extremum at the inflection point, which could cause an instability. To see this, consider three

infinitesimal layers, one just below the inflection point, one at the inflection point and one just above. If the vorticity increased monotonically, then a fluid particle descending from the upper layer into the middle would bring its vorticity with it. This excess vorticity in the middle layer would tend to replace the fluid to its right with higher vorticity and to its left with lower vorticity. The net effect being that the original fluid element is forced back up into the upper layer, and the flow is stable. However, when the vorticity is not monotonic this is not true. In this case, if a fluid element happened to arrive in the middle layer from above or below, it would not be forced back and the flow would be inviscidly unstable. The perturbation takes a local maximum in the vicinity of the inflection point, its gradient thus changes and it could increase the magnitude of the vorticity below the inflection point whilst decreasing that above. It thus has the capacity to accentuate the effects described.

We may relate this jet like instability to our previous Reynolds-Orr analyses. Noting that the velocity gradient of the base flow takes a local maximum in the vicinity of the base flow inflection point, which occurs in a region around the maximum of the perturbation, we see that the product of the base flow velocity gradient with the perturbation velocity takes a large value in this region. Referring once more to the Reynolds-Orr formulation, we see that there is thus a significant transfer of energy from the base flow to the perturbation, and the analyses are therefore consistent. However, referring once more to figures 6.25 to 6.28, we see that there are a number of cases which also have an inflection point in this region, where the perturbation responsible for the lower lobe takes its maximum, which yet do not lead to the formation of this lower lobe. This is simply because the flow is not inviscid, and the jet like instability only arises when the velocity gradients, and hence the energy transfer, are sufficiently large to overcome viscous dissipation.

In summary, it appears that when velocity gradients in the outer region of the boundary layer are sufficiently large, they create jet like profiles and excite centre modes leading to an additional lower lobe in the neutral curve. When velocity gradients in the outer region are smaller, below some critical size, there is insufficient energy transfer to these centre modes and the usual energy transfer to the wall modes dominates leading to the usual viscous instability corresponding to the upper lobe of the neutral curve. As with the jet, it appears we therefore have two primary modes of instability; an unstable large scale (low wave-number) disturbance in the form of a centre mode when outer velocity gradients are sufficiently large, and a small scale (large wave-number) disturbance in the form of a wall mode otherwise. The former may be considered an inviscid instability, and the latter associated with the wall region may be considered a viscous instability.

6.5.1.7 Stabilising and Destabilising Modifications

In order to confirm our assumptions, regarding the impact which both curvature and gradients have on the neutral curve it is useful to isolate each, and that is what we do below. The above analyses suggest a stabilising modification which significantly decreases curvature in the vicinity of the critical point without enhancing gradients in the central boundary layer region. Such a modification would push the upper lobe of the neutral curve to the right without the creation of a lower lobe. A modification with such properties would therefore be localised to the wall and decay fast away from the wall, such as an exponential decay. These are the exact modifications considered by Healey [32], of the form

$$U_{mod}(x_2) = x_2^2 \exp(\frac{-(a_0 x_2 - a_1)}{a_2}). \tag{6.23}$$

Setting $a_0 = 10$ and $a_1 = -1$ to effectively map from the Chebyshev grid to the physical, and selecting $a_2 = 0.3$, we plot the modification along with its gradient and curvature, as depicted in figure 6.33.

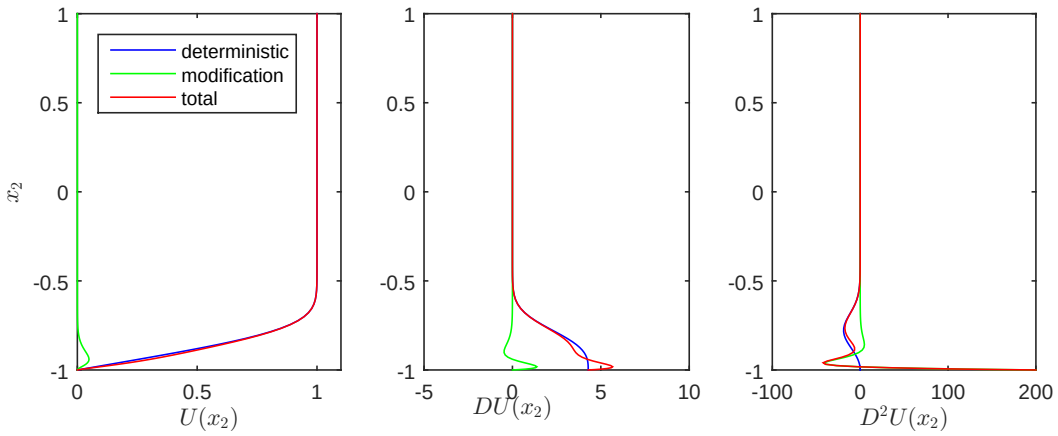

Figure 6.33: Exponential stabilising modification, flow (left), gradient (centre) and curvature (right) for the Blasius boundary layer. $a_0 = 10$, $a_1 = -1$ and $a_2 = 0.3$.

As can be seen, the modification makes very little difference to the base flow itself, yet significantly reduces the curvature in the region of the critical point, and should therefore shift the neutral curve to the right without the creation of an additional lobe. We also plot the neutral curve produced by such a modification below, in figure 6.34.

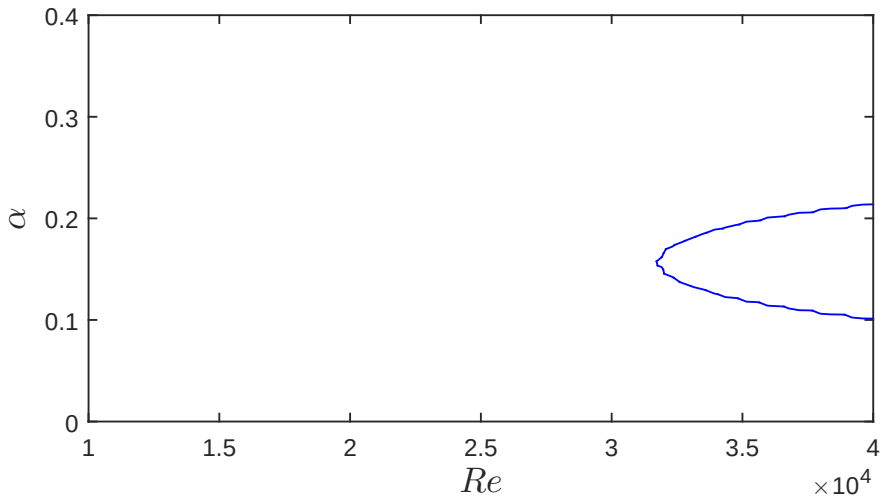

Figure 6.34: Neutral curve corresponding to the exponential stabilising modification for the Blasius boundary layer. $a_0 = 10$, $a_1 = -1$ and $a_2 = 0.3$.

As can be seen, stability is significantly enhanced, by two orders of magnitude in fact.

In addition, analyses would suggest a small modification which significantly enhanced central gradients without affecting wall curvatures would have the capacity to significantly reduce stability. We consider a modification of the form

$$U_{mod}(x_2) = a_3 x_2^2 \exp(\frac{-x_2}{a_2}) 1(x_2 > 0), \tag{6.24}$$

where $1(x_2 > 0)$ is the indicator function, taking a value of unity when x_2 is positive and 0 otherwise. We plot such a modification below in figure 6.35, for $a_3 = 5$ and various values of the parameter a_2.

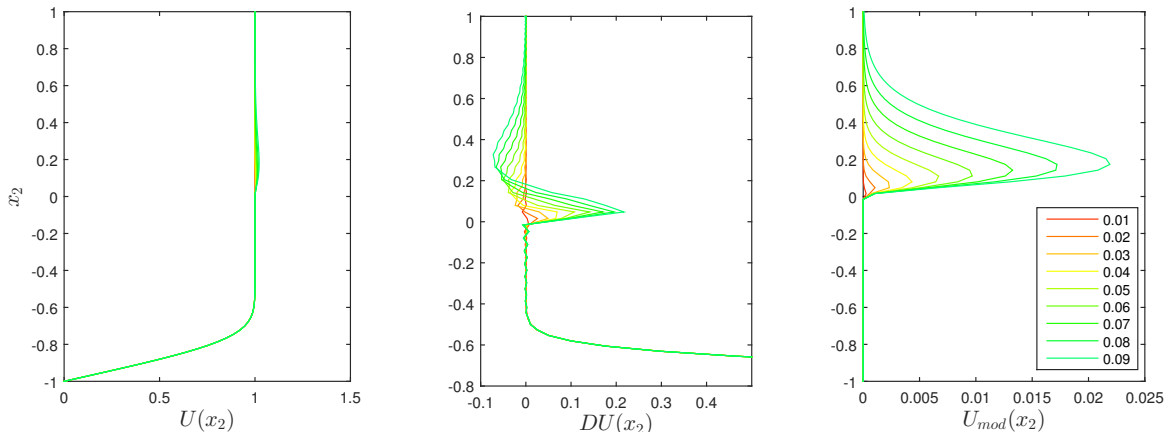

Figure 6.35: Exponential destabilising modification, flow (left), gradient (centre) and curvature (right) for the Blasius boundary layer. $a_3 = 5$, colours corresponding to parameter a_2.

We also plot the neutral curves corresponding to the above cases, as shown in figure 6.36.

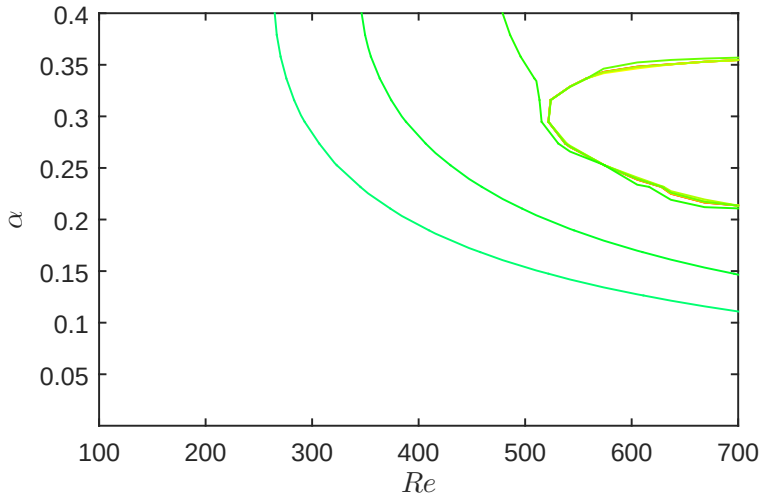

Figure 6.36: Neutral curve corresponding to the exponential destabilising modification for the Blasius boundary layer. Colours corresponding to parameter a_2 (as in figure 6.35).

Even with the largest modification, with $a_2 = 0.09$, the actual base flow is locally enhanced by a maximum value of about 2 percent, from unity to 1.02, whilst leaving the remainder of the flow mostly unchanged. As expected, this significantly reduces the critical Reynolds number. Hence, a small reduction in curvature or an increase in central gradients can significantly increase/decrease stability properties, if added in the right place.

6.6 Summary

In this chapter, we have studied the stability of the stochastic Blasius boundary layer. We conducted a number of numerical experiments, involving both modal and non modal analyses. In general, from a physical perspective, we have seen that all flows become more sensitive to stochastic defects as the correlation length of the stochastic base flow is decreased, and the profile thus becomes more erratic. From a numerical perspective, we have seen the superior efficiency offered by the WCE in low stochastic dimensions.

Through spectral analysis, we have shown that modes throughout the spectrum exhibit a similar sensitive to uncertainty. Furthermore, we showed that our structured perturbations are bounded by the log resolvent norm contours of the more general unstructured perturbations of the ϵ-pseudospectra.

As was the case with the Poiseuille flow, transient analyses revealed that stochastic defects have no initial impact on perturbation energy growth and, in general, the effects of stochasticity accumulate with time. We showed that variability (standard deviation) in the perturbation energy growth increased almost linearly, relative to the mean, with time, in the case of long span-wise perturbations ($\beta \approx 0$). We have also seen that neutral curves can be highly sensitive to stochastic defects, which can significantly reduce the critical Reynolds number. Stochastic defects not only shift neutral curves but can actually alter the entire shape. Wall curvatures are generally responsible for horizontal shifts of the neutral curve, where increases in wall curvature cause a leftward shift in the neutral curve and therefore a reduction in the critical Reynolds number. In addition to this, defects which cause moderate increases to central base flow gradients facilitate an additional energy transfer to much longer stream-wise waves (lower α) and result in the appearance of an additional lower lobe in the neutral curve. Further, we show that the additional lobe can be related to jet like instabilities. The modified flow not only resembles a jet in appearance, but an outer inflection point is created. The stream-wise velocity component of the eigenfunction associated with the large scale disturbance, corresponding to the leftmost point on the lower lobe, takes its maximum absolute value in the vicinity of the outer inflection point of the base flow. These disturbances are dominated by inertia and may be considered inviscidly unstable, and are exactly the kind found in jets. This additional lobe often times extends further to the left than the original, and therefore results in a significantly reduced critical Reynolds number, which we show varies in inverse proportion to the size of the input standard deviation.

Chapter 7

Conclusions and Future Work

7.1 Conclusions

This thesis makes a contribution to the ever growing literature on flow stability. More specifically, a broader view of stability analysis is introduced allowing for stochasticity, thus giving a probabilistic view of stability. In the introductory chapters, we review the theory that underpins the stability analysis of shear flows, and also review numerical techniques available for solving stochastic partial differential equations. In the latter chapters, we marry the theory of polynomial chaos and stability analysis, to study the stability of a range of shear flows subject to uncertainty in the base flow profile. From a numerical perspective, our results indicate that the Wiener chaos expansion provides a highly efficient framework for solving probabilistic flow problems in low stochastic dimensions, or equivalently when the stochasticity present is not too erratic, whilst more traditional Monte Carlo methods remain superior in higher dimensions. In general, we show that our stochastic approach to stability analysis takes nothing away from the deterministic analysis but simply gives a richer solution. That is, the deterministic results are recovered from the mean of the stochastic results. Nothing is lost, information is only gained, such as the higher statistical moments. Furthermore, as we have shown in a number of examples, we are able to assign probabilities to our results, such as the probability a stable solution become unstable, or the probability that the critical Reynolds number falls below a certain threshold.

In chapter four we motivate the choice of stochasticity, discuss the numerical implementation and provide a number of case studies to identify suitable levels of discretization. Based upon experimental observations, we show that a Gaussian kernel provides a suitable model for the type of randomness present in a Blasius boundary layer, and identify typical scales for the parameters required to model

such a flow. We investigate the relative merits of tensor Wiener chaos expansions, sparse Wiener chaos expansions and LHS based Monte Carlo sampling techniques, concluding that the optimal choice of stochastic method is highly dependent upon the stochastic dimension, and hence the correlation length of the process. In low dimensions the Wiener chaos expansion on a tensor grid is the most computationally efficient, but suffers from the curse of dimensionality which renders it inefficient in higher dimensions. In moderate stochastic dimensions the Wiener chaos expansion on a sparse grid is able to alleviate the problem and is shown to be more efficient than both tensor WCE and stratified Monte Carlo methods. Whilst the computational cost of the sparse WCE does not increase exponentially with the number of stochastic dimensions, it does still increase and in very high dimensions stratified Monte Carlo approaches prove to be more computationally efficient. However, WCE methods are far more efficient in moderate to low stochastic dimensions, and, furthermore, provide a much richer solution allowing for variance based sensitivity analysis.

In chapter five, the primary focus is on Poiseuille flow, where stochastic versions of the spectra, the neutral curve and the perturbation energy growth function are presented. From a physical perspective, stochasticity becomes increasingly important as the correlation length of the base flow is reduced. Stochastic spectral analyses show modes in the vicinity of the Y-branch to be much more sensitive to defects than those further away, with the results of our structured perturbations bounded by the log resolvent norm contours of the more general perturbations of the ϵ-pseudospectra. Neutral curves can be highly sensitive to stochastic defects, uncertainty can significantly reduce the critical Reynolds number and may partially explain the deviations between theory and experiment, which are commonly observed. Our transient analyses reveal that stochastic defects have no initial impact on perturbation energy growth and, in general, effects accumulate with time. For the limited cases investigated, the variability in the perturbation energy growth was observed to increases almost linearly, relative to the mean, with time, in the case of Poiseuille flow, whilst variability in the Couette flow remains of a negligible magnitude at all times. That is, transient growth of Poiseuille flow is far more sensitive than it is for Couette flow. For the Poiseuille flow, it appears that neither the number of inflection points in a defect, nor the input variance attributed to a defect, influence the variance in perturbation energy growth attributed to that defect. Instability, arising from stochastic imperfections, must not be of an inflectional nature, but viscous instead. Variance based sensitivity analyses reveal that only defects which are symmetric about the channel centre-line have the capacity to alter stability properties. Reynolds-Orr analyses explain such observations, showing

that anti-symmetric defects lead to an increase in energy transfer (from the base flow to the perturbations) in one region of the channel which is cancelled by a decrease in the opposite half of the channel. Conversely, symmetric defects can lead to an increase in the energy transfer across the whole channel, thus allowing sooner transition and reducing the critical Reynolds number.

In chapter six, we focus on the stochastic Blasius boundary layer, presenting stochastic versions of the spectra, the neutral curve and the perturbation energy growth function are presented. In contrast to the Poiseuille flow, spectral analysis shows modes across the spectrum to be equally sensitive to defects. Transient analyses show that the variability in transient growth grows almost linearly to the deterministic result for infinite span-wise ($\beta \approx 0$) waves, but at a much lower rate than that observed for Poiseuille flow. Interestingly, stochastic defects not only shift neutral curves but can actually alter the entire shape too. More specifically, results show that wall curvatures are responsible for horizontal shifts of the neutral curve, where increases in wall curvature cause a leftward shift in the neutral curve and therefore a reduction in the critical Reynolds number. In addition to this, defects which cause moderate increases to central gradients facilitate an additional energy transfer to much longer stream-wise waves (lower α) and result in the appearance of an additional lower lobe in the neutral curve. Further, we show that the additional lobe can be related to jet like instabilities, and often times extends further to the left than the original, and therefore results in a significantly reduced critical Reynolds number, which we show varies in inverse proportion to the size of the input standard deviation.

7.2 Future Work

There are a number of possible extensions to the work presented here, including:

- Investigating different models for the auto-covariance of the stochastic element of the flow field. Our analyses focused on a Gaussian auto-covariance, one could investigate other kernels, such as the exponential kernel which appears to be a good model for a forced Blasius boundary layer. More practically, one could use experimental flow data to build the auto-covariance structure which is found in other real life flow fields, such as the plane Poiseuille and Couette flow.
- Investigating more complex flows with more complex geometries, such as the Batchelor vortex, which is commonly used as a model for the vortex wake

created by aircraft.

- Designing control laws. The insights gained from stochastic stability analysis can inform us of which kind of defects can be troublesome, leading to asymptotic stability. Control laws could therefore be developed to detect such structures and eradicate them as necessary. Alternatively, flow laws could be developed to control the stochastic component of a flow, with the objective being to minimise flow variance. A stochastic framework effectively allows us to make risk based decisions, rather than focusing primarily on the deterministic part of a flow, or the expectation, we can also factor in higher statistical moments, such as variance. There is little point making concerted effort in controlling expectation when variance is disproportionately large.

Appendix

A.1 Orthogonal Polynomials

By a system of orthogonal polynomials, we denote a set $\{P_n(z)\}_{n=1}^{\infty}$, where n is the polynomial degree. The polynomials are deemed orthogonal if the inner product $< P_n, P_m >$ vanishes for $n \neq m$. If the variable z is continuous, then the inner product is defined as a weighted integral over a suitable interval:

$$< P_n, P_m >= \int_a^b P_n(z) P_m(z) w(z) dz$$

where $w(z)$ is a positive weight function.

More specifically, we are interested in orthogonal families of polynomials that form a basis on the function space $L_w^2 = \{f :< f, f >< \infty\}$. We further limit our attention to families for which expansions of the form:

$$f(z) = \sum_{n=1}^{N} a_n P_n(z)$$

result in spectra that decay as $N \to \infty$.

A.2 Probabalist's Hermite Polynomials

There are generally two definitions of Hermite polynomials, the probabalist's and the physicist's. We shall focus on the probabalist's Hermite polynomials, which are orthogonal with respect to the weight function $w(z) = \frac{1}{\sqrt{2\pi}} \exp\left(\frac{-z^2}{2}\right)$, and z is defined over the real line, i.e. $a = -\infty$, $b = \infty$. These Hermite polynomials are

defined according to [42]:

$$H_n(z) = (n!)^{-\frac{1}{2}}(-1)^n \exp\left(\frac{z^2}{2}\right)\frac{\partial^n}{\partial z^n}\exp\left(\frac{-z^2}{2}\right) \tag{7.1}$$

where we have included the normalising factor, $(n!)^{-\frac{1}{2}}$, such that the inner product $< H_n(z), H_m(z) >= \delta_{nm}$. In practice, one forms the non-normalised Hermite basis according to the recursive relationship:

$$H^u_{n+1}(z) = zH^u_n(z) - nH^u_{n-1}(z) \tag{7.2}$$

with $H^u_0(z) = 1$ and $H^u_1(z) = z$, and then normalises each with the scaling factor $(n!)^{-\frac{1}{2}}$, $H_n(z) = (n!)^{-\frac{1}{2}}H^u_n(z)$.

B.1 Multidimensional Polynomial Chaos Basis

The multidimensional polynomial chaos basis functions are defined from an incomplete temporization of the one dimensional basis functions. Each member of the multidimensional basis can be written as a product of one dimensional polynomials in the appropriate random variable. In order to specify and evaluate the elements of the multidimensional basis, we need to associate each basis function, $H_{\alpha^i}(\boldsymbol{\zeta}(\omega))$ to a multi-index, $\boldsymbol{\alpha}^i = (\alpha^i_1, ..., \alpha^i_d)$, with non negative integer components, where α^i_j indicates the order of the jth one-dimensional Hermite polynomial in the ith multidimensional Hermite polynomial. Once the multi-indices are constructed, evaluation of the multidimensional basis is quite simply performed via a tensor product. Together, knowledge of the one dimensional basis functions and the multi-indices provide a very convenient means of evaluating multidimensional polynomial chaos expansions.

$$H_{\alpha^i}(\boldsymbol{\zeta}(\omega)) = H_{\alpha^i}(\zeta_1(\omega), ..., \zeta_d(\omega)) = \prod_{j=1}^{d} H_{\boldsymbol{\alpha}^i_j}(\zeta_j(\omega))$$

$\{H_{\alpha^i}(\boldsymbol{\zeta}(\omega))\}$ forms an orthonormal basis in the Hilbert space $L^2(\mathbb{R}^d, \mu^d)$, where $\boldsymbol{\zeta}(\omega) = (\zeta_1(\omega), ..., \zeta_d(\omega))$, and μ^d is a d-dimensional measure on $\mathbb{R}^d$. Suppose $f(\boldsymbol{\zeta}(\omega))$ is a random function such that $\mathrm{E}[f^2(\boldsymbol{\zeta}(\omega))] < \infty$, then $f(.) \in L^2(\mathbb{R}^d, \mu^d)$, and the Fourier-Hermite expansion exists. This expansion must be truncated in two ways, in the number of random variables and the total order of the Wick products. Limiting the number of random variables to d and the total order of the Wick products to

O leads to an expansion with $N = \frac{(O+d)!}{O!d!}$ terms. One limits the total polynomial order of the Wick products by defining the index set:

$$I_O = \{\boldsymbol{\alpha} :| \boldsymbol{\alpha} | \leq O\}$$

where $| \boldsymbol{\alpha} | = \alpha_1 + ... + \alpha_d$.

B.2 Multi-Index Construction

To complete the construction, one needs to define the multi-indices. Multiple definition are available, but we adopt the same indexing scheme as used by Ghanem and Spanos [26]. In this scheme, multi-indices are defined recursively for arbitrary total order, O, and stochastic dimensions, d, as follows:

For the zeroth order polynomials set:
$\alpha_j^0 = 0, \forall j = 1, ..., d$
If $O = 0$, the process finishes here.

For the d first order polynomials, set:
$\alpha_j^i = \delta_{ij}, \forall i = 1, ..., d, j = 1, ..., d$
If $O = 1$, the process finishes here.
Set $p = d$.
Set $p_i(1) = 1, \forall i = 1, ..., d$
For $k = 2, ..., O$:
    Set $l = p$
    Set $p_i(k) = \sum_{m=1}^{d} p_m(k-1), \forall i = 1, ..., d$
    For $j = 1, ..., d$:
        For $m = l - p_j(k) + n, \forall n = 1, ..., l$
            Set $p = p + 1$
            Set $\boldsymbol{\alpha}_i^p = \boldsymbol{\alpha}_i^m, \forall i = 1, ..., d$
            Set $\boldsymbol{\alpha}_i^p = \boldsymbol{\alpha}_i^p + 1$

For a given k, l denotes the number of terms constructed thus far with order less than k. The terms of order k are then constructed from the terms of order $k-1$ by increasing the order of the factors in those terms belonging to a specific dimensions, one at a time. The terms of current order, where the order of the contribution of dimension j will be increased to get terms at the next order, are the terms that

were generated at the current order from the previous order by increasing the order of dimension j. This bookkeeping is done by $p_i(k)$.

B.3 Python Code for WCE on Tensor or Sparse Grids

```
import numpy
import numpy.polynomial.hermite_e as herm
import math
import SpectralToolbox
from SpectralToolbox import HeterogeneousSparseGrids, Spectral1D

def factorial(k):
    if k == 0 or k == 1:
        return 1
    else:
        i = 1
        while k≥1:
            i = i*k; k = k - 1
        return i

class SparseChaos:
    def __init__(self, o, d, lmax, sparse = True):
        self.ord = o
        self.dim = d
        self.lmax = lmax
        self.nterms = int(math.ceil(factorial(o + d)/(factorial(o)*factorial(d))))
        if sparse == True:
            self.z, self.w = self.sparse_colloc_grid()
        else:
            self.z, self.w = self.tensor_colloc_grid()
        self.nsc = len(self.w)
        self.multi_index()
        self.prods = self.multi_prod()

    def tensor_colloc_grid(self):
```

```
        n = int(math.ceil(0.5*(self.ord + 1))) + 1
        nsc = int(n**self.dim)
        z, w = herm.hermegauss(n)
        w = (1/numpy.sqrt(2*numpy.pi))*w
        zg = numpy.zeros((nsc, self.dim)); wg = numpy.zeros(nsc)
        if self.dim == 1:
                index = - 1
                for i in range(n):
                        index = index + 1
                        zg[index] = z[i]
                        wg[index] = w[i]
        elif self.dim == 2:
                index = - 1
                for i in range(n):
                        for j in range(n):
                                index = index + 1
                                zg[index,0] = z[i]; zg[index,1] = z[j]
                                wg[index] = w[i]*w[j]
        elif self.dim == 4:
        index = - 1
                for i in range(n):
                        for j in range(n):
                                for k in range(n):
                                        for m in range(n):
                                                index = index + 1
                                                zg[index,0] = z[i]; zg[index,1] = z[j]
                                                zg[index,2] = z[k]; zg[index,3] = z[m]
                                                wg[index] = w[i]*w[j]*w[k]*w[m]
        return zg, wg

def sparse_colloc_grid(self):
        polys = []
        for i in range(self.dim):
                p = Spectral1D.Poly1D(Spectral1D.HERMITEP_PROB, None)
                polys.append(p)
        levels = [self.lmax]*dim
        sg = HeterogeneousSparseGrids.HSparseGrid(polys, levels)
        (full_grid, weights, partial_grid) = sg.sparseGrid()
```

```
        zg = numpy.array(partial_grid); wg = numpy.array(weights)
        return zg, wg

    def multi_index(self):
        # reference: Ghanem, R., Spanos, P.
        # Stochastic Finite Elements: A Spectral Approach
        multi = numpy.zeros((self.nterms, self.dim))
        # 0th order polynomials
        multi[0, : ] = 0
        if self.ord == 0:
            return multi
        # 1st order polynomials
        for i in range(self.dim):
            multi[i+1, i] = 1
        if self.ord == 1:
            return multi
        # polynomials of 2nd order and higher
        P = self.dim
        p = numpy.zeros((self.dim, self.ord)); p[:, 0] = 1
        for k in range(1, self.ord):
            L = P
            for i in range(self.dim):
                for m in range(i,self.dim):
                    p[i,k] = p[i, k] + p[m, k-1]
            for j in range(self.dim):
                for n in range(int(L - p[j, k] + 1), int(L)+1):
                    P = P + 1
                    for i in range(self.dim):
                        multi[P, i] = multi[n, i]
                    multi[P, j] = multi[P, j] + 1
        self.wick_indices= multi
        return multi

    def all_numeric_1dhermite(self):
        if self.ord == 0:
            num_herm_1d = numpy.ones((len(self.z), self.dim, self.ord+1))
        else:
            num_herm_1d = numpy.zeros((len(self.z), self.dim, self.ord+1))
```

```
                num_herm_1d[:, :, 0] = 1; num_herm_1d[:, :, 1] = self.z
                for i in range(2, self.ord + 1):
                        num_herm_1d[:,:,i] = self.z*num_herm_1d[:, : ,i-1]
                        - (i-1)*num_herm_1d[:, :, i-2]
        self.num_herm_1d = num_herm_1d
        return num_herm_1d

    def all_numeric_ndhermite(self):
        num_herm_1d = self.all_numeric_1dhermite()
        num_herm_nd = numpy.zeros((self.nterms, len(self.z)))
        for k in range(len(self.z)):
                for i in range(self.nterms):
                        val = 1
                        for j in range(self.dim):
                                val = val*num_herm_1d[k, j, int(self.wick_indices[i, j])]
                        num_herm_nd[i,k] = val
        self.num_herm_nd = num_herm_nd
        return num_herm_nd

    def prod(self, i, j):
        if i == j:
                return factorial(i)
        else:
                return 0

    def multi_prod(self):
        prods = numpy.ones((self.nterms, 1))
        for i in range(self.nterms):
                for j in range(self.dim):
                        order = self.wick_indices[i, j]
                        prods[i] = prods[i]*factorial(order)
        self.prods = prods
        return prods

    def comp_expansion(self, data):
        num_herm_nd = self.all_numeric_ndhermite()
        coeffs = numpy.zeros((self.nterms, numpy.size(data, 1)), dtype = com-
plex)
```

```
            for i in range(self.nsc):
                wsc = self.w[i]
                lam = data[i,:]; lam = numpy.reshape(lam, (1, len(lam)))
                phi = self.num_herm_nd[:, i]
                phi = numpy.reshape(phi, (len(phi), 1))
                coeffs = coeffs + (wsc)*(numpy.dot(phi, lam))
            prods = numpy.tile(self.prods, numpy.size(data, 1))
            coeff = coeffs/prods
            self.coeffs = coeff
            return coeff

        def comp_mean(self):
            mu = self.coeffs[0, :]
            self.mu = mu
            return mu

        def comp_var(self):
            var = numpy.zeros(numpy.size(self.coeffs, 1))
            coeffs_square = numpy.square(numpy.real(self.coeffs[1:, :]))
            for i in range(len(var)):
                var[i] = sum(coeffs_square[:, i])
            self.var = var
            return var

        def sensitivity(self):
            mode_var = numpy.zeros((numpy.size(self.coeffs, 1), self.dim))
            norm_var = numpy.zeros((numpy.size(self.coeffs, 1), self.dim))
            for i in range(1, self.nterms):
                for j in range(self.dim):
                    if self.wick_indices[i, j]!=0.0:
                        mode_var[:, j] = mode_var[:, j] + numpy.square(abs(self.coeffs[i,
:]))
            for i in range(numpy.size(self.coeffs, 1)):
                norm_var[i, :] = mode_var[i, :]/sum(mode_var[i, :])
            return norm_var
```

C.1 Linear Combinations of Independent Normal Random Variables

If $Z_1 \sim \mathcal{N}(\mu_1, \sigma_1^2)$ and $Z_2 \sim \mathcal{N}(\mu_2, \sigma_2^2)$ are mutually independent normal random variables, then using moment generating functions it can be shown that $Z_1 + Z_2$ is also normally distributed. Noting that the moment generating function of a sum of independent random variables is the product of the corresponding moment generating functions, we have the moment generating function of Z_1, Z_2 and Z_1+Z_2,

$$M_{Z_1}(t) = E[\exp(tZ_1)] = \int_{-\infty}^{\infty} \exp(tZ_1) \frac{1}{\sqrt{2\pi\sigma_1^2}} \exp(-\frac{(Z_1-\mu_1)^2}{\sigma_1^2}) = \exp(t\mu_1 + \frac{1}{2}\sigma_1^2 t^2) \tag{3}$$

$$M_{Z_2}(t) = E[\exp(tZ_2)] = \int_{-\infty}^{\infty} \exp(tZ_2) \frac{1}{\sqrt{2\pi\sigma_2^2}} \exp(-\frac{(Z_2-\mu_2)^2}{\sigma_2^2}) = \exp(t\mu_2 + \frac{1}{2}\sigma_2^2 t^2) \tag{4}$$

$\mathrm{M}_{Z_1+Z_2}(t) = E[\exp(t(Z_1+Z_2))] = E[\exp(tZ_1)]E[\exp(tZ_2)] = M_{Z_1}(t)M_{Z_2}(t) = \exp(t\mu_1 + \frac{1}{2}\sigma_1^2 t^2)\exp(t\mu_2 + \frac{1}{2}\sigma_2^2 t^2) = \exp(t(\mu_1+\mu_2) + \frac{1}{2}(\sigma_1^2+\sigma_2^2)t^2)$

Noting that the moment generating function uniquely defines all the moments of a distribution, and hence uniquely defines the distribution, it is clear that the moment generating function of Z_1+Z_2 is that of a normal random variable with mean $\mu_1+\mu_2$ and variance $\sigma_1^2+\sigma_2^2$. That is $Z_1+Z_2 \sim \mathcal{N}(\mu_1+\mu_2, \sigma_1^2+\sigma_2^2)$, from which it follows that a linear combination of independent normal random variables is itself normal.

Bibliography

[1] Krishna B Athreya and Soumendra N Lahiri. Measure theory and probability theory. 2006. 31

[2] Kendall E Atkinson. *The numerical solution of integral equations of the second kind*. Number 4. Cambridge university press, 1997. 87

[3] Gunter Baszenski and Franz-Jürgen Delvos. Multivariate boolean midpoint rules. *INTERNATIONAL SERIES OF NUMERICAL MATHEMATICS*, pages 1–1, 1993. 26

[4] Bruce J Bayly, Steven A Orszag, and Thorwald Herbert. Instability mechanisms in shear-flow transition. *Annual review of fluid mechanics*, **20**[1]:359–391, 1988. 57

[5] A Bensoussan and R Temam. Equations stochastiques du type navier-stokes. *Journal of Functional Analysis*, **13**[2]:195–222, 1973. 1

[6] Heinrich Blasius. *Grenzschichten in Flüssigkeiten mit kleiner Reibung*. Druck von BG Teubner, 1907. 155

[7] AV Boiko, KJA Westin, BGB Klingmann, VV Kozlov, and PH Alfredsson. Experiments in a boundary layer subjected to free stream turbulence. part 2. the role of ts-waves in the transition process. *Journal of Fluid Mechanics*, **281**:219–245, 1994. 152

[8] Thomas Bonk. A new algorithm for multi-dimensional adaptive numerical quadrature. In *Adaptive Methods—Algorithms, Theory and Applications*, pages 54–68. Springer, 1994. 26

[9] Alessandro Bottaro, Peter Corbett, and Paolo Luchini. The effect of base flow variation on flow stability. *Journal of Fluid Mechanics*, **476**:293–302, 2003. 4, 5, 190

[10] John P Boyd. *Chebyshev and Fourier spectral methods*. Courier Dover Publications, 2001. 51

[11] R. H. Cameron and W. T. Martin. The orthogonal development of nonlinear func- tionals in series of fourier-hermite functionals. *Ann. Math*, **48**:385–392, 1947. 3, 16, 23

[12] D. H. Chun and W. H. Schwarz. Stability of the plane incompressible viscous wall jet subjected to small disturbances. *The Physics of Fluids*, **10**[5]:911–915, 1967. 193

[13] Richard Courant and David Hilbert. *Methods of mathematical physics*, **1**. CUP Archive, 1966. 18

[14] Barry J Crowley and Christopher J Atkin. Investigation of the discrete effects of suction in large scale arrays for laminar flow control. In *34th AIAA Applied Aerodynamics Conference*, page 3117, 2016. 77

[15] C. H. Su D. Xiu, D. Lucor and G. E. Karniadakis. Stochastic modeling of flow-structure interactions using generalized polynomial chaos. *J. Fluid Engrg*, **124**:51–59, 2002. 4

[16] P. J. Davis and P. Rabinowitz. Methods of numerical integration. *Academic Press, San Diego*, 1984. 8

[17] Philip J Davis and Philip Rabinowitz. Methods of numerical integration. 1975. 26

[18] F.J. Delvos. d-variate boolean interpolation. *J. Approx. Theory*, **34**:99–114, 1982. 28

[19] Philip G Drazin and William Hill Reid. *Hydrodynamic stability*. Cambridge university press, 2004. 151, 169

[20] H Fasel and U Konzelmann. Non-parallel stability of a flat-plate boundary layer using the complete navier-stokes equations. *Journal of Fluid Mechanics*, **221**:311–347, 1990. 151

[21] Bruce A Finlayson. *The method of weighted residuals and variational principles*, **73**. SIAM, 2013. 14

[22] Ragnar Fjørtoft. *Application of integral theorems in deriving criteria of stability for laminar flows and for the baroclinic circular vortex*. Grøndahl søns boktr. I kommisjon hos Cammermeyers boghandel, Oslo, 1950. 36

[23] Roger Fletcher. *Practical methods of optimization*. John Wiley & Sons, 2013. 81

[24] Robert A Frazer, William Neville Prichard Jones, and Sylvia W Skan. *Approximations to functions and to the solutions of differential equations*. HSMO, 1937. 14

[25] BG Galerkin. Series occurring in some problems of elastic stability of rods and plates. *Eng Bull*, **19**:897–908, 1915. 14

[26] Roger G Ghanem and Pol D Spanos. *Stochastic finite elements: a spectral approach*. Courier Corporation, 2003. 206

[27] David Gottlieb, Steven A Orszag, and CAMBRIDGE HYDRODYNAMICS INC MA. *Numerical analysis of spectral methods*. SIAM, 1977. 51

[28] Stef Graillat. A note on structured pseudospectra. *Journal of Computational and Applied Mathematics*, **191**[1]:68–76, 2006. 63

[29] L Håkan Gustavsson. Excitation of direct resonances in plane poiseuille flow. *Studies in Applied Mathematics*, **75**[3]:227–248, 1986. 67

[30] J. Uboe H. Holden, B. Øksendal and T. Zhang. *Stochastic Partial Differential Equations. A Modeling, White Noise Functional Approach*. Birkhauser, Boston, 1996. 3

[31] S. Harber. A modified monte carlo quadrature. *Mathematics of Computation*, 1966. 10

[32] J. Healey. Very stable boundary layer profiles with inflexion points. *Journal of Fluid Mechanics*, 2013. 150, 151, 196

[33] Dan Henningson. Comment on "transition in shear flows. nonlinear normality versus non-normal linearity"[phys. fluids 7, 3060 (1995)]. *Physics of Fluids*, **8**[8]:2257–2258, 1996. 43

[34] Dan S Henningson, Anders Lundbladh, and Arne V Johansson. A mechanism for bypass transition from localized disturbances in wall-bounded shear flows. *Journal of Fluid Mechanics*, **250**:169–207, 1993. 4

[35] Roger A Horn and Charles R Johnson. *Matrix analysis*. Cambridge university press, 1990. 63

[36] Daniel D Joseph. Stability of fluid motions. i, ii. *NASA STI/Recon Technical Report A*, **77**:12423, 1976. 40, 42

[37] B. Farrell K. Butler. Three-dimensional optimal perturbations in viscous shear flow. *Phys. Fuids*, 1992. 4, 69

[38] Kari Karhunen. *Über lineare Methoden in der Wahrscheinlichkeitsrechnung*, **37**. Universitat Helsinki, 1947. 11

[39] Tosio Kato. *Perturbation theory for linear operators*, **132**. springer, 1995. 57

[40] JM Kendall. Experimental study of disturbances produced in a pre-transitional laminar boundary layer by weak freestream turbulence. In *AIAA, 18th Fluid Dynamics and Plasmadynamics and Lasers Conference*, **1**, 1985. 152

[41] Peter E Kloeden and Eckhard Platen. *Numerical solution of stochastic differential equations*, **23**. Springer, 1992. 2

[42] Erwin Kreyszig and Edward J Norminton. *Advanced engineering mathematics*, **1002**. Wiley New York etc, 1993. 205

[43] Marten T Landahl. Wave breakdown and turbulence. *SIAM Journal on Applied Mathematics*, **28**[4]:735–756, 1975. 152

[44] MJ Lighthill. Group velocity. 1965. 37

[45] M Loève and Paul Lévy. Processus stochastiques et mouvement brownien. 1948. 11

[46] L. M. Mack. A numerical study of the temporal eigenvalue spectrum of the blasius boundary layer. *J. Fluid Mech*, **73**:497–520, 1976. 50

[47] O.L. Maitre and O.M. Knio. *Spectral Methods for Uncertainty Quantification: With Applications to Computational Fluid Dynamics*. Scientific Computation. Springer Netherlands, 2010. 11

[48] Michael D McKay, Richard J Beckman, and William J Conover. Comparison of three methods for selecting values of input variables in the analysis of output from a computer code. *Technometrics*, **21**[2]:239–245, 1979. 10, 95

[49] P. Mele, M. Morganti, M. F. Scibilia, and A. Lasek. Behavior of wall jet in laminar-to-turbulent transition. *AIAA Journal*, **24**:938, June 1986. 193

[50] James Mercer. Functions of positive and negative type, and their connection with the theory of integral equations. *Philosophical transactions of the royal society of London. Series A, containing papers of a mathematical or physical character*, pages 415–446, 1909. 11, 91

[51] Mark V Morkovin. On the many faces of transition. In *Viscous drag reduction*, pages 1–31. Springer, 1969. 151

[52] Erich Novak and Klaus Ritter. High dimensional integration of smooth functions over cubes. *Numerische Mathematik*, **75**[1]:79–97, 1996. 26, 30

[53] Erich Novak and Klaus Ritter. Simple cubature formulas with high polynomial exactness. *Constructive approximation*, **15**[4]:499–522, 1999. 26

[54] William M'F Orr. The stability or instability of the steady motions of a perfect liquid and of a viscous liquid. part ii: A viscous liquid. In *Proceedings of the Royal Irish Academy. Section A: Mathematical and Physical Sciences*, pages 69–138. JSTOR, 1907. 39, 42, 45, 151

[55] SA Orszag. Accurate solution of the orr-sommerfeld stability equation. *J. Fluid Mech*, **50**:659–703, 1971. 4

[56] Steven A Orszag. Numerical methods for the simulation of turbulence. *Physics of Fluids (1958-1988)*, **12**[12]:II–250, 1969. 51

[57] A. B. Owen. Monte carlo variance of scrambled equidistribution quadrature. *SIAM Journal of Numerical Analysis*, 1997. 11

[58] G. Papanicolaou. Wave propagation in an one-dimensional random medium. *SIAM J. Appl. Math*, **21**:13–18, 1971. 1

[59] G. Papanicolaou. Diffusion in random media. *Surveys in Applied Mathematics*, pages 205–255, 1995. 1

[60] Spassimir H Paskov and Joseph F Traub. Faster valuation of financial derivatives. *The Journal of Portfolio Management*, **22**[1]:113–123, 1995. 26

[61] V. C. Patel and M. R. Head. Some observations on skin friction and velocity profiles in fully developed pipe and channel flows. *J. Fluid mech*, **38**:181–201, 1996. 4

[62] KLEBANOF. PS. Effect of free-stream turbulence on a laminar boundary layer. In *Bulletin of the American Physical Society*, **16**, page 1323. AMER INST PHYSICS CIRCULATION FULFILLMENT DIV, 500 SUNNYSIDE BLVD, WOODBURY, NY 11797-2999, 1971. 152

[63] Carl Edward Rasmussen. Gaussian processes for machine learning. 2006. 86

[64] Lord Rayleigh. On the stability, or instability, of certain fluid motions. *Proceedings of the London Mathematical Society*, **1**[1]:57–72, 1879. 36

[65] Lord Rayleigh. On the stability, or instability, of certain fluid motions. *Proceedings of the London Mathematical Society*, **1**[1]:57–72, 1879. 150

[66] Satish C Reddy and Dan S Henningson. Energy growth in viscous channel flows. *Journal of Fluid Mechanics*, **252**:209–238, 1993. 77

[67] Satish C Reddy, Peter J Schmid, and Dan S Henningson. Pseudospectra of the orr-sommerfeld operator. *SIAM Journal on Applied Mathematics*, **53**[1]:15–47, 1993. 64, 77

[68] Osborne Reynolds. An experimental investigation of the circumstances which determine whether the motion of water shall be direct or sinuous, and of the law of resistance in parallel channels. *Proceedings of the royal society of London*, **35**[224-226]:84–99, 1883. 36

[69] Osborne Reynolds. On the dynamical theory of incompressible viscous fluids and the determination of the criterion. *Proceedings of the Royal Society of London*, **56**[336-339]:40–45, 1894. 42

[70] Siegfried M Rump. Structured perturbations part i: Normwise distances. *SIAM Journal on Matrix Analysis and Applications*, **25**[1]:1–30, 2003. 63

[71] Siegfried M. Rump. Eigenvalues, pseudospectrum and structured perturbations. *Linear Algebra and its Applications*, **413**[2]:567 – 593, 2006. Special Issue on the 11th Conference of the International Linear Algebra Society, Coimbra, 2004. 62, 115

[72] Andrea Saltelli. Sensitivity analysis for importance assessment. *Risk Analysis*, **22**[3]:579–590, 2002. 32

[73] Andrea Saltelli, Marco Ratto, Terry Andres, Francesca Campolongo, Jessica Cariboni, Debora Gatelli, Michaela Saisana, and Stefano Tarantola. *Global sensitivity analysis: the primer*. John Wiley & Sons, 2008. 30

[74] H. Schlichting. Berechnung der anfachung kleiner storungen bei der plattenstromung. *ZAMM*, **13**:171–174, 1933. 50

[75] Peter J Schmid and Dan S Henningson. *Stability and transition in shear flows*, **142**. Springer, 2001. 39, 55, 66

[76] James Serrin. On the stability of viscous fluid motions. *Archive for Rational Mechanics and Analysis*, **3**[1]:1–13, 1959. 42

[77] Peter Shirley et al. Discrepancy as a quality measure for sample distributions. In *Proc. Eurographics*, **91**, pages 183–194, 1991. 10

[78] S.A. Smolyak. Quadrature and interpolation formula for tensor products of certain classes of functions. *Dokl. Akad. Nauk*, **4**:240–243, 1963. 25

[79] Ilya M Sobol. *A primer for the Monte Carlo method*. CRC press, 1994. 8

[80] Il'ya Meerovich Sobol'. On sensitivity estimation for nonlinear mathematical models. *Matematicheskoe Modelirovanie*, **2**[1]:112–118, 1990. 32

[81] Ilya M Sobol. Global sensitivity indices for nonlinear mathematical models and their monte carlo estimates. *Mathematics and computers in simulation*, **55**[1-3]:271–280, 2001. 32

[82] A. Sommerfeld. Ein beitrag zur hydrodynamischen erklarung der turbulenten flussigkeitbewegungen. *Atti. dei 4. Congr. Internat. dei Mat. III*, 1908. 45, 151

[83] HB Squire. On the stability for three-dimensional disturbances of viscous fluid flow between parallel walls. *Proceedings of the Royal Society of London. Series A*, **142**[847]:621–628, 1933. 45

[84] Walter Tollmien. Über die entstehung der turbulenz. 1. mitteilung. *Nachrichten von der Gesellschaft der Wissenschaften zu Göttingen, Mathematisch-Physikalische Klasse*, **1929**:21–44, 1928. 150, 151

[85] Walter Tollmien. *Ein allgemeines kriterium der instabilität laminarer geschwindigkeitsverteilungen*. Vandenhoeck & Ruprecht, 1935. 50

[86] Lloyd Nicholas Trefethen and Mark Embree. *Spectra and pseudospectra: the behavior of nonnormal matrices and operators*. Princeton University Press, 2005. 4, 59, 61, 115

[87] LLOYDN TREFETHEN, Annee Trefethen, Satishc Reddy, Tobina Driscoll, et al. Hydrodynamic stability without eigenvalues. *Science*, **261**[5121]:578–584, 1993. 57, 77

[88] Yutaka Tsuji, Yoshinobu Morikawa, Toshihiro Nagatani, and Masaaki Sakou. The stability of a two-dimensional wall jet. *Aeronautical Quarterly*, **28**[4]:235–246, 1977. 193

[89] A Mazel W E, K Khanin and Y Sinai. Invariant measures for burgers equation with stochastic forcing. *Ann. Math*, **151**:877–960, 2000. 1

[90] E Weinan and ERIC VANDEN EIJNDEN. Statistical theory for the stochastic burgers equation in the inviscid limit. *Communications on Pure and Applied Mathematics*, **53**[7]:852–901, 2000. 1

[91] E Weinan, Konstantin Khanin, Alexandre Mazel, and Yakov Sinai. Probability distribution functions for the random forced burgers equation. *Physical review letters*, **78**[10]:1904, 1997. 1

[92] Norbert Wiener. The homogeneous chaos. *American Journal of Mathematics*, pages 897–936, 1938. 3

[93] David Williams. *Probability with martingales*. Cambridge university press, 1991. 31

[94] D. Xiu and G. E. Karnidakis. The wiener-askey polynomial chaos for stochastic differential equations. *SIAM J. Sci. Comput*, **24**:619–644, 2002. 3

[95] C. Zenger. *Notes on Numerical Fluid Mechanics*, **31**. Springer, 1991. 28